The Elasticity of Iron Alloys at Extreme Conditions

Eric Edmund

Thèse de Doctorat
Sorbonne Université

École Doctorale 397 - Physique et Chimie des Matériaux

The Elasticity of Iron-Alloys at Extreme Conditions

Présentée et soutenue par

Eric Edmund

Thèse dirigée par Daniele Antonangeli et Frédéric Decremps

réalisée à l'Institut de Minéralogie, de Physique des Matériaux et de Cosmochimie

soutenue le 24 octobre 2018

Jury :

Laurent Belliard	Sorbonne Université	Examinateur
Tiziana Boffa-Ballaran	BGI	Examinatrice
Giulio Monaco	Trento University	Rapporteur
Chrystèle Sanloup	Sorbonne Université	Examinatrice
Alexandre Schubnel	ENS	Rapporteur
Lidunka Vočadlo	UCL	Examinatrice
Frédéric Decremps	Sorbonne Université	Directeur de Thèse
Daniele Antonangeli	Sorbonne Université	Co-directeur de Thèse

Firstly I would like to thank my family and friends for sticking with me through thick and thin in this (at times) wild ride I've been on.

I would like to collectively thank the city of Paris for grimacing through my accent in my many attempts at speaking french.

I would like to thank a Mr. L. Dobinson for assistance with Python and scripting languages in general.

This project has been financed by Labex MATISSE

A postcard from my father which has remained on my desk these past few years reads:

"In the long run, we only hit what we aim at"

Abstract

For nearly 40 years, there has been a robust seismological model (PREM - Preliminary Reference Earth Model) which reports the elastic properties (compressional velocity - Vp, shear velocity - Vs, and density - ρ) of the Earth's interior, and yet there is still no clear consensus on the composition of the material which can match such properties at the pressures and temperatures of the core, the metallic portion of the planet. While iron has elastic properties which are close to those of the solid inner core, iron alone is too heavy to match the density (ρ) of the inner core. In light of this, and based on a series of cosmochemical and geochemical arguments, Si has been proposed for many years in varying quantities as a material which could explain the difference in material properties between Fe and PREM. Furthermore, Fe-Si alloys are important technological materials which are common in a wide variety of different industries.

Using a combination of Synchrotron X-ray Diffraction and Picosecond Acoustics, ρ and Vp of Fe-Si and Fe-Ni-Si alloys have been measured to pressures and temperatures exceeding 1 Mbar and 2000 K. This is the the first systematic experimental study of Fe alloys performed under quasihydrostatic conditions, using a direct method for the measurement of acoustic travel time at extreme conditions. Noteworthy, these studies were performed on well-characterized samples of high quality, synthesized by novel methods.

Obtained data allows an accurate determination of Velocity-Density relations, both P-V and P-V-T equations of state, and axial ratios of a variety of technologically and geophysically important Fe-Si and Fe-Ni-Si alloys. These results are used to discuss the elastic properties of Fe-Si alloys at high pressure - high temperature conditions in relation to Si concentration and Si ordering, and to place tight constraints on Si abundance in the Earth's inner core.

Contents

Chapter 1

Introduction

While seismic observations can provide direct measurements of the elastic properties of the Earth's deep interior, taken alone they cannot provide information on its chemical composition. However, the comparison of the compressional sound velocity (V_P) and density (ρ) of the Earth's metallic inner core with V_P and ρ for candidate core materials is one of the most effective ways to constrain core composition, which in turn is critical to our comprehension of the behaviour of the Earth's core, having wide-reaching geophysical and geochemical implications. As such, the elastic properties of iron and iron alloys at high pressures and temperatures underpins our knowledge of the composition and dynamics of the Earth's deep interior.

In this context, alloys of iron and silicon have been studied for decades in order to elucidate their potential role in the Earth's core (e.g. [Balchan and Cowan, 1966], [Lin et al., 2003a], [Antonangeli et al., 2018]). Despite the concerted effort to discern the properties of these alloys, there remains strong disagreement between different studies (e.g. [Lin et al., 2003b], [Fischer et al., 2014] for P-V, [Antonangeli et al., 2010], [Liu et al., 2016] for Vp-ρ) at ambient temperature and high pressure, let alone at simultaneous high temperatures and pressures - the conditions of direct relevance to geophysics.

A major limitation to the development of good systematic compositional constraints to the alloying effects of Fe-Si alloys is due to the dependence of these high-pressure studies on access to synchrotron light sources. Access to such facilities is necessarily limited and infrequent, and in the case of studies of Vp, the collection times are long, limiting data coverage.

Thanks to the advent of Picosecond Acoustics (PA), it is now possible to make direct measurements of acoustic echoes (as in classical ultrasonics) in metals and optically-opaque samples, and to do so in the form of a laboratory-based tabletop experiment which can be used up to Mbar pressures. In this Thesis, for the first time, PA has been used in conjunction with synchrotron X-ray diffraction experiments in order to determine the Pressure-Volume or Pressure-Volume-Temperature Equations of State (EoS), and V_P-ρ relations of Fe-Si and Fe-Ni-Si alloys as a function of pressure, temperature and composition. All ambient-temperature high-pressure experiments were performed under quasihydrostatic conditions, measuring Vp and P-V EoS up to pressures exceeding 1.2 Mbar. P-V-T EoS were determined to P-T conditions exceeding 1.1 Mbar and 2100 K.

As a result of this dataset, in Section 3 we discuss the effect of Si ordering on the physical properties of bcc-structured Fe-Si alloys, in particular their elastic and mechanical properties. This is of significant metallurgical importance, as bcc iron-silicon alloys are widely used for technological and industrial applications due to their useful magnetic and elastic properties, and low cost (e.g. [Jayaraman et al., 2018], [Fiorillo, 1996]).

In Section 4, we present results on hcp-structured Fe-Si (and Fe-Ni-Si) alloys which were measured under quasihydrostatic conditions up to 1.3 Mbar by XRD and PA. For Fe-5wt%Si we successfully performed isothermal compression at high temperatures using a laser-heated diamond anvil cell (DAC) up to 1.1 Mbar and 2100 K (and up to 90 GPa and 1500 K for Fe-5wt%Ni-5wt%Si). On the basis of Vp-ρ relations and the experimentally-derived P-V-T EoS for Fe-5wt%Si, we observe that the density and Vp of a binary Fe-Si alloy extrapolated to the P-T conditions of the Earth's inner core is incompatible with seismic observations. Notably, this is the first time that isothermal compression experiments have been performed successfully at high temperatures in a laser-heated DAC on either Fe or an Fe-alloy, marking an important technical step in the characterization of material properties at extreme conditions, coupled with the measurement of Vp of an Fe-Si alloy with unprecedented data coverage at high pressures, over an extremely wide range of densities ($\sim$2g/cm^3).

Furthermore, we also derive shear velocities for Fe5Si, showing that Si-alloying increases shear velocities relative to hcp-Fe, in addition to providing new insights on the thermoelastic properties of Fe-alloys at the conditions of the Earth's inner core. We measured c/a axial ratios of Fe-Si and Fe-Ni-Si alloys. These have been measured as a function of pressure and temperature in order to constrain the elastic anisotropy of these alloys with respect to hcp Fe and assess their suitability as core candidate materials in light of the seismic anisotropy observed in the Earth's inner core [Deuss, 2014].

Finally, the results of PA experiments under both hydrostatic and non-hydrostatic conditions have been used to benchmark synchrotron-based high-pressure velocity measurements, by constraining the effects of non-hydrostatic stress on bcc and hcp Fe-Si alloys, in addition to critically assessing reported literature.

1.1 High Pressure Physics and the Diamond Anvil Cell

The act of applying pressure on a material, at the most basic level, forces atoms closer together. This simple act can result in drastic reorganization of the atomic or electronic structure of even simple materials, and causes dramatic changes in material properties. Emblematic is the case of Li - while it is generally regarded as the archetypal free-electron metal at ambient pressures and temperatures, at high pressures it reorganizes into incredibly complex structures and can exhibit superconductivity with a fairly high Tc ([Guillaume et al., 2011], [Hanfland et al., 2000], [Schaeffer et al., 2015]). In the case of Fe, the ambient pressure bcc structure rearranges into an hcp structure, which is believed to be stable to the pressures and temperatures of the Earth's inner core ([Mao et al., 1967], [Tateno et al., 2010]). However to achieve such extremes of pressure and temperature (P = 329-364 GPa, T = 5000-7000 K), it was a very long road which began in earnest in the early 1900s.

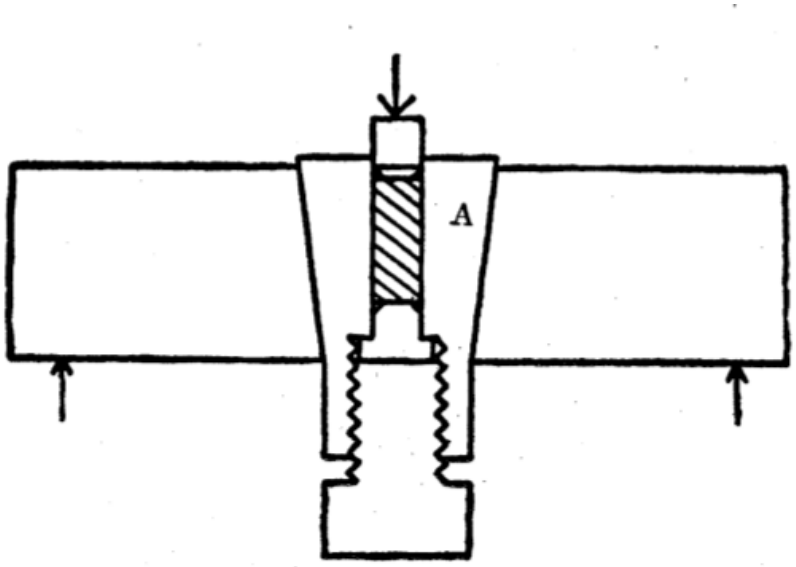

Figure 1.1: Schematic of a Bridgman opposed-anvil device ([Bridgman, 1946]). The critical innovation was that the force applied on one face of the apparatus also acts to contain the sample chamber (striped rectangle).

Until an important technical realization by Percy Bridgman in 1906, the pressure domain of high pressure physics (at static pressure) was limited to about 0.01 GPa due to problems with containing the sample and the massive stresses exerted on the high-pressure apparatus. The important advance that Bridgman made, was by incorporating a metal insert that was also compressed around the sample (one design shown in Figure 1.1), as due to frictional forces, such a setup produces well-contained pressures and reduces the risk of blow-outs of the apparatus.

While greatly improved relative to what was previously attainable, static pressures could be produced up to 7-10 GPa, much less than what is expected in the Earth's deep interior - up to 364 GPa. The principle of high pressure devices is simple - place something heavy (such as a tank of water or apply hydraulic pressure)

on a small object through a piston and observe what happens.

$$Pressure = \frac{Force}{Area} \tag{1.1}$$

In order to generate greater pressures, most of the earlier work attempted to apply greater and greater forces to the materials. However there was a roadblock which was reached due to the finite strength of materials. Due to scientific preference for big, bulky machines, it took a long time for the use of diamond to catch on as a way of applying pressure on samples. By equipping a miniaturized version of Bridgman's opposed anvil press with tiny diamond anvils, the first conventional Diamond Anvil Cell was made [Jamieson et al., 1959].

Diamond is the hardest bulk material known, and by using this material to apply pressure, it is possible to regularly achieve pressures exceeding 3 Mbar on a given sample.

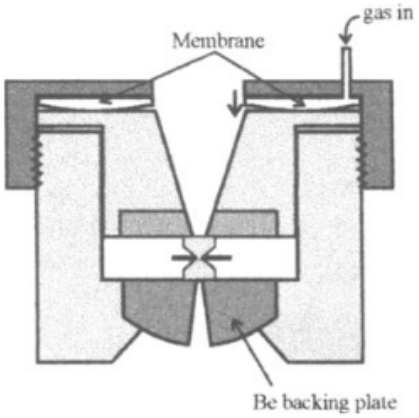

Figure 1.2: Schematic of a membrane-driven Diamond Anvil Cell (DAC) ([Soignard and McMillan, 2004]). A membrane inflates with gas in order to apply force onto an opposing pair of diamond anvils.

A modern DAC is shown in Figure 1.2. In this device, two parallel diamonds (Fig. 2.1) are cut to have flat opposed surfaces (referred to hereafter as the culets) that transmit pressure onto a gasket and a sample chamber. Force is applied on the diamonds through the use of either screws or a gas membrane which presses on the frame of the DAC. By varying the size of the diamond culets it is possible to generate multi-Mbar pressures on the sample chamber by pressing on the frame with up to 150 bar of membrane pressure.

The design of the sample chamber is critically important for producing high quality data, and depends on the type of experiment. The types of layout (type of loading) produced in this thesis involved two main setups: sample chambers loaded with noble gas media (Neon) and sample chambers for high-pressure high-temperature experiments. Pictures of the sample chamber of a gas loaded DAC at increasingly high pressures are shown in Figure 1.3. In such experiments, as Neon is considered to have relatively low shear strength compared to most materials under high pressure conditions, it readily deforms around the sample. This causes a nearly

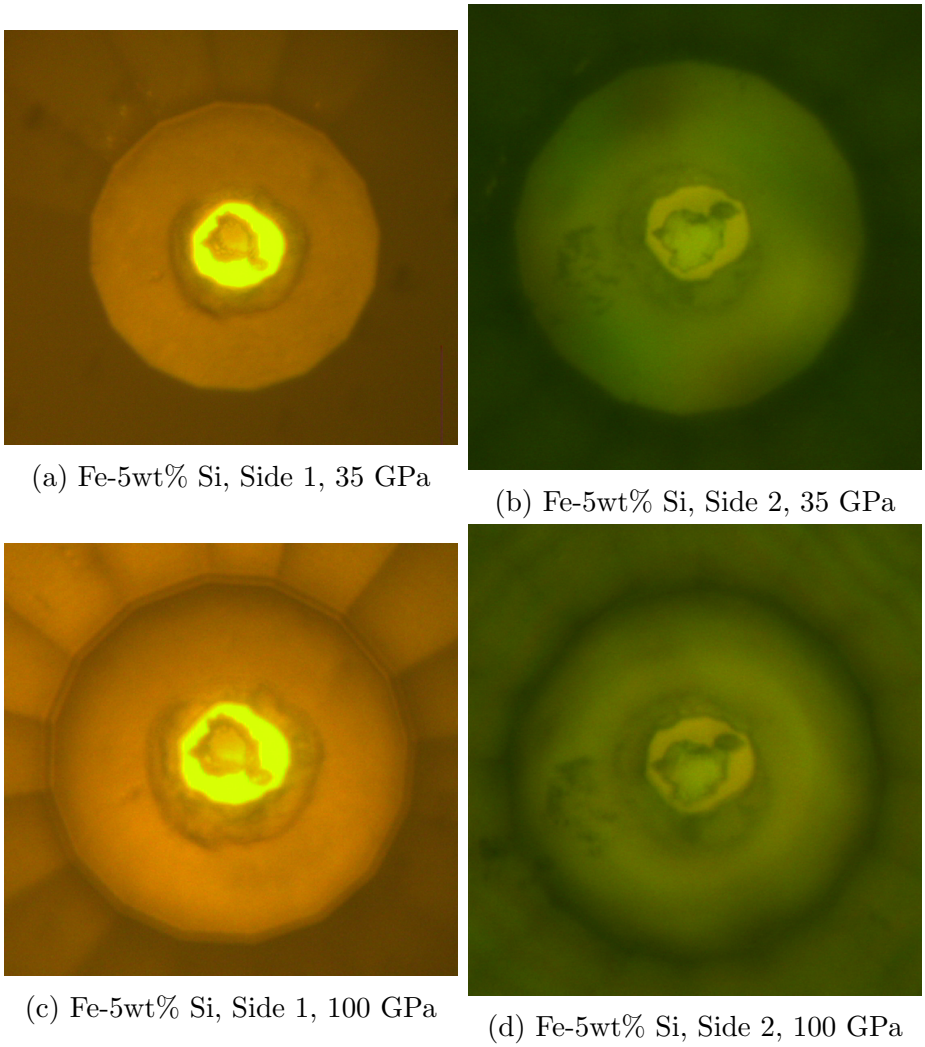

(a) Fe-5wt% Si, Side 1, 35 GPa

(b) Fe-5wt% Si, Side 2, 35 GPa

(c) Fe-5wt% Si, Side 1, 100 GPa

(d) Fe-5wt% Si, Side 2, 100 GPa

Figure 1.3: Fe-5wt% Si in Ne at high pressures. Neon PTM allows for quasi-hydrostatic conditions to extremely high pressures. Cupping (bending) of the $100/300\mu m$ beveled culets can be observed from the comparison of Side 2 at 35 GPa and 100 GPa. A small ruby chip is present in the sample chamber for pressure calibration.

uniform pressure distribution across the sample, resulting in a quasihydrostatic stress state [Klotz et al., 2009].

Such quasihydrostatic experiments are done with an internal pressure calibrant, allowing for the *in situ* measurement of sample pressure.

For high temperature experiments, as shown in Figure 1.4, the sample is sandwiched between potassium chloride (KCl) plates. KCl plates are used as this provides thermal and chemical insulation of the sample from the diamonds

While compression in KCl produces a more non-hydrostatic pressure in the sample chamber than Ne, it has a high melting point and is a good thermal insulator. At high temperatures, diamond both acts as a source of C contamination and a strong heat sink. For experiments using laser heating where there is only a local heating of the sample within the sample chamber, the loss of heat through the dia-

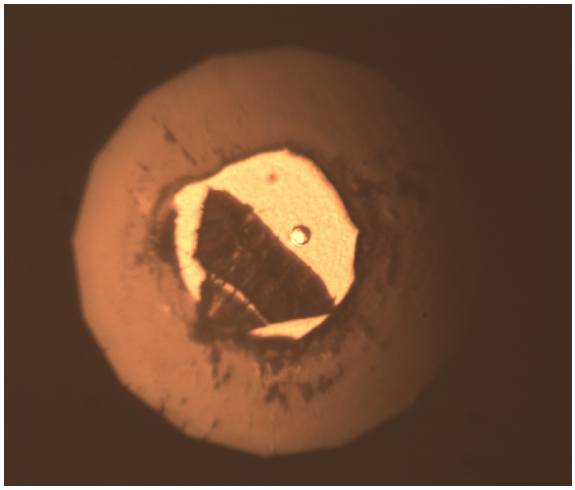

Figure 1.4: Sample chamber of a loading of Fe-10wt% Si in KCl PTM at 40 GPa before laser heating. A ruby is present as the calibrant for pressure determination.

monds can inhibit the heating of the sample. Furthermore, for Synchrotron X-ray diffraction experiments at high temperatures, the KCl can act as a calibrant for the measurement of pressure at high P-T conditions [Dewaele et al., 2012]. While KCl is a relatively stiff pressure-transmitting medium (PTM) at ambient temperature, high temperatures act to relax pressure gradients within the sample and KCl.

1.2 The Evolution of the Early Earth and the Composition of the Earth's Core

In the 15th and 16th century, it became accepted knowledge that magnetic north on a compass does not necessarily point towards the 'true' magnetic north [Norman, 1581]. As a result, in 1692, it was postulated that there was some 'inner globe' or 'nucleus' within the Earth, surrounded by liquid which was separate from the exterior of the Earth [Halley, 1692].

While this model remained largely unconstrained and ignored for the next few centuries, at the turn of the 20th century, the advent of the seismometer in 1880s revolutionized our capacity for elucidating the secrets of the Earth's interior. By 1906, Richard Oldham had determined that there was a seismic discontinuity deep within the Earth indicative of a large change in density and sound velocities - now known to mark the change between the rocky silicate mantle and metallic core. In 1936, Inge Lehmann was the first to interpret seismic signals coming from the 'shadow zone' of the Earth's liquid outer core as the signature of a solid inner core. Over the following decades, the modern view of the Earth's Crust, Mantle, and Core began to develop, with the most hotly contested large-scale questions being on the nature of the Earth's core [Brush, 1980]. Such questions have important ramifications for the accretionary history and dynamics of the Earth's interior.

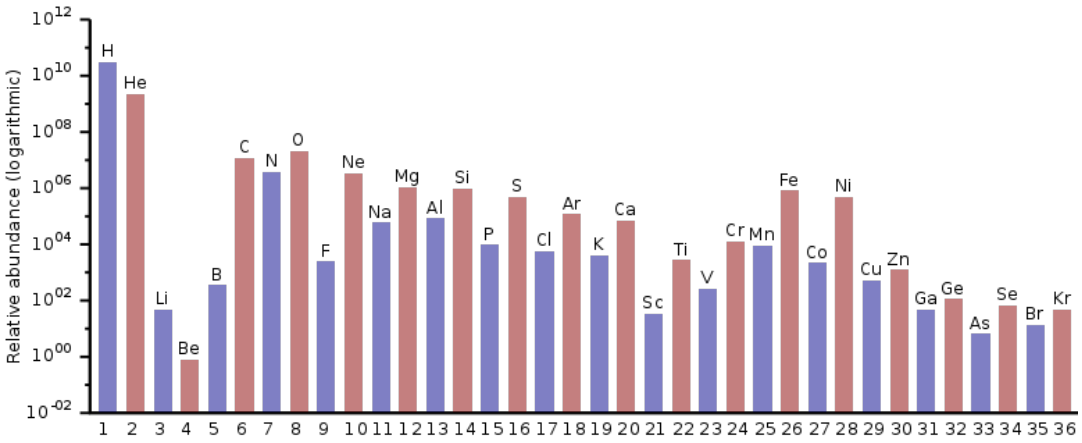

Figure 1.5: Estimated relative abundances of elements in the solar system up to Kr.

When the Earth was formed by the accretion of meteorites and planetesimals, this proto-Earth was initially completely or nearly-completely molten, composed of a homogeneous mix of elements based on their relative abundances within the starting meteorites and planetesimals.

To understand how these relative abundances arise, one must take a look to the processes which form said elements. Stars sustain themselves primarily with the fusion of Hydrogen into Helium. At later stages in their life cycles, they become hotter and more dense, and start 'burning' progressively heavier elements as well. At the final stages of the life cycle of most stars, the stars undergo core collapse and cause a nova or supernova, and these violent explosions are the origin of most atoms heavier than helium up to iron. The specifics of these processes and the evolution

of the early Solar System resulted in the relative abundances seen today. Shown in Figure 1.5, purely on the grounds of abundance, C, N, O, Ne, Mg, Si, S, Fe and Ni could be present in significant quantities in a proto-Earth.

As the Earth cooled, it started to differentiate. The differentiation and evolution of the Earth is still not completely understood, but in general terms these processes was a result of the relative volatility of the elements, their chemical affinities to the main elemental components of the Earth, and the density of the minerals formed by the mixed elements. It is generally accepted that N and Ne (and maybe C) would initially form extremely volatile molecules with low boiling points, and would be rapidly lost to the interplanetary medium during accretion [Ringwood, 1966].

On the other hand, Si and O readily react to form silicates, which can accomodate significant quantities of alkali metals (Mg, Na, Ca etc.) which are sufficiently dense, and with boiling points sufficiently high, that they would remain on the proto-Earth during formation [McDonough and Sun, 1995]. While these silicates can account for a large quantity of the main elements of the proto-Earth, it is seen that Fe and Ni can dissolve in small quantities in silicates and vice-versa, the large quantities present in the initial proto-Earth would have been largely immiscible with liquid silicates [Ringwood, 1966].

Since Fe and Ni readily form alloys with each other, and are considerably denser

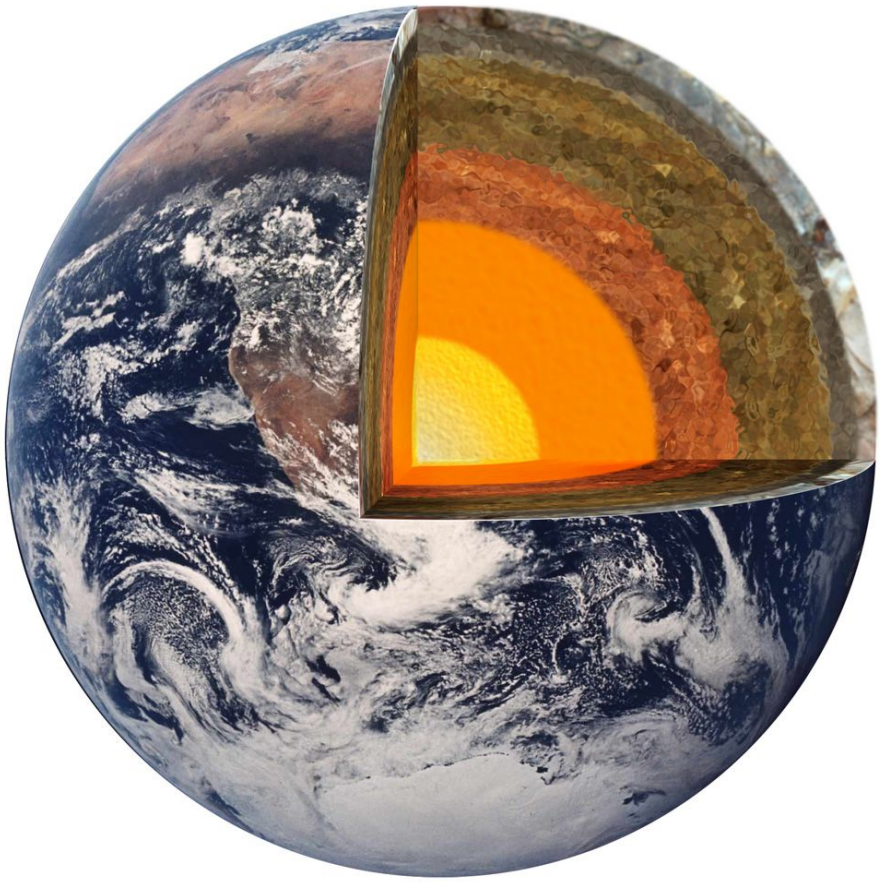

Figure 1.6: The Earth and it's layered interior.

than the silicates, they sank to the center of the Earth, forming a dense metallic core. This differentiation process is largely responsible for the structure of the Earth's interior, of an outer rocky crust and mantle, and a metallic core (Figure 1.6).

While Fe-alloy and silicate liquids are immiscible, most other elements in the Earth partition preferentially into one or the other. This results in an enrichment of lithophile elements in the mantle (elements which preferentially partition into liquid silicates), and an enrichment of siderophile (elements which preferentially partition into liquid iron) elements in the core. Furthermore, it is likely that core-mantle interaction continues to this day, however the nature and extent of this interaction is critically dependent on the quantity and type of elements, as certain elements such as Si and O both partition into Fe, but to a certain extent, do so under mutually exclusive redox conditions ([McCammon et al., 1983], [Hirose et al., 2017], [Ricolleau et al., 2011]).

Furthermore, as shown in Figure 1.6, the core (orange and yellow sections) consists of two layers - the solid inner (yellow in Figure 1.6) and liquid outer (orange in Figure 1.6) core. Along the geotherm, the P-T path through the Earth's interior, pressure and temperature increases with increasing depth. As seismological observations give no direct information on the thermal properties of the Earth's interior, the thermal profile of the Earth must be constrained by high-pressure high temperature melting experiments, and to anchor phase transitions and melting to seismological features within the Earth which indicate a change of phase. The inner-core boundary, which is the interface between solid and liquid iron alloys is the ideal structure for anchoring the thermal profile of the Earth's core system, as the geotherm must be above melting temperature at outer core conditions, and below melting temperature at inner core conditions. As the core is mostly made of iron, and light-element impurities tend to reduce melting temperature, the melting curve of pure Fe places upper bounds on the temperature of both the inner and outer core as shown in Figure 1.7.

At some point, the pressures in the Earth's core cause the melting temperature to exceed the temperature of the geotherm, and hence the deepest, innermost section of the Earth's interior is a crystalline solid as evidenced by the non-zero shear velocities observed for this area of the Earth [Dziewonski and Anderson, 1981].

It is impossible to directly sample material from the Earth's core, however certain physical properties of the Earth's inner and outer core can be determined by seismology. The study of the propagation of seismic waves and free oscillations provides (among other geophysical observables) values for the density (ρ), compressional sound velocity (V_P) and shear sound velocity (V_S) as a function of depth within the Earth, with the first robust model being the Preliminary Reference Earth Model (PREM, [Dziewonski and Anderson, 1981]). With the advent of new techniques for measuring materials at high P-T conditions (see Section 1.1) it was quickly observed that while Fe has properties not so dissimilar from the inner and outer core, it is far too dense at core P-T conditions to be the sole elemental constituent of the Earth's core (Figure 1.8).

Not only has there been abundant possibility over the Earth's history for the partitioning of elements (and more importantly light elements) between metal and

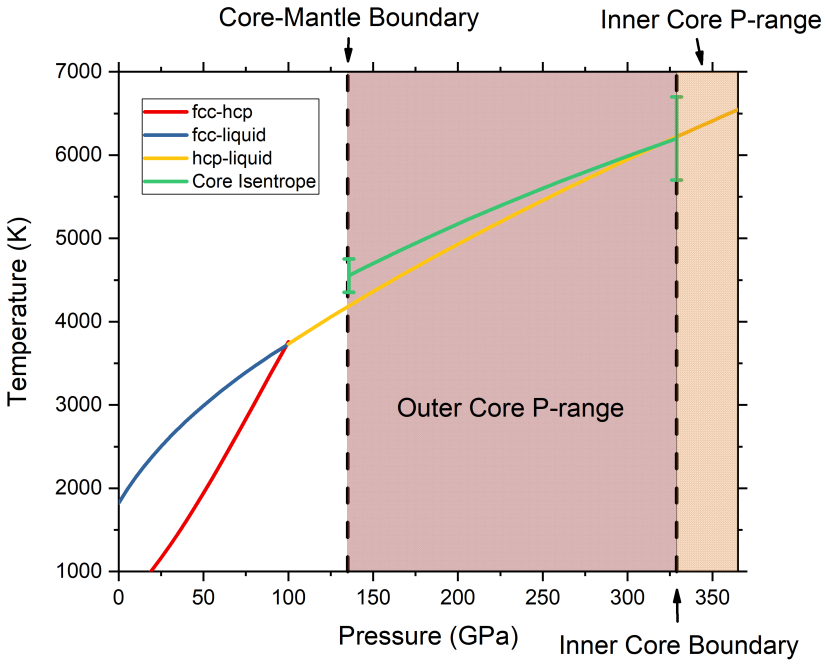

Figure 1.7: Phase Diagram of Fe after [Anzellini et al., 2013] and the outer core geotherm for a pure Fe core.

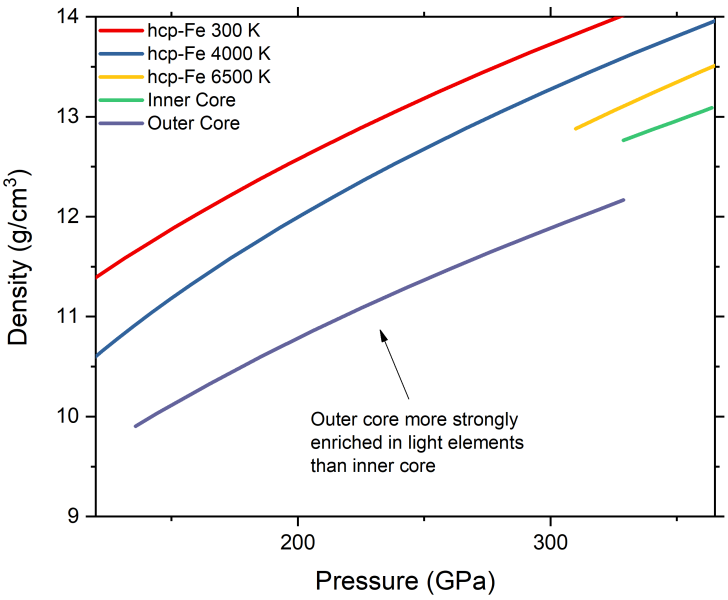

Figure 1.8: Density vs. Pressure for hcp-Fe at different temperatures [Fei et al., 2016] and PREM [Dziewonski and Anderson, 1981].

silicates, but there must be some significant quantity of light elements within the Earth's core in order to compensate for the density mismatch between Fe and seismological models such as PREM.

There is a case to be made for a variety of different elements, and the main candidates for core light element candidates are H, C, O, S and Si based on a variety of arguments. Each light element when reacted with iron produces different effect on the phase diagram, elastic and thermal properties of the Fe-alloy, and with the careful, systematic study of these materials it is possible to elucidate which of these elements (or mix of elements) may adequately describe core properties and structure. As the presence of each light element is inexorably linked to the mechanism which resulted in the light element being present, the presence or absence of each individual element within the Earth's core places tight constraints on the magnitude and extent of geochemical and geodynamical cycles within the Earth, in addition to the differentiation scenarios of the early proto-Earth [Badro et al., 2015]. As the presence of light elements also influences the melting temperature of Fe, the quantity and species of light element also places strong constraints on the geotherm and the bulk heat budget of the Earth's interior as it places constraints on the temperature at the core-mantle boundary and inner core boundary [Hirose et al., 2013].

Of these light elements, Si and C are of significant recent interest for the Earth's inner core. Si has perennially been regarded as the main light element candidate in the Earth's inner core for a variety of reasons. When modelling core formation from metal-silicate partitioning, virtually all modern models result in some quantity of Si being present in the Earth's inner core ([Wade and Wood, 2005], [Siebert et al., 2013], [Fischer et al., 2015]). Furthermore, on the basis of Mg/Si ratios in the mantle compared to the values of chondritic (undifferentiated) meteorites, shown in Figure 1.9, it is likely that the Earth's mantle is depleted in Si relative to the bulk Si budget of the Earth ([McDonough and Sun, 1995], [Fitoussi et al., 2009]).

Not only this, but Si partitions approximately evenly between solid and liquid Fe, meaning that a large portion of the Si present in the liquid outer core would remain present after solidification [Morard et al., 2014]. An important caveat of the presence or absence of Si in the Earth's inner core is that it is tightly linked to the presence or absence of O within the outer core. Si and O both partition into liquid Fe, but under different redox conditions which have important ramifications for the geochemistry which occurs at lower mantle conditions ([Wood et al., 1990], [Frost and Mccammon, 2008]). Notably it has been shown recently that in fact, Si and O can be simultaneously present in liquid Fe at high temperatures, but cannot be simultaneously present in significant quantities in the outer core [Hirose et al., 2017] as the result of crystallization of SiO_2 from core cooling.

While for a long time carbon was considered to be a volatile element, lost during planetary accretion [Poirier, 1994], it has been recently suggested to be present in the inner core to account for the anomalously low value of Vs measured through seismological observations in the inner core [Prescher et al., 2015]. It is well known that in certain regions of the mantle, there are significant quantities of C-bearing minerals and fluids [Hammouda, 2003]. More recently, it has been suggested that there may be a geochemical C-cycle within the mantle [Dasgupta and Hirschmann, 2010] and that carbon chemistry in the deep Earth may reach the core-mantle boundary [Satish-Kumar et al., 2011]. This can potentially provide a mechanism for the introduction of C into the Earth's core. However the properties of Fe-C alloys at

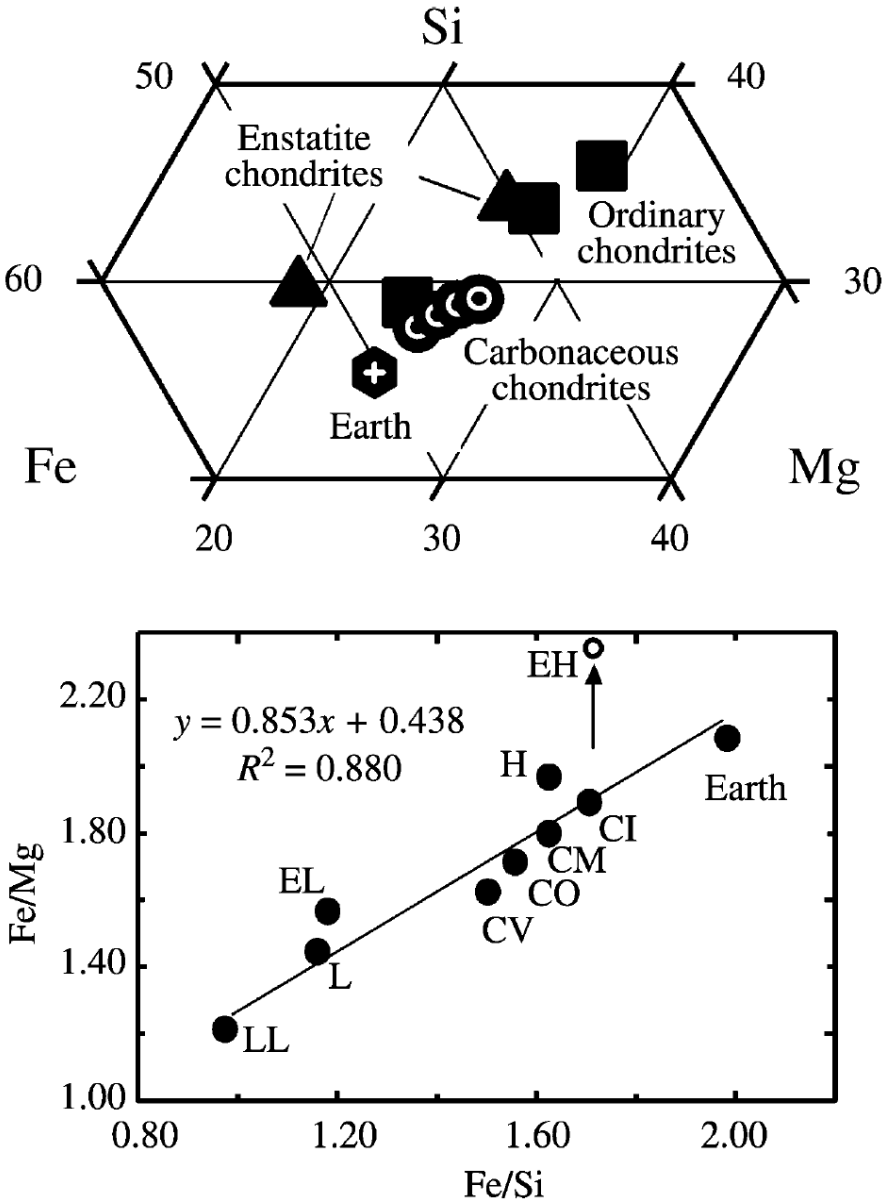

Figure 1.9: Ratio between Mg, Si and Fe for the bulk Earth and undifferentiated meteorites [McDonough, 2003].

these conditions, and even the phase diagram of these materials at relevant P-T conditions of the Earth's inner core is not well known.

A consistent asterisk in the study of Fe-alloys is the role that Ni plays within the core. On the basis of cosmochemical arguments, there is likely 5-15 wt% Ni alloyed with Fe in the Earth's core, however the effect of Ni on the alloy is generally regarded as negligible at this concentration based on a variety of studies ([Mao et al., 1990], [Martorell et al., 2013], [Wakamatsu et al., 2018], [Morrison et al., 2018]).

As a consequence of the potential importance of iron alloys with Si or C in the Earth's inner core, these alloys were measured and compose the main body of work within the Thesis. Some work was also done on Fe-Ni-Si alloys to examine potential

differences between Fe-Si and Fe-Ni-Si alloys, all of which is outlined further in the coming chapters.

1.3 Mineral Physics Constraints from X-Ray Diffraction in a Diamond Anvil Cell

In the context of mineral physics, the earliest tried-and-true method for constraining core composition with static compression experiments was by X-Ray Diffraction at high pressures. By measuring the evolution of density with Pressure and Temperature, it is possible to fit an Equation of State (EoS) and to use said EoS to extrapolate density and other derived quantities to core conditions. In this way, it is possible to place constraints on core composition. Due to the technical challenges of performing measurements on a sample only few microns thick through multiple mm of diamond, XRD was one of the first experimental methods adapted to the Diamond Anvil Cell (DAC) [Jamieson et al., 1959].

The Earth's inner core exists at pressures from 329-364 GPa [Dziewonski and Anderson, 1981] and temperatures of 4000-7000 K estimated by the melting temperature of Fe at these pressures ([Boehler, 1993], [Alfè et al., 2002], [Nguyen and Holmes, 2004], [Anzellini et al., 2013]). Consequently it is important to not only constrain the compressional properties of these alloys at high pressure, but to as well incorporate the effects of high temperature. While dynamic compression experiments have been used since the infancy of deep Earth geophysics to constrain the properties of the Earth's core and mantle, standard shock-compression can only measure along a defined P-T path depending on the strength of the shock generated in the sample. A major current effort in research employing dyanmic compression is the generation shock states off the hugoniot [Smith et al., 2014], [Wicks et al., 2018]. With such techniques, while it is possible to measure density of a material to TPa pressures at high temperatures, the effects of temperature and pressure on the sample are inextricably linked. Additionally, dynamic compression experiments are expensive, and provide limited information over a very short time-scale, inhibiting the measurement of many potentially interesting properties at these high P-T conditions. Thanks to the utility of DACs and the wide variety of tools and techniques available, in the last two decades there has been significant advances in the development of novel high-temperature instrumentation for the measurement of properties at simultaneous high pressures and temperatures. In this way, *in situ* laser heating of DACs has become an increasingly commonplace utility for measurement of material properties at extreme conditions, and especially so for XRD.

While it has been possible for a long time to generate high temperatures with a Laser-Heated Diamond Anvil Cell (LH-DAC) only recent advances in instrumentation have provided for good stability of the temperature profile over time, in conjunction with the development of reliable, consistent measurements of sample temperature. Indeed, it is an exciting time in the field of mineral physics thanks to the modern instrumental capacity to perform high-quality measurements of sample properties at the utmost extremes of pressure and temperature.

Early into the study of Fe-alloys, Si was proposed as an element in the Earth's outer core by the pioneering work of [Balchan and Cowan, 1966]. In this study, they showed using dynamic compression that an Fe-Si alloy containing 20 wt% percent Si could potentially match the density of the outer core at the relevant pressures. Shown in Figure 1.10a it can be seen that at some point along the P-T

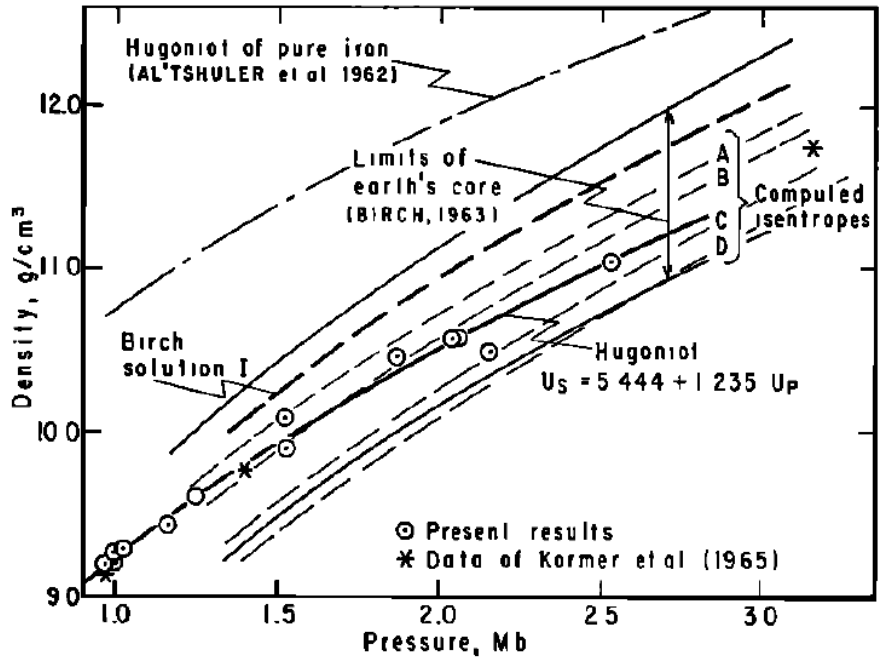

(a) The results of shock compression experiments, comparing Fe-20wt%Si to the density-pressure curves of the Earth's outer core.

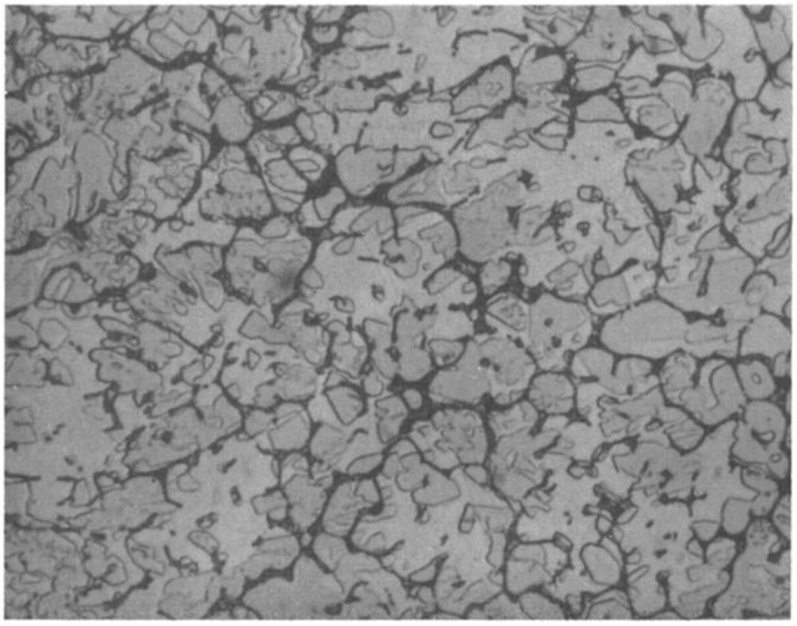

(b) Electron Micrograph of starting materials showing significant heterogeneity of the starting material, including a large quantity of tungsten impurities.

Figure 1.10: Early shock compression experiments in the Fe-xSi system [Balchan and Cowan, 1966].

path of the shock data, the density of this alloy crosses the density proposed for the outer core. However, this early study was plagued by problems stemming from

the potential uncertainties due to significant chemical inhomogeneity of the starting material as seen in Figure 1.10b showing an electron micrograph of the employed starting material.

While the Fe-Si system was studied by shock compression over a large compositional range ([Matassov, 1977], [Marsh, 1980]), it would require nearly two decades after these studies for static compression experiments to begin placing new constraints on the compressional behaviour of Fe-Si alloys in relation to the Earth's core. Due to the experimental challenges and initial lack of knowledge about the potential light element composition of the Earth's core, the first of such experiments focused on the study of bcc Fe-Si alloys. Dilute Fe-Si alloys referred to as Silicon Steel have been used since the early to mid 1900s as soft magnetic materials, used for transformers to convert direct currents into alternating currents [González Cámara and Houbaert, 2013]. More generally this class of steels is commonplace in applications requiring low coefficients of magnetostriction, as magnetostriction results in a significant loss of efficiency during power generation, or in applications where alternating currents or magnetic fields are passed through the material [Carr and Smoluchowski, 1951]. Iron-Silicon alloys were studied in this context relatively early on in the field of high pressure ([Bridgman, 1957], [Clendenen and Drickamer, 1966]), although these two studies would remain the only published articles on statically compressed samples until the 1990s. Performed on dilute Fe-Si alloys, aside from the 'negative compressibility' observed for Fe3Si [Clendenen and Drickamer, 1966], showed very little variation with respect to iron within instrumental error. The first 'modern' studies on the Fe-Si system were those of [Knittle and Williams, 1995] and Wood [Wood et al., 1996], the former ruling out Si in the core on the grounds of the high bulk modulus of the B20 phase of stoichiometric B20 FeSi, with the latter arguing that the bulk modulus is comparable to Fe. This study and the other experimental studies of B20 FeSi are shown in Figure 1.11 ([Knittle and Williams, 1995], [Wood et al., 1996], [Guyot et al., 1997], [Lin et al., 2003a], [Whitaker et al., 2009], [Fischer et al., 2014]). While the two original studies provide upper and lower bounds to the proposed equation of state parameters for this material, there is little systematic consistency between different datasets. A more thorough examination, and partial resolution of experimental discrepancies in stoichiometric FeSi will be discussed in section 4.1.5, both for B20 FeSi and its high pressure phase B2 FeSi.

An important progression in the study of Fe-xSi alloys however, was the shift towards off-stoichiometric alloys, which allow for a more robust comparison of material properties to the seismological observables of the Earth's core. [Zhang and Guyot, 1999] presented the first of such studies in the context of geophysics, performing co-compression experiments on Fe and Fe-9wt% Si, in order to directly compare how Si changes the compressional behaviour of Fe at high pressures and temperatures, indicating that Si addition acts to slightly soften Fe at these conditions. Following that, [Lin et al., 2003a] was the first study to determine the equation of state of the hcp phase of an Fe-Si alloy, performing static compression experiments on Fe-8wt%Si (Fe8Si), Fe-17wt%Si (Fe17Si) and B20 FeSi. Not only this, but they compressed the samples in an ethanol:methanol:water mixture, allowing for improved hydrostaticity under compression at low pressures - a detail of significant importance in the later chapters of this Thesis. In doing so they showed that an

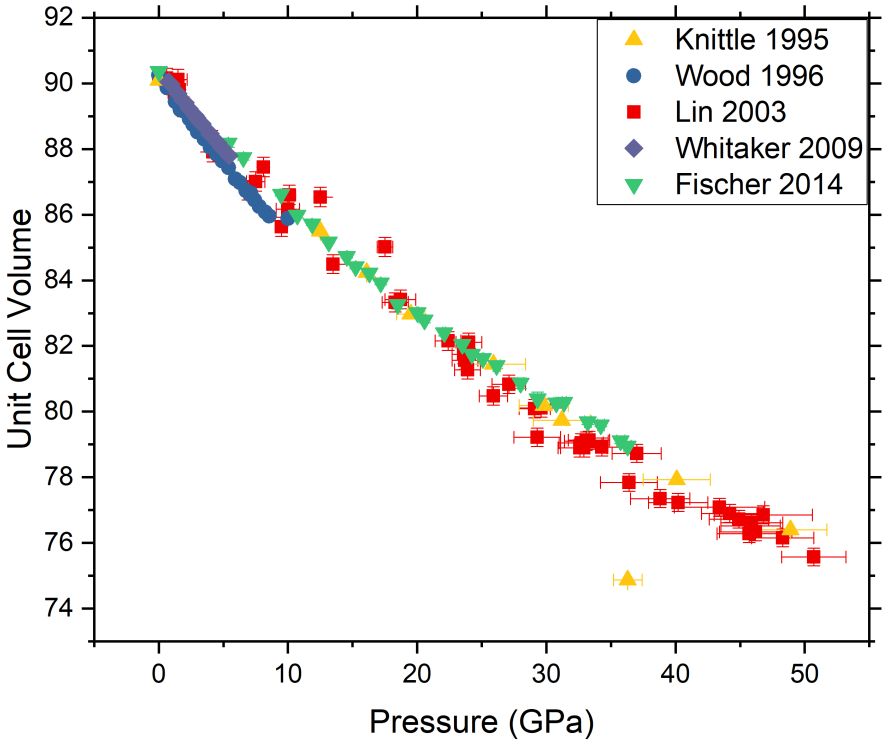

Figure 1.11: Pressure-Volume Equations of State of B20 FeSi from [Knittle and Williams, 1995], [Wood et al., 1996], [Lin et al., 2003a], [Whitaker et al., 2009], [Fischer et al., 2014].

iron-silicon alloy can match the density of both the outer (8-10 wt% Si) and inner core ($\sim$ 4wt% Si). As following studies performed experiments under an increasingly wide range of P-T conditions, additional complexity arose due to the effects of measurement under different experimental conditions. [Hirao et al., 2004] measured similar alloy compositions to [Lin et al., 2003a] (Fe9Si and Fe18Si) to pressures exceeding 1 Mbar at ambient temperature, however the measurements were performed under non-hydrostatic conditions, as they compressed the sample using no pressure-transmitting medium, resulting in P-V relations in nearly complete disagreement with previous works. [Asanuma et al., 2011] extended the measurement of Fe-Si and Fe-Ni-Si alloys to pressures comparable to that of the Earth's inner core, although again performed under non-hydrostatic conditions and with high resultant scatter in the measured P-V curve. Finally, Fischer 2012 and Fischer 2014 provided the most recent studies on the Fe-xSi system, measuring the P-V-T relations of Fe16Si ([Fischer et al., 2012]), Fe9Si, B20 and B2 FeSi ([Fischer et al., 2014]). A significant upgrade of the Fischer data was the use of Ne as the PTM for the ambient temperature experiments, using modern synchrotron sources for the measurements, and finally, all of this was coupled with studies at high temperatures exceeding 3000 K using laser heating. P-V relations of all off-stoichiometric bcc-like Fe-xSi alloys are shown in Figure 1.12a and 1.12b.

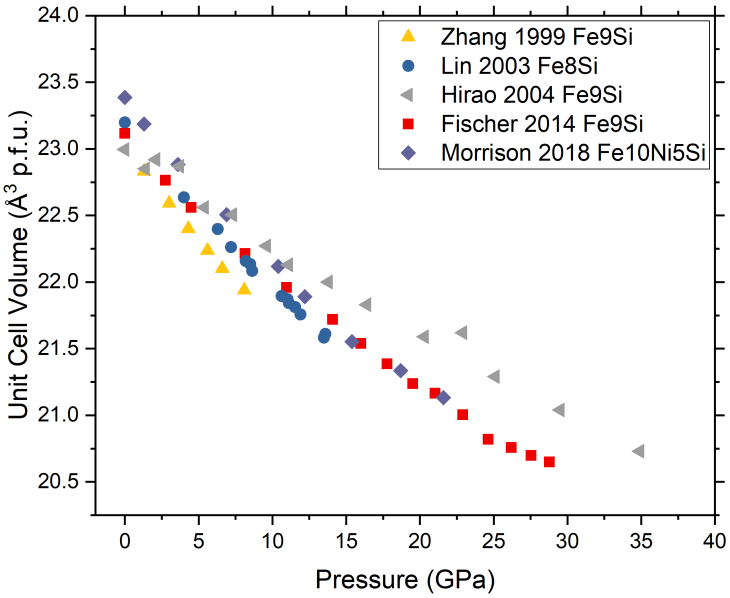

(a) Fe-xSi x = 5-9 wt%, [Zhang and Guyot, 1999], [Lin et al., 2003a], [Hirao et al., 2004], [Fischer et al., 2014] and [Morrison et al., 2018]

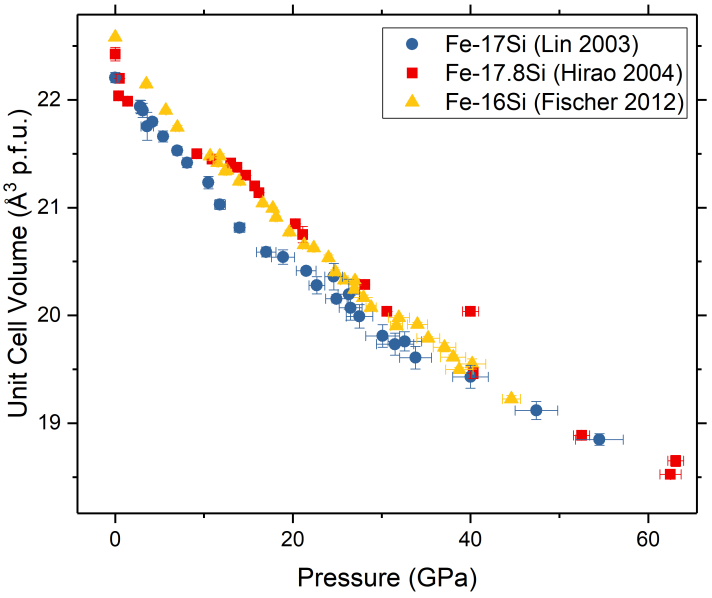

(b) Fe-xSi x = 16-18 wt% [Lin et al., 2003a], [Hirao et al., 2004], [Fischer et al., 2012]

Figure 1.12: Pressure-Volume relations for off-stoichiometric bcc and 'bcc-like' Fe-Si alloys.

For all of these studies, the bcc-like and B2 phases are the most well studied, and there is significantly less data available on hcp Fe-Si alloys. As the hcp-phase

is only accessible at high pressures, such alloys require careful measurements over exceedingly wide pressure ranges under quasihydrostatic conditions to well-constrain EoS parameters, as recently performed by [Morrison et al., 2018] for Fe-Ni and Fe-Ni-Si alloys.

Additionally, the pressure range of the bcc-hcp transition in Fe-xSi alloys is not well reproduced across different literature using similar alloy compositions. [Lin et al., 2003a] (Fe7.9Si) and [Morrison et al., 2018] (Fe-10Ni-5Si) report a phase transition from bcc to hcp starting at 12-13 GPa, whereas [Fischer et al., 2014] measured Fe9Si to 35 GPa and observed no evidence of a bcc-hcp transition at ambient conditions. While there are available equations of state for hcp-Fe-Si alloys shown in Figure 1.13, ([Lin et al., 2003a], [Hirao et al., 2004], [Asanuma et al., 2011], [Fischer et al., 2014], [Morrison et al., 2018]), it is still unclear as to the quality of previous literature or of quantitative trends in this system.

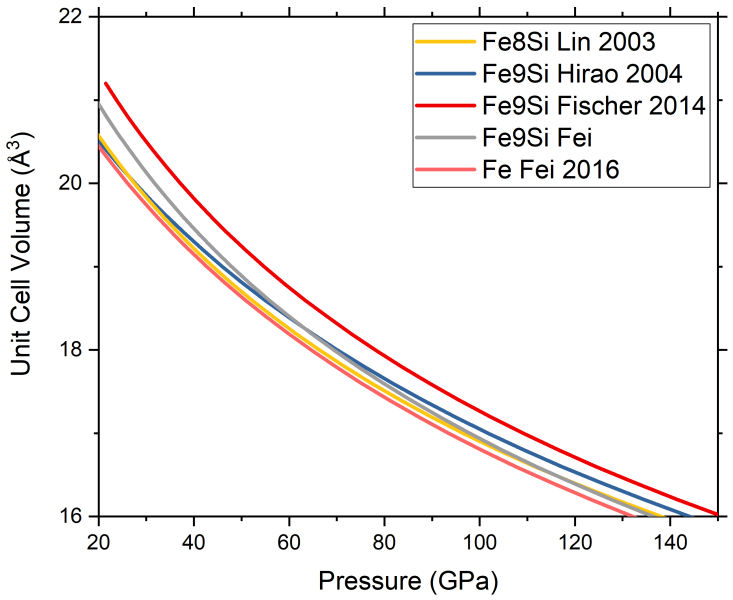

Figure 1.13: Selected 300 K EoS from literature on hcp Fe-Si and Fe-Ni-Si alloys ([Lin et al., 2003a], [Hirao et al., 2004], [Fischer et al., 2014], hcp-Fe9Si from Fei et al. is currently unpublished), compared to hcp-Fe [Fei et al., 2016].

All-in-all, while the compressional properties of Fe-Si alloys under high static pressure have been studied for a very long time, there is still little consensus on how these alloys behave at high pressures, let alone at high pressures and temperatures. As a result, it is difficult to critically assess the triumphs and drawbacks of Fe-Si literature due to the array of disagreeing results and conclusions. Fortunately, this paves the way for new insights into the mechanical and elastic properties of this class of alloys, has the potential to provide a new metrological baseline for the study of iron-alloys at high pressures, and to provide new, robust constraints on the chemical composition of the Earth's core.

1.4 The Elastic Properties of Iron Alloys and their Measurement

The measurement of sound wave propagation through elastic media has always been foundational to the understanding of the elastic and mechanical properties of materials, and the materials present in the Earth's interior remain as no exception. The velocity profiles of P and S waves which propagate through the Earth's core are strongly constrained by seismic observations, and are instrumental to the determination of the structure and properties of the Earth's deep interior.

On the basis of V_P and density measurements of a variety of rocks up to 1 GPa, [Birch, 1961] suggested an approximately linear evolution of V_P with density, an approximation still widely used in the study of the Earth's deep interior. Initial studies of sound wave propagation in minerals and metals at high static pressures relied on the use of ultrasonics. While ultrasonics remains the gold standard for the measurement of elastic properties of materials, it is a technique which is very limited in P-T space with respect to the temperatures and pressures expected in the Earth's core. Furthermore, most materials relevant to the Earth's mantle and core undergo phase transitions which can significantly alter their properties at relevant conditions of pressure and temperature ([Takahashi and Bassett, 1964], [Saxena et al., 1996]). As a consequence, with the advent of improved synchrotron radiation sources, new techniques were developed to extend V_P (and V_S) measurement to ever-higher conditions of P and T in order to place stronger constraints on the properties of geomaterials at conditions more comparable to that of the Earth's deep interior.

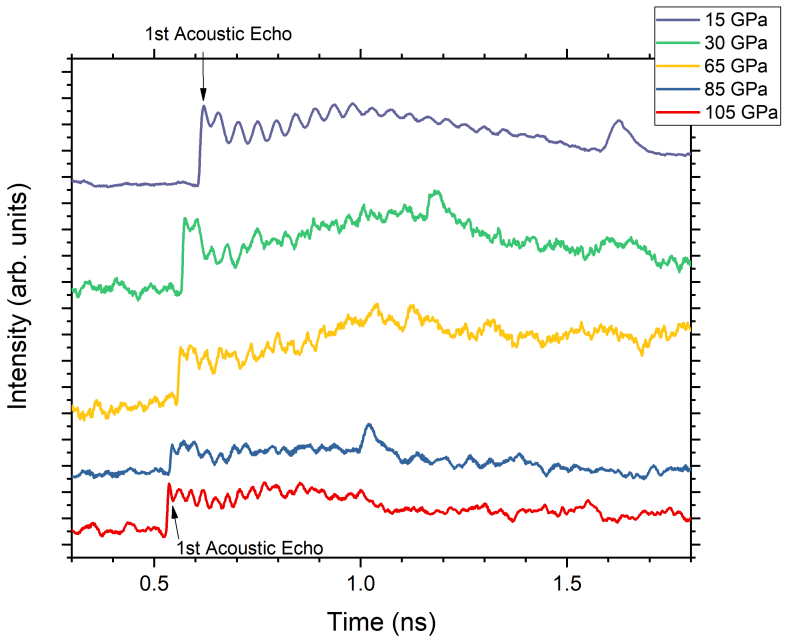

Figure 1.14: Measured time-domain reflectivity signals from a PA experiment up to 1 Mbar. It is seen that the first acoustic echo (used to determine the travel time of the sample) is well defined at all pressures.

These synchrotron techniques, while capable of measurements at pressures exceeding 1 Mbar ([Mao et al., 2001], [Fiquet et al., 2001]), are not direct measurements of the acoustic sound velocity of a material, they derive acoustic sound velocities from phonon measurements. Inelastic X-ray Scattering (IXS) measures phonon dispersion curves, and extrapolates these curves to the low wavelength limit to recover the compressional sound velocity and Nuclear-Resonant Inelastic X-ray Scattering (NRIXS) measures the phonon density-of-states of mössbauer isotopes, and uses this information to then derive the debye sound velocity (and hence V_P), assuming the EoS (and by extension the bulk modulus) of the measured material is known at pressure.

With the development of Picosecond Acoustics (PA), it is now possible to measure directly the travel time of acoustic echoes in metals and optically-opaque samples, as in classical ultrasonics, but to Mbar pressures [Decremps et al., 2014] as shown in Figure 1.14.

Not only that, but PA has less technical restrictions with respect to sample size and composition, which potentially allow for a wide range of applications in the realm of geophysics and material science.

With the development and popularization of IXS and NRIXS, the study of the V_P of hcp-Fe under static compression at Mbar pressures flourished in the 2000s, and after more than a decade of study using these new synchrotron-based techniques, there is an increasing consensus on V_P-ρ relations at ambient temperature across *ab initio* calculations and various experimental techniques, shown in Figure 1.15. Unfortunately, this consensus deteriorates strongly when considering iron alloys or the effects of high temperature.

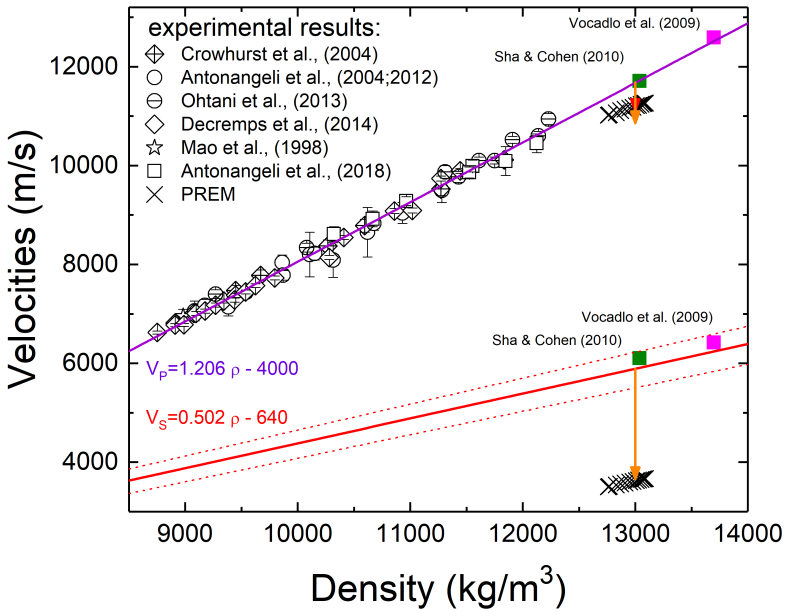

Figure 1.15: Velocity-Density relations for Vp and Vs for hcp-Fe after [Antonangeli et al., 2018] and [Antonangeli and Ohtani, 2015].

In fact, there have been questions as to whether Birch's law even applies to iron-alloys [Mao et al., 2012] at ambient temperatures, although more recent work has reaffirmed the (at least approximate) validity of Birch's law at ambient temperatures and core densities [Antonangeli et al., 2018]. Furthermore, in Fe and Fe-alloys, strong anharmonic effects are expected at high temperatures which act to reduce sound velocities at constant density, and a current open question is how to modify Birch's law (or some other functional form of the density-velocity relation) to accomodate such anharmonic effects ([Sakamaki et al., 2016], [Lin et al., 2005]). For the case of Fe-alloys, with the exception of end-members (e.g. FeSi, FeS, FeO, Fe3C, [Badro et al., 2007], [Fiquet et al., 2009]), there is generally little consensus between different studies done with different techniques. In the case of the Fe-xSi system, while IXS studies generally produce similar results when extrapolated to inner core densities ([Mao et al., 2012], [Antonangeli et al., 2018], [Sakairi et al., 2018]), they do not agree with NRIXS [Lin et al., 2003b], and poorly match with the results of ab initio calculations, as shown in Figure 1.16 ([Tsuchiya and Fujibuchi, 2009], [Martorell et al., 2016], [Li et al., 2018]). Despite the differences between extrapolated and calculated results on the expected magnitude Si alloying effects, it is seen in Figure 1.16 that there is a general agreement between different approaches, in that the effect of Si alloying on Vp decreases with increasing density (at ambient temperature).

Very recently, laser-heating has been used in conjunction with IXS measurements

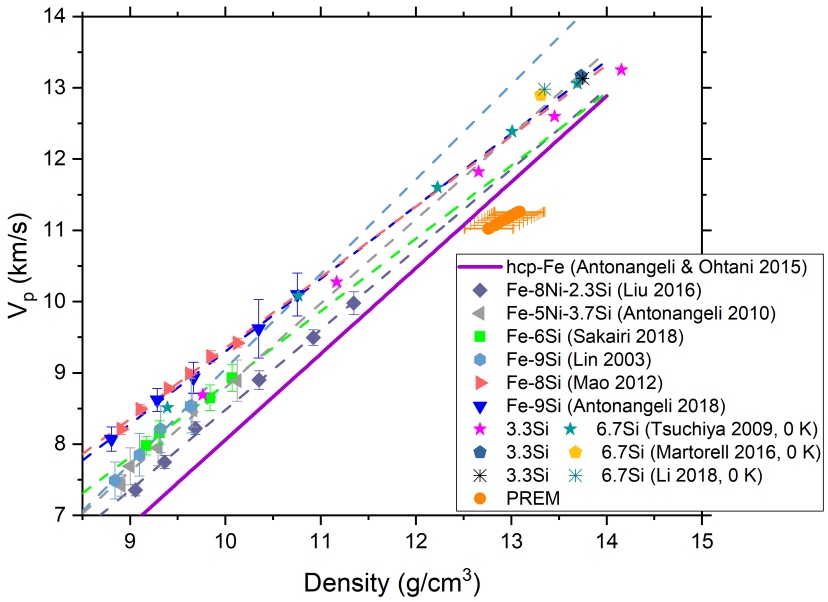

Figure 1.16: Vp vs density for Fe-Si and Fe-Ni-Si alloys [Lin et al., 2003b], [Tsuchiya and Fujibuchi, 2009], [Antonangeli et al., 2010], [Mao et al., 2012], [Liu et al., 2016], [Martorell et al., 2016], [Sakairi et al., 2018], [Antonangeli et al., 2018], [Li et al., 2018] compared to PREM [Dziewonski and Anderson, 1981] and hcp-Fe [Antonangeli and Ohtani, 2015]. In spite of the large scatter between individual studies, there is general agreement that Si decreases the slope of the Vp-ρ plot.

in order to constrain the Vp-ρ relations of iron and iron alloys at high temperatures ([Sakamaki et al., 2016], [Sakairi et al., 2018]). However, extrapolations of experimental data are critically dependent on the formalism used for extrapolations to core conditions, at present they do not agree with ab initio calculations on the magnitude of anharmonic effects, and do not agree with ab initio calculations on the compositional trends of anharmonic effects (discussed in depth in Section 4.2, [Martorell et al., 2016], [Li et al., 2018]). As a consequence, it is critically important to benchmark these studies against direct methods for the determination of sound velocities at high pressures, in order to better constrain material-specific and method-specific effects in the determination sound velocity at these extreme pressures and temperatures. In this way, experimental measurements of Vp using PA provides a unique opportunity to provide an experimental baseline for other techniques, and provide robust constraints on the properties and composition of the Earth's interior.

Chapter 2

Methods

2.1 High Pressure Generation

The DAC is a robust method for generating high static pressures, and was used in this thesis to generate pressures in excess of 130 GPa. The general idea is simple - Diamonds are glued into WC seats with epoxy, the diamond culets are carefully aligned with respect to each other, a metal gasket and sample chamber is prepared, and to achieve high pressures in the DAC, a force is applied to the DAC by a gas membrane.

2.1.1 Diamonds

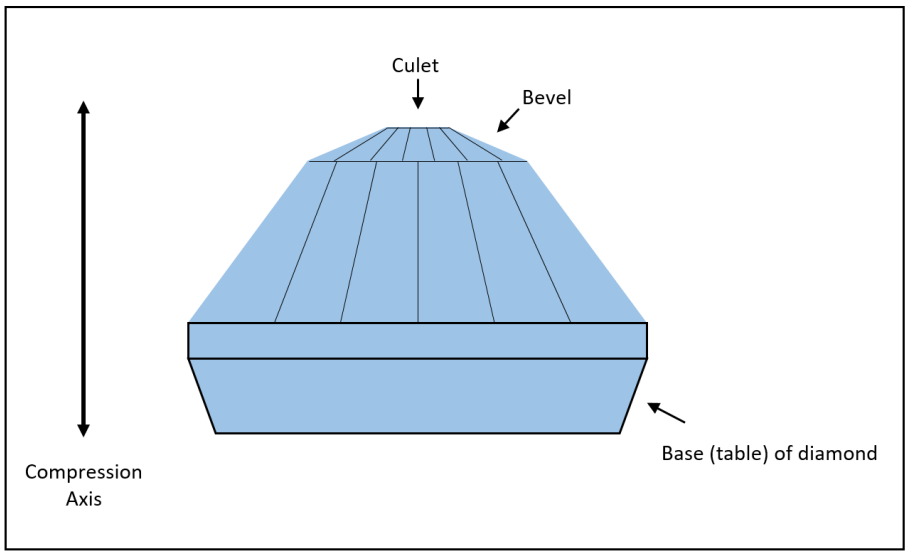

Figure 2.1: Schematic of a Boehler-Almax cut diamond anvil. The compression axis within a diamond anvil cell is shown for reference.

Shown in Figure 2.1 is the schematic of a bevelled Boehler-Almax diamond anvil. The principal features are as follows - 1) at the top is the flat diamond culet, where the sample and gasket are placed, 2) a shallow polishing is performed around the

culet, referred to as the bevel and 3) at the base of the diamond it is polished into a conical shape.

1) Force applied on a DAC is applied directly to the contact area between the diamond culets and the gasket.

2) The bevel acts to increase the range of pressures achievable before failure of the diamonds. At Mbar pressures, the stressed tip of the diamond bends and plastically deforms [Hemley et al., 1997], and so the bevel acts to support the culet under such conditions, to be deformed and damaged in place of the culet itself.

3) The conical base (Boehler-Almax cut) is designed such that the diamond anvil can support high forces while allowing for a wide optical aperture through the diamonds - essential for the measurement of angle-dispersive X-ray diffraction to high angles, and focusing the pump and probe beams onto the sample for Picosecond Acoustics.

2.1.2 Sample Preparation and Loading

For all runs, the Re foil gasket (initial thickness $\approx 200\mu m$) was indented to pressures between 15-24 GPa based on the shift in the Ruby R1 fluorescence line [Mao et al., 1986]. In general, gaskets were indented such that the thickness of the gasket at the tip of the diamond was less than 1/5th the diameter of the diamond culet (e.g. 100 micron culet $\leq$20 micron thick sample chamber). Furthermore, the sample chamber was drilled using a femtosecond pulsed laser with the gasket hole being a diameter slightly more than half that of the diamond culet.

For experiments where the sample was compressed in Ne, the sample chamber was loaded with Ne to 1.2-1.4 kbar before the start of the experiment.

For experiments performed in KCl, the sample was loaded in a sandwich KCl plate/sample/KCl plate assembly, where the plates were made by compressing grains of KCl to 100 bar between WC anvils and then using a femtosecond pulsed laser to cut the KCl plate to the desired diameter.

Technical details specific to loadings for XRD or PA are discussed in their respective sections.

2.1.3 Pressure Measurement

For all experiments, pressures were measured by the fluorescence shift of Ruby at high pressures (for PA measurements), the shift of the Diamond T_{2g} Raman mode (for PA measurements) or by measuring the shift of the lattice parameter of a known material (synchrotron XRD measurements).

As the experiments performed during this Thesis are not only reliant on the accurate measurement of pressure, but on the relative accuracy of different pressure calibrants, it is critically important to select pressure scales which are mutually consistent. As a consequence, pressure scales were carefully chosen to minimize artifacts related to different pressure calibrations.

Ruby Fluorescence

Ruby fluorescence has been a common tabletop method since the 1970s due to the simplicity of such measurements and the strong sensitivity of fluorescence wavelength with pressure. A thorough explanation of ruby fluorescence under pressure can be found in ref. [Syassen, 2008]. While a ruby pressure scale has been established for a long time [Mao et al., 1986], this scale has since been revisited by various authors (e.g. [Holzapfel, 2003], [Dewaele et al., 2004], [Chijioke et al., 2005], [Dorogokupets and Oganov, 2007], [Sokolova et al., 2013]). In the original 'quasihydrostatic' pressure scale (the Mao ruby scale), they used an Ar PTM which has fallen out of favor due to the observation that Ne and He are softer PTM at high pressures [Klotz et al., 2009]. Furthermore, the Mao ruby scale was based on the pressure scale of B1-NaCl at low pressures [Decker, 1971], and shock compression of Cu and Ag at high pressures. This NaCl pressure scale is now known to systematically underestimate pressures by 5-10% [Brown, 1999], and the Cu and Ag pressure scales used were not corrected for the effects of shock-induced hardness nor non-hydrostatic effects on the measured lattice parameters of Cu and Ag at high pressures [Lei et al., 2013]. The combination of these issues results in a significant underestimation of pressure at high P conditions. As a result, the Mao ruby scale underestimates pressure by up to 10 GPa at 100 GPa, and so for this Thesis the ruby scale of [Sokolova et al., 2013] has been used, Eq. 2.1.

$$P_{ruby}(GPa) = 1870\frac{\Delta\lambda}{\lambda_0}\left(1 + 6.0\frac{\Delta\lambda}{\lambda_0}\right) \tag{2.1}$$

In nearly all cases, initial ruby wavelength λ_0 was measured before each experiment, and if not, this value was set to $\lambda_0 = 694.25$ nm.

Diamond Raman Shift

In high pressure experiments, the Raman shift of the T_{2g} diamond vibration can be used to determine pressure using equation 2.2, [Akahama and Kawamura, 2006]. As this signal is also sensitive to less controllable experimental factors such as the geometry of the sample chamber, the dimensions of the diamonds and the material compressed [Howie et al., 2013], it is regarded as less accurate than *in situ* methods for pressure determination.

$$P_{DE}(GPa) \cong K_0\frac{\Delta\nu}{\nu_0}\left[1 + \frac{1}{2}\left(K_0'\right)\frac{\Delta\nu}{\nu_0}\right] \tag{2.2}$$

Where $K_0 = 547$ GPa and $K_0' = 3.75$ [Akahama and Kawamura, 2006]. This method was used as a secondary pressure calibrant to ruby, measured for PA experiments at pressures exceeding 60 GPa. The pressure measured by this method were consistent with pressures measured by the ruby fluorescence method to within 2 GPa at all pressures.

X-ray Diffraction Pressure Standards

Using synchrotron XRD it is possible to measure the lattice parameters of materials to high pressures with high accuracy and high statistical quality. For ambient temperature compression experiments, Pt ([Fei et al., 2007] and [Dorogokupets and Oganov, 2007]) and Mo ([Litasov et al., 2013] and [Huang et al., 2016]) were used as pressure calibrants (shown in table 2.1). On the basis of measured d-spacings as a function of pressure, Mo is an excellent pressure calibrant for the study of bcc-like and hcp Fe-alloys, as Mo is a well studied material by a variety of different methods ([Ragan et al., 1977], [Katahara et al., 1979], [Hixson and Fritz, 1992], [Huang et al., 2016]) and has few overlapping peaks with said Fe-alloys up to pressures exceeding 1 Mbar. With earlier calibrations for the EoS of Mo ([Dewaele et al., 2004], [Dorogokupets and Oganov, 2007]) there were small discrepancies at low pressures with the compression curves of other metals, however more recent work has largely resolved this effect ([Litasov et al., 2013], [Huang et al., 2016]). While most static compression studies report bulk moduli and K' which are quite close, from study to study there have often been differences in the choice of V0 of the material. Following recent measurements of Ruby fluorescence and Mo volume in the same experimental run (compressed with Ne PTM) show that at pressures lower than 10 GPa there is a systematic difference of ∼0.5 GPa between the pressure scales of ruby after [Sokolova et al., 2013] and virtually all of the literature Mo P scales. Fortunately, it has been observed that changing the V0 of a given EoS to 31.17 Å^3 (the reference value for Mo, [Ross and Hume-Rothery, 1963]) eliminates this discrepancy. Following an independent analysis of the available static compression literature, it has been observed that the Mo P scales proposed by [Dorfman et al., 2012] and [Litasov et al., 2013] (when a V_0 of 31.17 Å^3 is used in the case of [Litasov et al., 2013]) are the most consistent with measurements of ruby fluorescence when using Mo as a pressure calibrant in the 0-10 GPa range.

The Mo EoS of [Litasov et al., 2013] and [Huang et al., 2016] are both calibrated against [Sokolova et al., 2013], which is critically important for the mapping of measured XRD EoS to PA datasets.

	Pt[1]	Pt[2]*	Mo[1]	Mo[2]	KCl*
Formalism	Vinet	Vinet	3BM	Vinet	Vinet
V_0 (Å^3)	60.38(1)	60.38	31.14	31.17	54.5
$K_{T,0}$ (GPa)	277	277.3	255(1)	260(1)	17.2
$K'_{T,}$	5.08(2)	5.12	4.25(2)	4.21(5)	5.89

Table 2.1: Table of EoS parameters of X-ray pressure calibrants used. * errors not reported for these EoS. Pt[1] is from [Fei et al., 2007], Pt[2] is from [Dorogokupets and Oganov, 2007], Mo[1] is from [Huang et al., 2016], Mo[2] is from [Litasov et al., 2013] but with a modified V_0 and KCl is from [Dewaele et al., 2012]

On the basis of a recent assessment of the intercalibration of Au, Pt and MgO [Ye et al., 2017] it is seen that the Pt pressure scale of [Fei et al., 2007] is generally consistent with other modern pressure calibrations to within 1 GPa below 1 Mbar. This Pt scale was used in Section 4.2. However, the Pt scale of [Dorogokupets and Oganov, 2007] is regarded as the most internally consistent, and was used for the remainder of the work in this Thesis. A discussion of error analysis and the EoS formalisms used in this Thesis follows in sections 2.2 and 2.3.

For high temperatures, the potential for chemical reaction between Fe and other calibrants becomes critical for performing accurate measurements of Fe-alloy lattice parameters at simultaneous high P-T conditions, and so KCl [Dewaele et al., 2012] was used as both the PTM and the pressure calibrant.

2.2 X-ray Diffraction

An old and well-studied phenomena in physics is that of single-slit diffraction. When light passes through an opening of comparable length scale to the wavelength of the light, there is diffraction of the beam. This is a consequence of the quantum nature of light, and the result is destructive and constructive interference of the outgoing beam. X-ray diffraction utilises this effect in order to study the atomic structure of materials, as X-rays (used for this technique) typically have a wavelength of 0.4-2 Å which is the same order of magnitude of distance as the spacing between atoms in a solid (typically 1-3 Å). The constructive and destructive interference of the X-ray beam passing through the solid is dictated by the Bragg condition, Equation 2.3.

$$n\lambda = d\sin\theta \tag{2.3}$$

Where λ is the x-ray wavelength, n is an integer, d is the crystalline d-spacing, the distance between successive planes of atoms in a crystal, and θ is the angle at which the maximum in diffracted intensity occurs. The importance of this equation, is that for a fixed wavelength, successive d-spacings produce diffraction maxima at different angles θ. By measuring the diffraction maxima over a large quantity of crystal orientations, it is possible to measure successive d-spacings of different planes of atoms, which in general allows for the determination and refinement of the crystal structure. In this Thesis, unless specified otherwise all XRD pattern refinement was performed using Jana2006 [Václav et al., 2014].

2.2.1 Ambient Conditions X-ray Diffraction

Most alloys measured in this thesis were measured at ambient temperature and pressure by grazing-incidence XRD (GI-XRD) or transmission XRD. The instrument used for GI-XRD exploited the Co $K\alpha$ line $\lambda = 1.7888$Å.

The samples were either loose ribbons or films deposited on a glass substrate. The samples were placed on Si (100) oriented pastelles for measurement. The diffraction patterns were measured with a line-detector, with the angle of the incoming X-ray beam and detector changing to scan in 2θ. Diffraction patterns were collected both on stationary and rotating samples in order to detect potential textural effects and phase purity. There was little change in diffraction peak linewidth or intensity between diffraction patterns of stationary or rotated samples. Due to the absence of a well-defined signal from the glass substrate, the focussing of the X-ray beam on the surface of the sample was a challenge, resulting in systematic calibration errors. All alloys where an EoS were measured were characterized further in transmission geometry either at IMPMC or at a synchrotron source in an empty DAC.

2.2.2 Synchrotron X-ray Diffraction

Ambient temperature, high pressure XRD experiments were performed on PSICHÉ at Synchrotron-SOLEIL and ID27 at ESRF, and simultaneous high-pressure high-temperature experiments on ID27 at ESRF. At both sources, a monochromatic X-ray beam of wavelength $\lambda = 0.3738A$ was used. For all Synchrotron XRD, the

sample-detector distance was calibrated with a CeO_2 standard (NIST SRM 674b), and diffraction images were processed into radially averaged diffraction patterns using the software package DIOPTAS [Prescher and Prakapenka, 2015].

Synchrotron-SOLEIL

At Synchrotron-SOLEIL, the X-ray beam was focused to $\sim 12\mu m$ by $15\mu m$ (horizontal by vertical Full-Width-Half-Maximum), and diffraction images were collected on a Perkin-Elmer area detector (pixel size = $200\mu m$, measures diffraction lines up to angles of $2\theta \approx 28^o$). The collection time for images were 30-60 seconds, and after nearly every measurement a dark-current image was collected without the X-ray beam, in order to measure the ambient background of the detector plate. Diffraction images were collected in a centered geometry (with the diffraction plate centered w.r.t. the cell) in order to maximize azimuthal coverage of the sample diffraction lines. Figures 2.2 and 2.3 show a diffraction image from this set of experimental runs and the resultant radially-averaged diffraction pattern. Most diffraction patterns were collected in sweep mode, where the cell is rotated during collection in order to average over a larger quantity of crystallites. There was negligible difference between the lattice parameters determined from sweep collections or snap collections (where the cell is stationary) for samples compressed in Ne or measured at ambient pressure.

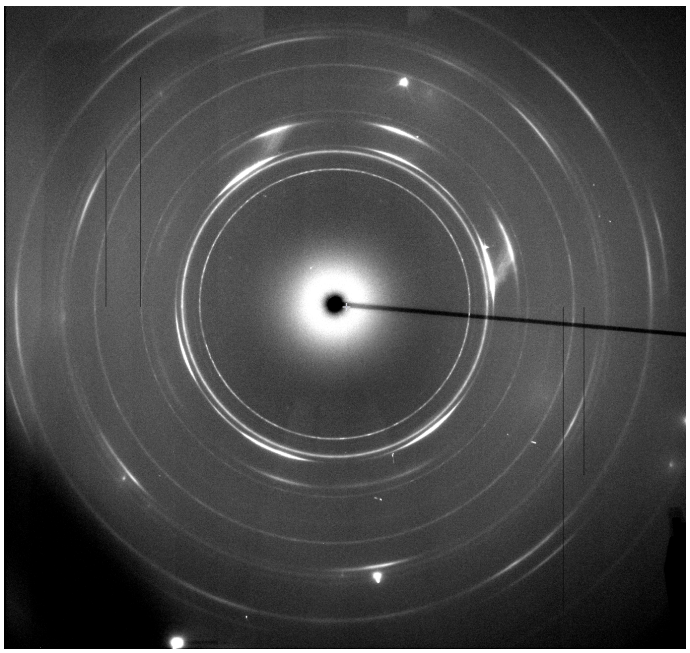

Figure 2.2: Diffraction image of Fe12Si compressed in Ne at 51 GPa at Synchrotron-SOLEIL.

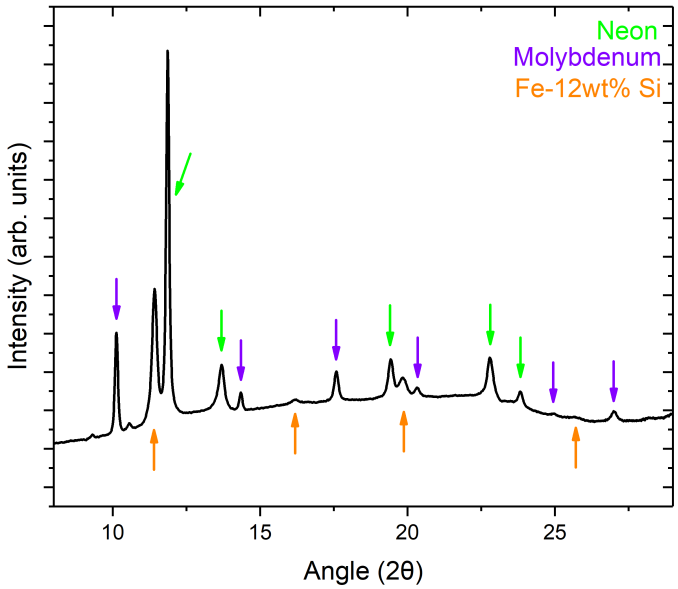

Figure 2.3: Integrated diffraction pattern of Fe12Si compressed in Ne at Synchrotron-SOLEIL. Arrows on pattern denote the diffraction peaks of Ne, Mo and Fe12Si.

ESRF

On ID27, the X-ray beam was focused to $\sim 3\mu m$ by $3\mu m$ (h x v FWHM), and diffraction patterns were collected on a MarCCD area detector (pixel size $= 79\mu m$). Due to the more tightly focused beam, it was possible to extend the measurement range up to pressures exceeding 1 Mbar both at ambient and elevated temperatures. Diffraction patterns were collected in a geometry offset from the center of the cell to maximize the quantity of diffraction lines measured, which is especially important at high pressures (the influence of pressure shifts measured diffraction lines to higher angles). Figures 2.4 and 2.5 show a diffraction image and the resultant radially-averaged diffraction pattern at 1.1 Mbar using Ne PTM. Collection times for diffraction images were between 5s and 60s depending on the experimental run and intensity of the measured peaks.

High temperature experiments were also performed, where XRD was coupled with double-sided laser heating in order to generate high, uniform temperatures in the XRD measurement spot. These experiments were performed using KCl as the PTM and pressure calibrant to minimize chemical reaction between sample and diamonds, and to thermally insulate the sample from the diamonds. In such experiments, the sample was heated by two continuous-wave Nd:YAG lasers. Temperatures were measured by the spectroradiometric method, which was found to result in reproducible, accurate measurements of sample temperature above $T \approx 1200K$. For all experiments, temperatures measured by this method were corrected downward by 3% to account for axial T gradients in the sample [Campbell et al., 2009]. While temperature varied only weakly over the duration of a diffraction measure-

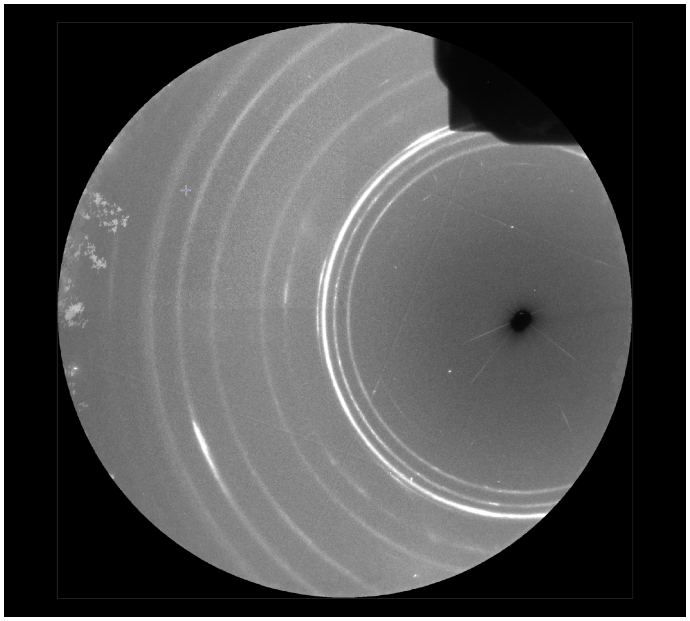

Figure 2.4: Diffraction image of Fe5Si compressed in Ne to 112 GPa at the ESRF.

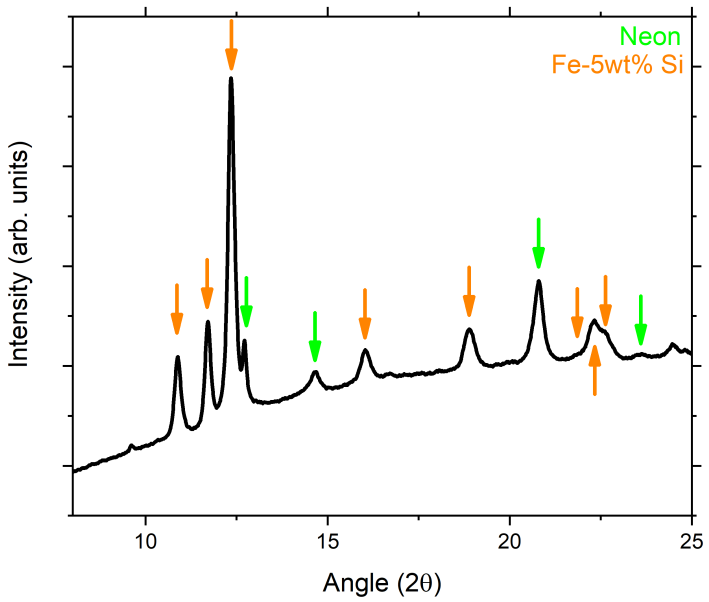

Figure 2.5: Integrated pattern of Fe5Si compressed in Ne to 112 GPa at the ESRF. Arrows denote sample and Ne peaks.

ment (< 50 K in nearly all cases), an error of ≈ 150 K was reported to account for the absolute accuracy of the spectroradiometric method.

As the temperature has an effect on the measured lattice parameter of KCl, the effects of thermal expansion of the material must be taken into account when used as a pressure standard. The bulk temperature of KCl was approximated as Equation 2.4 after [Campbell et al., 2009]

$$T_{KCl} = (3 * T_{meas} + 300) / 4 \tag{2.4}$$

The act of heating the KCl results in an increased pressure on the sample, and so the pressure exerted on the sample is [Dewaele et al., 2012]:

$$P(V, T_{sample}) = P_{300}(V_{KCl}) + 0.00224 * (T_{KCl} - 300) \tag{2.5}$$

Where P_{300} is the pressure due to the ambient temperature EoS of KCl (EoS details discussed in the following section).

2.2.3 Equations of State

In order to place constraints on the composition and properties of the Earth's core by synchrotron XRD experiments, the unit cell volumes of relevant materials must be fit to a P-V or P-V-T EoS in order to construct models of the variation of thermodynamic quantities with pressure and temperature. Assuming a model for the relation between pressure, volume and temperature and measuring such relations over a large P-T range, it is possible to constrain the evolution of the thermodynamic properties of measured iron-alloys up to core pressures and temperatures using Equation 2.6 to derive the free energy (F) of the system.

$$P = -\left(\frac{\partial F}{\partial V}\right)_T \tag{2.6}$$

Furthermore, these EoS provide constraints on the compressibility of Fe-alloys, through Equation 2.7.

$$K_T = -V\left(\frac{\partial P}{\partial V}\right)_T \tag{2.7}$$

This thermodynamic relation is critically important for deriving shear properties from PA measurements (Section 3.2.3). The following section discusses the main EoS used for modelling P-V and P-V-T behaviour of iron alloys.

Ambient Temperature, High Pressure Equations of State

The primary ambient temperature EoS used within the High-Pressure and Mineral Physics communities for ambient P-V relations are Equation 2.8, the 3rd order Birch-Murnaghan Equation of state (3BM, [Birch, 1947])

$$P(V) = \frac{3}{2}K_0\left[\left(\frac{V_0}{V}\right)^{7/3} - \left(\frac{V_0}{V}\right)^{5/3}\right]\left\{1 + \frac{3}{4}(K' - 4)\left[\left(\frac{V_0}{V}\right)^{2/3} - 1\right]\right\} \tag{2.8}$$

and Equation 2.9, the Rose-Vinet Equation of state (Vinet, [Vinet et al., 1989]).

$$P(V) = 3K_0\left(\frac{1-\eta}{\eta^2}\right) exp\left[\frac{3}{2}(K' - 1)(1 - \eta)\right] \tag{2.9}$$

In both Equations 2.8 and 2.9 V_0 is the ambient pressure unit cell volume, K_0 is the ambient pressure isothermal bulk modulus and K' is the first derivative of the isothermal bulk modulus at ambient pressure. In Equation 2.9 specifically, $\eta = \frac{V}{V_0}^{1/3}$. In general, these equations assume a functional form either for the inter-atomic potential, which provides a relationship between energy and interatomic distance, or a relationship between hydrostatic stress and strain. This provides a physical basis for the derivation of $K_T(V)$ from relations between P and V. 3BM is based on the assumption that the free energy of the material is a polynomial in (eulerian) strain (Equation 2.10)

$$F = F_2 f^2 + F_3 f^3 + ... \tag{2.10}$$

Where the free energy U is truncated at 3rd order in (eulerian) strain, and this strain is defined as:

$$f = \frac{1}{2}\left[\left(\frac{V_0}{V}\right)^{2/3} - 1\right] \tag{2.11}$$

For the Vinet EoS, the relation between P and V is based on the assumption of an empirical interatomic potential:

$$E(r) = A(1 + ar)\, exp(-br) \tag{2.12}$$

Where A, a and b are scaling factors and r is the interatomic distance. 3BM and Vinet EoS are readily employed for the study of elastic deformation at high pressure, as at GPa pressures (and even more so at core pressures), the applied stress to a material results in a strain well beyond the limit of infinitesmial strain theory, where volume decreases linearly with applied pressure. Consequently, these EoS can be invoked to model the non-linear evolution of the compressibility of materials at extreme pressures.

While both Equations 2.8 and 2.9 encode P(V) through the same set of constants (V_0, K_0, K'), such fitted constants are generally not interchangeable between the 3BM and Vinet equations at compressions $V/V_0 < 0.9$ [Angel, 2000]. While the Vinet EoS is generally regarded to better describe the compression of metals to high compressions [Dewaele et al., 2004], [Dewaele et al., 2008], when the P-V relation is measured over a wide range of pressures ($\sim$ >1 Mbar), the functional form of the EoS used has a negligible effect on extrapolations to core pressures. For this reason, the 3BM formalism is used in this Thesis, as the choice of EoS is primarily to facilitate comparisons between the present work and previous literature.

High Temperature, High Pressure Equations of State

In order to extrapolate density and derived thermodynamic quantities of a candidate core material to both the pressures and temperatures of the Earth's inner core, one must construct a thermodynamic model which describes the evolution of volume with both pressure and temperature.

For such EoS, the effects of pressure (as the variation of volume at T = 300 K) and temperature (at T > 300 K) are typically decoupled into a form such as

Equation 2.13.

$$P(V,T) = P(V,T=300K) + P_{vib}(V,T) + P_{el}(V,T) + P_{anh}(V,T) \tag{2.13}$$

In this equation, the first term refers to the reference isotherm at T = 300 K (Equation 2.8). The rest of the terms of Equation 2.13 act to elevate pressure with temperature at constant volume, with separate physical origins. P_{vib} is the vibrational contribution to thermal pressure. In a solid material at finite temperature, all atoms oscillate within a potential well a small distance from their equilibrium position. While in general, this potential well is asymmetric with respect to atomic position (e.g. [Mishin et al., 1999]), for simple solids up to moderate temperatures, it can be approximated that the oscillations of the atoms within the potential well are harmonic [Zharkov et al., 1972]. Furthermore, in the debye approximation, the number of lattice vibrations in a material is normalized to the number of available vibrational modes, with a characteristic thermal energy $\hbar\theta_D$. This thermal energy is the maximum energy of lattice vibrations in the solid at $T \leq \theta_D$. At $T > \theta_D$, V increases linearly with T (at constant P), as at high temperatures, the effect of lattice vibrations is dominated by the quantity of available vibrational modes, rather than the nature of the specific modes available. For P-V-T equations of state on Fe-alloys, the vibrational component of thermal pressure is given by Equation 2.14

$$P_{vib}(V,T) = \frac{9NR\gamma_{vib}}{V}\left[\frac{\theta_D}{8} + T\left(\frac{T}{\theta_D}\right)^3 \int_{300}^{\theta_D/T} \frac{x^3}{exp(x)-1}dx\right] \tag{2.14}$$

Where N is the number of atoms per formula unit, which for hcp-Fe and dilute hcp-Fe alloys is 1. R is the ideal gas constant, V is unit cell volume in cm^3/mol. γ_{vib} is the dimensionless vibrational grüneisen parameter, and θ_D is the debye temperature. In general, γ_{vib} and θ_D vary with pressure and temperature [Bina et al., 1992], and so an approximation must be used to parametrize the change of these parameters at high pressures and temperatures. At present, there is no consensus on the best formalism for the variation of these parameters at high P-T [Murphy et al., 2011], and so in this thesis they are assumed to be only explicitly a function of sample volume [Zharkov et al., 1972]. It has been shown ([McQueen et al., 1967] that the approximation:

$$\frac{\partial}{\partial P}\left(\frac{\gamma_{th}}{V}\right) \approx 0 \tag{2.15}$$

is reasonable for most materials, where γ_{th} is the thermodynamic grüneisen parameter, implying that

$$\left(\frac{\gamma_{th}}{\gamma_{th,0}}\right) = \left(\frac{V}{V_0}\right)^q \tag{2.16}$$

In this way, the variation of the grüneisen parameter with pressure and temperature is linked to the change in unit cell volume by a scaling parameter q, which is thermodynamically related to the variation of K' with temperature. Furthermore, the vibrational grüneisen parameter used in Equation 2.14 is related to the Debye temperature by the relation:

$$\gamma_{vib} = -\frac{d \ln \theta_D}{d \ln V} \tag{2.17}$$

By using Equations 2.16 and 2.17, it is possible to derive the evolution of θ_D with volume.

$$\theta_D = \theta_{D,0} \exp\left[\left(\gamma_{vib,0} - \gamma_{vib}\right)/q\right] \tag{2.18}$$

Equations 2.14, 2.16, and 2.18 describe the evolution of P with V and T in the quasiharmonic approximation, where $\gamma_{th} \approx \gamma_{vib}$, and the subscript 0 denotes ambient pressure values.

While lattice vibrations generally play the dominant role in the high temperature behaviour of materials, in metals such as iron, the conduction electrons also can contribute significantly to the P-V-T EoS and can not in general be neglected in extrapolations to core conditions. In metals, the conduction electrons act approximately as a Fermi gas, and for such a system the electrons generate a pressure proportional to T^2 at temperatures much lower than the fermi temperature. For metals, this temperature is on the order of 10^5 K and so for the temperature range relevant to geophysics (inner core temperatures are likely between 5000 - 7000 K), this T^2 term can be up to 40% the total thermal pressure [Fei et al., 2016]. Furthermore, this effect is expected to change in magnitude as a function of pressure (or correspondingly volume). As a consequence, for Section 4.2 of this thesis we use the formalism for electronic thermal pressure (Pel) after [Boness et al., 1986], Equation 2.19.

$$P_{el}\left(V,T\right) = \frac{\gamma_e}{V}\beta_0 \left(\frac{V}{V_0}\right)^k T^2 \tag{2.19}$$

Where γ_e is the electronic grüneisen parameter, β_0 is the ambient pressure electronic heat capacity and k is a scaling factor analogous to q.

While the quasiharmonic approximation assumes that atoms oscillate within a harmonic potential, in general this is not the case [Zharkov et al., 1972], and at high temperatures, additional corrections to the thermal pressure can be introduced based on the intrinsic anharmonicity of the 'real' interatomic potential. This effect typically scales as T^2, however it's magnitude is significantly less than Pel. In fact, on the basis of earlier ab initio parametrizations of Pel and Panh, at core conditions (300 GPa, 6000 K), Pel composes $\sim$ 30% of the total thermal pressure, while Panh composes $\sim$ 5%. In this way, for experimental studies (i.e. [Fei et al., 2016], this Thesis), anharmonic terms are ignored when fitting P-V-T equations of state.

Errors in X-ray Diffraction Experiments

While errors in unit cell volume can be simply propagated from the fitted lattice parameters using a standard XRD analysis program (e.g. GSAS, Jana2006, MAUD), the propagation of errors in pressure require a more detailed treatment. After [Angel, 2000], the total error in pressure (at either ambient or high temperature) is determined as:

$$\delta^2 = \delta_P^2 + \delta_V^2 \left(\frac{K_T}{V}\right)^2 + \delta_T^2 \left(\alpha K_T\right)^2 \tag{2.20}$$

δ_P is the intrinsic error of the EoS. For standard pressure calibrants, this parameter is either based off of reported errors on EoS parameters (Mo and Pt) or as a percentage of pressure (for KCl).δ_V is the experimental error in lattice parameter for the pressure calibrant. K_T and V are the bulk modulus and volume of the material at the respective P-T conditions at which the calibrant is measured. δ_T is the error in temperature of the pressure calibrant, assumed to be the same as that of the sample. α is the thermal expansion of the material at those P-T conditions, however for ambient temperature measurements, temperature errors are negligible, and for KCl the product αK_T is approximately constant [Dewaele et al., 2012]. The isothermal bulk modulus for 3BM is given by [Morard et al., 2013]:

$$K_T(V) = \frac{K_0}{2}\left\{\left[7\left(\frac{V_0}{V}\right)^{7/3} - 5\left(\frac{V_0}{V}\right)^{5/3}\right]\left[1 + \left(\frac{3K'}{4} - 3\right)\left(\left(\frac{V_0}{V}\right)^{2/3} - 1\right)\right]\right\} + \frac{3}{4}K_0(K' - 4)\left[\left(\frac{V_0}{V}\right)^{3} - \left(\frac{V_0}{V}\right)^{7/3}\right] \tag{2.21}$$

And for the Vinet EoS (used for KCl pressure calibrant), K_T is:

$$K_T(V) = K_0\left[\eta^{-1} + \frac{1-\eta}{\eta^3} + \frac{3}{2}(K' - 1)\left(\frac{1-\eta}{\eta}\right)^2\right] * exp\left[\frac{3}{2}(K' - 1)(1 - \eta)\right] \tag{2.22}$$

For high temperatures, the bulk modulus of KCl is assumed to be the same as ambient temperature, which results in a small overestimation of the error in pressure.

As a result of the high background in typical DAC XRD experiments, standard software underestimate experimental uncertainties on lattice parameter, leading to an underestimation of errors on pressure and sample volume. For a given set of data, the errors in unit cell volume for the pressure calibrant and sample are multiplied by a scaling factor based on the 'goodness of fit', the weighted chi-squared (χ^2), of the fitted EoS, such that $\chi^2 \approx 1$ [Angel, 2000].

2.3 Picosecond Acoustics

2.3.1 Compressional Sound Velocity and the Thermodynamics of Fe-alloys

Picosecond Acoustics is a technique which produces and detects picosecond pulses of longitudinal bulk waves in a sample. These waves are referred to as the compressional sound velocity, or V_P. Such waves are related to the density (ρ) of the material and the elastic moduli by Equation 2.23

$$V_P = \sqrt{\frac{K_S + \frac{4}{3}G}{\rho}} \tag{2.23}$$

Where K_S refers to the *adiabatic* bulk modulus, and G is the shear modulus. The term adiabatic refers to the thermodynamic regime where heat is not transferred out of the system. The passage of an acoustic wave through an elastic medium is an out-of-equilibrium process, occurring over shorter timescales than thermal equilibration. In contrast to this, the measurement of XRD in a DAC is an isothermal process, as the temperature of the measurement spot is equilibrated with its surroundings. In general, the adiabatic and isothermal bulk moduli are related by Equation 2.24

$$\frac{K_S}{K_T} = 1 + \alpha\gamma_{th}T \tag{2.24}$$

Where α is the volumetric thermal expansion coefficient of the material, and γ_{th} was previously defined as the thermodynamic grüneisen parameter. By constructing an isothermal P-V-T equation of state as outlined in Section 2.2.3, it is possible to numerically derive the conversion factors between K_S and K_T, as α is defined as:

$$\alpha \equiv \frac{1}{V}\left(\frac{\partial V}{\partial T}\right)_P \tag{2.25}$$

α can be determined numerically, allowing for the derivation of the shear modulus from Vp and other elastic parameters such as Poisson's ratio.

Furthermore, Vp is more strongly sensitive to the effects of alloying than XRD compression experiments, as while changes in bulk moduli of 1-2% have negligible effect on unit cell volumes, they can produce measurable differences in Vp. Additionally, measurements of Vp provide indirect measurements of the shear modulus of a material when combined with an EoS, and shear moduli are generally less experimentally accessible than bulk moduli at high pressures.

In this way, the measurement of Vp coupled with P-V or P-V-T EoS can be a powerful tool for determining the elasticity of materials at extreme conditions.

2.3.2 Instrument

PA experiments are performed in a pump-probe configuration, where laser pulses generated by a Maitai Ti:Sapphire laser (λ = 800 nm, pulse duration = 100 fs) are separated into two beams which are focused at the two opposing faces of a metallic sample. The majority of the intensity (∼80%) of the laser is directed towards the

pump side (30-100 mW depending on experimental conditions), where the beam generates a small thermal stress at the surface of the sample. The relaxation of this thermal stress generates a longitudinal elastic pulse (duration ∼1 ps, frequency of ∼ 1GHz) which propagates across the sample. Both the pump and probe beams are linearly polarized along most of the path length of the instrument, but are eliptically polarized before propagation into the DAC environment. This is done to maintain orthogonality between the optical pulse incident on the sample, and any reflected intensity, and to maintain orthogonality of the polarization of the the pump and the probe beam - so as to reject any incident intensity from the pump beam which arrives to the measurement photodiodes. Both the pump and probe beams are focused down to a$\sim 3\mu m$ spot on opposing faces of the sample. After generation of the longitudinal elastic pulse, the arrival of the elastic wave at the opposing sample surface generates variations in the reflectivity of the sample as a function of time described by Equation 2.26:

$$\frac{\Delta r\left(t\right)}{r_0} = ik_0 \left\{ 2u_0\left(t\right) + \frac{\partial n}{\partial \eta}\frac{4n}{1-n^2}\int_0^{+\infty} \eta\left(z,t\right)\exp\left(2ik_0 nz\right)dz \right\} \tag{2.26}$$

In Equation 2.26, $\frac{\Delta r(t)}{r_0}$ is the normalized change in reflectivity as a function of time, k_0 is the wavenumber of the acoustic wave, $u_0\left(t\right)$ is the displacement of the sample surface over time, n is the sample index of refraction, $\frac{\partial n}{\partial \eta}$ is the acousto-optic coefficient, and $\eta\left(z,t\right)\exp\left(2ik_0 nz\right)$ is a propagating strain field generated by the elastic wave. In addition to the two terms shown here, there is also an additional term caused by sample heating (on the order of 1-10 K) during the arrival of the pump beam, however the samples measured in this Thesis were too thick to observe such an effect.

Equation 2.26, highlights the two main quantities measured by PA: the induced changes in the real and imaginary components of the sample index of refraction by propagation of a longitudinal elastic wave. However, equation 2.26 is only strictly valid at ambient conditions in air, and while it reflects the basic physics of the processes which generate PA signals due to elastic wave propagation, due to several technical considerations at high pressures the measured signal is always a mixture of the real and imaginary components of the reflectivity.

The probe beam is analyzed in reflectometric mode or interferometric mode. In reflectometric mode, variations in the real component of the refractive index are observed, although as mentioned previously, in a high pressure environment the measured signal will be a mixture of both real and imaginary components of the sample refractive index. By contrast, interferometric mode involves the use of a stabilized Michelson Interferometer in order to measure the change of phase of the sample refractive index upon arrival of the acoustic wave.

Measurements at high pressures have been attempted at high pressures using both reflectometric mode and interferometric mode thanks to the ease and simplicity of changing measurement type at a given pressure. In practice however, it has been observed that interferometric signals provide a more reliable measurement of the travel time, as in many cases with reflectometry the time domain signal measured by disappears by 30-50 GPa, if observed at all (N.B. in Ne, observations of a signal

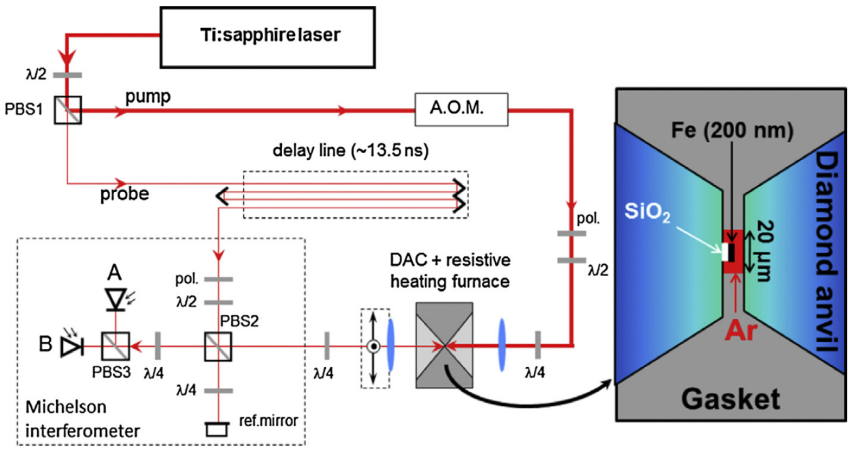

Figure 2.6: Picosecond Acoustics instrument after [Decremps et al., 2015]

by reflectometry are very limited even at near-ambient pressures, while in KCl it remains as reliable as interferometry up to at least 35 GPa). As a result, where available, interferometric measurements were the primary source of travel times in this Thesis.

The phase of the sample refractive index at the sample surface (measured by interferometry) increases rapidly abruptly upon arrival of the acoustic wave, and therefore provides an accurate determination of the acoustic travel time across the material. Depending on experimental conditions, brillouin oscillations (acousto-optic modulation of the probe beam by sound wave propagation) from the transparent PTM can also be observed, in addition to successive acoustic echoes, although these additional echoes are not used for the determination of the acoustic travel time at high pressures.

The sound velocity of a material measured by PA is:

$$V_P = \frac{e(P)}{t_{raw} - t_{PP}} \tag{2.27}$$

Where variation in thickness (e(P)) is given by

$$e(P) = e_0 \left[\frac{V(P)}{V_0}\right]^{1/3} \tag{2.28}$$

where e_0 is the ambient sample thickness, V(P) refers to the unit cell volume of the material at a given pressure, and V_0 is the ambient pressure unit cell volume. t_{raw} is the occurrence time of the 1st acoustic echo, and t_{PP} is the pump-probe coincidence time.

Further details on technical aspects of PA measurements and error analysis can be found in Appendix A.3.

2.4 Profilometry

For samples synthesized by PVD methods, Vp was measured using PA travel times measured at IMPMC, and thickness measurements by profilometry at l'Institut des NanoSciences de Paris (INSP). In profilometry, a diamond stylus drags along the sample surface, and the height of the stylus is measured as a function of distance across the sample. A Dektak 150 Veeco profilometer with a height measurement range of +/- 2.5 micron was used for these experiments. This experimental apparatus can measure variations in surface height down to an error of about 7 nm. In order to determine thickness of the sample, a section of the sample was mechanically removed from the substrate, and the height difference between sample and substrate was assumed to be the bulk thickness of the sample. The best measurement method is in the 'valley' configuration, where the measurement is performed on a section of exposed substrate between two sections of unadulterated sample. A typical measurement is shown in Figure 2.7.

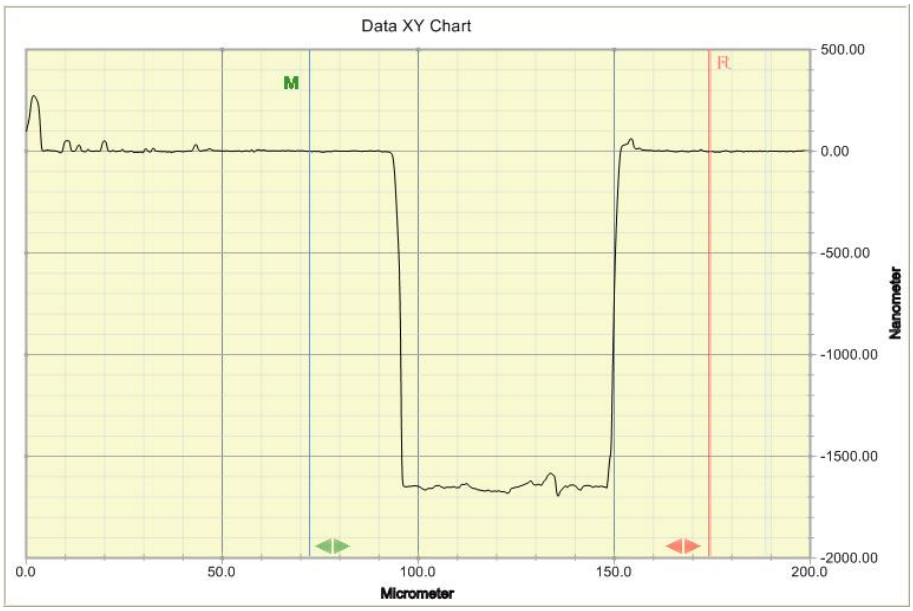

Figure 2.7: Profilometric measurement on Fe17Si. The sample thickness was determined to be 1640(30) nm.

For Si-rich Fe-Si alloys, the primary source of error is due to damage of the substrate during etching which equates to about 30 nm of error for Fe17Si (thickness = 1640 nm) and 150 nm of error for Fe26Si (Thickness = 2600 nm), as increased Si content at this level results in an increase in the strength of the interaction between sample and substrate. Conversely, it was not possible to perform profilometric measurements on samples with less than 5 wt% Si due to the high ductility of the sample, as sample removal resulted in significant damage to the substrate.

Most profilometric measurements of the samples were performed at an area proximal to the PA travel time measurement location to within 200 micron. It was observed that the variation of acoustic travel time was within experimental error on length scales exceeding 1 mm on the deposited samples. An image of the sample

prepared for profilometric and picosecond acoustic measurements is shown in Figure 2.8

For intermediate compositions between 5Si and 17Si, it was possible to determine the thickness down to about 10 nm, nearly the instrumental resolution of the profilometer.

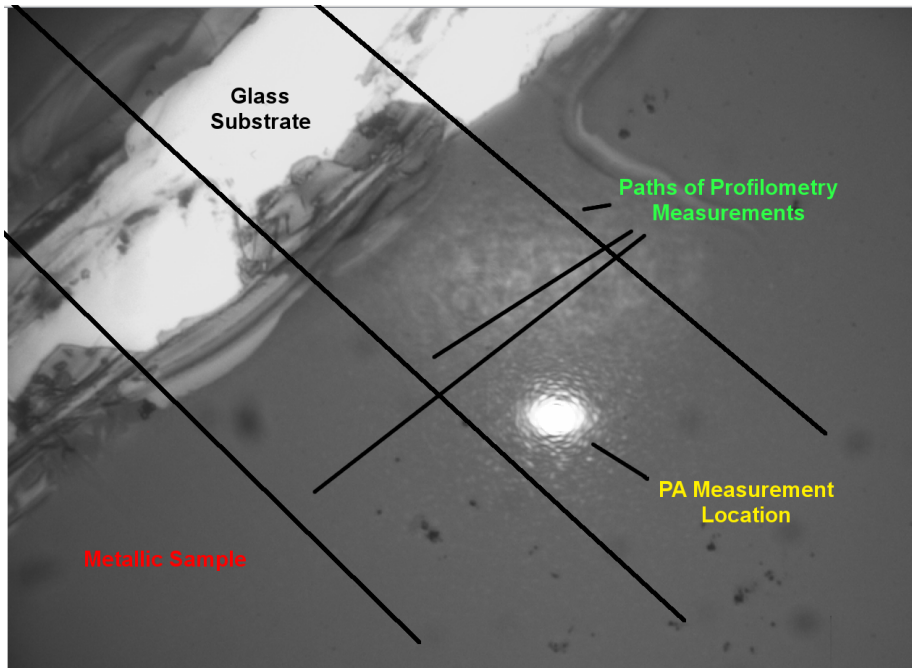

Figure 2.8: Image of the sample surface before a PA measurement. Marked on the picture are the typical measurement paths for profilometric measurements and the PA measurement location.

2.5 Scanning Electron Microscopy

All samples were checked for chemical homogeneity and light element quantity using Auger spectroscopy with a scanning electron microscope. A Zeiss Ultra55 FE-SEM apparatus was used, with each sample being measured between 2-4 times at different locations on the sample. Reported errors on composition are enlarged with respect to measurement errors to reflect the fact that the SEM is a measurement of local composition and does not measure bulk composition. However it is stressed that on the basis of combined PA measurements, XRD measurements and SEM, the sample is of high textural, chemical and structural homogeneity.

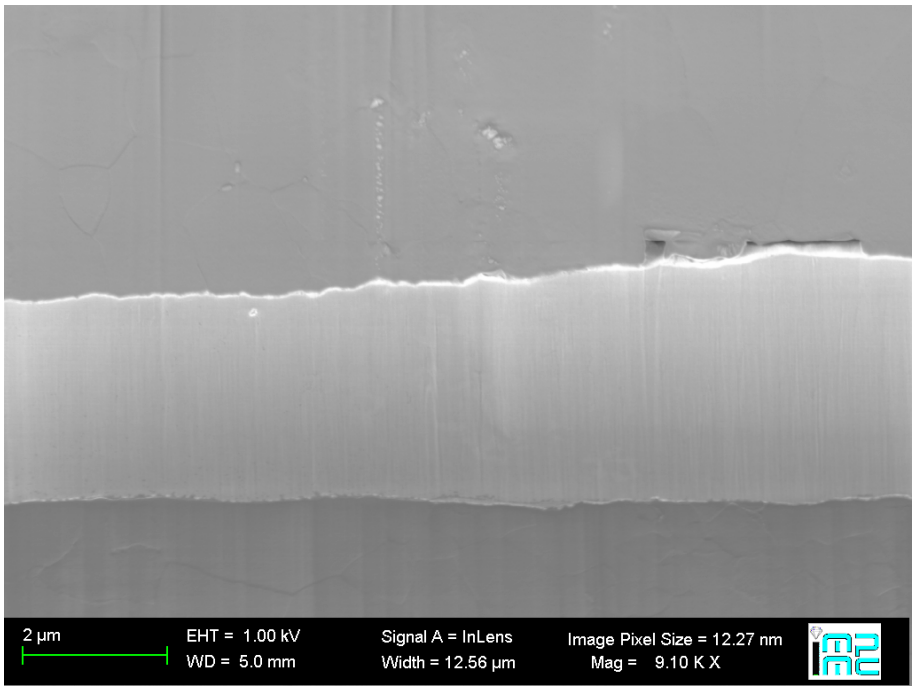

Figure 2.9: Fe10Si sample recovered from a high-pressure experiment in KCl PTM.

2.6 Synthesis of Fe Alloys

In this Thesis, two methods have been employed for the synthesis of the used iron alloys: rapid melt-spinning and physical vapor deposition techniques.

2.6.1 Rapid Melt-Spinning

Rapid melt-spinning is a technique where it is possible to quench high-temperature phases of materials by the rapid cooling of a liquid to ambient temperature. Such methods allow for the tailoring of structure and solute solubility in the Fe lattice, and hinder the precipitation of ordered structures (e.g. Fe_3C, DO_3 Fe-Si alloys). More specifically, a homogeneous liquid is obtained by induction melting in a Cu crucible under inert atmosphere. This is liquid is quenched into a solid alloy by the planar flow casting technique. Following this, the alloys are remelted and ejected through a pressurized quartz nozzle onto a rotating Cu-base wheel under inert atmosphere [Morard et al., 2011]. This results in a chemically homogeneous, ribbon-shaped sample with thickness between 5-30 micron depending on processing parameters (e.g. wheel speed). A schematic for rapid melt-spinning is shown in 2.10.

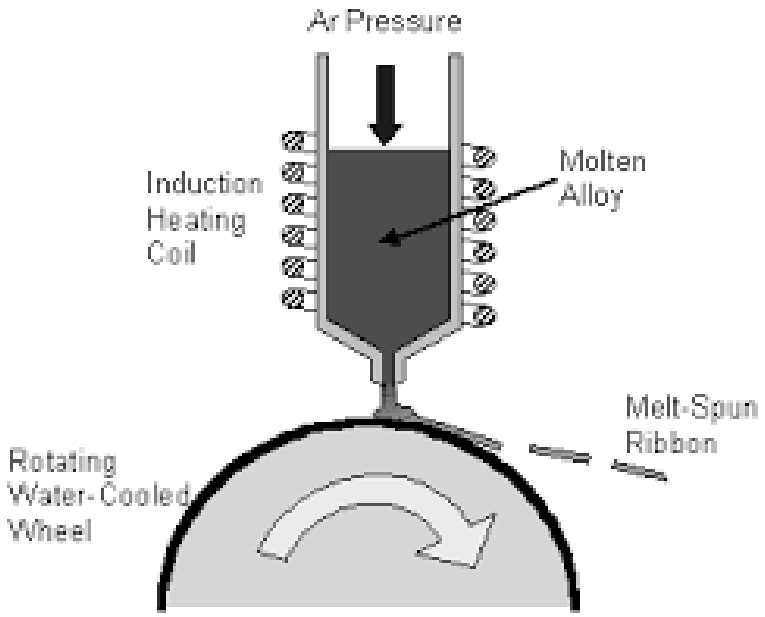

Figure 2.10: Schematic of an apparatus for rapid melt-spinning [Haidemenopoulos, 2018]. The desired base elements of the alloy are melted in a crucible and ejected onto a spinning wheel, which rapidly quenches the liquid to form homogeneous metallic ribbons

2.6.2 Physical Vapor Deposition

Physical vapor deposition (PVD) is a technique by which atoms are deposited directly on a substrate, allowing for the synthesis of alloys in which the components

are immiscible in the liquid phase (e.g. Fe-Si-O alloys, [Hirose et al., 2017]). Additionally, due to the availability of low synthesis temperatures (500-550 K for this Thesis), this technique can also be used to suppress precipitation of ordered phases, and in some cases induce amorphization of the alloy (however this has only been observed for Fe27Si in the alloys studied in this Thesis). The alloys of this Thesis were synthesized by Dephis Company. In the PVD synthesis of Fe-Si alloys, atoms of Fe and Si are sputtered onto a glass base from chemically uniform Fe and Si targets. The extraction of Fe and Si from the targets is enhanced by a magnetic field generated in a chamber of ionized argon plasma. This process results in a chemically homogeneous sample, with a nearly uniform thickness [Miozzi et al., 2018].

Chapter 3

Velocity-density systematics of bcc and 'bcc-like' Fe-alloys

3.1 Ambient Pressure Behaviour of bcc and 'bcc-like' Fe-Si alloys

3.1.1 Crystal structure and unit cell volume of bcc and 'bcc-like' Fe-Si alloys at ambient pressure

Due to the significant technological and commercial value of Fe-Si alloys, they have been the subject of scientific inquiry for more than a century [Phragmén, 1926]. In spite of this, the role of order, disorder, and the crystal structure of these alloys has been a major scientific challenge. In the words of Bridgman: "[from 0.39 to 5.75 at% Si.] The metallurgical phase diagram shows only a solid solution in this range, although at higher concentrations the [phase] diagram becomes exceedingly complicated" [Bridgman, 1957]. At present, the low temperature (< 1000 K) ambient pressure phase diagram between Fe and stoichiometric FeSi is considered to be composed of 4 primary phases: bcc Fe-xSi (Space group: Im-3m), B2 Fe-xSi (Space group: Pm-3m), DO_3 Fe-xSi (Space group: Fm-3m), and stoichiometric B20 FeSi (Space group: $P2_13$). While end-member B20 FeSi is approximately stoichiometric, for a wide range of more Fe-rich compositions, a given sample may be a mix of domains of B2, bcc and DO_3 Fe-xSi, depending on both Si content and the thermal history of the material [Shin et al., 2005]. At very low Si contents (approx. less than 3 wt% [Jayaraman et al., 2018]) the Fe-xSi alloys are primarily composed of the bcc phase, a simple solid solution with Si atoms randomly replacing Fe in the bcc structure. Figure 3.1 shows a schematic of the disordered bcc structure.

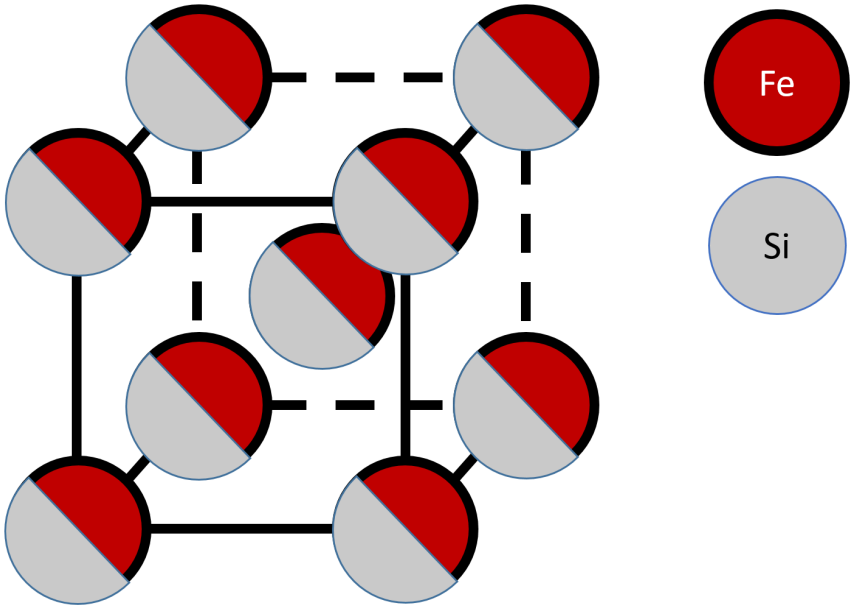

Figure 3.1: bcc Fe-Si structure. The bcc-Fe lattice with randomly distributed Si atoms (Fe/Si ratios not to scale).

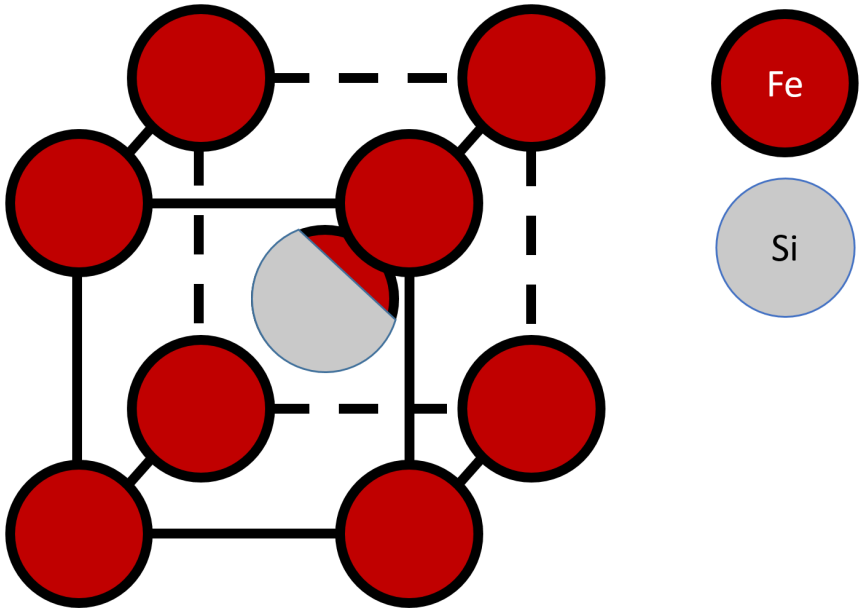

Figure 3.2: B2 Fe-Si structure. A CsCl-type structure where Si partitions into one crystallographic location in the bcc unit cell (Fe/Si ratios not to scale).

Above 3 wt% Si, short range ordering of the Si atoms within the bcc-Fe lattice occurs, where the Si and Fe atoms preferentially partition into different crystallographic locations, resulting in local B2 structure domains [Shin et al., 2005], shown in Figure 3.2. However, the presence of B2 in this compositional regime strongly depends on synthesis conditions, as it has been discussed that the B2 phase can

be avoided by using synthesis methods involving slow cooling from high temperatures [Machová and Kadečková, 1977]

At Si concentrations above ∼5 wt% Si, further long range ordering occurs, where the Fe-xSi alloy adopts a structural motif of alternating B2 Fe-Si unit cells and bcc-Fe unit cells in an fcc arrangement [Randl et al., 1995], shown in Figure 3.3.

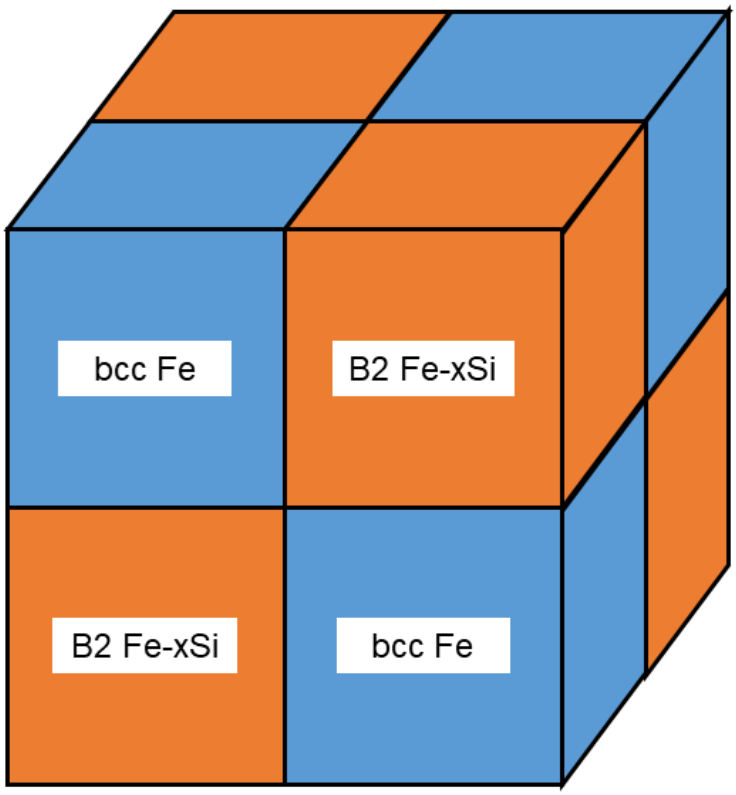

Figure 3.3: DO_3 Fe-Si structure. An fcc structural motif of alternating bcc-Fe and B2 FeSi unit cells. Up to 25 at% Si (14.4 wt% Si), the chemical disorder occurs within B2 portions of the lattice [Randl et al., 1995].

Up to about 20 wt%Si, Fe-Si alloys exhibit the DO_3 structure [Farquhar et al., 1945], however it has been shown that using out-of-equilibrium synthesis methods such as melt-spinning [Jayaraman et al., 2018] or mechanical annealing [Shyni and Alagarsamy, 2014] it is possible to suppress Si ordering. In Figure 3.4, it is shown that as well by Physical Vapor Deposition, it is also possible to strongly suppress Si ordering. As PVD is performed at relatively low temperatures (between ∼500-550 K), Si diffusion within the alloy is strongly suppressed, resulting in a homogeneous, disordered bcc alloy which has been observed for up to 12 wt% Si, although there may be small quantities of additional ordered phases below the detection limit of XRD.

Fe17Si shows a faint additional reflection associated with the (001) reflection of a B2 structure, more clearly visible when using synchrotron X-ray sources as shown in Figure 3.5.

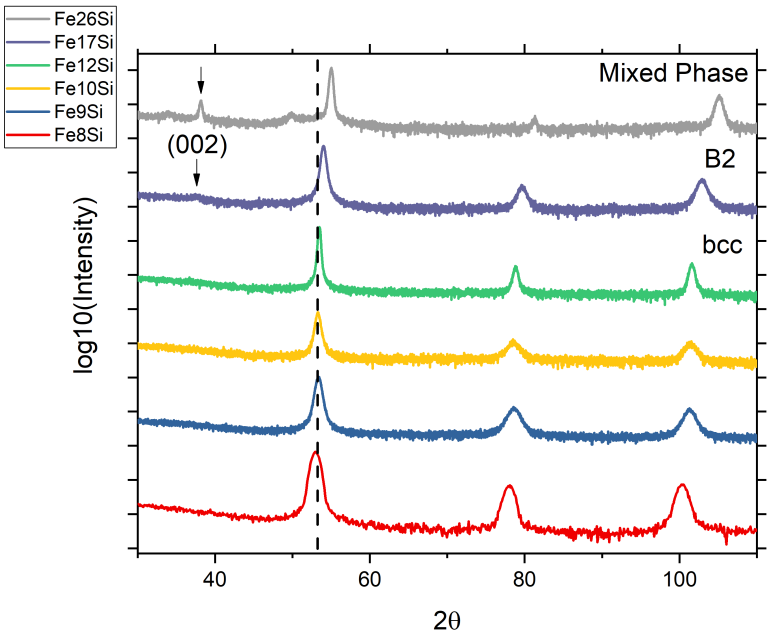

Figure 3.4: Grazing-Incidence X-ray Diffraction measurements of Fe-xwt% Si (x = 8, 9, 10, 12, 17, 26). Black dotted line is a guide for the eye showing the variation of diffraction peak with Si content with the (101) line of Fe-10wt% Si as reference.

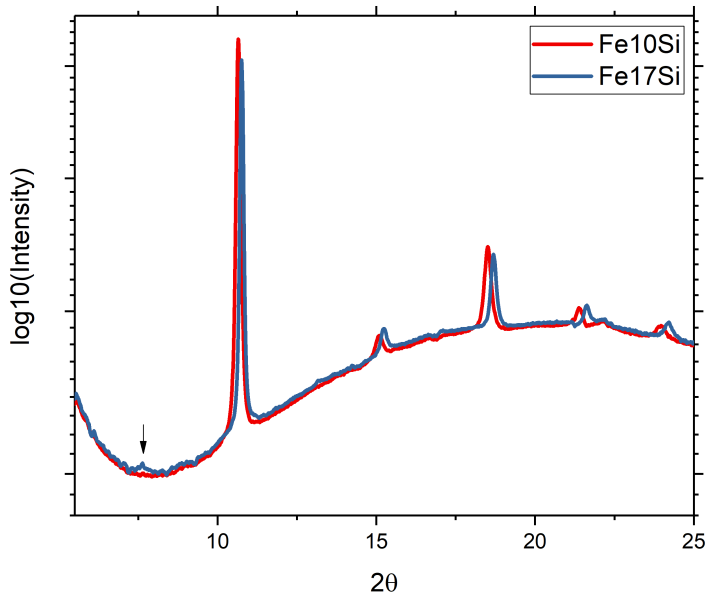

Figure 3.5: Fe-10 wt%Si and Fe-17 wt%Si measured at ambient pressure by synchrotron XRD in a diamond anvil cell.

At ambient conditions, the unit cell volumes of Fe-Si alloys have been measured repeatedly for nearly a century. Figure 3.6 shows the majority of the literature data

on the evolution of volume with Si content, and the bcc/B2/DO_3 phase diagram ([Phragmén, 1926], [Jette and Greiner, 1933], [Farquhar et al., 1945], [Lihl and Ebel, 1961], [Cockett and Davis, 1963], [Rausch, 1976], [Büchner and Kemnitz, 1981], [Polcarová et al., 1988], [Zuo et al., 2004], [Lin et al., 2003a], [Hirao et al., 2004], [Fischer et al., 2012], [Fischer et al., 2014], [Jayaraman et al., 2018]). It can be seen that the unit cell volume decreases with Si linearly, with two regimes at 0-4 wt% Si and about 6 - 20 wt% Si with an intermediary region between the two (4-6 wt%) where there is significant scatter in the literature. It is observed that while Fe5Si and Fe17Si measured here are both consistent with literature trends, all alloys intermediate to these compositions synthesized by PVD methods exhibit systematically higher volumes at the same concentration relative to literature.

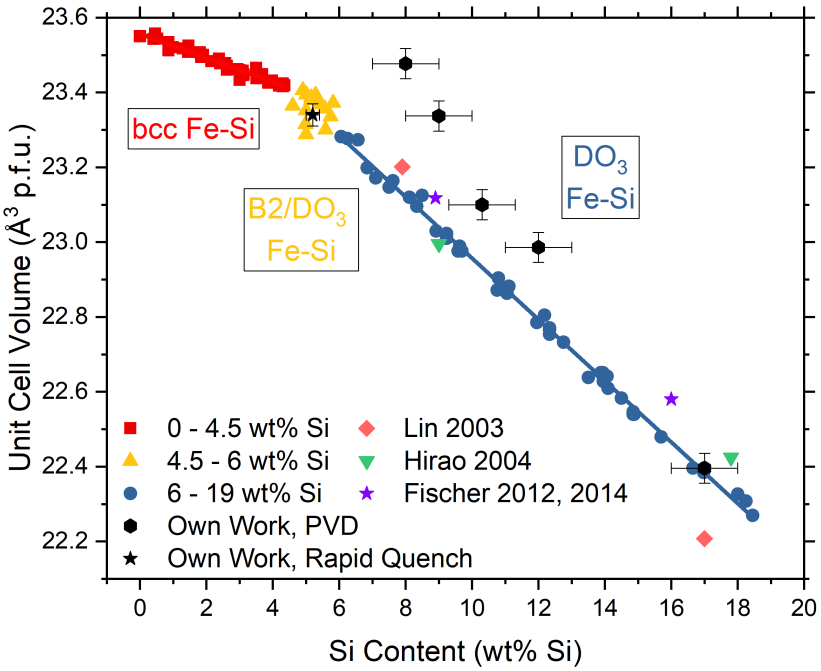

Figure 3.6: Ambient pressure bcc/B2/DO_3 Fe-Si unit cell volumes up to 19 wt% Si. For references see text.

Unweighted fits to the two regimes excluding newer data from the high-pressure community (due to significant scatter and limited compositional range) shows Volume - wt% Si trends as follows (Table 3.1):

As previously mentioned, the alloys synthesized by PVD for concentrations 8-12 wt%Si show significant differences in volume relative to literature trends. Such differences may be related to the differences in magnetic structure between bcc and DO_3 Fe-Si alloys, as B2/DO_3 ordering is linked to the change of slope in the V_0 vs. Si content plot at about 4.5 wt% Si [Kulikov et al., 2002]. While Fe and Si have similar atomic sizes, the volume per atom of bcc Fe is larger than that of diamond Si due to the magnetic pressure of Fe. Fe has unpaired d-electrons which generate a magnetic moment, and the interaction between the magnetic moments of Fe atoms

Compositional Range	V_0 (Å^3 p.f.u.)	$\frac{dV}{dx}$ (Å^3 p.f.u. per wt% Si)
0 - 4 wt% Si	23.5565(28)	-0.0319(11)
6 - 19 wt% Si	23.777(13)	-0.0820(7)

Table 3.1: Unweighted linear fits of unit cell volume (per formula unit) versus Si content.

in bcc-Fe results in an interatomic repulsion which expands the unit cell volume of bcc-Fe with respect to non-magnetic bcc-Fe [Wang et al., 1985].

Si is nonmagnetic and has no d-electrons, and as a consequence, alloying Fe with Si can weaken the bulk magnetic moment of the resulting alloy [Kulikov et al., 2002]. The broad trend of decreasing lattice constant with Si is due to the weakening of the magnetic pressure of the alloy. While the bulk magnetic moment decreases weakly up to ∼4.5wt% Si [Stearns, 1963], the kink in the Volume-Si content curve in this region (see Figure 3.6) arises from a splitting of the different crystallographic locations of Fe into high-spin and low-spin states in the Fe-Si DO_3 superstructure [Kulikov et al., 2002]. In this way, it is possible that the differences in unit cell volume observed between reported literature and the presented alloys arises due to differences in magnetic structure resulting from the suppression of chemical ordering in PVD Fe-Si alloys.

3.1.2 Elastic properties of Fe-Si alloys at ambient pressure

In the 1970s and 1980s ([Alberts and Wedepohl, 1971], [Routbort et al., 1971], [Rausch, 1976], [Machová and Kadečková, 1977], [Büchner and Kemnitz, 1981], [Kötter et al., 1989]) much work was performed studying the link between the elastic properties of Fe-Si alloys and their composition. Scatter in the reported Vp above ∼7 wt% Si is a direct consequence of the scatter in measured single crystal elastic moduli (C_{ij}) (Vp shown in Figs 3.7a and 3.7b). This may be due to porosity in Si-rich samples, as the two main systematic studies [Büchner and Kemnitz, 1981] and [Machová and Kadečková, 1977] both use similar methods for synthesis and measurement of the single-crystals, but the former uses the theoretical density derived from SEM and XRD, while the latter measured density directly (which was observed to deviate by up to 1.1% from theoretical densities where both were measured). In these two studies, while the error bars on elastic constants are about 1-1.5%, the derived bulk moduli (Figure 3.11 in next section) vary by up to 15% for Fe15Si. By a combination of picosecond acoustics and profilometry on PVD Fe-Si samples, it is shown in Figures 3.7a (Vp vs. Density) and 3.7b (Vp vs. Si Content) that Vp of our samples are generally close to the Reuss (isostress) bound derived from single crystal ultrasonics. In the samples measured for this Thesis, we could not detect void space within the samples by SEM, indicating that the effects of porosity in the present work is small. It is notable however that both Fe9Si and Fe10Si measured by PA are below Reuss bound. Due to the large variation of unit cell volume with Si content for Fe8Si, Fe9Si and Fe10Si, the densities of these alloys are nearly identical.

Within the ultrasonics literature, it is unambiguous that there is a change in the alloying effect of Si at the onset of the bcc/DO_3 transition region ([Machová and Kadečková, 1977], [Büchner and Kemnitz, 1981], indicating that both Si ordering and Si composition change the elasticity of these alloys. While Fe-Si alloys of 8, 12, 17 and 26 wt % Si measured by PA are in generally good agreement with trends observed in ultrasonics literature, there is significant discrepancy for alloys of Fe9Si and Fe10Si. At low Si contents, Si addition does not affect Vp significantly up to the disorder-order transition, and so this discrepancy between 8 and 12 wt%Si may be related to the suppression of Si ordering, as Vp of Fe-8,9,10Si synthesized by PVD have the same or lower Vp than that of pure iron [Guinan and Beshers, 1968]. The significant jump in Vp observed between Fe10Si and Fe12Si is likely related to an abrupt change in elastic moduli. Fe26Si was observed to be a mix of Fe-rich B2 FeSi (Volume = 21.42 $Å^3$, for stoichiometric B2 FeSi Volume $\approx$ 21.30 $Å^3$ [Ono, 2013] at ambient conditions) and an amorphous phase. As the density of the material was derived from the lattice parameter of the B2 unit cell volume, its Vp is generally consistent with that of an interpolation between Fe17Si and B20 FeSi [Petrova et al., 2010] when plotted as Vp vs. Density, while disagreement in Vp vs. Si content may be attributed to a possible enrichment of the amorphous phase with Si.

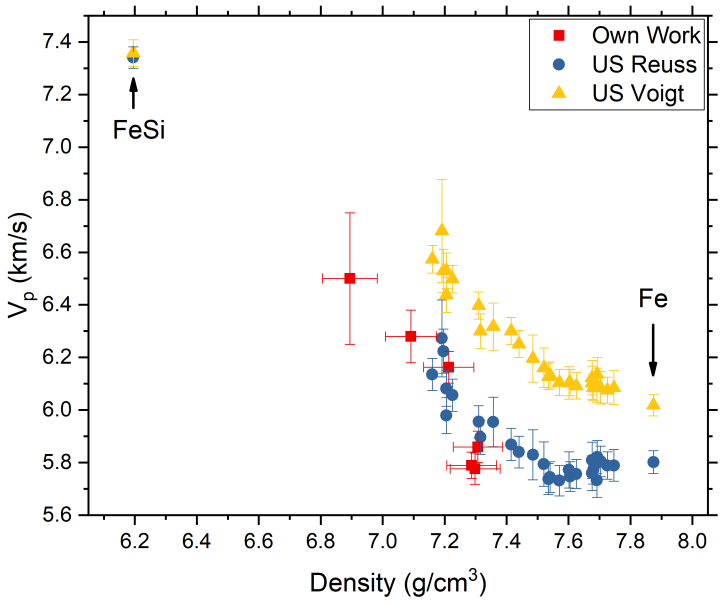

(a) Vp vs. Density

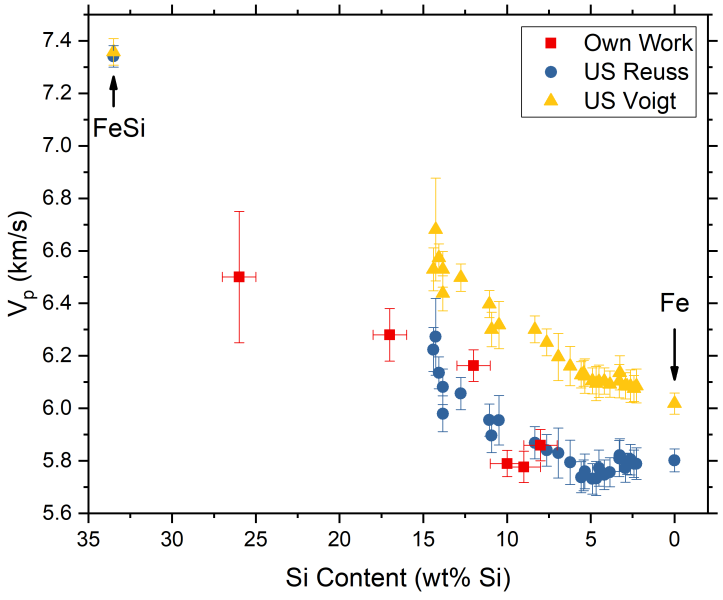

(b) Vp vs. Si Content

Figure 3.7: Vp vs. Density and Vp vs. Si Content at Ambient Conditions. Ultrasonics (US) literature in comparison to velocity-density and velocity-Si content relations determined in this Thesis at ambient conditions.

3.2 Velocity-density systematics of bcc and 'bcc-like' Fe-alloys: Properties of Fe-Si alloys at High Pressures

3.2.1 EoS of bcc and 'bcc-like' Fe-Si alloys at high pressures

The high pressure P-V relations of bcc and B2 Fe-alloys Fe5Si, Fe10Si, Fe12Si and Fe17Si were measured along 300 K isotherms up to the bcc-hcp transition (or up to 63 GPa in the case of Fe17Si, where a structural transition was not observed).

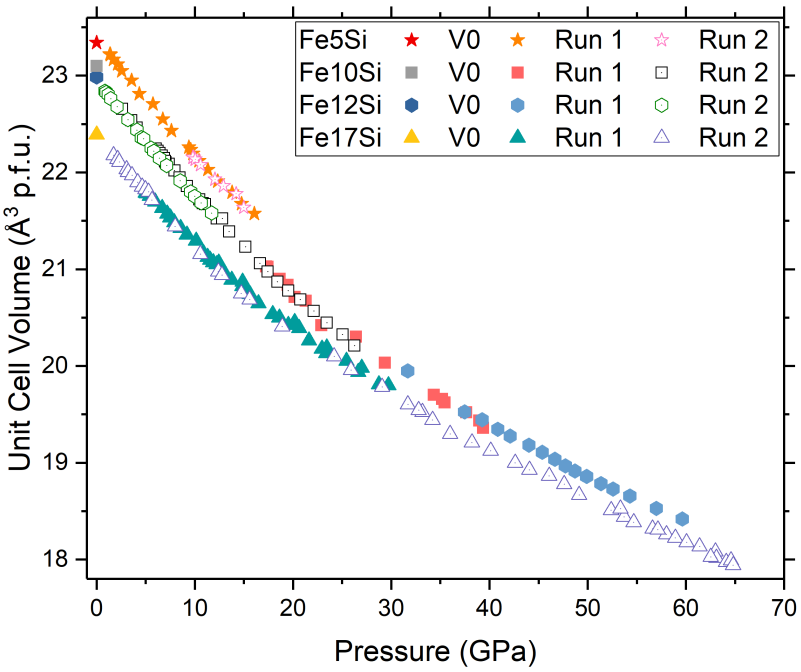

Figure 3.8: P-V data at 300 K of bcc Fe-Si alloys from this Thesis. All experiments have been carried out using Ne as PTM.

The results of such experiments are shown in Figure 3.8. Good consistency is observed cross different experimental runs. Bcc Fe5Si, Fe10Si and Fe12Si display almost parallel trends, although the volumes of Fe10Si and Fe12Si are virtually identical at high pressures despite the initial difference in volume at ambient pressure. The most remarkable difference between the two materials at high pressure is that the bcc-hcp transition in Fe10Si occurs 20 GPa below that of Fe12Si, as reported by both XRD and PA. Figure 3.9 shows the measured P-V data including selected literature EoS. It is seen that while Fe8Si [Lin et al., 2003a] is in very good agreement with the present dataset, the EoS of Fe16Si and Fe9Si of [Fischer et al., 2012] and [Fischer et al., 2014] are systematically different, despite being rescaled to a consistent pressure scale [Dewaele et al., 2012] and being compressed in Neon PTM.

When plotting Volume vs. Pressure, it can be difficult to graphically assess the

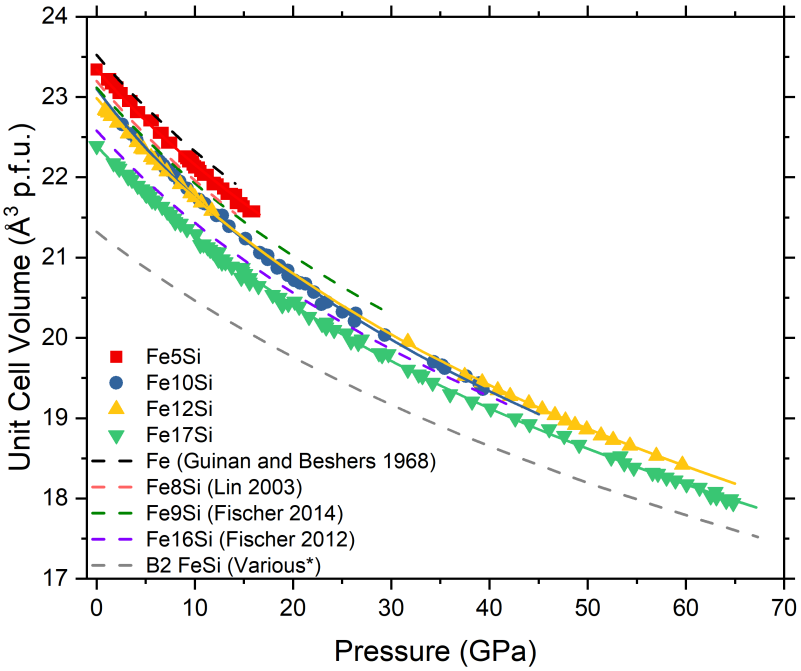

Figure 3.9: P-V data with EoS fits, in addition to literature Fe8Si [Lin et al., 2003a], Fe16Si [Fischer et al., 2012], Fe9Si [Fischer et al., 2014], B2 FeSi a fit to the combined datasets of [Ono, 2013] and [Sata et al., 2010]. [Fischer et al., 2012] and [Fischer et al., 2014] rescaled to the KBr pressure scale of [Dewaele et al., 2012].

variation of bulk modulus with composition, and so the data was also plotted in Figure 3.10 as Compressibility (V/V0) vs. Pressure, using the measured ambient V0 (with the exception of Fe5Si). It is shown here that Fe5Si and Fe17Si have comparable compressibilies at pressure, while Fe10Si and Fe12Si are softer relative to Fe5Si and Fe17Si.

The lower compressibility of Fe10Si and Fe12Si is reflected in the fitted EoS for these materials. K0 and K' of these alloys have been fit to either 3BM or Vinet EoS,the results of which are shown in Table 3.2. Over the compressional range measured, the difference between 3BM and Vinet formalisms results in only small differences in fitted parameters. For Fe5Si, as this was the only alloy where V0 was not measured by synchrotron sources in the dataset, the dataset was fit in two ways: one in which V0 is fixed to the measured V0 and K' = 5, and another in which all parameters are free. While over such a small compressional range K' cannot be well resolved, K0 of either fit are in good agreement. The variation of EoS parameters with Si content for this dataset shows that while K' does not significantly change over the measured compositional range, there is a 10-20% reduction in K0 of Fe10Si and Fe12Si relative to Fe5Si and Fe17Si. While the strong decrease of K0 for Fe10Si is remarkable in light of the observed K0 across the literature, this observation is supported by the anomalously low Vp measured by PA.

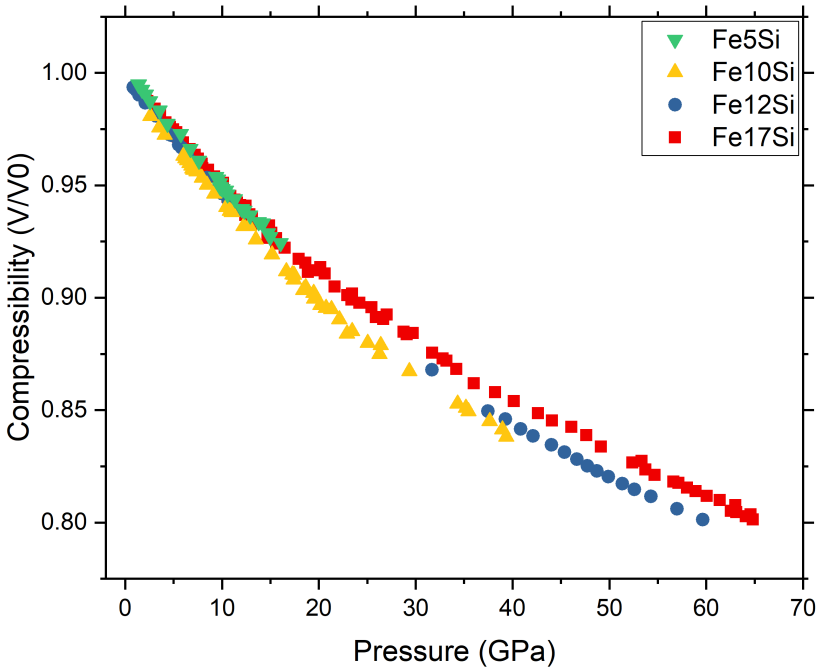

Figure 3.10: Compressibility vs. P for Fe5Si, Fe10Si, Fe12Si, Fe17Si. It is observed that Fe10Si and Fe12Si are softer than Fe5Si and Fe17Si.

Sample	Fe5Si^{3BM}	**Fe5Si**^{3BM}	Fe5Si^{RV}	Fe5Si^{RV}	**Fe10Si**^{3BM}
V_0 (Å^3)	23.40(2)	23.34(4)$^+$	23.40(2)	23.34(4)$^+$	23.10(4)$^+$
$K_{T,0}$ (GPa)	166.3(6.7)	168.9(1.2)	166.3(6.9)	169.2(1.2)	142.6(1.5)
$K'_{T,}$	4(1)	5(fixed)	4(1)	5(fixed)	5.1(2)
Sample	Fe10Si^{RV}	**Fe12Si**^{3BM}	Fe12Si^{RV}	**Fe17Si**^{3BM}	Fe17Si^{RV}
V_0 (Å^3)	23.10(4)$^+$	22.99(4)$^+$	22.99(4)$^+$	22.39(4)$^+$	22.39(4)$^+$
$K_{T,0}$ (GPa)	141.9(1.5)	157.5(1.0)	156.3(1.0)	172.1(1.2)	170.8(1.2)
$K'_{T,}$	5.3(2)	4.8(1)	5.0(1)	4.9(1)	5.1(1)

Table 3.2: Bold font indicates that the equation of state was used for the determination of volume for PA measurements, $^+$ denotes that V0 was fixed to the value determined at ambient conditions. The difference between the elastic parameters of Vinet and 3BM EoS fits are small, as systematic deviations due to the choice of formalism is limited for the degree of compression measured here [Angel, 2000].

Sample	G68*	V99*	L03 Fe8Si	H04 Fe9Si
V_0 (Å^3)	-	-	23.20(2)	22.98(2)
$K_{T,0}$ (GPa)	166.4	167.3	157.8(4.4)	268(5)
$K'_{T,}$	5.29	5.17	5.3(0.9)	5.3(fixed)
Sample	F12 Fe9Si	L03 Fe17Si	H04 Fe18Si	F14 Fe16Si
V_0 (Å^3)	23.12(6)	22.20(6)	22.43(1)	22.58(2)
$K_{T,0}$ (GPa)	166(4)	199.0(5.3)	207(15)	167(5)
$K'_{T,}$	5.0(5)	5.7(6)	5.1(6)	5.2(6)

Table 3.3: * indicates adiabatic values from single-crystal ultrasonics measurements. G68, V99, L03, H04, F12 and F14 refer to [Guinan and Beshers, 1968], [Voronov and Chernysheva, 1999], [Lin et al., 2003a], [Hirao et al., 2004], [Fischer et al., 2012] and [Fischer et al., 2014] respectively. F12 and F14 EoS presented here were rescaled using a pressure calibration which is more consistent with the calibrants used in this Thesis. All literature PV datasets described here employ the 3BM EoS formalism.

Literature EoS

This study is not the only one on Fe-Si alloys at high pressures- there are a significant quantity of previous studies proposing P-V EoS with different K0 and K'. A selection of static high-pressure K0 and Ultrasonics K0 data vs. Si content are shown in Figure 3.11, excluding significant outliers (e.g. [Hirao et al., 2004], [Knittle and Williams, 1995]). In Figure 3.11 all static K_T were converted to Ks using $\alpha = 4 * 10^{-5}$ and $\gamma = 1.8$.

It can be seen that within the high pressure datasets there is significant scatter between different experiments on different compositions. This can be primarily explained by two major effects- hydrostaticity and pressure metrology. Non-hydrostatic compression results in significant heterogeneity in the stress-state of the sample and leads to modification of sample texture. Figure 3.12 shows the development of stress in an Fe-Si alloy compressed at 300 K using KCl as PTM.

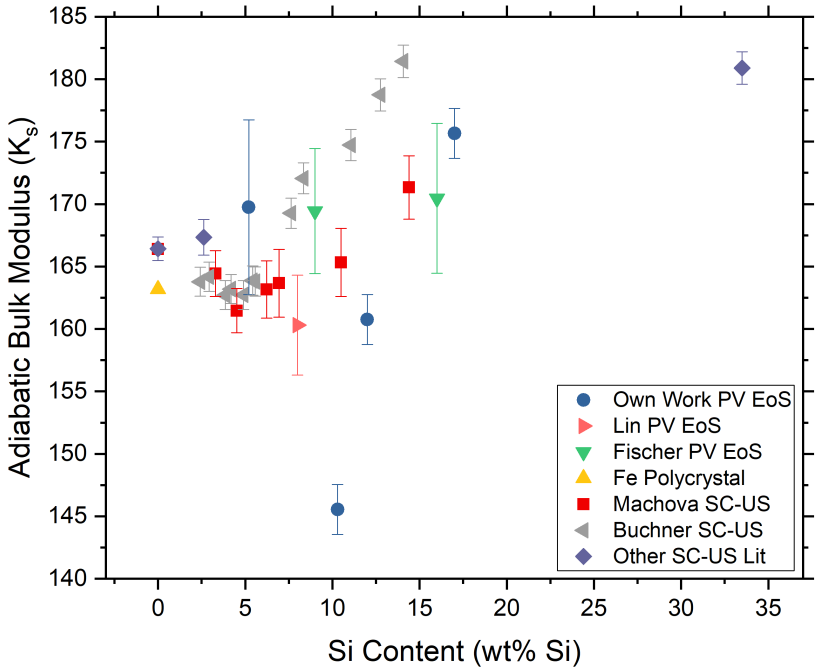

Figure 3.11: K0 vs. Si content, K0 which were determined by isothermal compression were converted to adiabatic K0 using $\alpha = 4 * 10^{-5}$ and $\gamma = 1.8$ (Discussed in Section 3.2.3). Polycrystal bulk modulus of Fe from [Shibazaki et al., 2016], single-crystal ultrasonics (SC-US) data from [Machová and Kadečková, 1977], [Büchner and Kemnitz, 1981], [Guinan and Beshers, 1968], [Voronov and Chernysheva, 1999], [Petrova et al., 2010]. Static compression data from [Lin et al., 2003a], [Fischer et al., 2012] and [Fischer et al., 2014].

This effect has been observed to cause significant deviations from quasihydrostatic measurements for cubic Fe-Si alloys over a wide pressure range when the resulting diffraction images are radially integrated and fitted as in a typical P-V experiment. The result of such fits is shown in Figure 3.13. It is seen that relative to the hydrostatic case, non-hydrostatic compression can lead to an overestimation of pressure by up to 20% at constant volume. While this effect may be less in hcp-Fe alloys, in the Fe-Si system we have observed strongly anomalous behaviour related to the textural variation of the samples under non-hydrostatic compression, and this behaviour worsens with increasing Si content.

As a consequence, non-hydrostatic compression should be avoided for ambient temperature PV EoS, or if not, treated with more advanced methods such as performing batch radial Rietveld refinement on small azimuthal slices of the diffraction image.

The EoS of Fe17Si of [Lin et al., 2003a] was fit using data involving ethanol:methanol:water mixture as the PTM for their experiments. This PTM is hydrostatic up to 11 GPa, but becomes strongly incompressible above this pressure [Klotz et al., 2009]. This would indicate that at higher pressures the dataset

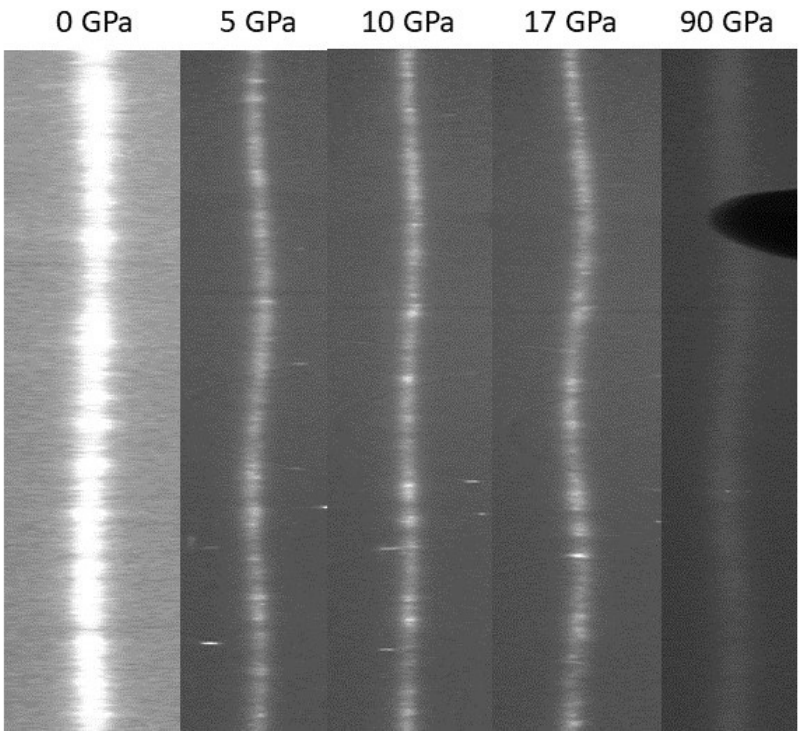

Figure 3.12: B2 (110) d-spacing of Fe-17Si compressed at 300 K using KCl as PTM, caked into a rectilinear projection. Oscillations in the line indicates non-hydrostatic stress on the unit cell. At 0 GPa, the sample is unstressed, and as the sample is compressed, the direction of stress on the unit cell changes. Above 12-15 GPa the lineshape stops changing appreciably, above which there is significant shearing of the Fe-17Si grains as shown by the significant broadening of the line at 90 GPa.

likely underestimates compressibility of the material and so it was omitted from the analysis. Differently, for Fe8Si, they used NaCl and stress-annealed the samples at high temperatures, and such methods can result in quasihydrostatic conditions for the sample [Dorfman et al., 2012].

A further consideration is the pressure calibration of the studies in question. It has been observed that the KBr pressure calibration used in [Fischer et al., 2012], [Fischer et al., 2013], [Fischer et al., 2014] overestimates sample pressure by nearly 10% at all pressures relative to another modern calibration [Dewaele et al., 2012]. As the pressure scales used in the current work are generally consistent with the calibration of [Dewaele et al., 2012], this leads to an intrinsic discrepancy in the presented data and resultant EoS fits. Shown in Figure 3.14 is the rescaled and unscaled datasets of Fe9Si and Fe16Si.

Further implications of pressure scale discrepancy can be expected for stoichiometric B20 and B2 (high pressure phase [Dobson et al., 2002]) FeSi, as [Fischer et al., 2014] represents the only experimental P-V-T study on both of these phases to Mbar pressures. A reanalysis of the 300 K P-V data using updated P-scales for such studies is shown in Figure 3.15. It is observed that when the Dewaele KBr scale is used to fit the Fischer B20 FeSi static compression data, the resultant EoS is in excellent agreement with ultrasonics measurements [Whitaker et al., 2009].

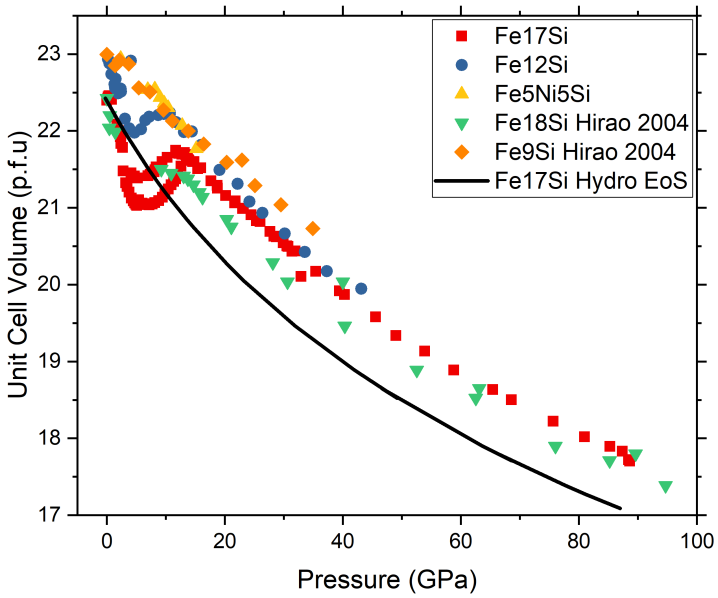

Figure 3.13: Non-hydrostatically compressed Fe-Si and Fe-Ni-Si alloys including Fe18Si from [Hirao et al., 2004]. It is observed that this results in anomalous behaviour at low pressures and a systematic overestimation of pressure at constant volume for a given sample.

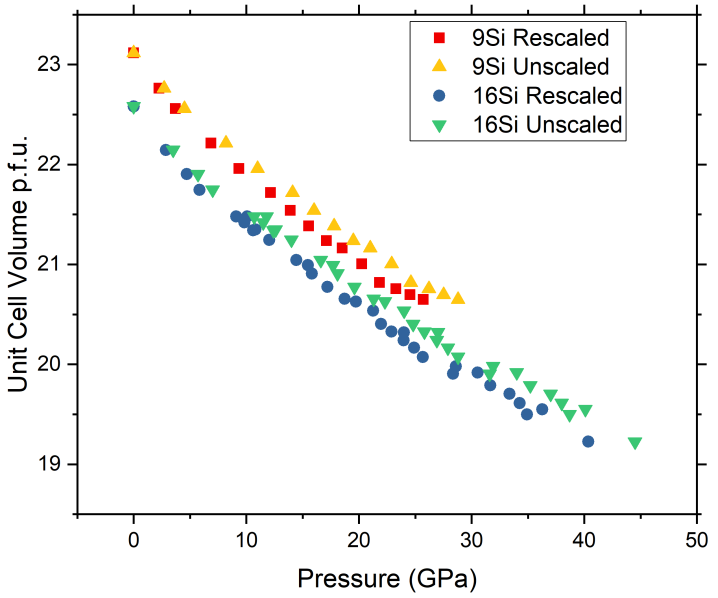

Figure 3.14: [Fischer et al., 2012] and [Fischer et al., 2014] rescaled using the KBr scale of [Dewaele et al., 2012].

Additionally, it is observed that the B2 FeSi EoS measured by [Sata et al., 2010] and [Ono, 2013] only differ by the pressure calibration used, as [Sata et al., 2010] uses the MgO scale of [Speziale et al., 2001] while [Ono, 2013] uses the B2-NaCl pressure scale of [Ono, 2010], which is calibrated against the MgO scale of [Tange et al., 2009]. The combined dataset and fit (based on the Tange MgO scale) is shown in Figure 3.15.

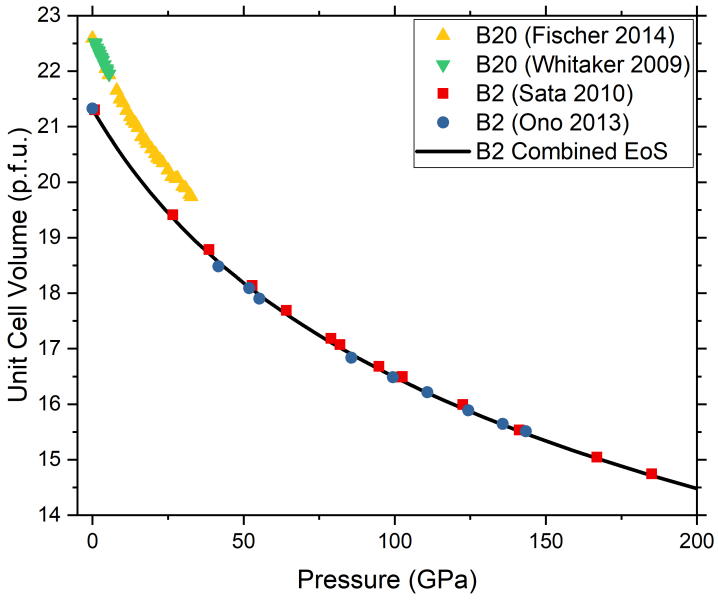

Figure 3.15: B20 and B2 FeSi after [Whitaker et al., 2009], [Fischer et al., 2014], [Sata et al., 2010] and [Ono, 2013].

Table 3.4 shows the recommended EoS parameters from available static compression data in this system at 300 K.

Sample	B20 FeSi Fischer 2014	B20 FeSi Whitaker 2009	B2 FeSi(Combined)
V_0 (Å^3)	90.36(11)	90.45(3)	21.32(6)
$K_{T,0}$ (GPa)	157(8)	168.9(7)	223(7)
$K'_{T,}$	6.6(1.0)	6.6(2)	4.3(1)

Table 3.4: Table of EoS parameters for B20 and B2 FeSi

3.2.2 Compressional velocity-density relations at high pressures

Generally, the Vp vs. P datasets of Fe5Si, Fe8Si and Fe10Si are quite close at ambient pressure, and remain close up to their respective bcc-hcp transition pressures, shown in Figure 3.16. All of the measured alloys appear to exhibit atleast weakly sublinear evolution of Vp with P, although for Fe17Si it is the most evident. At constant pressure, variation of Vp with Si content is strongly dependent on the Vp of the starting material, as Fe5Si, Fe8Si, Fe10Si and Fe12Si are roughly parallel in the evolution of Vp with P. In the case of Fe5Si, Vp at ambient pressure was derived from the Hashin-Strikman average of an interpolation of elastic constants between 4.5-6.2 wt%Si reported in [Machová and Kadečková, 1977] (derived Vp = 5.96 km/s). As the ambient Vp of Fe8Si and Fe10Si is lower than that derived for Fe5Si, at high pressures, Fe8Si and Fe10Si exhibit lower sound velocities at constant pressure. Conversely, the Vp of both Fe12Si and Fe17Si are higher than Fe5Si at ambient conditions, and retain higher Vp at high pressures (for a given pressure). With the exception of Fe17Si, Vp vs. P was measured up to the bcc-hcp transition pressure.

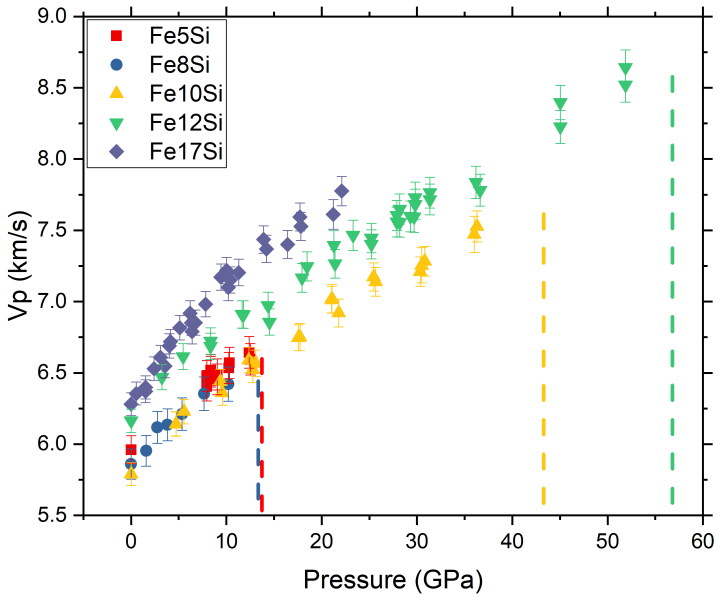

Figure 3.16: Vp vs Pressure of the present dataset. Colored dashed lines indicate the onset of the hcp transformation by XRD.

By combining the measured Vp vs. P curves with P-V measurements, it's possible to construct Vp-Density plots, which are typically linear with density in the absence of electronic, magnetic or structural transitions [Birch, 1961]. In the case of Fe8Si, in order to determine the variation of thickness and bulk modulus with pressure, an approximate EoS was constructed from a linear interpolation of the K0 of Fe5Si and Fe10Si, using the measured ambient V0 and assuming K' = 5. Due to the observation of a potential pre-transition effect in the vicinity of the bcc-hcp

transition, data points within a few GPa of this transition were omitted from Vp-ρ (and Vs-ρ) fitting. Figure 3.17 shows the measured Vp-Density diagrams for bcc and B2 Fe-Si alloys. At constant density, Vp is observed to increase with Si content.

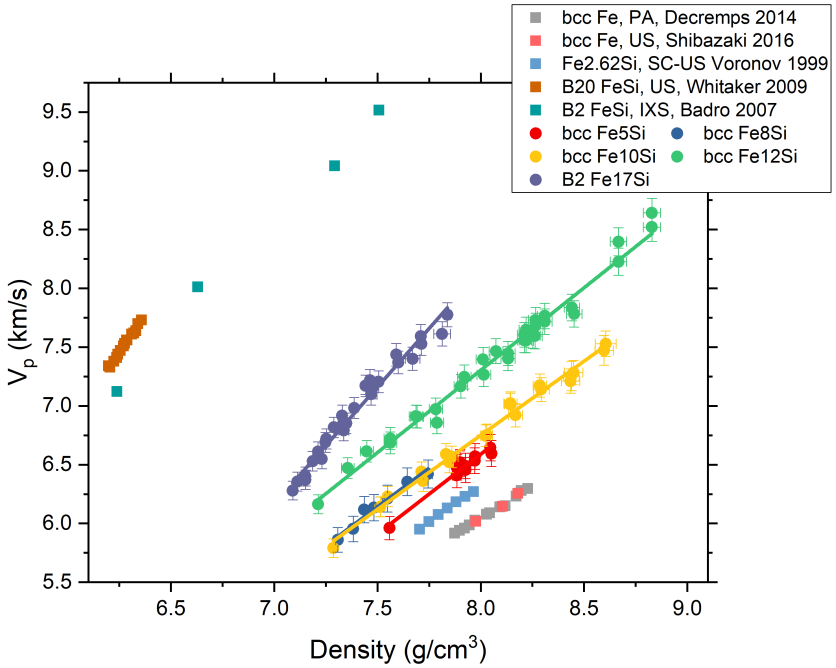

Figure 3.17: Velocity-Density relations of cubic Fe-Si alloys. This shows the present data in addition to literature ([Decremps et al., 2014], [Shibazaki et al., 2016], [Voronov and Chernysheva, 1999], [Badro et al., 2007], [Whitaker et al., 2009]).

It is observed that from bcc-Fe ([Shibazaki et al., 2016], [Decremps et al., 2014]) to Fe10Si, there is a small change in initial Vp and density, and little change in terms of the slope of the Vp-density plot. From 10 to 12wt% Si, there is a large jump in Vp related to that observed at ambient pressure. At 17wt%Si (and more so for stoichiometric B2 and B20 FeSi [Whitaker et al., 2009], [Badro et al., 2007]) there is a significant change in the Vp-Density plot with respect to Fe. Table 3.5 shows the Velocity-Density fits of the present dataset and some literature ([Decremps et al., 2014], [Voronov and Chernysheva, 1999]. The IXS dataset of [Liu et al., 2014] of Fe and Fe8Si was omitted from the present discussion due to the significant discrepancy between that dataset, ultrasonics and PA literature ([Shibazaki et al., 2016], [Decremps et al., 2014]).

3.2.3 Derivation of shear properties at high pressures for bcc-Fe-Si alloys

As mentioned in the methods chapter, Vp can be related to the bulk and shear moduli of a polycrystalline solid. Isothermal P-V equations of state give the isothermal bulk modulus of a material, while the bulk modulus probed by studies of elastic waves is adiabatic. In order to accurately derive the shear properties of these alloys from P-V data and Vp vs P curves, an approximate P-V-T equation of state must

Sample	Fe D14	Fe2.6Si V99	Fe5Si	Fe8Si	Fe10Si	Fe12Si	Fe17Si
$\frac{dV_p}{d\rho}$ km s^{-1} ρ^{-1}	1.09(3)	1.23(3)	1.36(10)	1.32(11)	1.28(3)	1.43(3)	1.99(6)
V_{p0} km s^{-1}	-2.6(2)	-3.5(3)	-4.3(8)	-3.7(8)	-3.4(2)	-4.1(3)	-7.8(5)

Table 3.5: Selected linear fits to Fe-Si Vp-Density datasets. Discussion follows in Section 3.3

be constructed to derive the thermodynamic quantities necessary to interconvert between adiabatic and isothermal moduli (see Equation 2.24). While there are high temperature EoS for cubic Fe-Si alloys Fe16Si [Fischer et al., 2012] and Fe9Si [Zhang and Guyot, 1999], due to the wide range of compositions measured here it is necessary to assess the variation of thermal properties with Si content. Furthermore, such P-V-T equations of state heavily rely on the quality of the measured 300 K P-V curve, and for the limited pressure range measured by [Zhang and Guyot, 1999], may not be suitable. Assuming a P-V-T model where the temperature term is purely vibrational, it is possible to provide constraints on the thermodynamic Grüneisen parameter and Debye temperature based on previous literature studies of V(T) at ambient pressure, after the formalism of [Vočadlo et al., 2002], and references therein. As there is a large quantity of available literature studying V-T relations at ambient pressure ([Cockett and Davis, 1963], [Lihl and Ebel, 1961]) up to 12 wt%Si, it is possible to reanalyze such data in the context of modern literature and use them to constrain the thermal expansion and gruneisen parameter of Fe-Si alloys as a function of Si content at near-ambient temperatures.

By assuming the value of q in a P-V-T EoS (which controls the volume and hence pressure dependence of thermal pressure), it is possible to extend the results of such V(T) measurements to high pressures, providing constraints on the conversion factor between adiabatic and isothermal bulk moduli at high pressures. In order to fit ambient pressure V(T) data Equation 3.1 was used, after [Hunt et al., 2017], [Vočadlo et al., 2002], where thermal expansion is considered to be equivalent to an elastic strain on the lattice.

$$V\left(T\right) = V_0 + \frac{V_0 U}{Q - bU} \tag{3.1}$$

Where in this case, V_0 refers to the ambient temperature volume and Q, b, U refer respectively to

$$Q = \frac{V_0 K_0}{\gamma} \tag{3.2}$$

$$b = \left(K' - 1\right)/2 \tag{3.3}$$

$$U = 9RT\left(\frac{T}{\theta_D}\right)^3 \int_{300}^{\theta_D/T} \frac{x^3}{exp\left(x\right) - 1} dx \tag{3.4}$$

From available literature and the P-V EoS established here, K' is likely ∼5 ([Guinan and Beshers, 1968], [Voronov and Chernysheva, 1999]), and K0 is likely 160-170 GPa (see Figure 3.11). As a result, the data was fit with K' = 5 and K0 = 165 GPa. Derived thermodynamic quantities do not vary outside of the reported error by changing K' by +/- 1 or K0 by +/- 10 GPa. Figure 3.18 shows the fit of the literature data. At high Si contents, there were significant anomalies at temperatures higher than 700-1000 K, potentially due to the effect of order/disorder phenomena [Randl et al., 1995] and anharmonic effects.

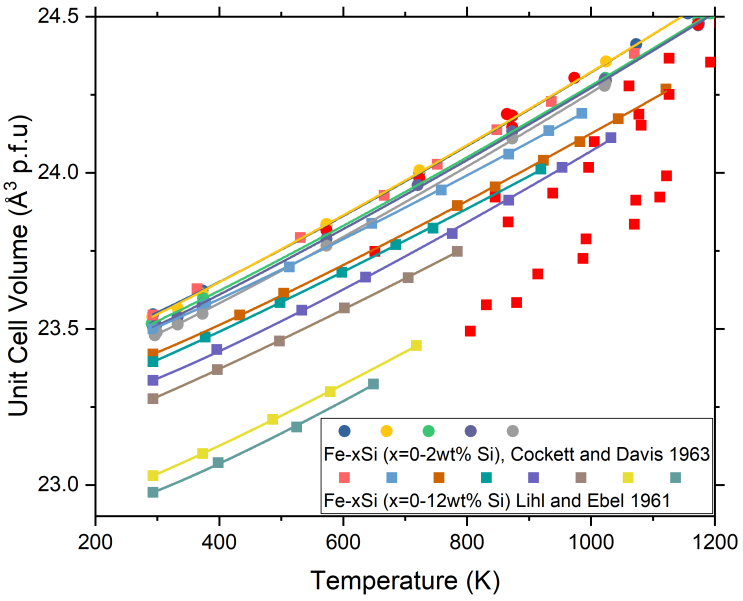

Figure 3.18: EoS fits to Volume vs Temperature relations of [Lihl and Ebel, 1961] and [Cockett and Davis, 1963].

As a result of this analysis, it is observed in Figure 3.19 that Debye temperature does not change significantly with Si content within error and the results of this analysis is in agreement with other determinations of the Debye temperature at low temperatures of both Fe (476 K, [Adams et al., 2006]) and Fe15Si (501 K, [Rausch and Kayser, 1977]).

While γ vs. Si content shows significant scatter between different compositions, such variability only reflects an effect of about 5-10% in the derived quantities desired from the equation of state. Using this information, it is possible to derive a thermodynamic gruneisen parameter from Equation 3.20, assuming the heat capacity of bcc-Fe at ambient conditions ($25.1 Jmol^{-1}K^{-1}$, [Chase, 1998]).

$$\gamma_{th} = \frac{\alpha K_T V_M}{C_v} \tag{3.5}$$

Where α is the volumetric thermal expansion of the material, K_T is the isothermal bulk modulus and C_V is the volumetric heat capacity. Table 3.6 shows the

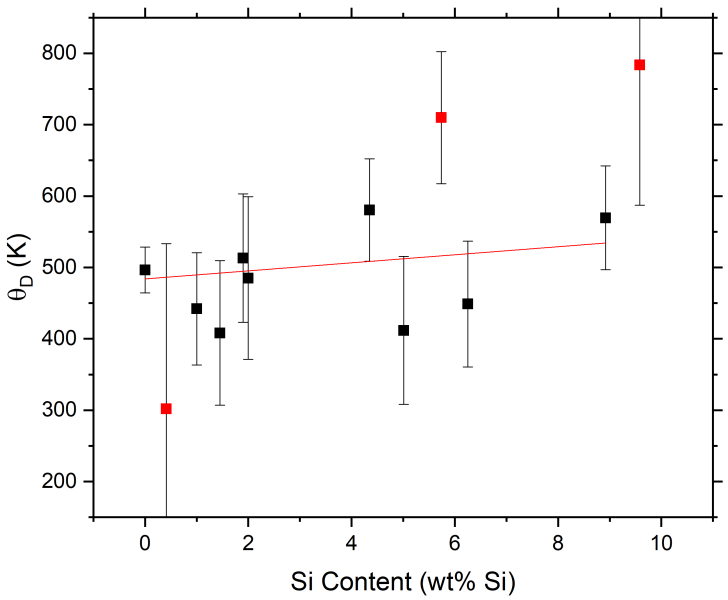

Figure 3.19: Fitted Debye temperature with K0 = 165 GPa and K' fixed to 5.

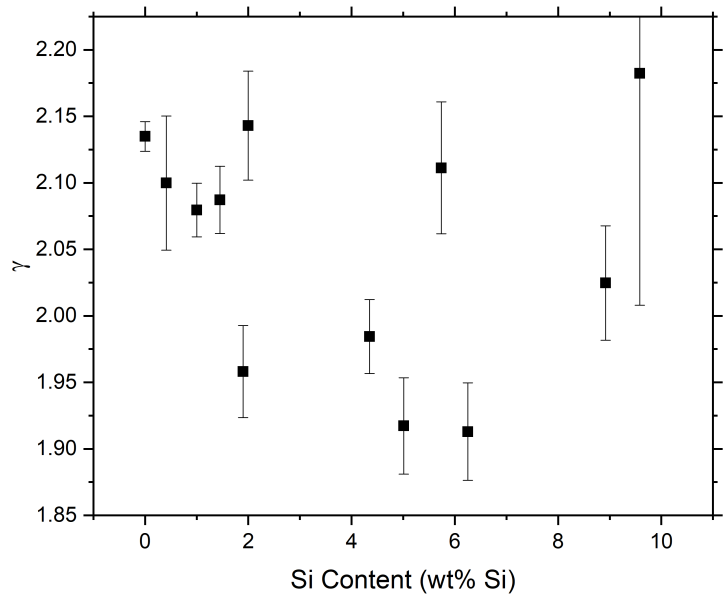

Figure 3.20: Fitted Gruneisen parameter with K0 = 165 GPa and K' fixed to 5.

results of this analysis. It is seen that using the thermal expansion and thermodynamic gruneisen parameter derived here the difference between isothermal and adiabatic bulk moduli at ambient pressure is ∼2.0(8)% for these alloys.

Assuming a value of q = 1 and the vibrational thermal model derived above, shear velocities were calculated based on the present P-V equation of states and

Sample	Fe A06	Fe15Si R95	Fe16Si F14	Fe-xSi (Present Analysis)
θ_D	476.4	440(7)	417	480(80)
γ	1.65	-	1.89(6)	1.8(2)

Table 3.6: Selected Debye temperatures and thermodynamic grüneisen parameters from literature. A06, R95 and F14 are [Adams et al., 2006], [Randl et al., 1995] and [Fischer et al., 2014] respectively.

measured Vp (Figure 3.21).

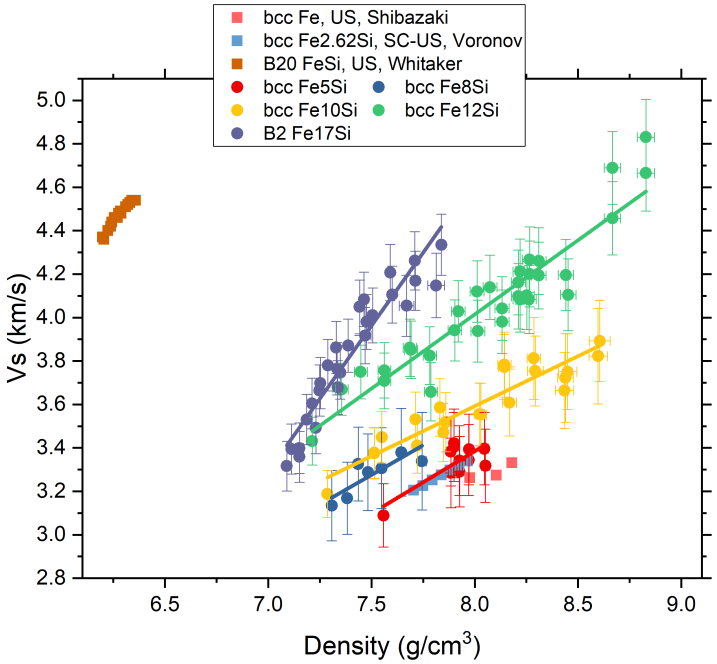

Figure 3.21: Vs vs Density plots showing Vs derived from the present PA experiments in addition to [Voronov and Chernysheva, 1999], [Shibazaki et al., 2016] and [Whitaker et al., 2009].

It is observed that despite of the large scatter, it is possible to discern clear trends in the Vs vs Density plot shown in Figure 3.21. Furthermore, such data appears to be in good agreement with ultrasonics literature [Shibazaki et al., 2016], [Voronov and Chernysheva, 1999].

Sample	Fe2.6Si V99	Fe5Si	Fe8Si	Fe10Si	Fe12Si	Fe17Si
$\frac{dV_S}{d\rho}$ km s^{-1} ρ^{-1}	0.518(5)	0.57(14)	0.55(16)	0.46(4)	0.69(4)	1.34(9)
V_{S0} km s^{-1}	-0.79(4)	-1.2(1.1)	-0.8(1.2)	-0.1(3)	-1.5(4)	-6.1(7)

Table 3.7: Selected linear fits to Fe-Si Vs-Density datasets. Discussion follows in Section 3.3

3.3 On the effects of Si ordering and Si content in bcc Fe-Si alloys

3.3.1 Shear and Bulk Moduli of Fe-Si alloys: Si ordering revisited

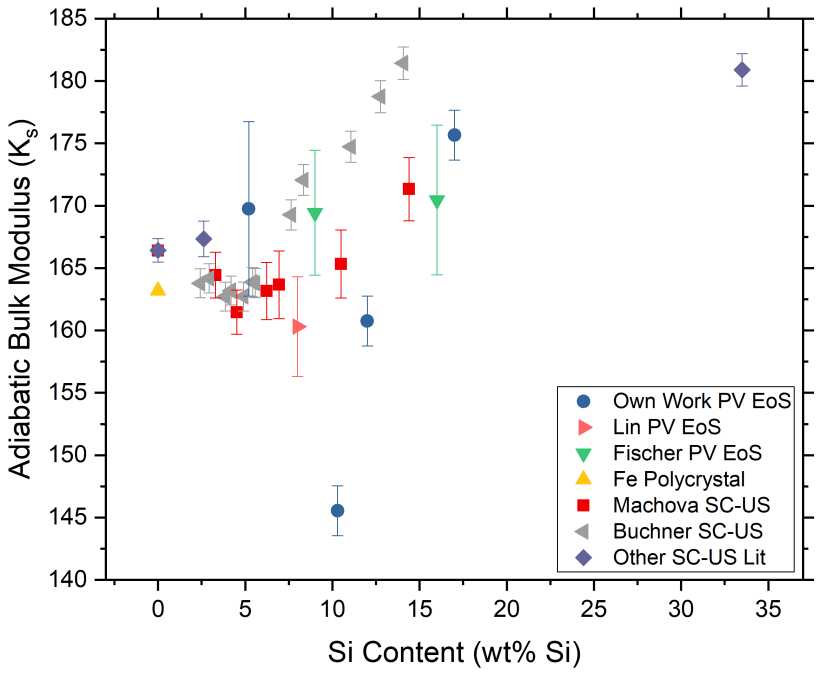

Figure 3.22: K0 vs. Si Content. In the present work, K0 is systematically lower than literature between 5 and 17 wt%Si.

It is observed in ultrasonics literature that in the vicinity of the bcc/DO_3 ordering transition, there is a hardening of the bulk modulus and as well an increase in the shear modulus. Both shown in Figures 3.22 and 3.23, up to 5 wt% Si there is little change in Ks, but a small decrease in G and decrease in density. This results in a nearly constant Vp with increasing Si content. Above the DO_3 ordering transition, there is a marked increase in both Ks and G with Si content [Machová and Kadečková, 1977], [Büchner and Kemnitz, 1981]. On the contrary, it is seen for the PVD alloys measured here that samples with 10 and 12 wt%Si have systematically lower derived Ks.

For PVD alloys, G slightly increases with increasing Si content by about 5-10 GPa from Fe8Si to Fe17Si, although Fe17Si is anomalously low relative to the trend established by the rest of the dataset. This may be caused by enhanced challenges with sample thickness measurement, as described in Section 2.4. A possible explanation for the observed behaviour of K0 vs. Si content is that in the absence of significant Si-ordering, Si continues to soften the Fe-Si alloy above the bcc/DO_3

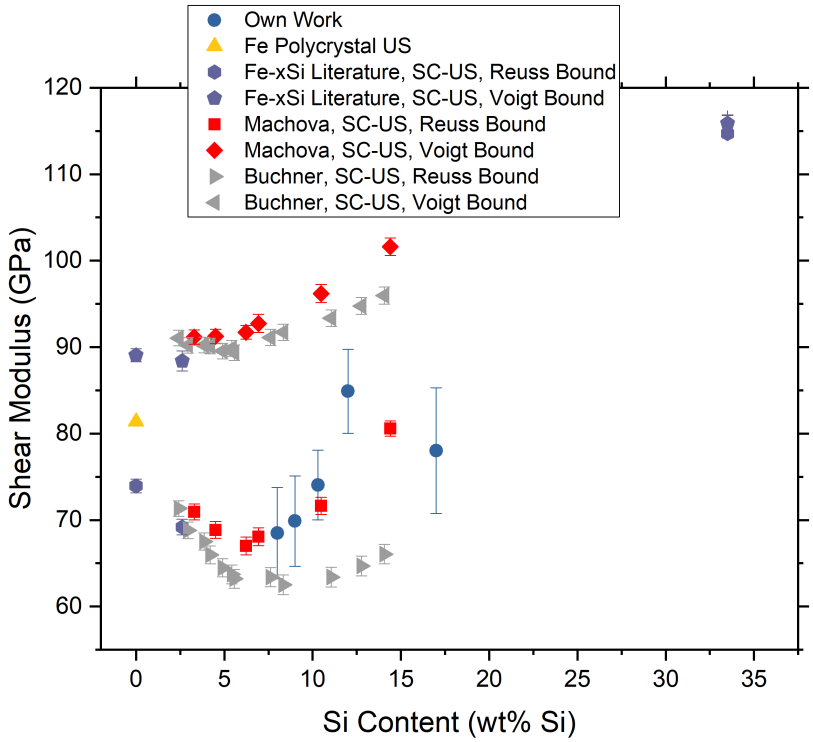

Figure 3.23: G0 vs. Si Content. G is generally within error of the Reuss bound of ultrasonics literature.

ordering transition. This idea is supported by *ab initio* calculations of local elastic moduli of Fe-Si octahedra within bulk Fe-Si alloys [Bhattacharya et al., 2017], where they show that the bulk moduli of Si-disordered Fe-Si alloys weakly decreases due to a weakening of d-d bonding between Fe atoms. In their calculations of more Si-rich compositions, the 2 or 3 dimensional structure which results from DO_3 ordering induces a change in bonding between Fe and Si atoms, resulting in an increase of the bulk modulus with increasing Si content. As a result, the suppression of Si-ordering by PVD significantly alters the physical and mechanical properties of these alloys in comparison to conventional methods.

Furthermore, by comparing the relative variation of compressibility of Fe-Si alloys between the present study and the studies of [Fischer et al., 2012] and [Fischer et al., 2014] (Figure 3.24), it is seen that the difference in compressibility between DO_3 Fe9Si and DO_3 Fe16Si is small, while for the alloys measured in the present study, there is much more significant variation between bcc Fe10Si (or Fe12Si) and B2 Fe17Si (which in itself is very close to the DO_3 datasets), indicating that compressional behaviour may be strongly dependent on the degree of Si ordering in this system.

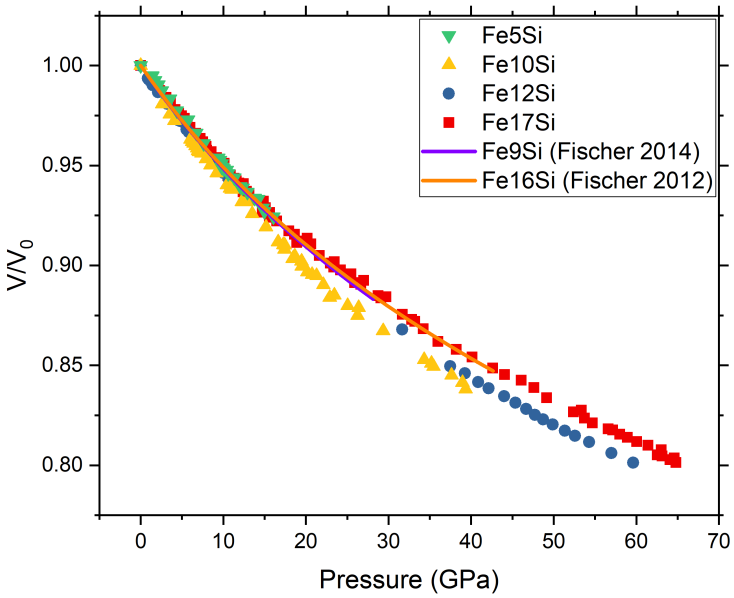

Figure 3.24: Compressibility data revisited. The compressibility of Fe17Si is nearly identical to the DO_3-ordered samples of [Fischer et al., 2012] and [Fischer et al., 2014], however Fe10Si and Fe12Si are significantly more compressible.

3.3.2 Evolution of compressional and shear velocities with Si content at high pressures

Following this discussion of the effects of ordering and composition, Figure 3.25 shows the effect of Si content on the slope of Vp-density plots. It is observed that while Si acts to increase dVp/dρ with increasing Si content, this quantity changes most significantly with changes in structure - B2 Fe17Si has a slope about 100% higher than pure iron, and is comparable to the slope of B2 FeSi measured by [Badro et al., 2007].

In the Fe-xSi system, it is apparent that for Vp a linear-mixing approximation- a model of elastic properties which is constructed by the linear interpolation of two end-member compositions- is not valid. While it likely holds for alloys between 0 to 5 wt% Si, extrapolations of elastic behaviour to higher compositions is not certain. It is seen here that such models cannot reliably reproduce intermediary compositions, because it appears that crystal structure and chemical ordering strongly influence the change in elastic properties of these materials at pressure.

For the slope of Vs-Density plots, a similar trend is observed (Figure 3.26). It is seen that dVs/dρ slightly decreases with Si content up to 10wt% Si, after which there is a significant increase in curvature. Also shown in Figure 3.26 is a comparison of the dVs/dρ derived with adiabatic or isothermal bulk moduli. Using isothermal moduli results in a systematic decrease in the slope of dVs/dρ, although due to the fact that $K_T < K_S$, the magnitude of the derived Vs is also slightly higher. As a result, the two effects likely trade off against each other when extrapolated to higher

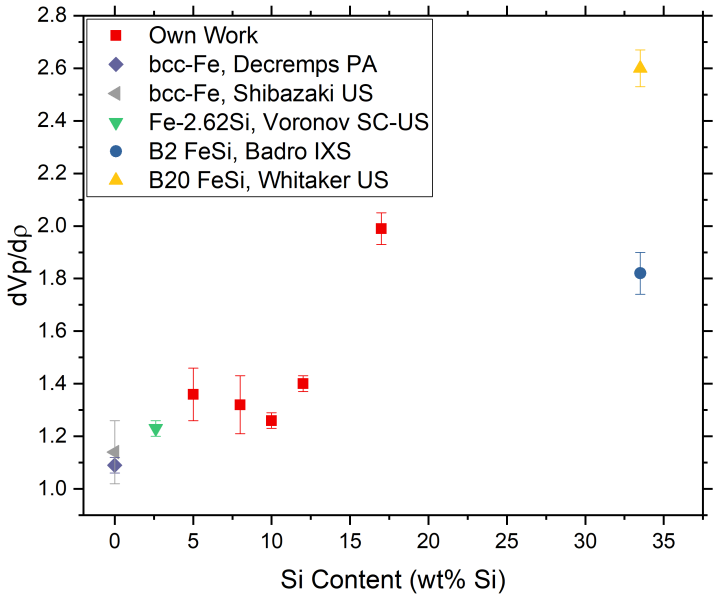

Figure 3.25: Slope of compressional velocity-density plot with Si content. This quantity is strongly dependent on the structure of the Fe-Si alloy. Plotted alongside [Decremps et al., 2014], [Shibazaki et al., 2016], [Voronov and Chernysheva, 1999], [Badro et al., 2007] and [Whitaker et al., 2009].

densities.

An important technical consideration in the derivation of Vs from Vp data and a P-V EoS, is that the resulting Vs-ρ relation is highly sensitive to the choice of K' of the EoS for materials where the sampled density range is limited. In the case of Fe10Si where Vp and the P-V EoS are both measured over a density range of nearly 1.2 g/cm^3, (or hcp-Fe5Si, $\approx$2 g/cm^3, discussed later in Section 4.2), the choice of K' changes the slope of dVs/dρ by less than 5%, while for Fe5Si and Fe17Si where the density range is more limited ($\approx$ 0.8 g/cm^3 and $\approx$ 0.5 g/cm^3 respectively) the difference between K' = 4 and K' = 5 can change dVs/dρ by up to 15% (for Fe17Si) and 50% (for Fe5Si). It is stressed however, that the present XRD and Vp dataset is of very high quality, and for the more Si-rich alloys where P-V data could be measured to very high pressures (Fe10Si, Fe12Si and Fe17Si) it is shown that K' does not significantly change with Si content. As a consequence, K' is not expected to deviate strongly for Fe5Si and Fe8Si and so the presented Vs-Rho relations remain reliable for these alloys.

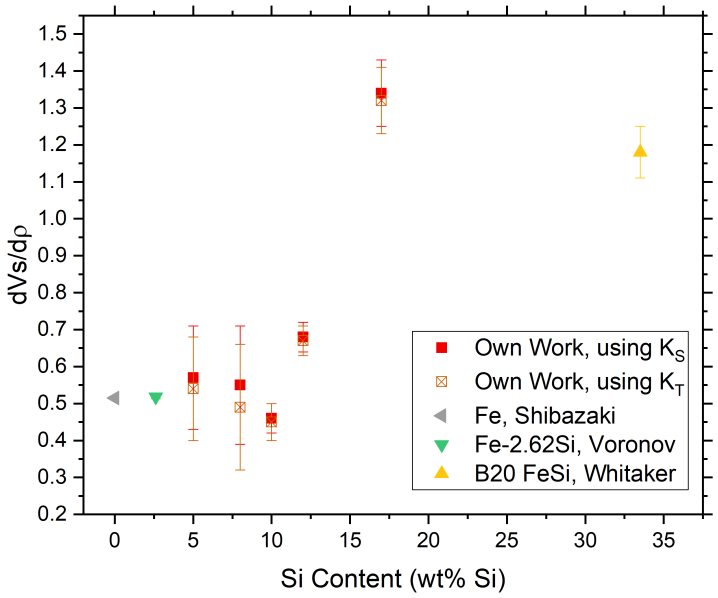

Figure 3.26: Slope of derived shear velocity-density plot. It is observed that Si-disordered bcc alloys are in good agreement with ultrasonics literature on Fe2.6Si [Voronov and Chernysheva, 1999] and Fe [Shibazaki et al., 2016]. Plotted with [Whitaker et al., 2009].

Chapter 4

On the hcp phase of Fe-Si alloys: Constraints on Earth's core composition and anisotropy

4.1 On the bcc-hcp transition in Fe-Si alloys at high pressures

The hcp structure is expected to be the stable crystal structure of iron at the Earth's core pressures and temperatures [Tateno et al., 2010]. Although bcc-Fe is magnetic, the current consensus is that hcp-Fe is not, and that the structural transition of Fe from bcc to hcp is driven by the disappearance of magnetism at high pressures (e.g. [Monza et al., 2011], [Dewaele and Garbarino, 2017]). While structural transitions under pressure are commonplace across the periodic table, typically phase transitions occur between structures which are related by symmetry. However bcc and hcp structures in general are not related by symmetry, and it is common for transitions between them to be preceded by some type of elastic instability (e.g. the Burgers mechanism, [Burgers, 1934]). By contrast, bcc-Fe appears to show no pre-transition effect [Klotz and Braden, 2000], [Decremps et al., 2014], which has been a strong argument to establish the current view of a magnetism-driven bcc-hcp transition. It has been established that the incorporation of Si into bcc-Fe generally acts to weaken its bulk magnetic moment [Fallot, 1936], [Stearns, 1963]. Consequently, studying the effect of Si on the elastic properties of Fe-Si alloys in the vicinity of the bcc-hcp transition provides new insights into the underlying mechanism of the bcc-hcp transition in Fe.

Indeed, in the case of Fe-Si alloys, Si addition stabilizes the bcc phase relative to hcp at high pressures. Up to about 8-9 wt%Si, the effect of Si on the transition pressure is relatively weak [Clendenen and Drickamer, 1966], [Lin et al., 2003a], [Morrison et al., 2018], [Zukas et al., 1963], [Hirao et al., 2004], where transition pressure shifts by only a few GPa from elemental Fe. However, above ≈9wt%Si the transition rapidly increases in pressure, as [Fischer et al., 2014] did not observe a transition in Fe9Si up to 36 GPa, and for more Si rich compositions (containing between 15-18 wt% Si) a transition has not been observed ([Wicks et al., 2018],

[Fischer et al., 2012], [Lin et al., 2003a], [Hirao et al., 2004]). Consequently between 9-15 wt% Si there are few experimental constraints on the evolution of the bcc-hcp transition pressure with Si content. Additionally, while there have been *ab initio* calculations which have reproduced observations of an increase in transition pressure with Si content [Côté et al., 2008], at present there has been no discussion of why this change in behaviour occurs.

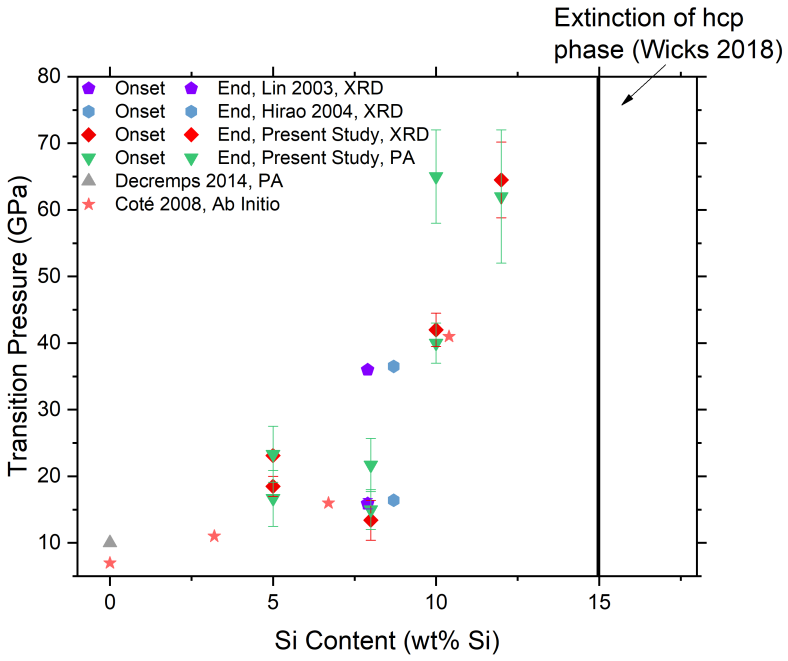

Figure 4.1: Transition pressure vs. Si content from the present work and selected literature. It is observed by both PA and XRD that there is an abrupt increase in transition pressure between 8 and 10 wt% Si. Transition pressures are in good agreement with literature.

In this Thesis, we have studied Fe5Si, Fe8Si, Fe10Si and Fe12Si to pressures exceeding the bcc-hcp transition and have observed behaviour in good agreement with literature. Shown in Figure 4.1 is the observed onset and end of the bcc-hcp transition of the present dataset (measured by either PA or XRD) compared to results from literature.

For XRD measurements from the present thesis, the onset of the hcp transition was defined as the first pattern in which there was an observable hcp (002) peak. For PA, observation is less direct, and the onset of the transition and mixed phase region are related to the 'smearing' of the measured time domain signal. Shown in Figure 4.2 are selected travel times collected during high pressure PA runs of Fe10Si before, during and after the bcc-hcp transition. It is observed that well within the stability field of bcc or hcp Fe-Si alloys, the first acoustic echo is sharp and unambiguous. However, in the transition region (as determined by XRD), there is significant distortion of the shape and intensity of the initial rise of the time domain signal. This likely arises because in the transition region PA probes a mechanical mixture of two elastically distinct phases. Figures 4.3, 4.4, 4.5, 4.6 show normalized

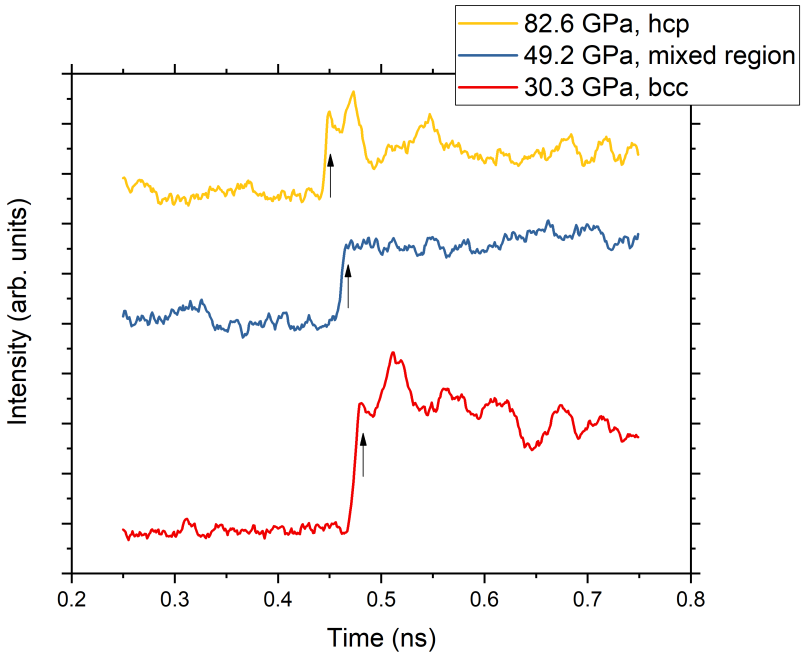

Figure 4.2: bcc-hcp transition observed by PA time domain measurements for Fe10Si. The signal shows a sharp, well defined initial acoustic echo above and below the transition region observed by XRD

travel times as a function of pressure. It is seen that in each case, the bcc-hcp transformation results in some anomaly in the pressure evolution of the normalized travel time (t/t0), which is somewhat different from alloy to alloy, due to complex changes in the texture, stress, thickness and elasticity of the sample. In these figures, dashed lines denote estimated error bars for the transition pressure.

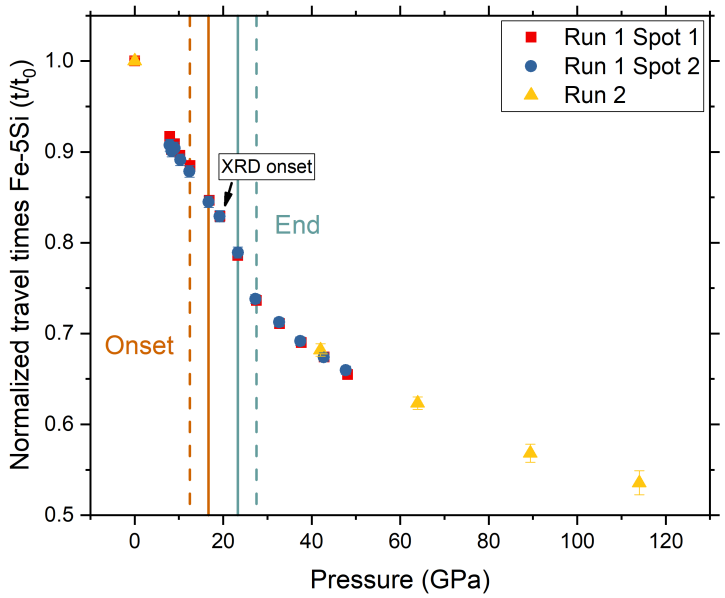

Figure 4.3: t/t0 vs P for Fe5Si, the transition results in a significant reduction in scatter of the measured travel times.

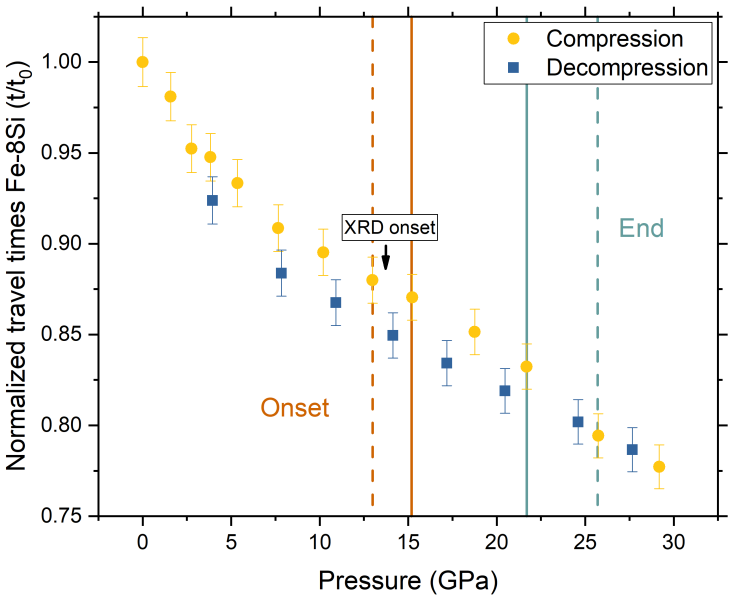

Figure 4.4: t/t0 vs P for Fe8Si. There is clear transformation hysteresis upon compression and decompression.

4.1.1 The bcc-hcp transition by X-ray Diffraction

It is observed in the present dataset, as in literature, that up to Fe8Si, the composition dependence of the bcc-hcp transition is all in all, relatively weak, with the

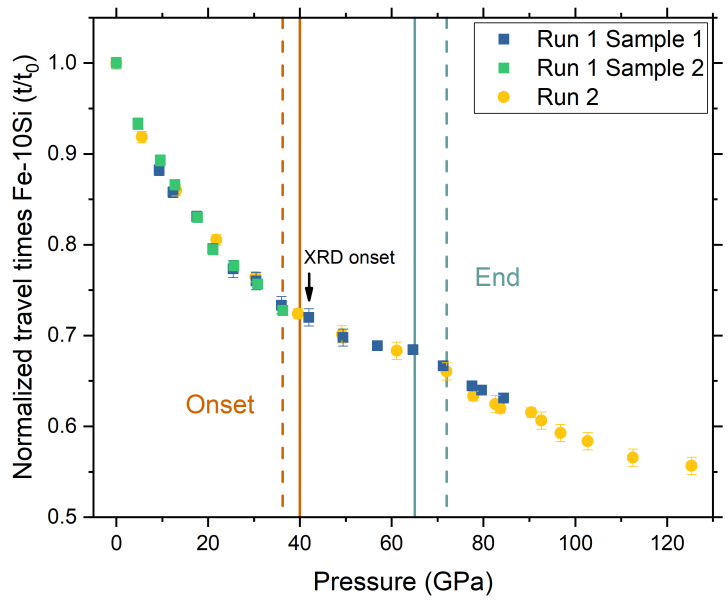

Figure 4.5: t/t0 vs P for Fe10Si. Fe10Si shows a wide transition region by PA, reflecting the sluggish kinetics of the transition.

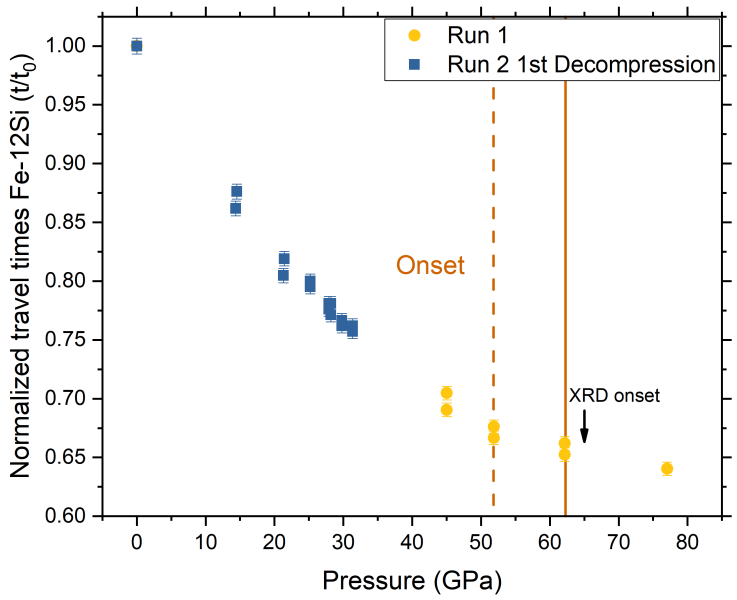

Figure 4.6: t/t0 vs P for Fe12Si. Due to the high pressures at which the transition occurs, it was not possible to unambiguously measure hcp Fe12Si.

transition pressure progressively shifting to higher pressures. By contrast, at more Si-rich compositions there is a very strong increase of the transition pressure with Si content, going from ≈12-13 GPa for Fe8Si (in fair agreement with 16 GPa of [Lin

et al., 2003a]), to >42 GPa for Fe10Si (in agreement with [Côté et al., 2008]), and >60 GPa for Fe12Si.

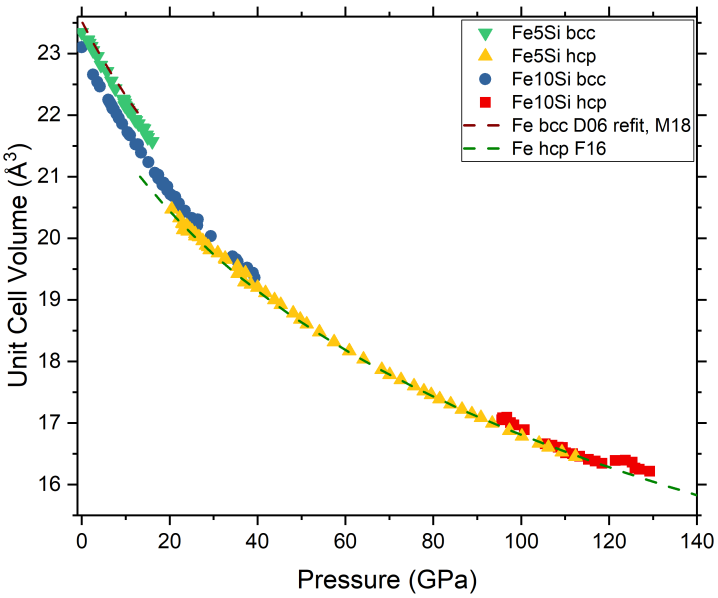

Figure 4.7: Unit Cell Volume vs. Pressure for Fe5Si and Fe10Si compressed in Ne at 300 K, in addition to Fe literature. It is observed that while the volumes of bcc Fe-Si alloys change significantly with Si content, the variation is only weak with Si content for the hcp phase. F07 denotes [Fei et al., 2007], D06 denotes [Dewaele et al., 2006], M18 denotes [Morrison et al., 2018], F16 denotes [Fei et al., 2016].

For Fe8Si, it is rather interesting to note that while the onset of the Fe8Si bcc-hcp transformation (measured by PA and XRD) is in very good agreement with [Lin et al., 2003a], they are in stark disagreement over the width of the coexistence region. While [Lin et al., 2003a] reports a pressure range of ≈20 GPa for the bcc-hcp transition to complete, here we observe a significantly smaller pressure range of about 10 GPa. It is posited that for alloys in this compositional range, the pressure range of coexistence is a strong function of compositional heterogeneity, as differences in alloy composition on the order of 1 wt% can result in changes in the transition onset pressure of nearly 10 GPa. Furthermore, [Lin et al., 2003a], [Hirao et al., 2004] and [Fischer et al., 2014] all report P-V EoS on Fe9Si, with samples bought from the same company, where the first two studies report similar transition pressures and hysteresis ranges (about 15/16 GPa - 36 GPa), but [Fischer et al., 2014] measured a bcc phase up to 35 GPa in Ne with no indication of a bcc-hcp phase transformation.

Figure 4.7 shows a clear trend within the present work (and literature) on Fe-Si alloys: increasing Si content decreases the volume of the bcc phase, but has a much smaller effect on the volume of the hcp phase. In this way, as Si content increases, ΔV between the two phases is reduced. As a consequence, the free energy change of the transition, $P\Delta V$, is reduced with increasing Si concentration. As shown

in Figure 4.7, by 9-10 wt% Si, the volumes of 'bcc-like' and hcp alloys are nearly identical when comparing the present bcc Fe10Si data with the hcp phase of Fe ([Fei et al., 2016], Fe5Si and Fe10Si. This results in a sluggish transition which occurs at very high pressures compared to elemental Fe.

As the bcc-hcp transition in pure Fe is generally thought of as a consequence of the magnetic collapse of the bcc phase, and Si addition changes the magnetism of Fe-Si alloys, it is unclear how the magnetism of these alloys changes at high pressures, and how this may be related to the change in transition pressure. It is interesting to note however, that the effective disappearance of the hcp-phase occurs in the vicinity of stoichiometric Fe3Si- around 15 wt% Si [Wicks et al., 2018]- where one finds fully stoichiometric DO_3 alloys. As mentioned in previous sections, DO_3 ordering causes a splitting of the magnetic moment of different Fe atoms within the crystallographic unit cell [Kulikov et al., 2002], and strongly modifies the bonding scheme of the alloy [Bhattacharya et al., 2017]. As discussed in the following sections, Si addition affects elasticity in the vicinity of the bcc-hcp transition and the elasticity of the hcp phase itself.

4.1.2 Elasticity in the vicinity of the bcc-hcp transition of Fe-Si alloys

Simply based on the comparison between PA studies, it is immediately clear that there is a difference in the bcc-hcp transition between Fe and Fe-Si alloys. Figure 4.8 shows Fe, Fe5Si and Fe10Si over the pressure ranges measured by PA. The hcp phase of Fe5Si and Fe10Si will be discussed more fully in the following sections. Across the transition for pure Fe, there is a discontinuity in Vp, whereas for Fe5Si and Fe10Si a jump in Vp only occurs at the end of the coexistence region and is significantly less pronounced.

As the bcc and hcp crystal structures are not related by symmetry, the transition proceeds by a stacking fault which occurs within the bcc crystal structure [Burgers, 1934]. For a typical burgers mechanism, there is an elastic instability which occurs in the vicinity of the transition which results in a visible effect on the elastic moduli [Voronov and Stal'gorova, 1965]. Anomalously for bcc-Fe, there is no evidence of a pre-transition effect as observed in [Decremps et al., 2014] and [Klotz and Braden, 2000]. This is in stark contrast to the present work on Fe-Si alloys, and measurements of single-crystal elastic constants of an Fe2.6Si alloy [Voronov and Chernysheva, 1999]. In [Voronov and Chernysheva, 1999], elastic softening of the C11 elastic constant was observed from 4 GPa and C12 from 6 GPa, up to 9 GPa (the highest measured pressure) indicating a pre-transition effect which, when extrapolated to higher pressures, leads to a compressive instability in the bcc Fe-Si lattice.

When plotting the bcc data as Vp vs. Density (see section 3.2.2), deviations from linearity for Fe10Si could be observed from $\sim$35 GPa, while the structural transition observed by XRD (and the variations of echo shape by PA) occur near 42 GPa.

While this elastic behaviour is different from what has been observed for bcc-Fe, as expected for a traditional burgers mechanism - the pre-transition effects arise from an instability in the shear modes of the bcc lattice. Regardless of the exact

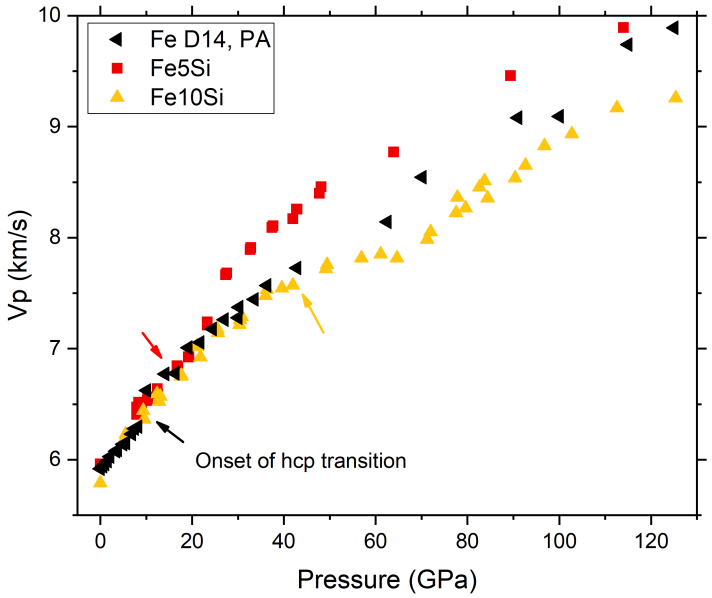

Figure 4.8: Vp vs P for Fe, Fe5Si and Fe10Si compressed quasihydrostatically. While at the transition for Fe there is a sharp increase in Vp, this only occurs in Fe5Si and Fe10Si towards the end (if not after) the hcp transition. Fe dataset from [Decremps et al., 2014].

nature of the transition mechanism in these alloys, it appears that it may be different from pure Fe.

4.1.3 XRD of Si-rich hcp alloys under quasihydrostatic conditions

On the basis of XRD measurements of Fe8Si and Fe10Si under differing conditions of hydrostaticity, the bcc-hcp transition pressure can differ greatly due to nonhydrostatic stress. It has been observed in all of the PVD samples (discussed more fully in section 4.3) that the transition in Ne is coupled with a significant reduction in the already sub-micrometric grain size, which has prevented quantitative structure refinement at high pressures. It follows that for the accurate determination of EoS for hcp-Fe-Si alloys at ambient T, it is recommended to employ laser annealing to recrystallize the sample above the transition, or use samples with a large initial grain size (for Fe8Si and Fe10Si the initial grain size was ∼50-100 nm). For Fe10Si, laser annealing was used to recrystallize the alloy at 1 Mbar, and the resultant P-V dataset is generally consistent with the EoS of Fe9Si presented in [Antonangeli et al., 2018] (as shown in Figure 4.7).

4.2 Velocity-Density Systematics of Fe-5wt.% Si at Extreme Conditions: Constraints on Si content in the Earth's Inner Core

Sections 4.2 and 4.2.1 reflects a scientific manuscript to be submitted for publications in the near future.

Iron and iron alloys at extreme conditions have garnered significant interest due to their relevance to Earth's deep interior. While a first 1D reference seismological model providing density (ρ), compressional (Vp) and shear (Vs) sound velocities as a function of depth into the Earth (PREM – Preliminary Reference Earth Model) was established in the 1980s [Dziewonski and Anderson, 1981], there is still considerable debate over the chemical composition of the Earth's core. Various lines of evidence point towards iron as the most abundant element in the Earth's core (Allegre et al., 1995). However, early on in the study of Fe at extreme conditions, it was observed that Fe is too dense at the pressure (P) and temperature (T) conditions of the core to be the sole element present (Birch, 1964). Earth's solid inner core exists at pressures of 330-360 GPa, and at temperatures of 5000-7000K based on the melting curve of Fe ([Boehler, 1993], [Nguyen and Holmes, 2004], [Anzellini et al., 2013]). As a consequence of the density difference between Fe and PREM, there needs to be some quantity of elements lighter than Fe alloyed to it in order to compensate for this density deficit. Among the potential light element candidates, Si has been favored by many recent studies but without reaching a firm consensus. Regardless of the nature of accretionary materials and redox path, all recent core differentiation models based on metal-silicate partitioning support the presence of Si in the core ([Siebert et al., 2013], [Fischer et al., 2015]). The presence of Si is also advocated on the basis of isotopic arguments [Fitoussi et al., 2009]. The possible presence and the quantity of Si in the Earth's core has important implications for geodynamic processes and the bulk redox state of the Earth's interior ([Wood et al., 1990], [Wade and Wood, 2005], [Hirose et al., 2017]). One possible way to constrain the Si content of the inner core is the comparison between seismological data and experimental measurements, or calculations, of ρ, Vp and Vs of candidate materials at pertinent PT conditions ([Sakamaki et al., 2016], [Sakairi et al., 2018]). Based off the measurement of Vp vs. ρ at extreme conditions, estimates have varied from 1-2 wt% Si ([Badro et al., 2007], [Antonangeli et al., 2010]) to $\sim$8 wt% Si ([Mao et al., 2012], [Fischer et al., 2014]), with the most recent measurements putting an upper limit of 5wt% Si ([Antonangeli et al., 2018], [Sakairi et al., 2018]).

Thanks to the adaptation of Picosecond Acoustics (PA) to the Diamond Anvil Cell (DAC), it is possible to make direct measurements of the acoustic travel time of Fe-alloys, and metals in general, at very high pressures ([Decremps et al., 2008], [Decremps et al., 2014]). Additionally, PA has fewer limitations on sample dimensions than conventional synchrotron-based techniques, allowing the measurement of Vp under quasihydrostatic conditions to Mbar pressures. We thus used PA to probe acoustic echoes and the compressional sound velocity of an Fe-Si alloy with 5wt. % Si up to 115 GPa. We complemented these measurements with synchrotron x-ray diffraction measurements in laser-heated diamond anvil cells up to

110 GPa and 2100 K, deriving a P-V-T equation of state. Our results provide tight constraints on the Si abundance in the Earth's inner core.

The methods with regards to PA, XRD and pressure calibration for the present study have been previously outlined in the Methods Section (Section 2)

4.2.1 Velocity-Density Systematics of Fe-5wt%Si at Extreme Conditions

XRD at Ambient Temperature

Two runs were performed in Ne, one of which used Pt as pressure calibrant to 41 GPa, and another run measured to 1.1 Mbar with Mo as the pressure calibrant. Diffraction of the pressure calibrant was collected independently from that of the sample by translating the cell a few microns from the sample position. This was performed before and after each sample measurement at a given pressure step. Errors in measured unit cell volume were lower than 0.2% throughout the entire pressure range. The bcc-hcp transition started at about 14 GPa and all bcc reflections were absent by 21 GPa. The resultant P-V curve was fit to a 3BM EoS.

To facilitate comparison to literature, K' of the hcp phase was fixed to that of hcp-Fe from [Fei et al., 2016] at a value of 4.79. Table 4.1 shows the fits to the present EoS for when K' is fixed to 4.79 and when K' is left free.

Sample	Fe5Si	Fe5Si	Fe F16	Fe10Ni5Si M18	Fe9SiA18
V_0 (Å^3)	22.564(20)	22.385(53)	**22.428**	22.836(71)	**23.5**
$K_{T,0}$ (GPa)	165.2(1.0)	184.3(5.5)	172.7(1.4)	135.8(5.2)	129.1
$K'_{T,}$	**4.79**	4.29(12)	4.79(5)	5.84(14)	5.24

Table 4.1: Table of EoS parameters for hcp-Fe5Si and selected literature on hcp-structured Fe-Si and Fe-Ni-Si alloys. Parameters in bold have been fixed during the fitting process. All presented EoS employ the 3BM formalism.

At 300 K, the compressional behavior of Fe-5Si is similar to that of hcp-Fe [Fei et al., 2016] and the nickel and silicon-bearing alloy Fe-8Ni-3Si, [Liu et al., 2016]– the EoS parameters of these alloys are similar, and as shown in Fig. 4.9, there is a negligible difference between the volumes of Fe and Fe-5Si for most pressures. Very recent measurements of an Fe-10Ni-5Si alloy in He [Morrison et al., 2018], while virtually identical to the results of the present study below ∼90 GPa, show lower compressibility than the present study at pressures above 90 GPa and, as a consequence, different equation of state parameters.

XRD at High Temperatures

In another set of experiments, Fe-5Si was compressed in a laser-heated membrane DAC along two high-temperature isotherms, at about 1450 K and at about 2100 K.

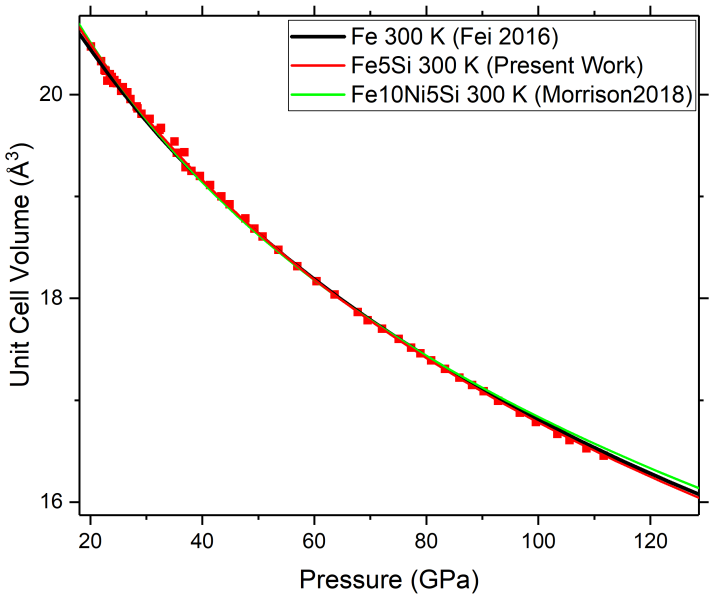

Figure 4.9: PV data of Fe-5Si compared with the 300 K P-V relations of [Fei et al., 2016] and [Morrison et al., 2018] up to 120 GPa. It is observed that all of the present alloys are very similar at low pressures, but start to diverge by 90 GPa.

Temperatures varied by less than 100 K along each isotherm (1σ = 30 K at 1450 K and 1σ = 50 K at 2100 K). Temperatures were corrected downwards by around 3% following standard methods [Campbell et al., 2009] to account for axial T gradients (however this had a negligible effect on the fitted equation of state parameters). No phase other than hcp-Fe-5Si was observed at the HP-HT conditions of the present study, consistent with [Tateno et al., 2015]. The ambient temperature quantities (V0, K0 and K') of the derived P-V-T equation of state were fixed to the fit of the ambient T data. The thermal parametrization is shown in Equation 4.1.

$$P_{vib}\left(V,T\right)+P_{el}\left(V,T\right)=\frac{9NR\gamma_{vib}}{V}\left[\frac{\theta_D}{8}+T\left(\frac{T}{\theta_D}\right)^3\int_{300}^{\theta_D/T}\frac{x^3}{exp\left(x\right)-1}dx\right]+\frac{\gamma_e}{V}\beta_0\left(\frac{V}{V_0}\right)^k T^2 \tag{4.1}$$

Where γ_{vib} is the vibrational Grüneisen parameter, θ_D is the Debye temperature, γ_e is the electronic Grüneisen parameter, β is the electronic heat capacity and k is an exponent which characterizes the volume dependence of the electronic contribution to thermal pressure. N is the number of atoms per formula unit, R is the ideal gas constant, V and T are the unit cell volume (in units of cm^3/mol) and temperature (in K) respectively. The volume dependence of the vibrational Grüneisen parameter and Debye temperature are given by Equations 4.2 and 4.3 respectively.

$$\left(\frac{\gamma_{th}}{\gamma_{th,0}}\right)=\left(\frac{V}{V_0}\right)^q \tag{4.2}$$

	Fe5Si	Fe5Si	Fe5Si	Fe F16	Fe Y12	Fe9Si F14
θ_D	**422**	**422**	**422**	**422**	1173(62)	**420**
γ_0	2.0(1)	2.0(1)	2.0(1)	1.74	3.2(2)	1.14(14)
q	**0.78**	**1**	0.3(1)	0.78	0.8(3)	**1**
β_0	2.8(7)	3.5(7)	1.9(7)	3.91	*ab initio*	-
k	**1.34**	**1.34**	**1.34**	**1.34**	*ab initio*	-

Table 4.2: θ_D has units of K, β_0 has units of $cm^3\ mol^{-1}JK^{-2}10^{-6}$, the other thermoelastic parameters are dimensionless. F16 denotes [Fei et al., 2016], Y12 denotes [Yamazaki et al., 2012], and F14 denotes [Fischer et al., 2014]. Parameters in bold font are those which have been fixed during the fitting process. The three thermal models of Fe5Si are based on different choices of q during fitting, coupled with the fitted 300 K P-V EoS when K' was fixed to 4.79.

$$\theta_D = \theta_{D,0} \exp\left[\left(\gamma_{vib,0} - \gamma_{vib}\right)/q\right] \tag{4.3}$$

In Equations 4.2 and 4.3 q characterizes the volume dependence of the vibrational contributions to thermal pressure. In the fitting process, $\theta_{D,0}$ was fixed to 422 K, q was fixed to 0.78 and k was fixed to 1.34, after the thermal parametrization of [Fei et al., 2016].

It is stressed that while electronic contributions to thermal pressure are relatively small (up to ∼5 GPa at 2100 K), it was not possible to fit the present dataset to a purely vibrational model, as such a model could not reproduce the difference in the volume dependence between the 1450 K and 2100 K isotherms. The fitted thermal parameters of this dataset are shown in Table 4.2.

It is immediately noticeable in Fig. 4.10 that the P-V-T EoS of Fe-5Si measured here is virtually indistinguishable from that of hcp-Fe modeled according to [Fei et al., 2016]. Unsurprisingly, the fitted γ_0 and β_0 are in good agreement between Fe-5Si ($\gamma_0 = 2.0(1)$ and $\beta_0 = 2.8(7)$) and Fe ($\gamma_0 = 1.78$ and $\beta_0 = 3.91$). The difference in β_0 is likely due to the significant covariance between the vibrational and electronic contributions to thermal pressure, and, in any case the difference between $\beta_0 = 2.8$ and $\beta_0 = 3.91$ yields only 1 GPa difference at 2100 K, which is compensated by a change in P_{vib}. It is remarkable that the present XRD dataset composed purely of static compression data is capable of producing a P-V-T EoS which is directly comparable to others requiring extensive parametrization using shock compression data, ab initio calculations and/or NRIXS e.g. [Dewaele et al., 2006], [Fei et al., 2016].

As the direct measurement of thermal EoS are at the cutting edge of experimental capabilities, and data like the present one are rare, it has been common in recent past to use *ab initio* parametrizations to account for P_{el} (e.g. [Dewaele et al., 2006]). Inputs from calculations have been used to constrain P_{el} and fit a purely vi-

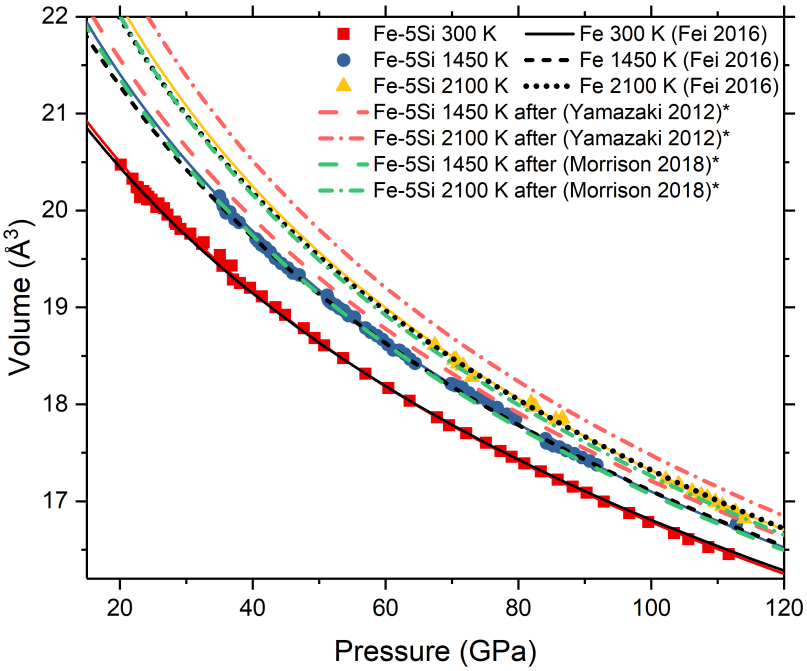

Figure 4.10: PVT data of Fe-5Si - Measured isotherms of Fe-5Si shown with isotherms of pure Fe modeled according to [Fei et al., 2016]. Asterisk denotes fictive P-V-T EoS constructed for Fe-5Si with our 300 K data and thermal parametrization after [Yamazaki et al., 2012] and after [Morrison et al., 2018].

brational model [Yamazaki et al., 2012], or to construct thermal models using purely ambient temperature experimental data (Morrison et al., 2018, [Lin et al., 2003b]). Fictive P-V-T EoS of Fe-5Si constructed in such manners starting from our 300 K data are shown in Fig. 4.10. In view of the high value of γ_0, the thermal model after [Yamazaki et al., 2012] systematically overestimates experimental volumes at high pressure, while MGD parameters of $\gamma_0 = 2$ and q = 1 after [Morrison et al., 2018] can suitably match the low temperature isotherm measured. However, the *ab initio* parametrization of P_{el} by [Dewaele et al., 2006], also recently used by [Morrison et al., 2018] systematically underestimates the electronic contributions to the thermal pressure at 2100 K, and, all the more so, at core conditions.

Travel times were measured as a function of pressure (Fig. 4.11 and Section 4.1 Figure 4.3) in two independent runs performed on samples of Fe-5Si alloy of different initial thickness. Errors in Vp were about 2% up to 60 GPa, and about 3% at 115 GPa. Shown in Figure 4.11 are background-subtracted time domain signals at 47 GPa before and after data treatment to extract Brillouin oscillations. Larger errors at high pressures are due to an increase in diffuse background caused by the progressive depolarization of the pump and probe beams resulting from increased defect scattering, stress gradients across the diamond anvil, and the cupping of the diamond culet- classical issues encountered by optical measurements at Mbar conditions [Merkel et al., 1999]. Uncertainties of sample thickness, especially at

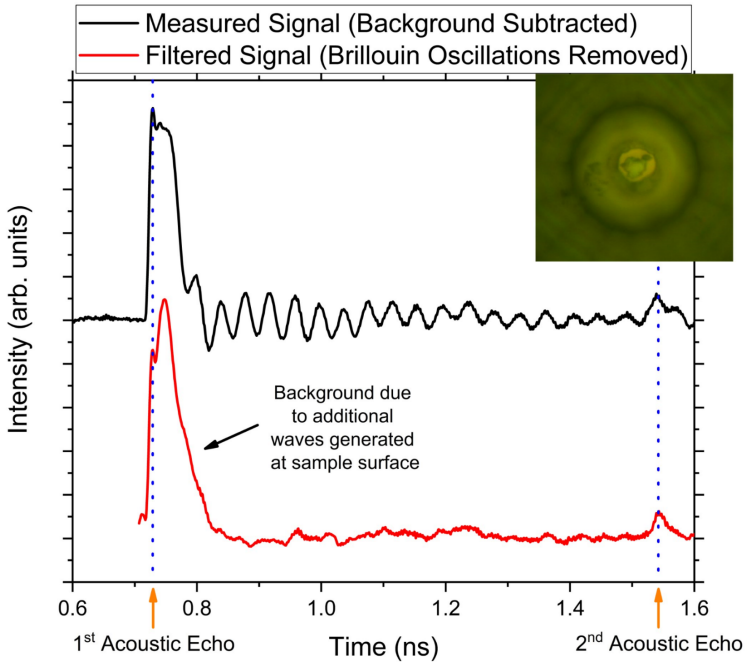

Figure 4.11: Travel Time measurement by Picosecond Acoustics at 47 GPa. The sharp peak associated with the 1st acoustic echo is clearly visible, followed by a background signal related to the generation of surface waves and Brillouin scattering in the Ne PTM (filtered in the red curve). The difference between the travel time of filtered and unfiltered data changes by a maximum of 2 ps, or an error of 0.1-0.5% of Vp depending on sample thickness. Inset is the sample chamber of Run 2 at ∼100 GPa.

high pressure, has only a small effect on the travel time compared to the change in velocity. As a matter of fact, by 1 Mbar, the thickness has changed by ∼10% relative to ambient pressure, while the acoustic travel time is typically 50% its original value. Sample tilt within the sample chamber has a negligible effect on measured travel times due to the instrumental configuration used. In Run 1, it was seen that there were some residual stresses in the sample which induced local variation in measured travel times of about 2-3% in the bcc phase, and so for Run 2, the sample was additionally annealed under vacuum at ∼ 400 K for 12 h. This procedure effectively reduced scatter in measured travel times to less than 1% in the bcc phase.

In Run 2, the initial travel time and travel time of the recovered samples are within error bar of each other, indicating negligible plastic deformation of the sample when compressed in Ne PTM up to 1.1 Mbar. Provided the volume decrease at the bcc-hcp transition is accounted for, the measured Vp varies by less than 0.5% depending on the choice of Fe or Fe-Si EoS, well within error at all pressures. For discussion of the effects of the bcc-hcp transition measured by PA refer to Section 4.1. Following the transition region determined by both XRD and PA, a sharp rise in Vp is observed. While bcc peaks are absent from XRD at 21 GPa, there are still large nonlinear variations in acoustic velocity until ∼27 GPa where the variation becomes regular. This is attributed to the slight development of preferred orientations in

hcp-Fe-5Si at the end of the phase transition – XRD highlight a moderate change in the intensity ratio of the (002)/(100) peaks between 20 to 30 GPa, while at higher pressures this ratio does not vary any more. Due to the difference in measurement geometry between PA and XRD, the intensity reduction of the (002) peak observed by XRD reflects a larger contribution of the c-axis to the measured travel time and hence a small increase in Vp [Antonangeli et al., 2006]. Linearity in the Vp – ρ relation for hcp-Fe-5Si was observed from 27 GPa, and the following discussion will be limited to data measured at and above this pressure.

Discussion

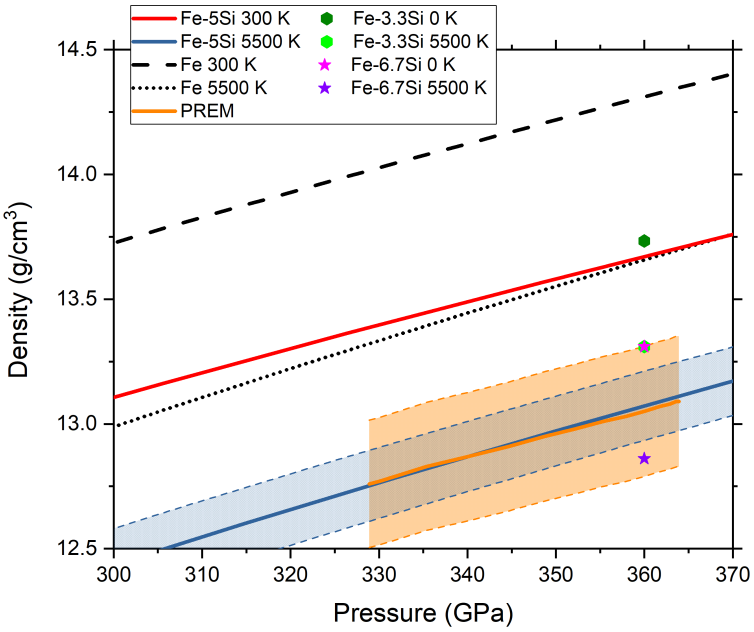

Figure 4.12: Density of Fe and Fe-5Si at the pressures of the IC. Fe-5Si is within error bar of PREM for all reasonable core temperatures (5000-7000 K). Shaded blue region indicates error bar of Fe-5Si 5500 K isotherm. Figure 4.13 shows ρ – P extrapolations when varying q of the thermal model.

Extrapolated to IC pressures and temperatures, the density of Fe-5Si is within error of PREM (∼2%, Masters and Gubbins, 2003) for all reasonable core temperatures, with the best match for T = 5500 K (Fig. 4.12). As the compressional behaviour of Fe-5Si and Fe are similar over the wide range of P-T conditions measured in this study, the dominant mechanism for density reduction even at core conditions is simply the difference in atomic mass between Fe and Si. Indeed, the density reduction between hcp-Fe and hcp-Fe-5Si is ∼4.4-4.8% both at 300 K and at temperatures exceeding 5000 K.

We note that our results are well compatible with the most recent ab initio calculations on Fe-Si alloys [Martorell et al., 2016], with improved agreement at high temperature (the 5500 K isotherm extrapolates to the midpoint between calculations

of Fe-3.3Si and Fe-6.7Si at the same temperatures).

While such extrapolations were performed fixing q and k, the result of changing q is shown in Figure 4.13. It is seen that large differences in q have virtually no effect on the extrapolated density at core pressures and temperatures for a given 300 K P-V EoS. In fact, the primary source of error for extrapolations to core conditions is the choice of ambient temperature K', as fitting the present dataset with K' = 5.84 as in [Morrison et al., 2018] results in an Fe-5Si alloy which is ∼1-1.5% less dense than PREM for a constant composition, while leaving K' free (K' = 4.3) results in an Fe-5Si alloy which at core pressures and temperatures is about 1% more dense than PREM (but both within PREM uncertainties).

The effects of different values of k are discussed in Section 4.2.2.

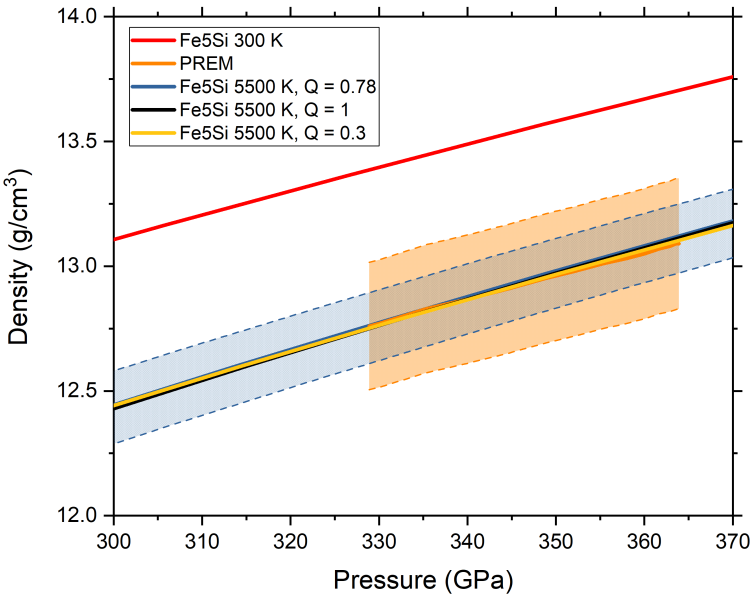

Figure 4.13: Dependence of extrapolated density on choice of P-V-T thermal parameters. Due to the tradeoff between electronic and vibrational contributions to thermal pressure, the choice of q in the present study has little effect on extrapolated densities.

Vp measurements show a clear linear trend for the entire density range studied, with the fitted parameters Vp (km/s) = 1.156(21)*ρ (g/cm^3) – 2.50(20) as shown in Figure 4.14. dVp/dρ of Fe-5Si is reduced with respect to hcp- Fe [Antonangeli and Ohtani, 2015], although the effect is not as large as that reported by previous IXS measurements on samples with higher Si content, shown inset in Figure 4.14 ([Mao et al., 2012], [Antonangeli et al., 2018], [Sakairi et al., 2018]).

Our measurements extrapolate at inner core densities somewhat higher than recent measurements by IXS on more Si-rich samples ([Mao et al., 2012], [Antonangeli et al., 2018], [Sakairi et al., 2018]), but are in very good agreement with the result of athermal ab initio calculations on Fe-3.3Si and Fe-6.7Si [Martorell et al., 2016]. While the present work is in excellent agreement with the athermal calculations

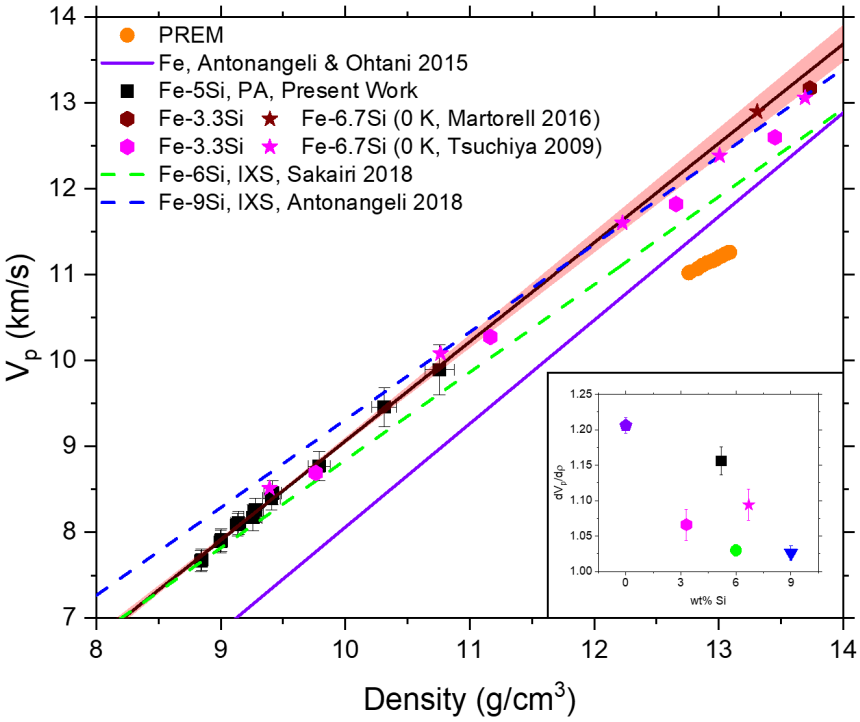

Figure 4.14: Compressional Sound Velocity vs. Density for Fe and Fe-Si alloys in the hcp structure, inset: dVp/dρ vs. wt% Si for the Fe-xSi datasets. Figure 4.15 shows data points for [Mao et al., 2012], [Antonangeli et al., 2018], [Sakairi et al., 2018].

of [Tsuchiya and Fujibuchi, 2009] over the measured pressure range, the agreement between datasets worsens at higher densities. Fig. 4.14 shows that IXS results are generally parallel to each other ([Mao et al., 2012], [Antonangeli et al., 2018], [Sakairi et al., 2018]), but in disagreement with the present work. It is evident based on the combined results of ([Tsuchiya and Fujibuchi, 2009], [Mao et al., 2012], [Sakairi et al., 2018] and [Antonangeli et al., 2018]), and the results of the present study that dVp/dρ decreases with increasing Si content (shown inset in Fig. 4.14). While a linear decrease in dVp/dρ with Si content can rationalize a significant amount of the difference between PA and IXS, there are also systematic differences due to the different measurement geometries of the two techniques. PA measures acoustic travel times along the compression axis of the DAC, and as the sample is expected to develop texture, PA will preferentially sample the c-axis of the alloy. By contrast, IXS measures phonon dispersions perpendicular to the DAC compression axis, and as such preferentially samples the basal plane of the Fe-alloy upon development of texture. In this way, textural effects bias PA and IXS measurements in opposite directions. Additionally, IXS measurements require larger sample volumes, and so are often measured in a solid PTM ([Sakairi et al., 2018], [Sakamaki et al., 2016]) or no PTM at all [Antonangeli et al., 2018]. We note however, that the difference in extrapolations of PA and IXS measurements here observed for the Fe-Si system is much more significant than for the case of hcp-Fe ([Antonangeli and Ohtani, 2015],

references therein).

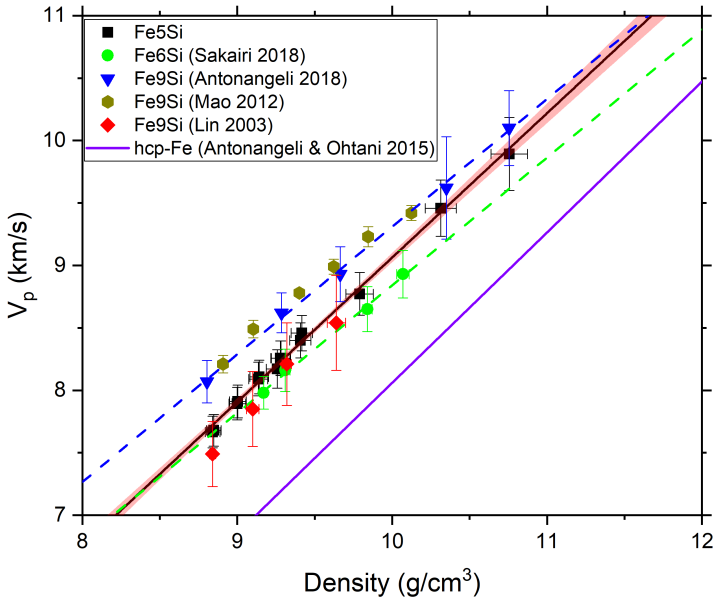

Figure 4.15: Vp vs Density measured for Fe-Si alloys in the hcp structure by different techniques ([Lin et al., 2003a], [Mao et al., 2012], [Sakairi et al., 2018], [Antonangeli et al., 2018]).

As it is not known how to quantitatively correct the probed velocities for texture in these experiments, it is important to minimize texture by performing the experiments under quasi-hydrostatic conditions with noble gas media. While there is still some texturing under compression in Ne, it is significantly weaker than the texture observed to occur in IXS experiments at comparable pressure conditions ([Antonangeli et al., 2018], [Sakairi et al., 2018]). Such considerations are more thoroughly explored in Section B.2. Figure 4.15 shows the individual datapoints of various studies in the hcp-Fe-Si system. Ultimately, the effect of preferred orientation is a relatively small effect, but is shown to systematically bias extrapolations (upward in the case of NRIXS) and downwards (in the case of IXS) in Vp at core densities, which strongly hinders compositional modelling at core conditions. It can also be observed in Figure 4.15 that the present work has significantly improved data coverage to typical IXS or NRIXS experiments, and is measured over an extremely wide density range, under quasihydrostatic conditions, allowing for more robust extrapolations to core densities.

To meaningfully compare obtained Vp with PREM, high temperature effects have to be accounted for. At a constant density of 13 g/cm^3, the T corrections after experiments by [Sakamaki et al., 2016] (on hcp-Fe) and [Sakairi et al., 2018] (on Fe-6Si) yield Vp reductions of $\sim$0.09 m s^{-1} K^{-1}, with almost no difference between Fe and Fe-6Si. Alternatively, by converting the constant pressure simulations of [Martorell et al., 2016] or [Li et al., 2018] to a constant density of 13 g/cm^3, it is possible to estimate the magnitude of anharmonic temperature effects determined

by ab initio simulations. Anharmonic T corrections from [Martorell et al., 2016] on Fe and Fe-3.3Si are derived to be ∼0.11 m s^{-1} K^{-1} and ∼0.05 m s^{-1} K^{-1} for Fe-6.7Si. Irrespectively of the chosen thermal correction, Vp of Fe-5Si is always higher than PREM, even for T = 6500 K, showin in Figure 4.16.

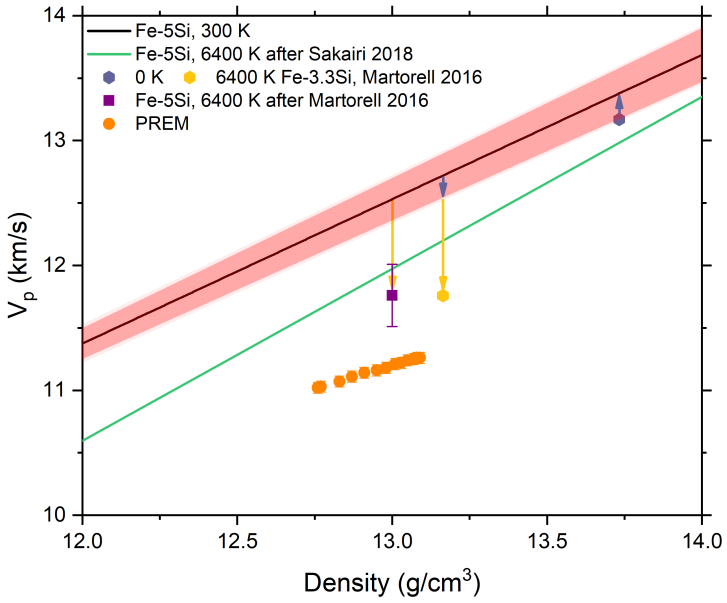

Figure 4.16: Vp vs density for Fe-5Si with anharmonic T corrections. Black line shows the 300 K extrapolation of the present work, red square and light green line show anharmonic T corrections to the present work at 6400 K after, respectively, [Martorell et al., 2016] and [Sakairi et al., 2018]. It is seen that such an alloy extrapolates significantly higher than PREM even incorporating strong anharmonic effects and high core temperatures. 95% confidence band of the Fe-5Si linear fit shown in red.

Regardless of the magnitude of anharmonic corrections at high temperature ([Sakamaki et al., 2016], [Sakairi et al., 2018], [Martorell et al., 2016], [Li et al., 2018]), PREM Vp is expected to be matched by an Fe- Si alloy containing <2wt% Si for T = 6500 K and <1wt% Si for T = 5500 K. The largest anharmonic effects reported in recent literature come from *ab initio* calculations [Martorell et al., 2016], but a more recent ab initio study using larger simulation cells [Li et al., 2018] supports significantly reduced anharmonic effects compared to [Martorell et al., 2016], such that the magnitude of anharmonic effects are more in line with those observed by IXS [Sakairi et al., 2018]. As such, constraints imposed by compressional sound velocity (at maximum <2wt% Si) are incompatible with constraints imposed by density (an Si alloy containing 5wt% Si has a density matching PREM at realistic core conditions). As a result, Si likely cannot be the sole light element in the Earth's core.

On the basis of reported literature, the addition of Ni likely does not significantly change this conclusion, as it has been seen that Ni has a minor effect both on

Vp [Antonangeli et al., 2010], [Martorell et al., 2013], [Liu et al., 2016], [Wakamatsu et al., 2018] and density [Morrison et al., 2018]. This highlights the important point that density or velocity information alone can only be used to exclude possible core compositions, and must be coupled together in order to develop accurate models of the Earth's interior.

4.2.2 Shear velocities and derived quantities

Shear Velocities of hcp-Fe5Si at High Pressures

On the basis of the P-V-T EoS and Vp measurements presented in the previous section, it is possible to derive other thermodynamic quantities to place further constraints on core composition and properties. It has been discussed earlier that the adiabatic and isothermal bulk moduli can be related by the Equation:

$$K_S = K_T\,(1 + \alpha\gamma_{th}T) \tag{4.4}$$

Where K_S is the adiabatic bulk modulus, K_T is the isothermal bulk modulus, α is the coefficient of thermal expansion of the material and γ_{th} is the thermodynamic grüneisen parameter. It follows that knowing $\mathrm{Vp}(\rho)$ and $K_S(\rho)$ allows for the determination of shear velocities (Vs) through the equation:

$$\frac{K_S}{\rho} = V_P^2 - \frac{4}{3}V_S^2 \tag{4.5}$$

For this system, it is seen that adiabatic bulk moduli are only marginally different from isothermal bulk moduli under pressure - about 2% higher at 20 GPa and about 1% higher at 1.2 Mbar. It follows that using either isothermal or adiabatic bulk moduli to derive Vs at ambient temperatures results in similar extrapolations to core densities, albeit with isothermal moduli resulting in a slight overestimation of Vs. Derived Vs-Density relations of the present alloy and pure Fe are shown in Figure 4.17. We observe that Vs of Fe5Si is increased relative to Fe, with a clear linear velocity-density trend.

Additionally, the slope is identical to Fe - after [Antonangeli et al., 2018] $\mathrm{dVs/d}\rho$ of 0.502 is suggested for hcp-Fe, while $\mathrm{dVs/d}\rho$ of 0.502(3) is derived from the present dataset. Consequently, Vs of Fe5Si is likely also incompatible with PREM, although it is stressed that Vs is more strongly affected by anharmonic effects than V_P at core conditions [Martorell et al., 2016], [Li et al., 2018].

Electronic Pressure at core conditions and thermodynamic quantities derived from P-V-T EoS

While it is possible to use the presented P-V-T dataset to refine the electronic thermal pressure of Fe5Si, what is not possible is to determine the volume dependence of this term, characterized by the exponent k. At near ambient conditions, and modest temperatures, this has little effect on the derived thermodynamic quantities, but can change these quantities by a few percent at core conditions. Ks is weighted more heavily by temperature effects due to the addition of the $\alpha\gamma T$ term when computed from K_T. While most literature sources for electronic parametrizations

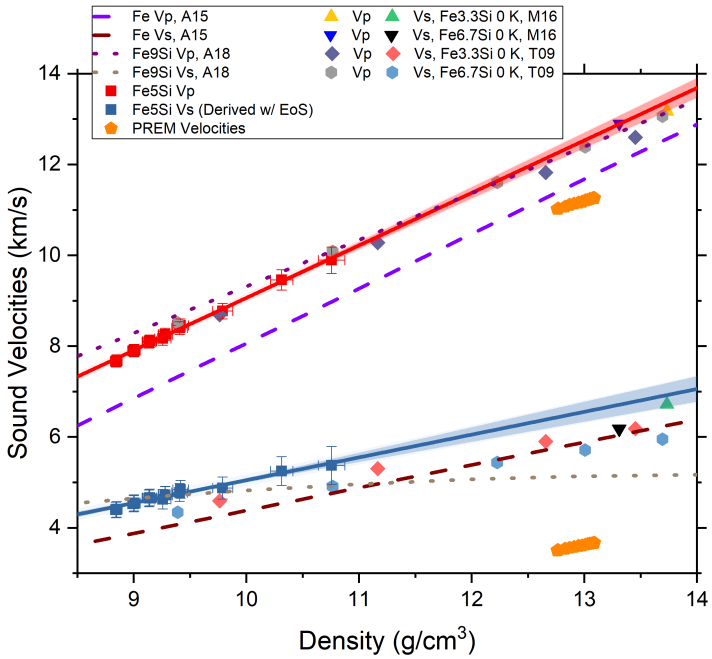

Figure 4.17: Vp and Vs vs. Density of Fe5Si and selected literature. A15 denotes [Antonangeli and Ohtani, 2015], A18 is [Antonangeli et al., 2018], M16 is [Martorell et al., 2016], T09 is [Tsuchiya and Fujibuchi, 2009]. PREM values after [Dziewonski and Anderson, 1981].

use k = 1.34 ([Boness et al., 1986], [Dewaele et al., 2006], [Fei et al., 2016]), these parametrizations were done for hcp-Fe, and may not be valid for Fe-alloys.

The present P-V-T dataset was also fit using k = 1 and k = 2, in order to better constrain errors. The extrapolation of these fits is shown in Figure 4.18. It is observed that the variation of Ks between k = 1 (estimated upper limit) and k = 2 (estimated lower limit) at 360 GPa and 7000 K is about 2%, and the difference in density between these two fits is about 0.9% at the same conditions.

α and γ were computed numerically using the identities:

$$\alpha = \left(\frac{\partial P}{\partial T}\right)_V \frac{1}{K_T} \tag{4.6}$$

and

$$\gamma = \frac{\alpha V_M K_T}{C_V} \tag{4.7}$$

where

$$C_V = C_{Vvib} + C_{Vel} + C_{Vanh} \tag{4.8}$$

and

$$C_{Vi} = \frac{V_M}{\gamma_i}\left(\frac{\partial P_i}{\partial T}\right)_V \tag{4.9}$$

Where V_M is the molar volume and C_V is the heat capacity at constant volume [Dorogokupets et al., 2017]. P_i denotes the component of pressure in the fitted EoS. Due to the T^2 dependence of the electronic pressure, d/dT of this term contributes

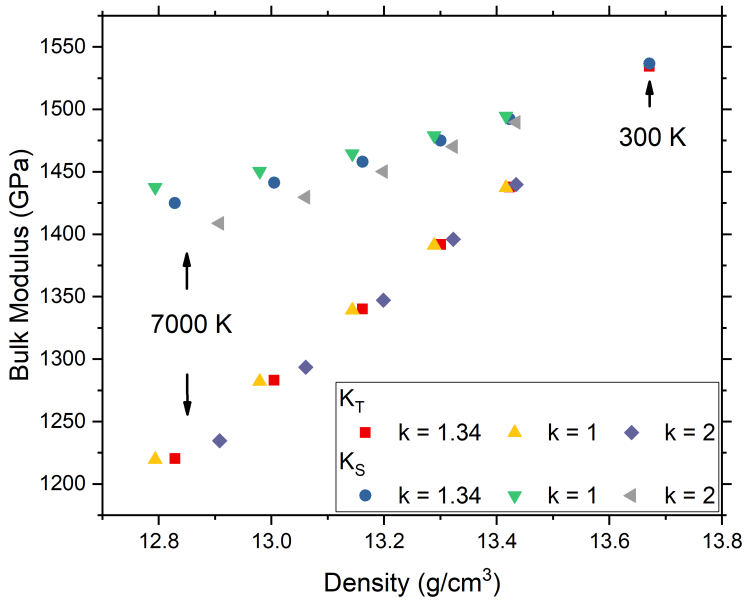

Figure 4.18: Ks and K_T vs. Density using different values of k for fitting the P-V-T EoS of Fe5Si.

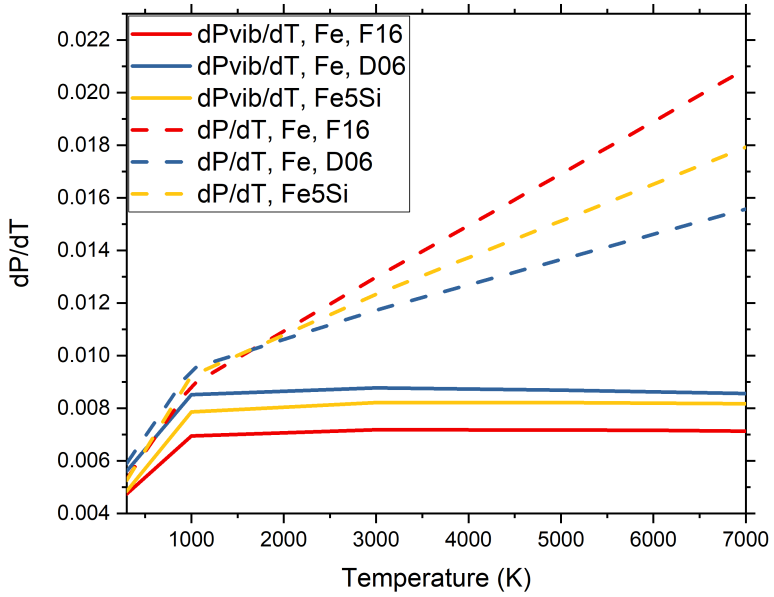

Figure 4.19: dP/dT vs T at 360 GPa. D06 denotes [Dewaele et al., 2006] and F16 denotes [Fei et al., 2016]. dP/dT is a component of the thermal EoS which strongly influences the behaviour of α, γ_{th} and C_V

strongly to the magnitude of α and γ at core temperatures. Figure 4.19 shows the breakdown of vibrational and electronic contributions to dP/dT as a function of

temperature at P = 360 GPa. Regardless of the choice of parametrization, it is observed that vibrational and electronic terms are similar in magnitude at the P-T conditions of the Earth's inner core. Furthermore, it is observed that the electronic pressure derived with the Fe5Si P-V-T dataset is in good agreement with more recent ab initio parametrizations [Bouchet et al., 2013]. At core conditions, understanding how the electronic pressure changes as a function of alloy composition is critical to constraining the thermodynamic properties of the Earth's inner core.

4.2.3 The Influence of Thermoelastic Parameters on Theory and Experiment

K_T vs. Density, an athermal diagnostic for assessing Fe-alloys at extreme conditions.

It has been discussed previously, that the electronic and anharmonic components of thermal pressure have a strong influence on extrapolations of K_S to inner core conditions. However, this may not be the case for K_T. Figure 4.20 shows the difference at constant density between the isothermal bulk moduli of two P-V-T EoS of hcp Fe between 300 K and 6000 K extrapolated beyond inner core densities. It is observed that K_T varies by less than 2% from its ambient temperature value up to core temperatures and densities. Indeed, recall that:

$$K_T = -V\left(\frac{\partial P}{\partial V}\right)_T \equiv \rho\left(\frac{\partial P}{\partial \rho}\right)_T \tag{4.10}$$

For the thermal parameters typical of Fe and Fe-alloys, the volume (or density) derivative of pressure at a given temperature is dominated by the ambient temperature EoS so as to be nearly independent of temperature for a fixed density. This could be useful for EoS studies where P-V-T data is unavailable as a diagnostic for more accurately comparing candidate core materials.

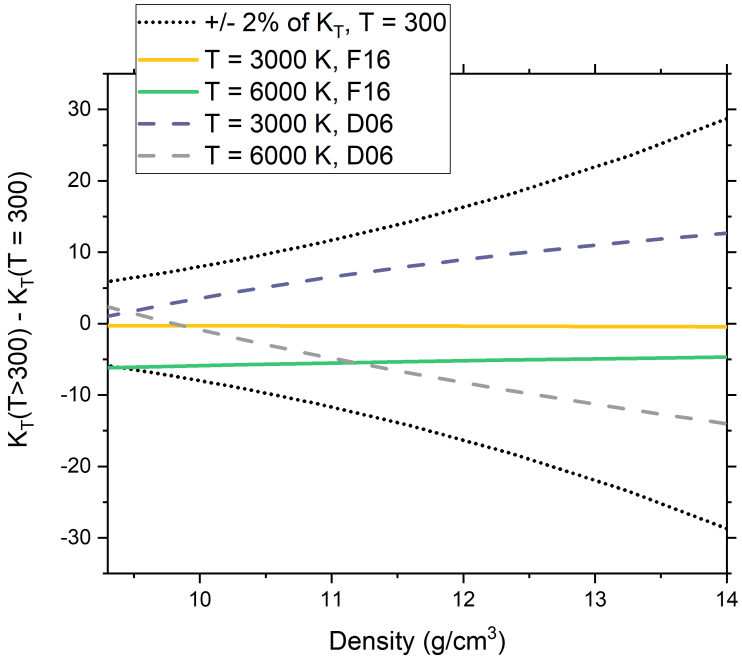

Figure 4.20: Difference between isothermal bulk moduli at constant density up to densities exceeding that of the inner core and to temperatures up to 6000 K. D06 denotes [Dewaele et al., 2006] and F16 denotes [Fei et al., 2016]. It is observed that K_T vs. Density is only weakly affected by changes in temperature over all geophysically relevant P-T conditions for the P-V-T EoS of [Dewaele et al., 2006] and [Fei et al., 2016].

ab initio Molecular Dynamics Calculations

In light of the immense technical challenges that still hinder quantitative experimental studies of material properties at inner core conditions, ab initio calculations remain a powerful method for the direct study of the properties of Fe-alloys at such conditions. Ab initio calculations generally report values of $\alpha * \gamma \sim 1.5 * 10^5$, however the present EoS for Fe5Si and that of [Fei et al., 2016] (both determined primarily using experimental parametrizations) exhibit much larger values at IC conditions as shown in Figure 4.21.

In fact, in [Dewaele et al., 2006] and [Fei et al., 2016], both studies use the same dynamic compression dataset [Brown et al., 2000] coupled with very similar 300 K compression datasets. The only significant difference between the P-V-T EoS of [Dewaele et al., 2006] and [Fei et al., 2016] is that in the former, anharmonic and electronic thermal pressure is derived from earlier ab initio calculations [Alfè et al., 2001] (vibrational parameters refined with shock data) while in the latter the vibrational thermal pressure is determined by P-V-T static compression and NRIXS studies [Murphy et al., 2011] (electronic thermal pressure refined with shock data). The subtle difference between these two studies underlies a deeper challenge within theoretical and experimental investigations of geomaterials - the constraint of dP/dT at geophysically relevant conditions, as nearly all of the discrepancy in $\alpha * \gamma$ across different studies arises from variation of α, which can differ by more than

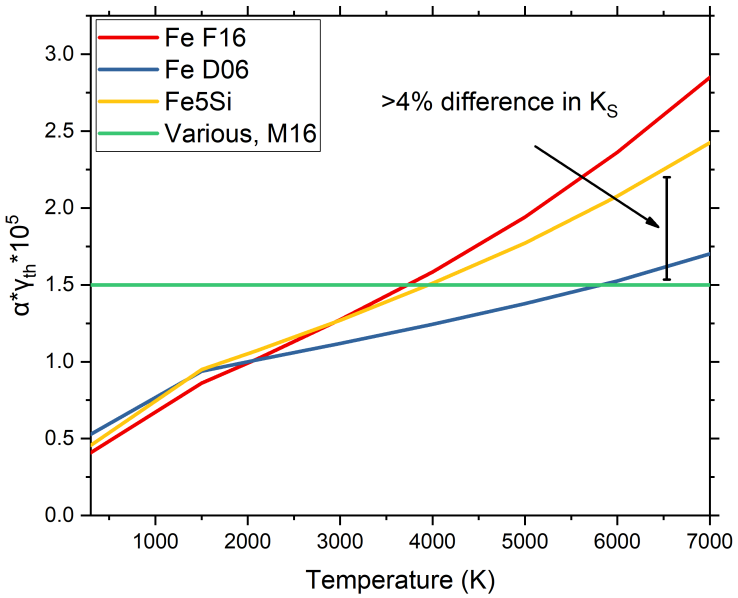

Figure 4.21: $\alpha * \gamma$ vs T at 360 GPa. D06 denotes [Dewaele et al., 2006], M16 denotes [Martorell et al., 2016] and F16 denotes [Fei et al., 2016].

50% from study to study (e.g. [Alfè et al., 2001], [Dewaele et al., 2006], [Bouchet et al., 2013], [Fei et al., 2016]).

4.3 High pressure behaviour of PVD hcp Fe-Si alloys

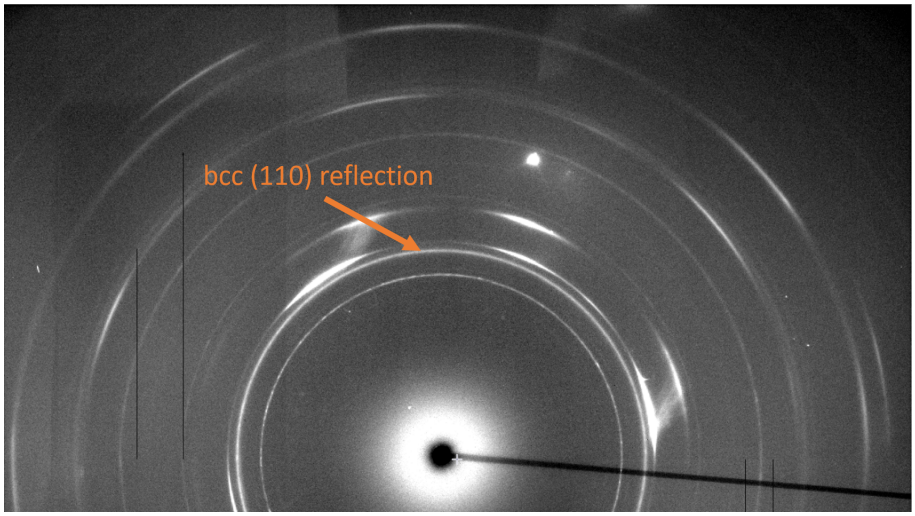

Figure 4.22: A diffraction image from Synchrotron-SOLEIL of Fe12Si in the bcc structure compressed in Ne PTM with Mo pressure calibrant at 60 GPa. The orange arrow points to the (110) diffraction ring of Fe12Si, showing even texture and a clearly identifiable peak.

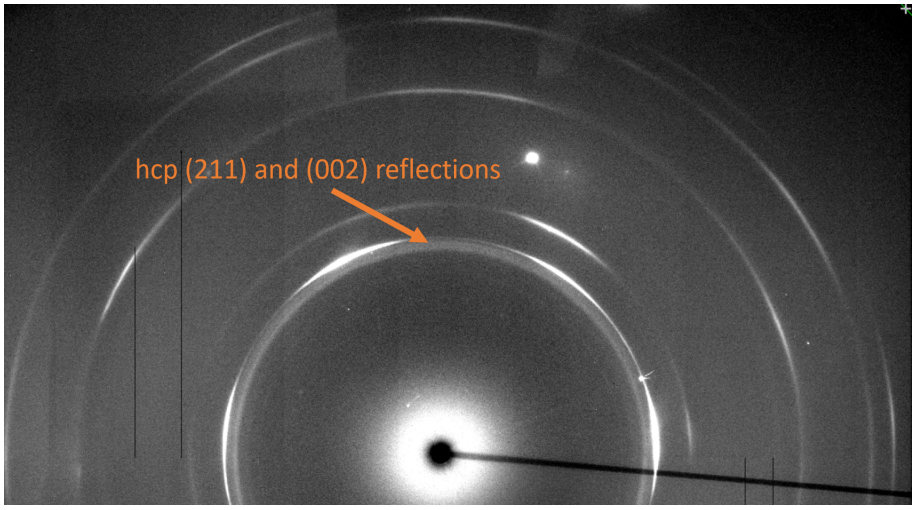

Figure 4.23: Diffraction image from Synchrotron-SOLEIL of Fe12Si in the hcp structure compressed in Ne PTM with Mo pressure calibrant at 65 GPa. The orange arrow points to the location of the (211) and (002) peaks of Fe12Si. Due to the significant broadening of the diffraction lines above the bcc-hcp transition, these peaks are not indexable.

In this Thesis, it has been seen by XRD that these PVD-synthesized alloys transform into a quasi-amorphous phase when compressed under noble gas media. This is likely in no small part due to the increasingly more sluggish kinetics of the

bcc-hcp transition at higher silicon contents, and due to the small grain size of the starting materials. In these alloys, there is a significant reduction in grain size (shown in Figures 4.22 and 4.23), resulting in broad diffraction lines which could not be reliably indexed.

As a consequence, while data in the hcp phase for Fe8Si, 10Si and 12Si has been systematically collected to very high pressures, quantitative P-V relations could only be determined at high pressures for Fe10Si, where the sample was briefly laser-annealed and subsequently recrystallized into an hcp-structured alloy. The recrystallized hcp- Fe10Si alloy is consistent with the P-V relations used in [Antonangeli et al., 2018] for Fe9Si.

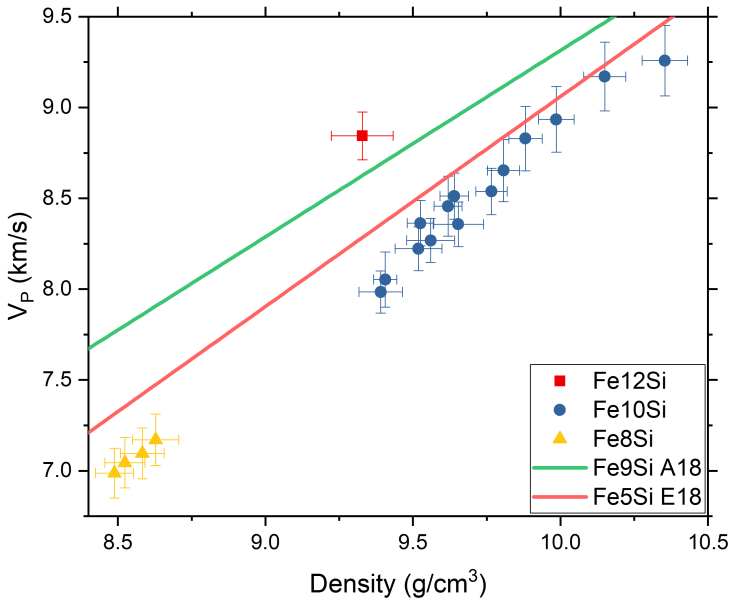

Figure 4.24: Vp vs ρ for Fe-Si alloys synthesized by PVD. It is observed that while Fe8Si and Fe10Si produce similar velocity-density trends, Fe12Si is significantly higher, albeit more consistent with the behaviour of Fe5Si (Section 4.2) and Fe9Si (A18, [Antonangeli et al., 2018]).

When combining the Vp-ρ dataset on hcp Fe8Si, hcp-Fe10Si and the single datum of Fe12Si (possibly pure hcp) it is not possible to glean any clear trend from the data, although Fe8Si and Fe10Si appear to plot along the same Vp-ρ line, as shown in Figure 4.24. The discrepancy between Fe10Si measured here and Fe9Si measured in [Antonangeli et al., 2018] is likely due to the grain size reduction which occurs upon transition when compressed quasihydrostatically, as nonhydrostatic compression of the alloy as in [Antonangeli et al., 2018] results in a material with significantly larger grain size after the hcp transition. While the unit cell volume of Fe8Si was not measurable above the hcp transition when compressed in Ne, it was indexable when compressed in KCl.

4.4 Effect of Ni alloying in Fe-Ni-Si alloys and the c/a axial ratios of hcp Fe-Si and Fe-Ni-Si alloys at high P-T conditions.

4.4.1 The effect of Ni on dilute Fe-Si alloys at high P-T conditions

While the Earth's core is believed to be composed of predominantly iron, there is likely a significant fraction of Ni on the basis of cosmochemical arguments. At ambient temperature and high pressure, there is general consensus that Fe-Ni alloying does not significantly modify the elasticity of pure iron [Mao et al., 1990], [Antonangeli et al., 2010], [Asanuma et al., 2011], [Martorell et al., 2013], [Liu et al., 2016], [Wakamatsu et al., 2018], [Morrison et al., 2018]. Furthermore, there have been studies of the Fe-Ni phase diagram up to inner core pressures and temperatures, the number of studies of ternary Fe-Ni-Si alloys is still limited [Asanuma et al., 2011], [Sakai et al., 2011]. In this Thesis, we have carried out preliminary work studying the phase diagram of Fe-Ni-Si alloys, and making progress towards a P-V-T Equation of state for Fe5Ni5Si in order to assess the effects of Ni alloying in this system.

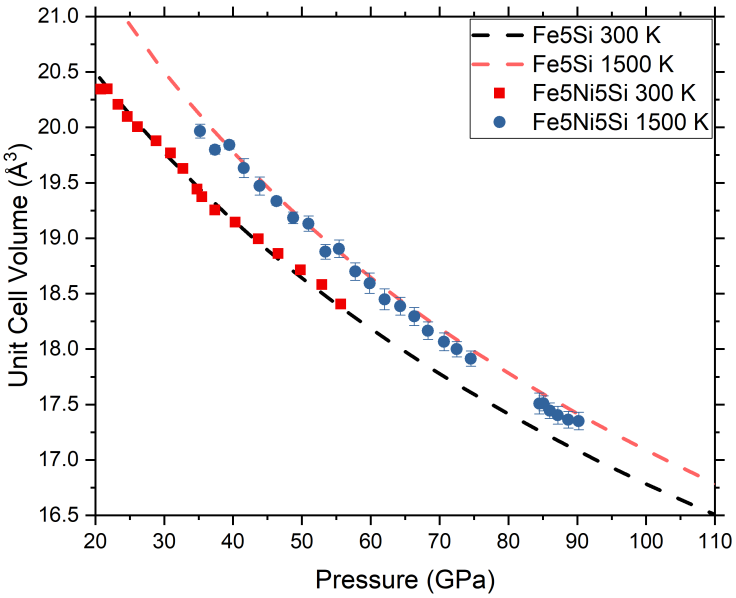

Figure 4.25: Measured PVT relations of Fe5Ni5Si vs. Fe5Si. It is observed that Ni may act to reduce thermal expansion of this alloy at high temperatures and pressures.

Employing isothermal compression at high temperatures with a similar experimental protocol to Section 4.2, combined with a measured 300 K P-V relation, it is observed that while Ni alloying does not have a strong effect at ambient tempera-

ture over the pressure range measured, it may act to reduce thermal expansion of the Fe-Si alloy at high temperatures and pressures, as shown in Figure 4.25. It is stressed however, that a degree of analysis is still ongoing and further studies are likely needed to assess these effects to higher pressures and temperatures, in order to produce reliable extrapolations to inner core conditions. Furthermore, Fe5Ni5Si adopted a mixture of fcc-hcp crystal structures over a very wide range of pressures at 1500 K - pure fcc was observed up to 35 GPa, but a mixed region of fcc and hcp structures was observed to 55 GPa.

4.4.2 c/a axial ratios of Fe-Si and Fe-Ni-Si alloys at high pressures and high temperatures

It has been suggested that the axial (c/a) ratio of hcp Fe-alloys can be linked to the elastic anisotropy of the alloy. More specifically, it has been shown that the variation of the c/a ratio with pressure is related to the ratio of C_{33}/C_{11}, which can be related to the elastic anisotropy of the material [Morrison et al., 2018]. This has direct importance to the composition of the Earth's inner core, as significant P-wave anisotropy has been observed with seismic waves travelling faster along polar paths than in the equatorial plane ([Deuss, 2014], references therein). Additionally, in order to accurately determine the elastic constants of Fe alloys by ab initio stress-strain calculations, it is critically important to use a correct c/a ratio for the material in question at relevant P-T conditions [Vočadlo et al., 2009]. For an ideal packing of spheres in a hcp lattice, the c/a ratio is 1.633, and so it is believed that ratios close to this value are more elastically isotropic. While information on the c/a ratio at high pressures and temperatures provides valuable constraints on the elasticity of potential core candidates, the available experimental literature exhibits a level of scatter which prevents quantitative analysis. This is posited to be due to a wide array of experimental issues, partially addressed in the following chapter. These effects as a whole are due to the deviatoric stresses exerted on the sample during compression, and potential technical issues which may arise throughout the course of the experiments. In order to minimize experimental artifacts, Figure 4.26 shows c/a ratios vs. P only measured in noble gas media. This allows for the measurement of high-quality diffraction data with weak pressure gradients and textures.

The present measurements of Fe5Si and Fe5Ni5Si are in good agreement with Fe10Ni5Si measured by [Morrison et al., 2018]. This indicates that while Fe-Ni alloys have higher axial ratios relative to Fe [Morrison et al., 2018], [Dewaele et al., 2006], when Fe is alloyed with both Ni and Si, only Si contributes strongly to the change in axial ratio at ambient temperature.

In order to assess what factors may potentially hinder the measurement of accurate c/a ratios, XRD meshes from the IXS experiments of [Antonangeli et al., 2018] were reanalyzed to determine the c/a ratio as a function of location within the cell from this set of experiments. In these experiments, there was no PTM used in order to maximize IXS signal, and so it presents a good case study for the effects of non-hydrostatic conditions on the Fe-Si axial ratios at ambient temperatures.

It follows that there are 3 main considerations for the reliable measurement and analysis of axial ratios which will be discussed in the following sections:

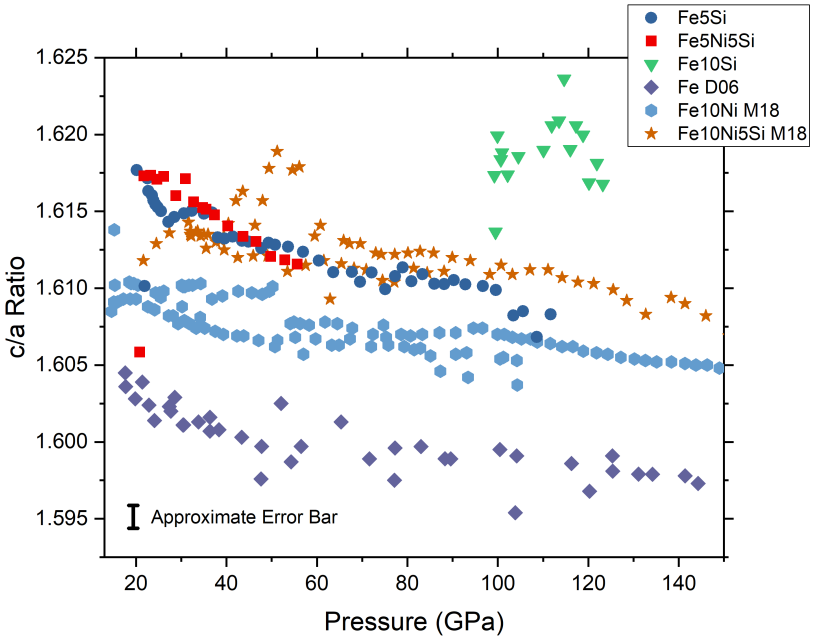

Figure 4.26: Axial Ratios of Fe, Fe-Ni-Si and Fe-Si alloys at high pressures compressed in Ne or He. It is observed that the axial ratios of Fe-xNi-5Si are not significantly affected by Ni content at ambient temperature.

1) Effects of texture and stress
2) Effects of plasticity
3) Statistical quality of diffraction image

Effects of Texture and Deviatoric Stress on the c/a Ratio

Under non-hydrostatic compression, the unit cell volume not only decreases with increasing compression, but the lattice parameters of the material distort relative to the compression axis of the DAC. This effect can be partially mitigated by indexing a large number of diffraction rings of the sample - in a powder diffraction image, each diffraction ring is comprised of approximately iso-stress planes of crystallites with a specific orientation relative to the compression axis. As each diffraction ring arises from grains with distinct orientations relative to the compression axis, the local heterogeneity of the sample stress-state can be partially averaged. However, under applied deviatoric stress, all elastically anisotropic materials orient such that the hard axis lies in the direction of the applied stress. It follows that hcp Fe-alloys which are elastically anisotropic with a hard c-axis and softer basal plane, will orient under compression such that the c-axis is aligned with the axis of compression, developing texture. When strong textures are present in the sample, the effect of deviatoric stress is enhanced because the measurement samples much fewer grain orientations than the untextured case.

Using the Fe9Si EoS given in [Antonangeli et al., 2018], unit cell volumes as a function of location in the gasket hole were used to determine pressure to make a

series of pressure maps of experimental points during IXS, and coupled with maps of the c/a ratio. Figures 4.27 and 4.28 show the pressure distribution and c/a ratio map of Fe9Si in a cell compressed uniaxially in a typical DAC experiment at $\sim$ 78 GPa - that of no PTM confined by a Re gasket using 150/300 μm bevelled anvils. It is observed in this case that there is no clear link between the pressure gradient observed in the cell and the variation of the c/a ratio, although the pressure map shows a clear conical symmetry with the maximum of pressure at the center of the gasket hole. There are some anomalous values of the c/a ratio with position at the edge of the map, but this is likely due to plasticity of the sample in the vicinity of the Re gasket. While the c/a ratio is roughly 1.611-1.613 at the location of maximum pressure, this is significantly lower than the c/a measured in Ne for Fe10Si - about 1.617-1.621, and comparable to that of Fe5Si at similar pressures. This anomalously low value is caused by the distortion of the c and a lattice parameters - the sampled c-axis is strongly oriented towards the axis of highest applied stress, and so is more strongly compressed than the 'hydrostatic' case, while the sampled a axis is more strongly aligned to the axis of lowest applied stress, and is more weakly compressed than the 'hydrostatic' case.

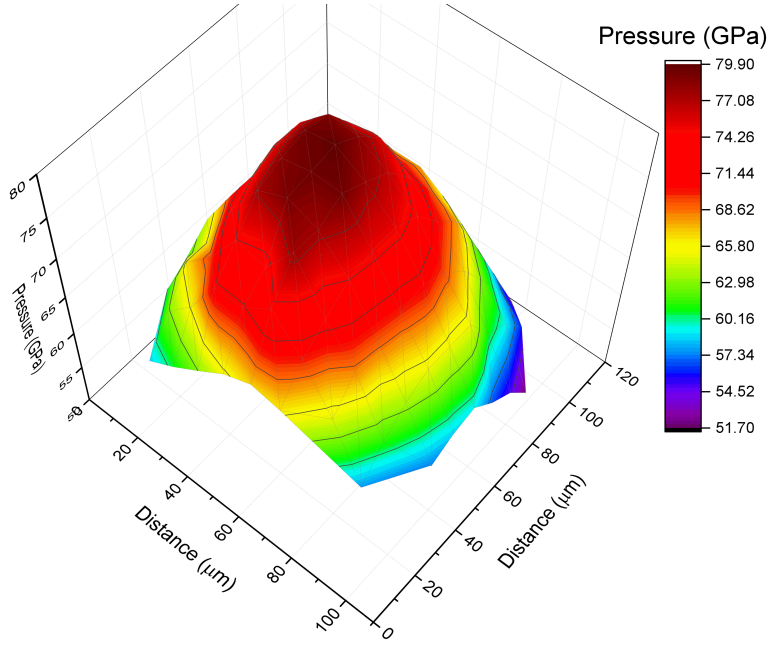

Figure 4.27: Map of pressure over the sample chamber of an experiment on Fe9Si at a pressure of $\sim$ 76 GPa. 150/300 μm culets, $\sim$80μm gasket hole diameter.

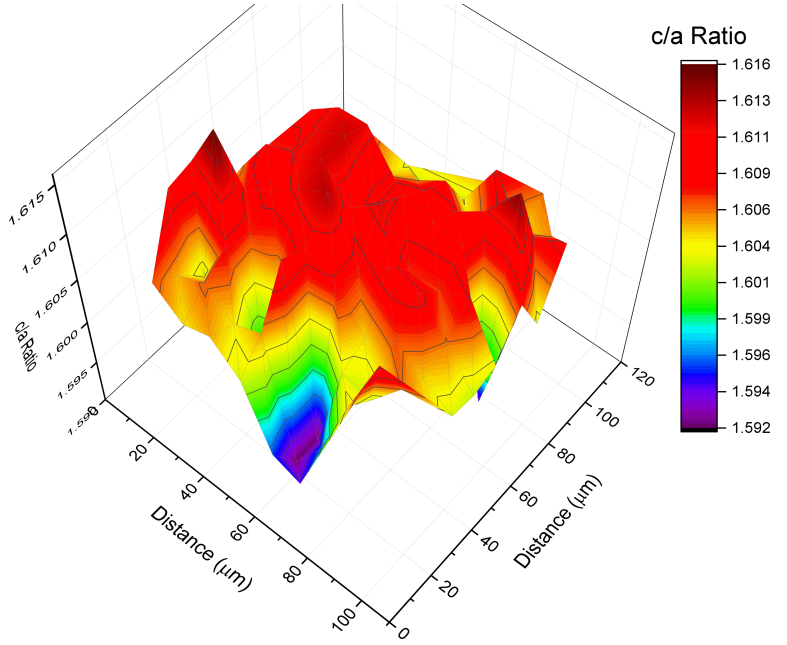

Figure 4.28: Map of c/a ratio over the sample chamber of an experiment on Fe9Si at a pressure of $\sim$76 GPa. 150/300 μm culets, $\sim$80μm gasket hole diameter.

Additionally, in [Antonangeli et al., 2018], a different construction of sample chamber was also used for achieving high signal quality at Mbar pressures, by using FIB-machined 40/100/300 anvils equipped with Re/cBN gaskets after [Fei et al., 2016]. It is observed in Figures 4.29 and 4.30 that for similar pressures to Figs. 4.27 and 4.28, the pressure distribution and variation of the axial ratio is completely different. While there are regions of the cBN cell where the axial ratio is very low indicating strong deviatoric stress, at the saddle point of the pressure distribution in Figure 4.29 there is a maximum of the axial ratio, where it is comparable to that of Fe10Si compressed in Ne. This observation may indicate that using this experimental design the compressive stress at the center of the cell is more uniform than using a standard Re gasket. It is stressed however that the difference in P gradients between the two experiments is related to the difference in the length scale at which the meshes were measured - in Figs. 4.27 and 4.28 the mesh is over a 100 μm by 100 μm grid while that of Figs. 4.29 and 4.30 is 50 μm by 50 μm .

This saddle-point type P distribution remains up to the highest pressures achieved using the cBN construction. At a pressure of $\sim$144 GPa the center of the cell exhibits a clear minimum in pressure, and in this region the axial ratio remains consistent with that of Fe10Si in Ne. Interestingly, the pressure gradients in this cell remain similar in magnitude between 80 GPa and 144 GPa - a difference of about 8 GPa and 10 GPa respectively, corresponding to P gradients of $\sim$10% and $\sim$6.5. In [Fei et al., 2016], such a cell design was used to measure the P-V relations of hcp-Fe to 2 Mbar using MgO as the PTM and calibrant (from 140-200 GPa), and it was remarked that the results are in good agreement with [Dewaele et al., 2006] where Fe was compressed in Ne and He to 2 Mbar. This may be a direct result of similarities at in pressure gradients at Mbar pressures, as by 2.5 Mbar He and Ne are expected to support pressure gradients of around 4-5% [Dorfman et al., 2012].

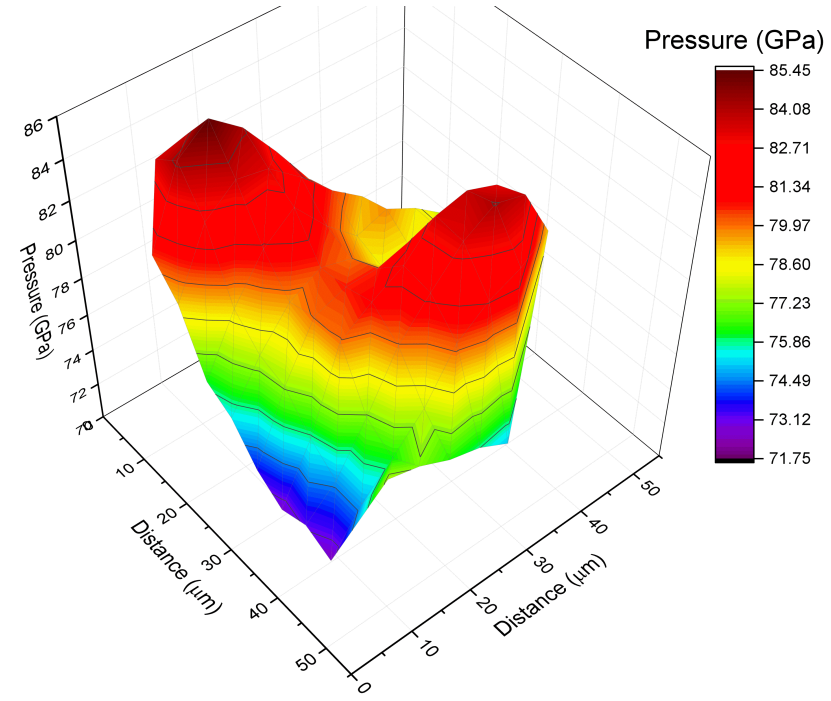

Figure 4.29: Pressure map of a cell with a cBN gasket at ∼80 GPa. Shows a saddle point of pressure at the center of the sample chamber.

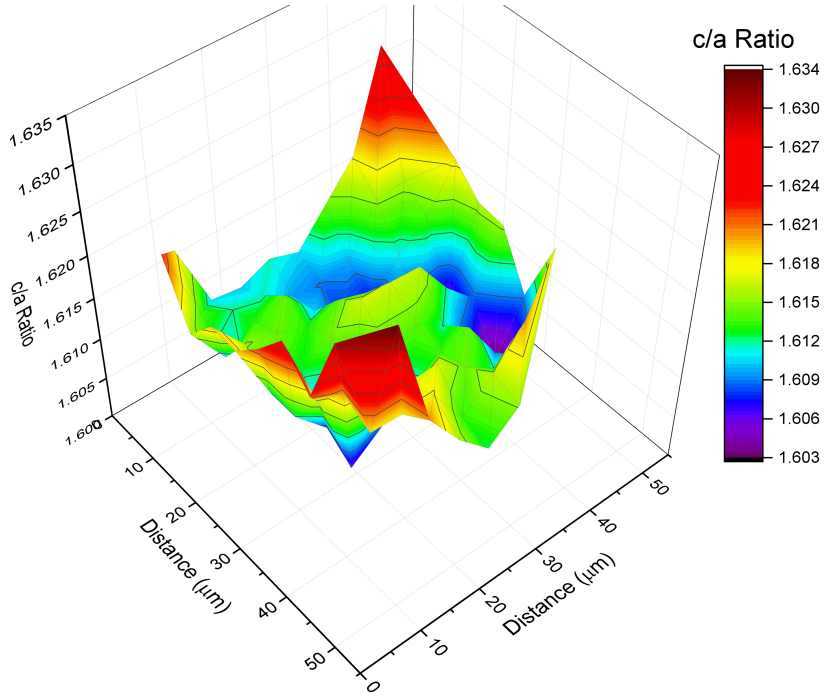

Figure 4.30: c/a ratio map of a cell with a cBN gasket at ∼ 80 GPa.

.

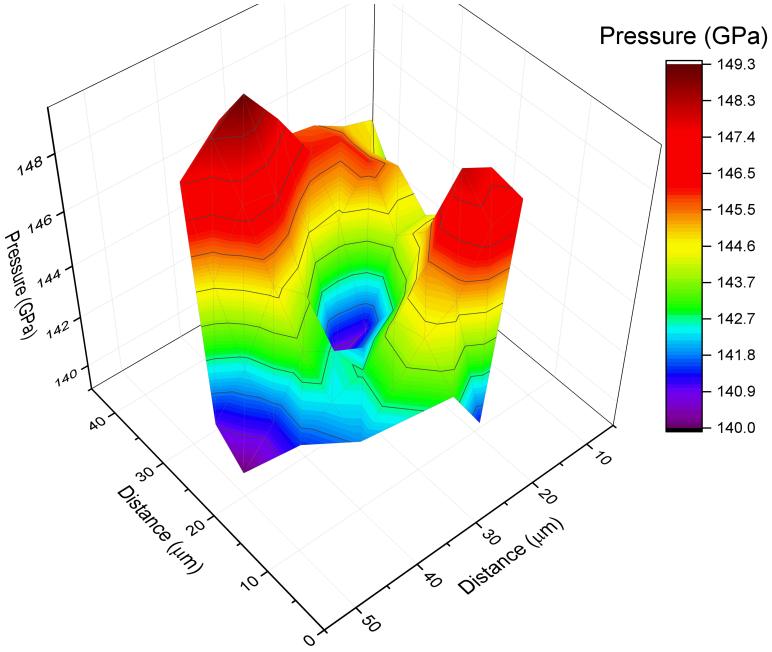

Figure 4.31: Pressure map of a cell with a cBN gasket at ∼144 GPa.

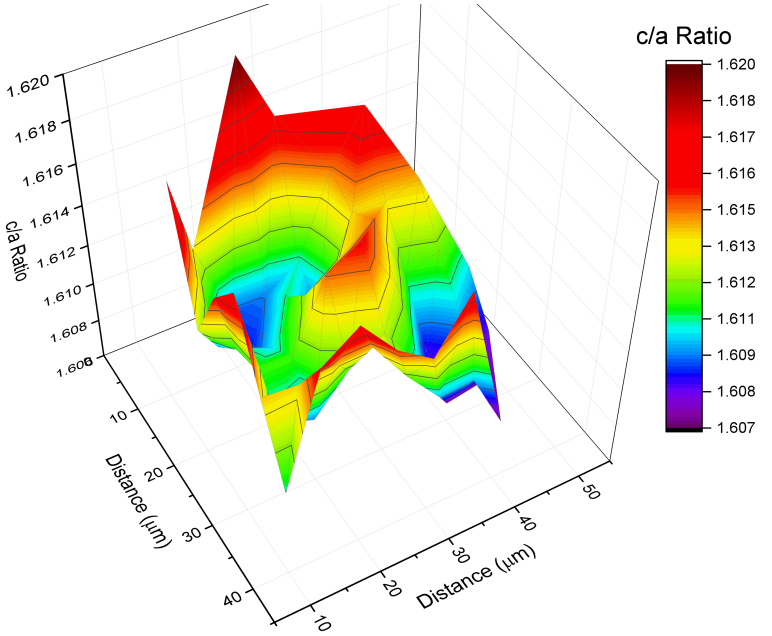

Figure 4.32: c/a ratio map of a cell with a cBN gasket at ∼144 GPa.

Effects of Plasticity on the c/a Ratio

In one experimental run, instability of the gasket hole (Re gasket, 150/300 μmculets) resulted in the sample nearly reaching the edge of the diamond culets. This was observed to strongly modify the c/a ratio, as plastic flow of the sample resulted in significant complexity of the orientation and stress-state of the sample. This behaviour caused strong variation of the c/a which corresponds to the direction of

hole-opening rather than the P-gradients of the cell. The pressure and axial ratio maps are shown in Figures 4.33 and 4.34.

While under hydrostatic conditions the c/a ratio is linked to the ratio of C_{33} and C_{11} elastic constants [Morrison et al., 2018], the effects of plasticity and deviatoric stress are extrinsic mechanisms which act to alter the c/a ratio at a given pressure. For the case of hcp-Fe the axial ratios of samples compressed in He and those of samples which were annealed at high temperatures to relax stress gradients ([Dewaele et al., 2006] and [Boehler et al., 2008]) are observed to be similar. However, such delicate measurements can be strongly influenced by using non-ideal pressure media (e.g. KCl, ethanol:methanol:water etc.) or simple experimental issues such as the movement of the gasket hole which may induce plastic flow of the sample.

These considerations highlight the considerable quality of the present dataset - it is very difficult to measure accurate axial ratios, and agreement between datasets for c/a ratios reported in literature is the exception rather than the rule.

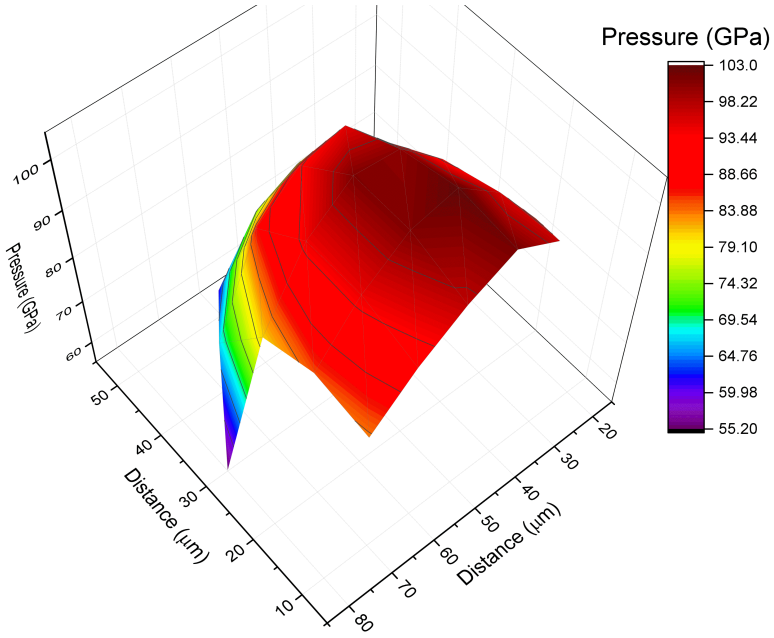

Figure 4.33: Pressure map of a cell with 150/300 μm culets equipped with a Re gasket at $\sim$ 1 Mbar. In this experiment the gasket was unstable and opened under pressure.

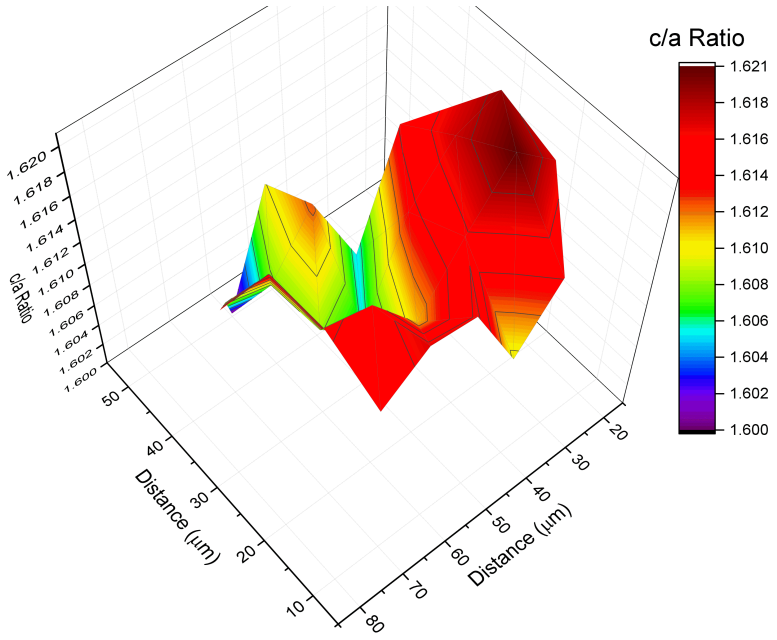

Figure 4.34: c/a ratio map of a cell with 150/300 μmculets equipped with a Re gasket at $\sim$ 1 Mbar. In this experiment the gasket was unstable and opened under pressure, the c/a ratios are shown to be strongly distorted across the sample chamber.

Diffraction Quality and Fitting

For diffraction images with spotty, weak peaks or with strong overlap between the sample, calibrant etc., the measurement of the c/a ratio varies strongly with the data-treatment strategy. In the case of Fe5Ni5Si, while it was possible to reliably reproduce similar unit cell volumes using both PDIndexer and Jana2006, the axial ratios were different, due to differences in peak weighting and the fitting algorithms between the two programs. It follows that while the data for Fe5Ni5Si was of sufficient quality for the measurement of sample volume, it was not sufficient to reliably determine the axial ratio of the material (shown in Figure 4.35). Another technical note on these studies is that the diffraction patterns at high temperatures of hcp-Fe5Ni5Si show significant preferred orientation, while those of Fe5Si do not. The only significant difference between the experimental protocol of the two studies is how the pressure was increased over the experimental run. For Fe5Ni5Si, pressure was raised stepwise, with diffraction patterns being collected after sharp rises in pressure, whereas for Fe5Si pressure was raised gradually and continually up to the maximum pressure. It is evident in Figure 4.35 that this detail has important consequences for the quality of the measured datasets.

As observed in Figure 4.38 in the next section, as the intensity of diffraction rings from hcp Fe-alloys are more strongly weighted by the a-axis than the c-axis, scatter in axial ratio measurements typically arises from scatter in the determination of the c-axis lattice parameter. This issue of statistics is enhanced by deviatoric stress, due to the development of texture, with the c-axis aligning to the axis of compression.

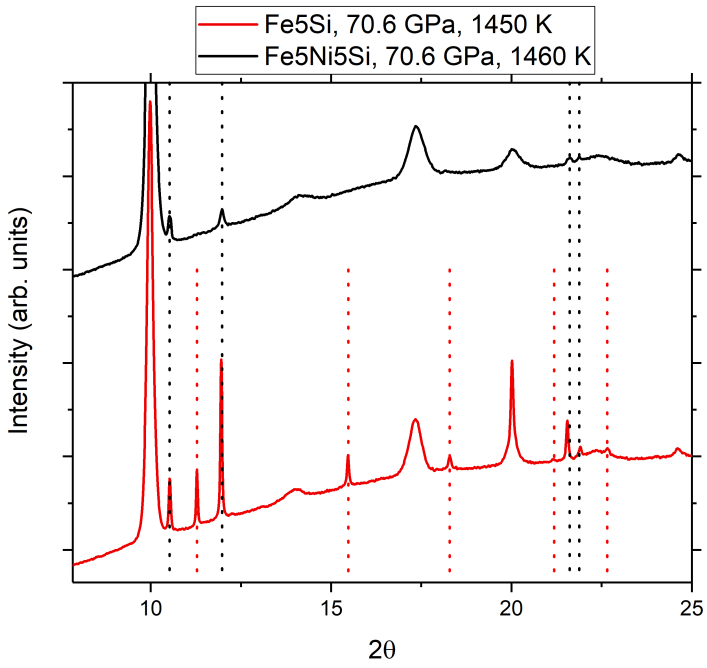

Figure 4.35: Comparison of diffraction patterns of Fe5Si and Fe5Ni5Si at similar pressures and temperatures. Dotted black lines indicate lines used for analysis that are present for both Fe5Ni5Si and Fe5Si, whereas dotted red lines indicate lines present in the Fe5Si run only. It is observed that the data quality of Fe5Si at high temperatures is excellent due to the low preferred orientation and sharp peaks - the latter indicates weak temperature gradients.

Axial Ratios of Fe5Si at high temperatures

Using the XRD dataset from section 4.2, high quality axial ratios were derived from the measured lattice parameters as a function of pressure and temperature up to high pressures for Fe5Si. Figure 4.36 shows the axial ratios of Fe5Si as a function of pressure and temperature. It is observed that the decrease of the axial ratio with pressure at constant temperature is significantly higher than for the ambient temperature dataset.

This large change in the axial ratio is strongly linked to the thermal expansion of the c-axis - the thermal expansion of the a-axis displays only weak anharmonic effects and displays extremely weak volume dependence as shown in Figure 4.37. By contrast, the expansion of the c-axis exhibits strong anharmonicity and pressure dependence as shown in Figure 4.38. In both Figures, only Run 2 of the 300 K XRD diffraction runs is presented due to the significant scatter in Run 1 (from 20-40 GPa), attributed to the tearing of the gasket and significant peak overlap between sample and calibrant.

In the case of an isotropic solid, the bulk modulus of a material scales by d^{-3} - d^{-5} where d is the interatomic distance [Haines et al., 2001]. As a consequence, if the axial thermal expansion remains strongly asymmetric up to core conditions it is likely that Si alloying would reduce elastic anisotropy in the inner core, because of the enhanced softening of the c-axis relative to the a-axis.

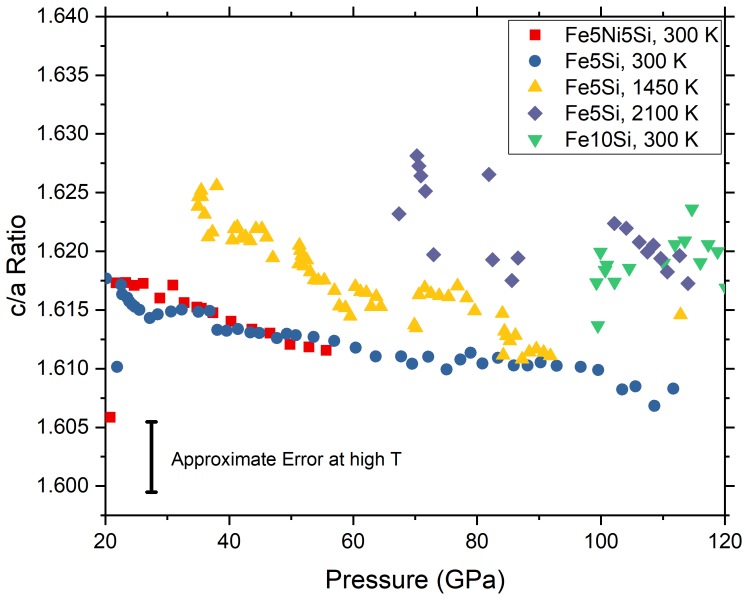

Figure 4.36: Fe-Ni-Si c/a ratios as a function of pressure and temperature. It is observed that the c/a ratios of Fe5Si increase significantly with temperature, but also decrease significantly with increasing pressure.

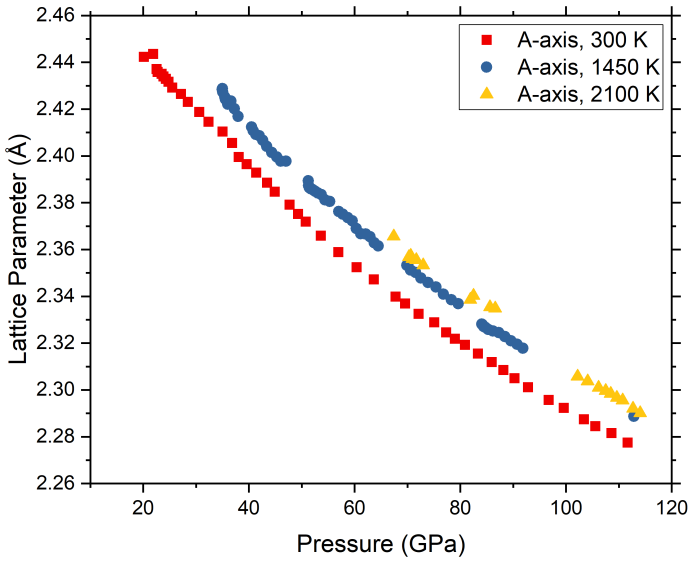

Figure 4.37: a-axis vs. P and T. Thermal expansion does not vary significantly with P or T.

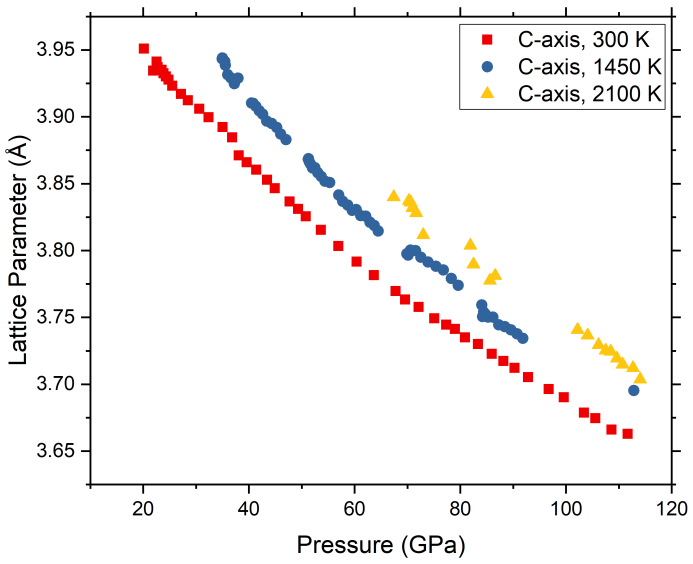

Figure 4.38: c-axis vs. P and T. Thermal expansion is observed to decrease with increasing pressure and is significantly higher than the a axis.

Chapter 5

Conclusions

In summary, we combined Picosecond Acoustics at pressures up to 1.3 Mbar using Ne PTM and Synchrotron X-ray Diffraction at simultaneous high pressures and temperatures exceeding 1.1 Mbar and 2100 K to study Fe-Si and Fe-Ni-Si alloys. In doing so, we have advanced the understanding of the influence of Si content and chemical ordering on the physical properties of Fe-Si alloys. These results have also been used to place strong constraints on the composition of the Earth's inner core.

We have performed measurements of compressional sound velocities and P-V equations of state under quasihydrostatic conditions, measured over the entire stability field of the bcc phase of Fe-xSi alloys (x = 5, 8, 10, 12, 17), which increases from ∼14 GPa for 5wt%Si up to ∼62 GPa for Fe12Si. In line with reported literature, no hcp phase was observed for Fe17Si up to 65 GPa under quasihydrostatic conditions (e.g. [Fischer et al., 2012], [Wicks et al., 2018]). It is observed that due to the suppression of chemical ordering in the Fe-Si alloys synthesized by Physical Vapor Deposition, the bulk compressibility and sound velocities are lower and exhibit more variability than reported literature on chemically ordered DO_3 alloys of the same composition. Remarkably, the ambient pressure bulk modulus for Fe10Si is decreased by nearly 20% relative to Fe5Si and Fe17Si. In this way, by using Physical Vapor Deposition to synthesize bcc Fe-Si alloys it is possible to strongly alter the physical properties of the resulting alloy, and to engineer taylored materials.

On the basis of the combined datasets on the evolution of Vp with density, it is clear that a linear-mixing approximation is not valid between end-member compositions Fe and stoichiometric FeSi. This result is a direct consequence of the observation that that the derivatives of Vp and Vs with density show nonlinear variation as a function of Si content, which is correlated with changes in crystal structure and chemical ordering. As such, outcomes of many geophysical studies which assume linearity have to be revisited.

We observe a change in the bcc-hcp transition mechanism of Fe-Si alloys with respect to hcp-Fe, and have mapped the transition pressure as a function of Si content by both PA and XRD for alloys of up to 12 wt% Si. Transition pressures observed by PA and XRD are in excellent agreement with each other, and the compositional trends are in good agreement with the results of ab initio calculations [Côté et al., 2008]. It is seen that while earlier PA studies exhibit no pre-transition effect in the bcc-hcp transition for elemental Fe [Decremps et al., 2014], we observe a pre-

transition effect for Fe10Si, and we note markedly different elastic and mechanical behaviour over the course of the transition. This would indicate that Si alloying alters the bcc-hcp transition mechanism of Fe.

A thermoelastic equation of state of hcp Fe-5Si was determined from P-V and Vp measurements up to 1.1 Mbar under quasihydrostatic conditions, and P-V-T measurements to the same pressures and temperatures exceeding 2100 K. This study is the first instance of the sound velocity of an iron alloy being measured to Mbar pressures under quasihydrostatic conditions, and the first study on an iron alloy to perform isothermal compression experiments at high temperatures employing a laser-heated DAC. This combination of datasets has been used to extrapolate density, Vp and Vs to core conditions, showing that the physical properties of Fe-Si alloys are incompatible with seismological observations of the Earth's inner core [Dziewonski and Anderson, 1981]. Further insights have been drawn on the effect of electronic thermal pressure at core conditions - the P-V-T EoS determined here represents the first successful determination of anharmonic thermal parameters for Fe or an Fe alloy at high pressures without requiring extensive parametrization by other methods (e.g. [Dewaele et al., 2006], [Fei et al., 2016]).

Preliminary P-V-T measurements up to 1500 K and 90 GPa of an Fe-5wt%Ni-5wt%Si shows that Ni may reduce thermal expansion at core conditions, and hence increase the density deficit relative to the inner core, however further studies are needed to make robust geophysical conclusions. The axial c/a ratios of Fe and Fe alloys are related to the ratio of the elastic constants C_{33} and C_{11}, and so axial ratios place constraints on the elastic anisotropy of the alloy. Such measurements are of great importance to geophysics, due to observations of seismic anisotropy in the Earth's inner core [Deuss, 2014], which is expected to stem from preferred orientation of the alloy which composes the inner core [Karato, 1993], [Wenk et al., 2000]. High quality measurements of Fe-Si and Fe-Ni-Si axial ratios were performed for Fe-5Si, Fe-5Ni-5Si and Fe10Si up to 1.1 Mbar, 55 GPa and 1.3 Mbar respectively under quasihydrostatic conditions. Compared to hcp-Fe, the axial ratios of all of these alloys are higher, increasing with increasing Si content, and it is observed that Ni alloying has no effect on the axial ratios in the presence of Si.

The axial ratios of Fe5Si were also measured as a function of pressure and temperature, showing that they increase significantly with temperature but show strong pressure dependence and anharmonicity. On the basis of the axial ratios of these alloys at high pressures and temperatures, it is observed that the presence of Si in the Earth's inner core would reduce elastic anisotropy relative to hcp-Fe.

Using the results of PA measurements performed under non-hydrostatic conditions, we see that for Fe-Si alloys such conditions can result in deviations of measured Vp of several percent in both the bcc and hcp phases.

To summarize, we have determined the variation of elastic properties with Si content in bcc and B2 Fe-Si alloys at high pressures, and we have determined that the effect of Si on geophysically important parameters (namely Vp, Vs and anisotropy) leads to the conclusion that Si cannot be the sole light element in the Earth's inner core. While an alloy of Fe with 5 wt% Si can match the density of PREM for all reasonable inner core temperatures, both Vp and Vs of such an alloy are too high relative to those observed for the inner core. Furthermore, Si alloying reduces the

elastic anisotropy of Fe, which may cast doubt on the ability of an Fe-Si alloy to support the seismic anisotropy observed for the inner core.

On the basis of cosmochemical arguments, Ni is expected to be present in the Earth's inner core. A variety of studies have been performed at ambient temperatures and high pressures which show that Ni has little effect on the properties of core candidate materials [Mao et al., 1990], [Martorell et al., 2013], [Wakamatsu et al., 2018], [Morrison et al., 2018]. The preliminary equation of state measurements reported here indicate that an Fe-Ni-Si alloy at HP HT conditions exhibit lower thermal expansion relative to the same Fe-Si alloy, suggesting that the influence of Ni at high temperatures would require a larger quantity of light elements to match the density deficit with PREM. It follows that Ni may also then have an effect on the grüneisen parameter, which would have important consequences for the Earth's thermal profile. On the contrary, comparing the axial ratios of Fe5Ni5Si and Fe5Si, Ni likely does not have a strong influence on seismic anisotropy of the Earth's inner core relative to the effect of Si.

Perspectives

Si however, is not the only candidate core material. Other studies have pointed to the presence of C or S in the Earth's inner core. Unfortunately, for such materials the literature is primarily focused on endmember compositions, due to the significant challenges inherent to synthesizing disordered Fe-C and Fe-S alloys. Carbon solubility in bcc-Fe is extremely low at ambient conditions, and Sulfur only becomes soluble in Fe as an alloy at high pressures.

Recently, rapid-quench and PVD methods have been used to synthesize Fe-C alloys of varying C contents in order to assess the alloying properties of C at geophysically relevant concentrations. Their characterization in the hcp phase at high pressures was started at the end of this Thesis (synchrotron experiments in July 2018). In addition to the importance of finding a match to seismic observations, constraining C abundances in the core is of significant geochemical importance as it has been shown that the presence of carbon may play an important role in the geochemistry of hydrogen-bearing minerals at the core-mantle boundary [Boulard et al., 2018].

In principle, thermoreflectance signals are also detectable using PA methods on sufficiently thin samples. In such experiments, a variation in reflectivity is observed due to the sample's thermal decay. Very recently, similar instrumentation has been used to determine the thermal conductivity of mantle minerals at high pressures [Hsieh et al., 2018]. Using the instrumentation already developed at IMPMC, combined with high quality sample synthesis methods, it may be possible to place strong constraints on the thermal conductivity of iron and iron alloys, in order to constrain the dynamics and thermal history of the Earth and those of telluric planets in general. While flash heating and electrical conductivity measurement techniques are employed regularly to constrain thermal conductivity of geomaterials (e.g. [Ohta et al., 2016], [Konôpková et al., 2016]), these techniques require significant assumptions or thermal modeling, and are often employed under non-hydrostatic conditions. With PA, it would be possible to perform simultaneous measurements of both sample thickness (through travel times) and thermal conductivity, which would significantly

improve data quality and hence provide more robust geophysical conclusions. As well, by developing a P-V-T equation of state for the material studied, it is possible to directly derive heat capacities at high P-T conditions, which are a necessary pre-requisite for the determination of thermal conductivity through flash heating and thermoreflectance methods.

Finally, while the PA experiments in this Thesis were performed at ambient temperature, soon there will be laser-heating capabilities incorporated into the PA instrumental setup at IMPMC. It is expected that at high temperatures, there will be anharmonic effects in Fe-alloys which act to reduce sound velocities at constant density. As PA is a direct method for the measurement of acoustic travel times, and collection times can be relatively short compared to synchrotron experiments (anywhere from a few minutes to a few hours), it lends itself better to the study of elastic waves at HP HT conditions. Due to the shorter time-scale of experiments, temperature stability of the laser is less technically challenging, and there is a lower chance for chemical reaction between the Fe-bearing sample and diamonds. Such measurements provide crucial constraints on the elastic properties of Fe-alloys at geophysically relevant conditions, in addition to allowing a laboratory-based method to determine the phase boundaries and melting temperatures of these materials. The feasibility of such measurements at lower PT conditions have already been demonstrated on metallic liquids [Ayrinhac et al., 2014], [Ayrinhac et al., 2015].

Such measurements will be crucial to new and exciting advances in our comprehension of the properties of the Earth's deep interior.

Chapter 6

Bibliography

Bibliography

[Adams et al., 2006] Adams, J. J., Agosta, D. S., Leisure, R. G., and Ledbetter, H. Elastic constants of monocrystal iron from 3 to 500 K. *Journal of Applied Physics*, 100(11):113530.

[Akahama and Kawamura, 2006] Akahama, Y. and Kawamura, H. Pressure calibration of diamond anvil Raman gauge to 310GPa. *Journal of Applied Physics*, 100(4):043516.

[Alberts and Wedepohl, 1971] Alberts, H. and Wedepohl, P. Elastic constants of dilute iron-silicon alloy single crystals below room temperature. *Physica*, 53(4):571 – 580.

[Alfè et al., 2001] Alfè, D., Price, G. D., and Gillan, M. J. Thermodynamics of hexagonal-close-packed iron under Earth's core conditions. *Phys. Rev. B*, 64:045123.

[Alfè et al., 2002] Alfè, D., Price, G. D., and Gillan, M. J. Iron under Earth's core conditions: Liquid-state thermodynamics and high-pressure melting curve from ab initio calculations. *Phys. Rev. B*, 65:165118.

[Angel, 2000] Angel, R. J. Equations of State. *Reviews in Mineralogy and Geochemistry*, 41(1):35.

[Antonangeli et al., 2006] Antonangeli, D., Merkel, S., and Farber, D. L. Elastic anisotropy in hcp metals at high pressure and the sound wave anisotropy of the Earth's inner core. *Geophysical Research Letters*, 33(24):L24303.

[Antonangeli et al., 2018] Antonangeli, D., Morard, G., Paolasini, L., Garbarino, G., Murphy, C. A., Edmund, E., Decremps, F., Fiquet, G., Bosak, A., Mezouar, M., and Fei, Y. Sound velocities and density measurements of solid hcp-Fe and hcp-Fe-Si (9 wt.the Earth's inner core. *Earth and Planetary Science Letters*, 482:446 – 453.

[Antonangeli and Ohtani, 2015] Antonangeli, D. and Ohtani, E. Sound velocity of hcp-Fe at high pressure: experimental constraints, extrapolations and comparison with seismic models. *Progress in Earth and Planetary Science*, 2(1):3.

[Antonangeli et al., 2010] Antonangeli, D., Siebert, J., Badro, J., Farber, D. L., Fiquet, G., Morard, G., and Ryerson, F. J. Composition of the Earth's inner core from high-pressure sound velocity measurements in Fe-Ni-Si alloys. *Earth and Planetary Science Letters*, 295(1):292 – 296.

[Anzellini et al., 2013] Anzellini, S., Dewaele, A., Mezouar, M., Loubeyre, P., and Morard, G. Melting of Iron at Earth's Inner Core Boundary Based on Fast X-ray Diffraction. *Science*, 340(6131):464–466.

[Asanuma et al., 2011] Asanuma, H., Ohtani, E., Sakai, T., Terasaki, H., Kamada, S., Hirao, N., and Ohishi, Y. Static compression of Fe0.83Ni0.09Si0.08 alloy to 374GPa and Fe0.93Si0.07 alloy to 252GPa: Implications for the Earth's inner core. *Earth and Planetary Science Letters*, 310(1):113 – 118.

[Ayrinhac et al., 2014] Ayrinhac, S., Gauthier, M., Bove, L. E., Morand, M., Le Marchand, G., Bergame, F., Philippe, J., and Decremps, F. Equation of state of liquid mercury to 520 K and 7 GPa from acoustic velocity measurements. *The Journal of Chemical Physics*, 140(24):244201.

[Ayrinhac et al., 2015] Ayrinhac, S., Gauthier, M., Marchand, G. L., Morand, M., Bergame, F., and Decremps, F. Thermodynamic properties of liquid gallium from picosecond acoustic velocity measurements. *Journal of Physics: Condensed Matter*, 27(27):275103.

[Badro et al., 2015] Badro, J., Brodholt, J. P., Piet, H., Siebert, J., and Ryerson, F. J. Core formation and core composition from coupled geochemical and geophysical constraints. *Proceedings of the National Academy of Sciences*, 112(40):12310–12314.

[Badro et al., 2007] Badro, J., Fiquet, G., Guyot, F., Gregoryanz, E., Occelli, F., Antonangeli, D., and d'Astuto, M. Effect of light elements on the sound velocities in solid iron: Implications for the composition of Earth's core. *Earth and Planetary Science Letters*, 254(1):233 – 238.

[Balchan and Cowan, 1966] Balchan, A. S. and Cowan, G. R. Shock compression of two iron-silicon alloys to 2.7 megabars. *Journal of Geophysical Research*, 71(14):3577–3588.

[Bhattacharya et al., 2017] Bhattacharya, S. K., Kohyama, M., Tanaka, S., Shiihara, Y., Saengdeejing, A., Chen, Y., and Mohri, T. Mechanical properties of Fe rich Fe-Si alloys: ab initio local bulk-modulus viewpoint. *Materials Research Express*, 4(11):116518.

[Bina et al., 1992] Bina, C. R., , and Helffrich, G. R. Calculation of Elastic Properties from Thermodynamic Equation of State Principles. *Annual Review of Earth and Planetary Sciences*, 20(1):527–552.

[Birch, 1947] Birch, F. Finite Elastic Strain of Cubic Crystals. *Phys. Rev.*, 71:809–824.

[Birch, 1961] Birch, F. The velocity of compressional waves in rocks to 10 kilobars: 1. *Journal of Geophysical Research*, 65(4):1083–1102.

[Boehler, 1993] Boehler, R. Temperatures in the Earth's core from melting-point measurements of iron at high static pressures. *Nature*, 363:534–.

[Boehler et al., 2008] Boehler, R., Santamaría-Pérez, D., Errandonea, D., and Mezouar, M. Melting, density, and anisotropy of iron at core conditions: new x-ray measurements to 150 GPa. *Journal of Physics: Conference Series*, 121(2):022018.

[Boness et al., 1986] Boness, D. A., Brown, J., and McMahan, A. The electronic thermodynamics of iron under Earth core conditions. *Physics of the Earth and Planetary Interiors*, 42(4):227 – 240.

[Bouchet et al., 2013] Bouchet, J., Mazevet, S., Morard, G., Guyot, F., and Musella, R. Ab initio equation of state of iron up to 1500 GPa. *Phys. Rev. B*, 87:094102.

[Boulard et al., 2018] Boulard, E., Guyot, F., Menguy, N., Corgne, A., Auzende, A.-L., Perrillat, J.-P., and Fiquet, G. CO2-induced destabilization of pyrite-structured FeO2Hx in the lower mantle. *National Science Review*, 1:nwy032.

[Bridgman, 1946] Bridgman, P. W. Recent Work in the Field of High Pressures. *Rev. Mod. Phys.*, 18:1–93.

[Bridgman, 1957] Bridgman, P. W. Effects of Pressure on Binary Alloys V Fifteen Alloys of Metals of Moderately High Melting Point. *Proceedings of the American Academy of Arts and Sciences*, 84(2):131–177.

[Brown, 1999] Brown, J. M. The NaCl pressure standard. *Journal of Applied Physics*, 86(10):5801–5808.

[Brown et al., 2000] Brown, J. M., Fritz, J. N., and Hixson, R. S. Hugoniot data for iron. *Journal of Applied Physics*, 88(9):5496–5498.

[Brush, 1980] Brush, S. G. Discovery of the Earth's core. *American Journal of Physics*, 48(9):705–724.

[Büchner and Kemnitz, 1981] Büchner, A. R. and Kemnitz, H. D. The Elastic Constants of Iron-Silicon Alloys in Dependence on Order and Composition. *Zeischrift für Metallkunde*, 72(8):575–578.

[Burgers, 1934] Burgers, W. On the process of transition of the cubic-body-centered modification into the hexagonal-close-packed modification of zirconium. *Physica*, 1(7):561 – 586.

[Campbell et al., 2009] Campbell, A. J., Danielson, L., Righter, K., Seagle, C. T., Wang, Y., and Prakapenka, V. B. High pressure effects on the iron-iron oxide and nickel-nickel oxide oxygen fugacity buffers. *Earth and Planetary Science Letters*, 286(3):556 – 564.

[Carr and Smoluchowski, 1951] Carr, W. J. and Smoluchowski, R. The Magnetostriction of Single Crystals of Iron-Silicon Alloys. *Phys. Rev.*, 83:1236–1243.

[Chase, 1998] Chase, M. W. J. (1998). *NIST-JANAF Thermochemical Tables*. American Institute of Physics, fourth edition edition.

[Chijioke et al., 2005] Chijioke, A. D., Nellis, W. J., Soldatov, A., and Silvera, I. F. The ruby pressure standard to 150GPa. *Journal of Applied Physics*, 98(11):114905.

[Clendenen and Drickamer, 1966] Clendenen, R. L. and Drickamer, H. G. Effect of High Pressure on the Compressibilities of Five Alloys. *The Journal of Chemical Physics*, 44(12):4385–4386.

[Cockett and Davis, 1963] Cockett, G. H. and Davis, C. D. The lattice expansion of Fe-Si alloys and the volume change at the A3 point. *Journal of the Iron and Steel Institute*, 201:110–115.

[Côté et al., 2008] Côté, A. S., Vočadlo, L., and Brodholt, J. P. The effect of silicon impurities on the phase diagram of iron and possible implications for the Earth's core structure. *Journal of Physics and Chemistry of Solids*, 69(9):2177 – 2181. Study of Matter Under Extreme Conditions 2007.

[Dasgupta and Hirschmann, 2010] Dasgupta, R. and Hirschmann, M. M. The deep carbon cycle and melting in Earth's interior. *Earth and Planetary Science Letters*, 298(1):1 – 13.

[Decker, 1971] Decker, D. L. High-Pressure Equation of State for NaCl, KCl, and CsCl. *Journal of Applied Physics*, 42(8):3239–3244.

[Decremps et al., 2014] Decremps, F., Antonangeli, D., Gauthier, M., Ayrinhac, S., Morand, M., Marchand, G. L., Bergame, F., and Philippe, J. Sound velocity of iron up to 152 GPa by picosecond acoustics in diamond anvil cell. *Geophysical Research Letters*, 41(5):1459–1464.

[Decremps et al., 2008] Decremps, F., Belliard, L., Perrin, B., and Gauthier, M. Sound Velocity and Absorption Measurements under High Pressure Using Picosecond Ultrasonics in a Diamond Anvil Cell: Application to the Stability Study of AlPdMn. *Phys. Rev. Lett.*, 100:035502.

[Decremps et al., 2015] Decremps, F., Gauthier, M., Ayrinhac, S., Bove, L., Belliard, L., Perrin, B., Morand, M., Marchand, G. L., Bergame, F., and Philippe, J. Picosecond acoustics method for measuring the thermodynamical properties of solids and liquids at high pressure and high temperature. *Ultrasonics*, 56:129 – 140.

[Deuss, 2014] Deuss, A. Heterogeneity and Anisotropy of Earth's Inner Core. *Annual Review of Earth and Planetary Sciences*, 42(1):103–126.

[Dewaele et al., 2012] Dewaele, A., Belonoshko, A. B., Garbarino, G., Occelli, F., Bouvier, P., Hanfland, M., and Mezouar, M. High-pressure–high-temperature equation of state of KCl and KBr. *Phys. Rev. B*, 85:214105.

[Dewaele et al., 2015] Dewaele, A., Denoual, C., Anzellini, S., Occelli, F., Mezouar, M., Cordier, P., Merkel, S., Véron, M., and Rausch, E. Mechanism of the $\alpha - \epsilon$ phase transformation in iron. *Phys. Rev. B*, 91:174105.

[Dewaele and Garbarino, 2017] Dewaele, A. and Garbarino, G. Low temperature equation of state of iron. *Applied Physics Letters*, 111(2):021903.

[Dewaele et al., 2004] Dewaele, A., Loubeyre, P., and Mezouar, M. Equations of state of six metals above 94 GPa. *Phys. Rev. B*, 70:094112.

[Dewaele et al., 2006] Dewaele, A., Loubeyre, P., Occelli, F., Mezouar, M., Dorogokupets, P. I., and Torrent, M. Quasihydrostatic Equation of State of Iron above 2 Mbar. *Phys. Rev. Lett.*, 97:215504.

[Dewaele et al., 2008] Dewaele, A., Torrent, M., Loubeyre, P., and Mezouar, M. Compression curves of transition metals in the Mbar range: Experiments and projector augmented-wave calculations. *Phys. Rev. B*, 78:104102.

[Dobson et al., 2002] Dobson, D. P., Vočadlo, L., and Wood, I. G. A new high-pressure phase of FeSi. *American Mineralogist*, 87:784–.

[Dorfman et al., 2012] Dorfman, S. M., Prakapenka, V. B., Meng, Y., and Duffy, T. S. Intercomparison of pressure standards (Au, Pt, Mo, MgO, NaCl and Ne) to 2.5 Mbar. *Journal of Geophysical Research: Solid Earth*, 117(B8):B08210.

[Dorogokupets et al., 2017] Dorogokupets, P. I., Dymshits, A. M., Litasov, K. D., and Sokolova, T. S. Thermodynamics and Equations of State of Iron to 350 GPa and 6000 K. *Scientific Reports*, 7:41863.

[Dorogokupets and Oganov, 2007] Dorogokupets, P. I. and Oganov, A. R. Ruby, metals, and MgO as alternative pressure scales: A semiempirical description of shock-wave, ultrasonic, x-ray, and thermochemical data at high temperatures and pressures. *Phys. Rev. B*, 75:024115.

[Dziewonski and Anderson, 1981] Dziewonski, A. M. and Anderson, D. L. Preliminary reference Earth model. *Physics of the Earth and Planetary Interiors*, 25(4):297 – 356.

[Fallot, 1936] Fallot, M. Ferromagnetisme des alliages de fer. In *Annales de Physique*, volume 11, pages 305–387. EDP Sciences.

[Farquhar et al., 1945] Farquhar, M. C. M., Lipson, H., and Weill, A. R. X-ray study of Fe-rich Fe-Si alloys. *Journal of the Iron and Steel Institute*, 152:457–462.

[Fei et al., 2016] Fei, Y., Murphy, C., Shibazaki, Y., Shahar, A., and Huang, H. Thermal equation of state of hcp-iron: Constraint on the density deficit of Earth's solid inner core. *Geophysical Research Letters*, 43(13):6837–6843.

[Fei et al., 2007] Fei, Y., Ricolleau, A., Frank, M., Mibe, K., Shen, G., and Prakapenka, V. Toward an internally consistent pressure scale. *Proceedings of the National Academy of Sciences*, 104(22):9182–9186.

[Fiorillo, 1996] Fiorillo, F. Advances in Fe-Si properties and their interpretation. *Journal of Magnetism and Magnetic Materials*, 157-158:428 – 431. European Magnetic Materials and Applications Conference.

[Fiquet et al., 2009] Fiquet, G., Badro, J., Gregoryanz, E., Fei, Y., and Occelli, F. Sound velocity in iron carbide (Fe3C) at high pressure: Implications for the carbon content of the Earth's inner core. *Physics of the Earth and Planetary Interiors*, 172(1):125 – 129. Diffusion, deformation and mineral properties of the Earth's interior. A Special Volume to honour the scientific contribution of Professor Olivier Jaoul.

[Fiquet et al., 2001] Fiquet, G., Badro, J., Guyot, F., Requardt, H., and Krisch, M. Sound Velocities in Iron to 110 Gigapascals. *Science*, 291(5503):468–471.

[Fischer et al., 2012] Fischer, R. A., Campbell, A. J., Caracas, R., Reaman, D. M., Dera, P., and Prakapenka, V. B. Equation of state and phase diagram of Fe-16Si alloy as a candidate component of Earth's core. *Earth and Planetary Science Letters*, 357-358:268 – 276.

[Fischer et al., 2014] Fischer, R. A., Campbell, A. J., Caracas, R., Reaman, D. M., Heinz, D. L., Dera, P., and Prakapenka, V. B. Equations of state in the Fe-FeSi system at high pressures and temperatures. *Journal of Geophysical Research: Solid Earth*, 119(4):2810–2827.

[Fischer et al., 2013] Fischer, R. A., Campbell, A. J., Reaman, D. M., Miller, N. A., Heinz, D. L., Dera, P., and Prakapenka, V. B. Phase relations in the Fe-FeSi system at high pressures and temperatures. *Earth and Planetary Science Letters*, 373:54 – 64.

[Fischer et al., 2015] Fischer, R. A., Nakajima, Y., Campbell, A. J., Frost, D. J., Harries, D., Langenhorst, F., Miyajima, N., Pollok, K., and Rubie, D. C. High pressure metal-silicate partitioning of Ni, Co, V, Cr, Si, and O. *Geochimica et Cosmochimica Acta*, 167:177 – 194.

[Fitoussi et al., 2009] Fitoussi, C., Bourdon, B., Kleine, T., Oberli, F., and Reynolds, B. C. Si isotope systematics of meteorites and terrestrial peridotites: implications for Mg/Si fractionation in the solar nebula and for Si in the Earth's core. *Earth and Planetary Science Letters*, 287(1):77 – 85.

[Frost and Mccammon, 2008] Frost, D. J. and Mccammon, C. The Redox State of Earth's Mantle. *Annual Review of Earth and Planetary Sciences*, 36:389–420.

[González Cámara and Houbaert, 2013] González Cámara, F. and Houbaert, Y. A review of ordering phenomena in iron-silicon steels. *REVISTA DE METALURGIA*, 49(3):178–199.

[Guillaume et al., 2011] Guillaume, C. L., Gregoryanz, E., Degtyareva, O., McMahon, M. I., Hanfland, M., Evans, S., Guthrie, M., Sinogeikin, S. V., and Mao, H.-K. Cold melting and solid structures of dense lithium. *Nature Physics*, 7:211–214.

[Guinan and Beshers, 1968] Guinan, M. W. and Beshers, D. N. Pressure derivatives of the elastic constants of alpha-iron to 10 kbs. *Journal of Physics and Chemistry of Solids*, 29(3):541 – 549.

[Guyot et al., 1997] Guyot, F., Zhang, J., Martinez, I., Matas, J., Ricard, Y., and Javoy, M. P-V-T measurements of iron silicide (ϵ-FeSi) Implications for silicate-metal interactions in the early Earth. *European Journal of Mineralogy*, 9(2):277–286.

[Haidemenopoulos, 2018] Haidemenopoulos, G. N. (2018). *Physical Metallurgy: Principles and Design*. CRC Press.

[Haines et al., 2001] Haines, J., Léger, J., and Bocquillon, G. Synthesis and Design of Superhard Materials. *Annual Review of Materials Research*, 31(1):1–23.

[Halley, 1692] Halley, E. An account of the cause of the change of the variation of the magnetical needle. with an hypothesis of the structure of the internal parts of the earth: as it was proposed to the Royal Society in one of their late meetings. *Philosophical Transactions*, 17(195):563–578.

[Hammouda, 2003] Hammouda, T. High-pressure melting of carbonated eclogite and experimental constraints on carbon recycling and storage in the mantle. *Earth and Planetary Science Letters*, 214(1):357 – 368.

[Hanfland et al., 2000] Hanfland, M., Syassen, K., Christensen, N. E., and Novikov, D. L. New high-pressure phases of lithium. *Nature*, 408:174–178.

[Hemley et al., 1997] Hemley, R. J., Mao, H.-k., Shen, G., Badro, J., Gillet, P., Hanfland, M., and Häusermann, D. X-ray Imaging of Stress and Strain of Diamond, Iron, and Tungsten at Megabar Pressures. *Science*, 276(5316):1242–1245.

[Hirao et al., 2004] Hirao, N., Ohtani, E., Kondo, T., and Kikegawa, T. Equation of state of iron–silicon alloys to megabar pressure. *Physics and Chemistry of Minerals*, 31(6):329–336.

[Hirose et al., 2013] Hirose, K., Labrosse, S., and Hernlund, J. Composition and State of the Core. *Annual Review of Earth and Planetary Sciences*, 41(1):657–691.

[Hirose et al., 2017] Hirose, K., Morard, G., Sinmyo, R., Umemoto, K., Hernlund, J., Helffrich, G., and Labrosse, S. Crystallization of silicon dioxide and compositional evolution of the Earth's core. *Nature*, 543:99–.

[Hixson and Fritz, 1992] Hixson, R. S. and Fritz, J. N. Shock compression of tungsten and molybdenum. *Journal of Applied Physics*, 71(4):1721–1728.

[Holzapfel, 2003] Holzapfel, W. B. Refinement of the ruby luminescence pressure scale. *Journal of Applied Physics*, 93(3):1813–1818.

[Howie et al., 2013] Howie, R. T., Gregoryanz, E., and Goncharov, A. F. Hydrogen (deuterium) vibron frequency as a pressure comparison gauge at multi-Mbar pressures. *Journal of Applied Physics*, 114(7):073505.

[Hsieh et al., 2018] Hsieh, W.-P., Deschamps, F., Okuchi, T., and Lin, J.-F. Effects of iron on the lattice thermal conductivity of Earth's deep mantle and implications for mantle dynamics. *Proceedings of the National Academy of Sciences*, 1:201718557.

[Hu et al., 2003] Hu, M. Y., Sturhahn, W., Toellner, T. S., Mannheim, P. D., E. Brown, D., Zhao, J., and Alp, E. E. Measuring velocity of sound with nuclear resonant inelastic x-ray scattering. *Phys. Rev. B*, 67:094304.

[Huang et al., 2016] Huang, X., Li, F., Zhou, Q., Meng, Y., Litasov, K. D., Wang, X., Liu, B., and Cui, T. Thermal equation of state of Molybdenum determined from in situ synchrotron X-ray diffraction with laser-heated diamond anvil cells. *Scientific Reports*, 6:19923–.

[Hunt et al., 2017] Hunt, S. A., Wann, E. T. H., Dobson, D. P., Vočadlo, L., and Wood, I. G. The thermal expansion of (Fe 1-y Ni y)Si. *Journal of Physics: Condensed Matter*, 29(33):335701.

[Jamieson et al., 1959] Jamieson, J. C., Lawson, A. W., and Nachtrieb, N. D. New Device for Obtaining X-Ray Diffraction Patterns from Substances Exposed to High Pressure. *Review of Scientific Instruments*, 30(11):1016–1019.

[Jayaraman et al., 2018] Jayaraman, T., Meka, V., Jiang, X., Overman, N., Doyle, J., Shield, J., and Mathaudhu, S. Investigation of structural and magnetic properties of rapidly-solidified iron-silicon alloys at ambient and elevated temperatures. *Journal of Alloys and Compounds*, 741:409 – 419.

[Jette and Greiner, 1933] Jette, E. R. and Greiner, E. S. X-Ray study of Fe-Si alloys containing 0 to 15 % Si. *American Institute of Mining and Metallurgical Engineers*, 105:259–273.

[Kamada et al., 2014] Kamada, S., Ohtani, E., Fukui, H., Sakai, T., Terasaki, H., Takahashi, S., Shibazaki, Y., Tsutsui, S., Alfred, Q. B., Hirao, N., and Ohishi, Y. The sound velocity measurements of Fe3S. *American Mineralogist*, 99:98–.

[Kantor et al., 2007] Kantor, A. P., Kantor, I. Y., Kurnosov, A. V., Kuznetsov, A. Y., Dubrovinskaia, N. A., Krisch, M., Bossak, A. A., Dmitriev, V. P., Urusov, V. S., and Dubrovinsky, L. S. Sound wave velocities of fcc Fe–Ni alloy at high pressure and temperature by mean of inelastic X-ray scattering. *Physics of the Earth and Planetary Interiors*, 164(1):83 – 89.

[Karato, 1993] Karato, S.-i. Inner Core Anisotropy Due to the Magnetic Field—induced Preferred Orientation of Iron. *Science*, 262(5140):1708–1711.

[Katahara et al., 1979] Katahara, K. W., Manghnani, M. H., and Fisher, E. S. Pressure derivatives of the elastic moduli of BCC Ti-V-Cr, Nb-Mo and Ta-W alloys. *Journal of Physics F: Metal Physics*, 9(5):773.

[Klotz and Braden, 2000] Klotz, S. and Braden, M. Phonon Dispersion of bcc Iron to 10 GPa. *Phys. Rev. Lett.*, 85:3209–3212.

[Klotz et al., 2009] Klotz, S., Chervin, J.-C., Munsch, P., and Marchand, G. L. Hydrostatic limits of 11 pressure transmitting media. *Journal of Physics D: Applied Physics*, 42(7):075413.

[Knittle and Williams, 1995] Knittle, E. and Williams, Q. Static compression of epsilon-FeSi and an evaluation of reduced silicon as a deep Earth constituent. *Geophysical Research Letters*, 22(4):445–448.

[Konôpková et al., 2016] Konôpková, Z., McWilliams, R. S., Gómez-Pérez, N., and Goncharov, A. F. Direct measurement of thermal conductivity in solid iron at planetary core conditions. *Nature*, 534:99–.

[Kötter et al., 1989] Kötter, G., Nembach, K., Wallow, F., and Nembach, E. Stiffness constants and dislocation line energies and tensions of binary and ternary iron-rich Fe-Al-Si alloys. *Materials Science and Engineering: A*, 114:29 – 36.

[Kulikov et al., 2002] Kulikov, N. I., Fristot, D., Hugel, J., and Postnikov, A. V. Interrelation between structural ordering and magnetic properties in bcc Fe-Si alloys. *Phys. Rev. B*, 66:014206.

[Lei et al., 2013] Lei, L., Yan, B., and Ji-An, X. Ruby fluorescence pressure scale: Revisited. *Chinese Physics B*, 22(5):056201.

[Li et al., 2018] Li, Y., Vočadlo, L., and Brodholt, J. P. The elastic properties of hcp-Fe alloys under the conditions of the Earth's inner core. *Earth and Planetary Science Letters*, 493:118 – 127.

[Lihl and Ebel, 1961] Lihl, V. F. and Ebel, H. Röntgenographische Untersuchungen über den Aufbau eisenreicher Eisen-Silizium-Legierungen. *Archiv für das Eisenhüttenwesen*, 32(7):489–491.

[Lin et al., 2003a] Lin, J.-F., Campbell, A. J., Heinz, D. L., and Shen, G. Static compression of iron-silicon alloys: Implications for silicon in the Earth's core. *Journal of Geophysical Research: Solid Earth*, 108(B1):2045.

[Lin et al., 2003b] Lin, J.-F., Struzhkin, V. V., Sturhahn, W., Huang, E., Zhao, J., Hu, M. Y., Alp, E. E., Mao, H.-k., Boctor, N., and Hemley, R. J. Sound velocities of iron-nickel and iron-silicon alloys at high pressures. *Geophysical Research Letters*, 30(21):2112.

[Lin et al., 2005] Lin, J.-F., Sturhahn, W., Zhao, J., Shen, G., Mao, H.-k., and Hemley, R. J. Sound Velocities of Hot Dense Iron: Birch's Law Revisited. *Science*, 308(5730):1892–1894.

[Litasov et al., 2013] Litasov, K. D., Dorogokupets, P. I., Ohtani, E., Fei, Y., Shatskiy, A., Sharygin, I. S., Gavryushkin, P. N., Rashchenko, S. V., Seryotkin, Y. V., Higo, Y., Funakoshi, K., Chanyshev, A. D., and Lobanov, S. S. Thermal equation of state and thermodynamic properties of molybdenum at high pressures. *Journal of Applied Physics*, 113(9):093507.

[Liu et al., 2014] Liu, J., Lin, J.-F., Alatas, A., and Bi, W. Sound velocities of bcc-Fe and Fe0.85Si0.15 alloy at high pressure and temperature. *Physics of the Earth and Planetary Interiors*, 233:24 – 32.

[Liu et al., 2016] Liu, J., Lin, J.-F., Alatas, A., Hu, M. Y., Zhao, J., and Dubrovinsky, L. Seismic parameters of hcp-Fe alloyed with Ni and Si in the Earth's inner core. *Journal of Geophysical Research: Solid Earth*, 121(2):610–623.

[Machová and Kadečková, 1977] Machová, A. and Kadečková, S. Elastic constants of iron-silicon alloy single crystals. *Czechoslovak Journal of Physics B*, 27(5):555–563.

[Mao et al., 1967] Mao, H.-K., Bassett, W. A., and Takahashi, T. Effect of Pressure on Crystal Structure and Lattice Parameters of Iron up to 300 kbar. *Journal of Applied Physics*, 38(1):272–276.

[Mao et al., 1990] Mao, H. K., Wu, Y., Chen, L. C., Shu, J. F., and Jephcoat, A. P. Static compression of iron to 300 GPa and Fe0.8Ni0.2 alloy to 260 GPa: Implications for composition of the core. *Journal of Geophysical Research: Solid Earth*, 95(B13):21737–21742.

[Mao et al., 1986] Mao, H. K., Xu, J., and Bell, P. M. Calibration of the ruby pressure gauge to 800 kbar under quasi-hydrostatic conditions. *Journal of Geophysical Research: Solid Earth*, 91(B5):4673–4676.

[Mao et al., 2001] Mao, H. K., Xu, J., Struzhkin, V. V., Shu, J., Hemley, R. J., Sturhahn, W., Hu, M. Y., Alp, E. E., Vocadlo, L., Alfè, D., Price, G. D., Gillan, M. J., Schwoerer-Böhning, M., Häusermann, D., Eng, P., Shen, G., Giefers, H., Lübbers, R., and Wortmann, G. Phonon Density of States of Iron up to 153 Gigapascals. *Science*, 292(5518):914–916.

[Mao et al., 2012] Mao, Z., Lin, J.-F., Liu, J., Alatas, A., Gao, L., Zhao, J., and Mao, H.-K. Sound velocities of Fe and Fe-Si alloy in the Earth's core. *Proceedings of the National Academy of Sciences*, 109(26):10239–10244.

[Marsh, 1980] Marsh, S. P. (1980). *LASL shock Hugoniot data*, volume 5. Univ of California Press.

[Martorell et al., 2013] Martorell, B., Brodholt, J., G. Wood, I., and Vočadlo, L. The effect of nickel on the properties of iron at the conditions of Earth's inner core: Ab initio calculations of seismic wave velocities of Fe-Ni alloys. *Earth and Planetary Science Letters*, 365:143–151.

[Martorell et al., 2016] Martorell, B., Wood, I. G., Brodholt, J., and Vočadlo, L. The elastic properties of hcp-Fe1-xSix at Earth's inner-core conditions. *Earth and Planetary Science Letters*, 451:89 – 96.

[Matassov, 1977] Matassov, G. (1977). *The Electrical Conductivity of Iron Silicon Alloys at High Pressures and the Earth's Core*. PhD thesis, Lawrence Livermore Laboratory.

[McCammon et al., 1983] McCammon, C. A., Ringwood, A. E., and Jackson, I. Thermodynamics of the system Fe-FeO-MgO at high pressure and temperature and a model for formation of the Earth's core. *Geophysical Journal of the Royal Astronomical Society*, 72(3):577–595.

[McDonough, 2003] McDonough, W. 2.15 - Compositional Model for the Earth's Core. In Holland, H. D. and Turekian, K. K., editors, *Treatise on Geochemistry*, pages 547 – 568. Pergamon, Oxford.

[McDonough and Sun, 1995] McDonough, W. F. and Sun, S.-s. The composition of the Earth. *Chemical Geology*, 120(3):223 – 253. Chemical Evolution of the Mantle.

[McQueen et al., 1967] McQueen, R. G., Marsh, S. P., and Fritz, J. N. Hugoniot equation of state of twelve rocks. *Journal of Geophysical Research*, 72(20):4999–5036.

[Merkel et al., 1999] Merkel, S., Hemley, R. J., and Mao, H.-k. Finite-element modeling of diamond deformation at multimegabar pressures. *Applied Physics Letters*, 74(5):656–658.

[Miozzi et al., 2018] Miozzi, F., Morard, G., Antonangeli, D., Clark, A. N., Mezouar, M., Dorn, C., Rozel, A., and Fiquet, G. Equation of State of SiC at Extreme Conditions: New Insight Into the Interior of Carbon-Rich Exoplanets. *Journal of Geophysical Research: Planets*, 123(9):2295–2309.

[Mishin et al., 1999] Mishin, Y., Farkas, D., Mehl, M. J., and Papaconstantopoulos, D. A. Interatomic potentials for monoatomic metals from experimental data and ab initio calculations. *Phys. Rev. B*, 59:3393–3407.

[Monza et al., 2011] Monza, A., Meffre, A., Baudelet, F., Rueff, J.-P., d'Astuto, M., Munsch, P., Huotari, S., Lachaize, S., Chaudret, B., and Shukla, A. Iron Under Pressure: "Kohn Tweezers" and Remnant Magnetism. *Phys. Rev. Lett.*, 106:247201.

[Morard et al., 2011] Morard, G., Andrault, D., Guignot, N., Siebert, J., Garbarino, G., and Antonangeli, D. Melting of Fe–Ni–Si and Fe–Ni–S alloys at megabar pressures: implications for the core–mantle boundary temperature. *Physics and Chemistry of Minerals*, 38(10):767–776.

[Morard et al., 2013] Morard, G., Siebert, J., Andrault, D., Guignot, N., Garbarino, G., Guyot, F., and Antonangeli, D. The Earth's core composition from high pressure density measurements of liquid iron alloys. *Earth and Planetary Science Letters*, 373:169 – 178.

[Morard et al., 2014] Morard, G., Siebert, J., and Badro, J. Partitioning of Si and platinum group elements between liquid and solid Fe-Si alloys. *Geochimica et Cosmochimica Acta*, 132:94 – 100.

[Morrison et al., 2018] Morrison, R. A., Jackson, J. M., Sturhahn, W., Zhang, D., and Greenberg, E. Equations of state and anisotropy of Fe-Ni-Si alloys. *Journal of Geophysical Research: Solid Earth*, in press:–.

[Murphy et al., 2011] Murphy, C. A., Jackson, J. M., Sturhahn, W., and Chen, B. Gruneisen parameter of hcp-Fe to 171 GPa. *Geophysical Research Letters*, 38(24):L24306.

[Nguyen and Holmes, 2004] Nguyen, J. H. and Holmes, N. C. Melting of iron at the physical conditions of the Earth's core. *Nature*, 427:339–.

[Norman, 1581] Norman, R. The newe attractive shewing the nature, propertie, and manifold vertues of the loadstone; with the declination of the needle, touched therewith, under the plaine of the horizon. Found out and discovered by Robert Norman.

[Ohta et al., 2016] Ohta, K., Kuwayama, Y., Hirose, K., Shimizu, K., and Ohishi, Y. Experimental determination of the electrical resistivity of iron at Earth's core conditions. *Nature*, 534:95–.

[Ono, 2010] Ono, S. The equation of state of B2-type NaCl. *Journal of Physics: Conference Series*, 215(1):012196.

[Ono, 2013] Ono, S. Equation of state and elasticity of B2-type FeSi: Implications for silicon in the inner core. *Physics of the Earth and Planetary Interiors*, 224:32 – 37.

[Petrova et al., 2010] Petrova, A. E., Krasnorussky, V. N., Shikov, A. A., Yuhasz, W. M., Lograsso, T. A., Lashley, J. C., and Stishov, S. M. Elastic, thermodynamic, and electronic properties of MnSi, FeSi, and CoSi. *Phys. Rev. B*, 82:155124.

[Phragmén, 1926] Phragmén, G. The Constitution of Iron-Silicon Alloys. *The Journal of the Iron and Steel Institute*, 114:397–404.

[Poirier, 1994] Poirier, J.-P. Light elements in the Earth's outer core: A critical review. *Physics of the Earth and Planetary Interiors*, 85(3k):319 – 337.

[Polcarová et al., 1988] Polcarová, M., Kadečková, S., Brądler, J., Godwod, K., and Bąk-misiuk, J. Lattice parameters of Fe-Si alloy single crystals. *physica status solidi (a)*, 106(1):17–23.

[Prescher et al., 2015] Prescher, C., Dubrovinsky, L., Bykova, E., Kupenko, I., Glazyrin, K., Kantor, A., McCammon, C., Mookherjee, M., Nakajima, Y., Miyajima, N., Sinmyo, R., Cerantola, V., Dubrovinskaia, N., Prakapenka, V., Raffer, R., Chumakov, A., and Hanfland, M. High Poisson's ratio of Earth's inner core explained by carbon alloying. *Nature Geoscience*, 8:220–.

[Prescher and Prakapenka, 2015] Prescher, C. and Prakapenka, V. B. DIOPTAS: a program for reduction of two-dimensional X-ray diffraction data and data exploration. *High Pressure Research*, 35(3):223–230.

[Ragan et al., 1977] Ragan, C. E. I., Silbert, M. G., and Diven, B. C. Shock compression of molybdenum to 2.0 TPa by means of a nuclear explosion. *Journal of Applied Physics*, 48(7):2860–2870.

[Randl et al., 1995] Randl, O. G., Vogl, G., Petry, W., Hennion, B., Sepiol, B., and Nembach, K. Lattice dynamics and related diffusion properties of intermetallics: I. Fe 3 Si. *Journal of Physics: Condensed Matter*, 7(30):5983.

[Rausch, 1976] Rausch, J. B. (1976). *The Lattice Parameters and Structures of Iron-Silicon Single Crystals and the Elastic Constants of Fe3Si*. Masters thesis, Iowa State University.

[Rausch and Kayser, 1977] Rausch, J. B. and Kayser, F. X. Elastic constants and electrical resistivity of Fe3Si. *Journal of Applied Physics*, 48(2):487–493.

[Ricolleau et al., 2011] Ricolleau, A., Fei, Y., Corgne, A., Siebert, J., and Badro, J. Oxygen and silicon contents of Earth's core from high pressure metal-silicate partitioning experiments. *Earth and Planetary Science Letters*, 310(3):409 – 421.

[Ringwood, 1966] Ringwood, A. Chemical evolution of the terrestrial planets. *Geochimica et Cosmochimica Acta*, 30(1):41 – 104.

[Ross and Hume-Rothery, 1963] Ross, R. and Hume-Rothery, W. High temperature X-ray metallography: I. A new debye-scherrer camera for use at very high temperatures II. A new parafocusing camera III. Applications to the study of chromium, hafnium, molybdenum, rhodium, ruthenium and tungsten. *Journal of the Less Common Metals*, 5(3):258 – 270.

[Routbort et al., 1971] Routbort, J., Reid, C., Fisher, E., and Dever, D. High-temperature elastic constants and the phase stability of silicon-iron. *Acta Metallurgica*, 19(12):1307 – 1316.

[Sakai et al., 2011] Sakai, T., Ohtani, E., Hirao, N., and Ohishi, Y. Stability field of the hcp-structure for Fe, Fe-Ni, and Fe-Ni-Si alloys up to 3 Mbar. *Geophysical Research Letters*, 38(9):L09302.

[Sakairi et al., 2018] Sakairi, T., Sakamaki, T., Ohtani, E., Fukui, H., Kamada, S., Tsutsui, S., Uchiyama, H., and Baron, A. Q. Sound velocity measurements of hcp Fe-Si alloy at high pressure and high temperature by inelastic X-ray scattering. *American Mineralogist*, 103(1):85.

[Sakamaki et al., 2016] Sakamaki, T., Ohtani, E., Fukui, H., Kamada, S., Takahashi, S., Sakairi, T., Takahata, A., Sakai, T., Tsutsui, S., Ishikawa, D., Shiraishi, R., Seto, Y., Tsuchiya, T., and Baron, A. Q. R. Constraints on Earth's inner core composition inferred from measurements of the sound velocity of hcp-iron in extreme conditions. *Science Advances*, 2(2):e1500802.

[Sata et al., 2010] Sata, N., Hirose, K., Shen, G., Nakajima, Y., Ohishi, Y., and Hirao, N. Compression of FeSi, Fe3C, Fe0.95O, and FeS under the core pressures and implication for light element in the Earth's core. *Journal of Geophysical Research: Solid Earth*, 115(B9):B09204.

[Satish-Kumar et al., 2011] Satish-Kumar, M., So, H., Yoshino, T., Kato, M., and Hiroi, Y. Experimental determination of carbon isotope fractionation between iron carbide melt and carbon: 12C-enriched carbon in the Earth's core? *Earth and Planetary Science Letters*, 310(3):340 – 348.

[Saxena et al., 1996] Saxena, S. K., Dubrovinsky, L. S., Lazor, P., Cerenius, Y., Häggkvist, P., Hanfland, M., and Hu, J. Stability of Perovskite (MgSiO3) in the Earth's Mantle. *Science*, 274(5291):1357–1359.

[Schaeffer et al., 2015] Schaeffer, A. M., Temple, S. R., Bishop, J. K., and Deemyad, S. High-pressure superconducting phase diagram of 6Li: Isotope effects in dense lithium. *Proceedings of the National Academy of Sciences*, 112(1):60–64.

[Shibazaki et al., 2016] Shibazaki, Y., Nishida, K., Higo, Y., Igarashi, M., Tahara, M., Sakamaki, T., Terasaki, H., Shimoyama, Y., Kuwabara, S., Takubo, Y., and Ohtani, E. Compressional and shear wave velocities for polycrystalline bcc-Fe up to 6.3 GPa and 800 K. *American Mineralogist*, 101(5):1150.

[Shibazaki et al., 2012] Shibazaki, Y., Ohtani, E., Fukui, H., Sakai, T., Kamada, S., Ishikawa, D., Tsutsui, S., Baron, A. Q., Nishitani, N., Hirao, N., and Takemura, K. Sound velocity measurements in dhcp-FeH up to 70GPa with inelastic X-ray scattering: Implications for the composition of the Earth's core. *Earth and Planetary Science Letters*, 313-314:79 – 85.

[Shin et al., 2005] Shin, J., Bae, J., Kim, H., Lee, H., Lee, T., Lavernia, E., and Lee, Z. Ordering-disordering phenomena and micro-hardness characteristics of B2 phase in Fe-(5-6.5 *Materials Science and Engineering: A*, 407(1):282 – 290.

[Shyni and Alagarsamy, 2014] Shyni, P. and Alagarsamy, P. Thermomagnetic properties of nanocrystalline Fe-Si alloys with high Si content. *Physica B: Condensed Matter*, 448:60 – 63. Selected papers from International Conference on Magnetic Materials and Applications (MagMA-2013).

[Siebert et al., 2013] Siebert, J., Badro, J., Antonangeli, D., and Ryerson, F. J. Terrestrial Accretion Under Oxidizing Conditions. *Science*, 339(6124):1194–1197.

[Smith et al., 2014] Smith, R. F., Eggert, J. H., Jeanloz, R., Duffy, T. S., Braun, D. G., Patterson, J. R., Rudd, R. E., Biener, J., Lazicki, A. E., Hamza, A. V., Wang, J., Braun, T., Benedict, L. X., Celliers, P. M., and Collins, G. W. Ramp compression of diamond to five terapascals. *Nature*, 511:330–.

[Soignard and McMillan, 2004] Soignard, E. and McMillan, P. F. An Introduction to Diamond Anvil Cells and Loading Techniques. In Katrusiak, A. and McMillan, P., editors, *High-Pressure Crystallography*, pages 81–100, Dordrecht. Springer Netherlands.

[Sokolova et al., 2013] Sokolova, T., Dorogokupets, P., and Litasov, K. Self-consistent pressure scales based on the equations of state for ruby, diamond, MgO, B2-NaCl, as well as Au, Pt, and other metals to 4 Mbar and 3000 K. *Russian Geology and Geophysics*, 54(2):181 – 199.

[Speziale et al., 2001] Speziale, S., Zha, C., Duffy, T. S., Hemley, R. J., and Mao, H. K. Quasi-hydrostatic compression of magnesium oxide to 52 GPa: Implications for the pressure-volume-temperature equation of state. *Journal of Geophysical Research: Solid Earth*, 106(B1):515–528.

[Stearns, 1963] Stearns, M. B. Internal Magnetic Fields, Isomer Shifts, and Relative Abundances of the Various Fe Sites in FeSi Alloys. *Phys. Rev.*, 129:1136–1144.

[Sturhahn and Jackson, 2007] Sturhahn, W. and Jackson, J. M. Geophysical applications of nuclear resonant spectroscopy. In Ohtani, E., editor, *Advances in High-Pressure Mineralogy*, pages –. Geological Society of America.

[Syassen, 2008] Syassen, K. Ruby under pressure. *High Pressure Research*, 28(2):75–126.

[Takahashi and Bassett, 1964] Takahashi, T. and Bassett, W. A. High-Pressure Polymorph of Iron. *Science*, 145(3631):483–486.

[Tange et al., 2009] Tange, Y., Nishihara, Y., and Tsuchiya, T. Unified analyses for P-V-T equation of state of MgO: A solution for pressure-scale problems in high P-T experiments. *Journal of Geophysical Research: Solid Earth*, 114(B3):B03208.

[Tateno et al., 2010] Tateno, S., Hirose, K., Ohishi, Y., and Tatsumi, Y. The Structure of Iron in Earth's Inner Core. *Science*, 330(6002):359–361.

[Tateno et al., 2015] Tateno, S., Kuwayama, Y., Hirose, K., and Ohishi, Y. The structure of Fe–Si alloy in Earth's inner core. *Earth and Planetary Science Letters*, 418:11 – 19.

[Tsuchiya and Fujibuchi, 2009] Tsuchiya, T. and Fujibuchi, M. Effects of Si on the elastic property of Fe at Earth's inner core pressures: First principles study. *Physics of the Earth and Planetary Interiors*, 174:212–219.

[Václav et al., 2014] Václav, P., Michal, D., and Lukáš, P. Crystallographic Computing System JANA2006: General features.

[Vinet et al., 1989] Vinet, P., Rose, J. H., Ferrante, J., and Smith, J. R. Universal features of the equation of state of solids. *Journal of Physics: Condensed Matter*, 1(11):1941.

[Voronov and Chernysheva, 1999] Voronov, F. F. and Chernysheva, E. V. Anomalies in the elastic properties of silicious iron single crystals at pressures of up to 9 GPa and the α-ϵ phase transformation. *Physics of the Solid State*, 41(3):462–467.

[Voronov and Stal'gorova, 1965] Voronov, F. F. and Stal'gorova, O. V. Elastic Properties of Barium at Pressures up to 22 000 kg/cm2. *Soviet Physics JETP*, 22(3):524–527.

[Vočadlo et al., 2009] Vočadlo, L., Dobson, D. P., and Wood, I. G. Ab initio calculations of the elasticity of hcp-Fe as a function of temperature at inner-core pressure. *Earth and Planetary Science Letters*, 288(3):534 – 538.

[Vočadlo et al., 2002] Vočadlo, L., Knight, K. S., Price, G. D., and Wood, I. G. Thermal expansion and crystal structure of FeSi between 4 and 1173 K determined by time-of-flight neutron powder diffraction. *Physics and Chemistry of Minerals*, 29(2):132–139.

[Wade and Wood, 2005] Wade, J. and Wood, B. Core formation and the oxidation state of the Earth. *Earth and Planetary Science Letters*, 236(1):78 – 95.

[Wakamatsu et al., 2018] Wakamatsu, T., Ohta, K., Yagi, T., Hirose, K., and Ohishi, Y. Measurements of sound velocity in iron–nickel alloys by femtosecond laser pulses in a diamond anvil cell. *Physics and Chemistry of Minerals*, -:1–7.

[Wang et al., 1985] Wang, C. S., Klein, B. M., and Krakauer, H. Theory of Magnetic and Structural Ordering in Iron. *Phys. Rev. Lett.*, 54:1852–1855.

[Wenk et al., 2000] Wenk, H.-R., Matthies, S., Hemley, R. J., Mao, H.-K., and Shu, J. The plastic deformation of iron at pressures of the Earth's inner core. *Nature*, 405:1044–.

[Whitaker et al., 2009] Whitaker, M. L., Liu, W., Liu, Q., Wang, L., and Li, B. Thermoelasticity of epsilon-FeSi to 8 GPa and 1273 K. *American Mineralogist*, 94(7):1039.

[Wicks et al., 2018] Wicks, J. K., Smith, R. F., Fratanduono, D. E., Coppari, F., Kraus, R. G., Newman, M. G., Rygg, J. R., Eggert, J. H., and Duffy, T. S. Crystal structure and equation of state of Fe-Si alloys at super-Earth core conditions. *Science Advances*, 4(4):eaao5864.

[Wood et al., 1990] Wood, B. J., Bryndzia, L. T., and Johnson, K. E. Mantle Oxidation State and Its Relationship to Tectonic Environment and Fluid Speciation. *Science*, 248(4953):337–345.

[Wood et al., 1996] Wood, I. G., David, W. I. F., Hull, S., and Price, G. D. A high-pressure study of ε-FeSi, between 0 and 8.5 GPa, by time-of-flight neutron powder diffraction. *Journal of Applied Crystallography*, 29(2):215–218.

[Yamazaki et al., 2012] Yamazaki, D., Ito, E., Yoshino, T., Yoneda, A., Guo, X., Zhang, B., Sun, W., Shimojuku, A., Tsujino, N., Kunimoto, T., Higo, Y., and Funakoshi, K.-i. P-V-T equation of state for epsilon-iron up to 80 GPa and 1900 K using the Kawai-type high pressure apparatus equipped with sintered diamond anvils. *Geophysical Research Letters*, 39(20):L20308.

[Ye et al., 2017] Ye, Y., Prakapenka, V., Meng, Y., and Shim, S.-H. Intercomparison of the gold, platinum, and MgO pressure scales up to 140GPa and 2500K. *Journal of Geophysical Research: Solid Earth*, 122(5):3450–3464.

[Zhang and Guyot, 1999] Zhang, J. and Guyot, F. Thermal equation of state of iron and Fe0.91Si0.09. *Physics and Chemistry of Minerals*, 26(3):206–211.

[Zharkov et al., 1972] Zharkov, V., Kalinin, V., and Panjkov, V. Equations of state and their geophysical applications. *Physics of the Earth and Planetary Interiors*, 5:332 – 343.

[Zukas et al., 1963] Zukas, E. G., Fowler, C. M., Minshall, F. S., and O'Rourke, J. The behaviour of iron silicon alloys under impulsive shock loading. *Metallurgical Society of AIME*, 227:746.

[Zuo et al., 2004] Zuo, B., Saraswati, N., Sritharan, T., and Hng, H. Production and annealing of nanocrystalline Fe-Si and Fe-Si-Al alloy powders. *Materials Science and Engineering: A*, 371(1):210 – 216.

Appendix A

Other technical aspects of Picosecond Acoustic measurements

A.1 Further Experimental Details of Picosecond Acoustics

In general, the pump-probe coincidence time can change when there is a change in the optical path length of the pump and probe beams, which typically occurs when changing the sample environment. For instance, a sample being measured on a glass slide will have a t_{PP} of ∼0.33 ps, whereas in DAC experiments t_{PP} is typically ∼ 0.32 ps. Pump-probe coincidence time is determined at ambient pressures based on the time interval between the first and second acoustic echoes, as this allows the independent determination of both the acoustic travel time, and t_{PP} from the occurrence time of the first acoustic echo. At high pressures, the travel time is not determined by the difference between first and second acoustic echoes because typically successive echoes are weaker than the brillouin oscillations of the Ne, and so their determined position can change appreciably depending on the treatment of the brillouin signal. The maximum of the first acoustic echo is used for t_{raw} because it has been observed that the shape of the wave measured at high pressures can change under pressure due to experimental conditions or changes of phase such that other features can be unreliable (e.g. the initial rise of the pulse). The first maximum of the acoustic time domain signal was observed to provide the most consistent, reliable determination of the travel time across the studied pressure range.

It is noted as well that while t_{PP} can change by a few ps between the measurement of an empty DAC with sample and a loaded cell at high pressure, changes in the optical path length of the pump and probe beams are sufficiently small with increasing pressure that their effect on t_{PP} has been observed to be negligible compared to reported experimental errors.

Schematically, the sample is placed in the focused pump and probe beams, and measurement software is launched. On the basis of trial-and-error, it has been determined that the best software measurement settings for optimizing the signal-

to-noise ratio of signals for samples of these dimensions, at these conditions is shown in Table A.1.

Time Interval	Delay Line Speed	Time Constant	Timestep (ps)
[0,3]	20	3x	1

Table A.1: Recommended settings for optimal signal-to-noise ratio in PA experiment performed at IMPMC under the experimental conditions of this Thesis.

A.2 Sample Preparation and Technical Observations

A.2.1 Sample Preparation: Sample Loading and General Observations

There are two main considerations when preparing a DAC for PA measurements: the first is to have a sample which is sufficiently large to block the pump beam, and the second is to have a sample which is not pressed uniaxially by the gasket or the diamonds.

While the pump and probe beams are focused to a $\sim 2\mu m$ x $2\mu m$ spot, the effect of diffuse scattering can be significant if the sample is not significantly larger than these dimensions. At ambient pressures, the signal from the pump beam on the measurement photodiodes of the instrument can be effectively blocked by changing its polarization to be orthogonal to that of the probe beam. However this condition deteriorates strongly with pressure due to the birefringence of the diamond, combined with the stress gradients which develop across the diamond. As a result, signal quality typically worsens significantly once diamonds become stressed to a certain percentage of their maximum pressure range. Qualitatively, this occurs for diamonds of 250 μm culet size, at pressures exceeding 50 GPa, while for $150\mu m$ culets this corresponds to pressures exceeding 100 GPa. The pump beam typically comprises around 80% of the total intensity of light impinging on the sample, and so if a significant quantity diffuse scattering from the pump is detected by the photodiodes, it can inhibit measurement of the signal due to elastic wave propagation.

From these experiments, it was observed that the lower limit of diameter of a measurable sample up to the utmost highest pressures achieved in this thesis is approximately 14-15 μm .

An important point when assuming uniform thickness variation is that if the sample bridges the diamonds, or is pressed on by the gasket, it is likely that there will be the development of both texture and the plastic flow of the sample. In such cases, the measured travel time does not sample the 'quasihydrostatic' thickness of the sample and this has been shown to significantly alter measured Vp-ρ relations as shown in Figure B.2, discussed in Section B.2. Since Ne is very soft, it produces a quasihydrostatic stress state in the sample chamber of experiments, but this results in a significant reduction of the dimensions of the sample chamber at increased

pressure. It has been observed that compressing a sample in Ne, the sample chamber diameter and height decrease by approximately half during the experiment. In this way it is critically important that the sample is well-centred within the sample chamber and a bit less than half the diameter. For experiments using 100 μm culets, the gasket was cut to $\sim$ 55 μm in diameter and loaded with a sample of 18-20 μm in diameter.

For samples which were synthesized by Physical Vapor Deposition, they were scraped off a glass substrate using a WC needle. These samples have some degree of curvature due to how they were removed, and in some cases this can result in some difficulty when measuring a travel time at ambient pressure. In some cases, it was attempted to press the sample flat in order to provide a better surface for measurements, however this resulted in changes to the measured acoustic travel time and lowered reproducibility of said travel time. As a result, all samples synthesized in this way were loaded without additional manipulation to improve the quality of the measured Vp-ρ relations.

A final consideration for maximizing the quality of the acoustic signal is the measurement geometry. As the sample must be loaded onto one side of the diamond anvil, one can focus the probe beam onto the free surface of the sample embedded within the Ne, or onto the diamond-sample interface. It has been observed that when measuring the diamond-sample interface, the Ne can embed in a thin layer between the two surfaces, resulting in anomalous additional oscillations which occur very close to the occurrence time of the first acoustic echo. This inhibits the unambiguous assignment of the acoustic peak, and results in increased measurement error. As a consequence, it is best to measure the surface of the sample opposite to the sample-diamond interface.

A.2.2 Instrument Setting Tests

When collecting data using Picosecond Acoustics, the system is capable of measuring reflectivity over a $\sim$13 ns interval based on the length of the delay line used for changing the optical path length of the probe beam. An important consideration, however, is that this collection time is an average of the reflectivity measurements from a large quantity of individual pulses, and that the effective start time of the measurement must remain constant across these measurements, and be reproducible across different collections of the same measurement. The 'time reference' is controlled by the electronics and PA labview program, and can potentially be altered by using different settings which are changed to improve the signal-to-noise ratio of the measured signals. In order to constrain such effects, the acoustic travel time of an Al sample has been measured using a wide variety of instrumental settings to check for shifts in the observed travel times. The results of such experiments are shown in Table A.2.

The results show that the largest effects on pump-probe coincidence time are caused by reducing the delay line speed or reducing the timestep of the measurements. It is seen that this can cause variations in the 'measured' acoustic travel time by up to 3 ps. Curiously, the shift of coincidence time due to a reduction

Time Interval	Delay Line Speed	Time Constant	Timestep (ps)	Pump Arrival Time
[0,13.33]	20	3x	1	0.325
[0,9]	20	3x	1	0.324
[0,7]	20	3x	1	0.324
[0,5]	20	3x	1	0.324
[0,3]	100	1x	1	0.324
[0,3]	100	3x	1	0.324
[0,3]	50	1x	1	0.323
[0,3]	50	3x	1	0.324
[0,3]	20	1x	1	0.324
[0,3]	20	3x	1	0.324
[0,3]	20	1.4m	1	0.324
[0,3]	10	1x	1	0.324
[0,3]	10	3x	1	0.325
[0,2]	20	1x	1	0.324
[0,2]	20	3x	1	0.325
[0,1.5]	20	3x	1	0.324
[0,1]	20	3x	1	0.325
[0,1]	5	1x	1	0.325
[0,1]	1	1x	1	0.325
[0,1]	10	3x	0.5	0.324
[0,1]	2	3x	0.2	0.324
[0,1]	1	1x	0.1	**0.328**
[0,0.5]	20	3x	1	0.324
[0,0.5]	1	1x	1	0.324
[0,0.5]	10	3x	0.5	0.324
[0,0.5]	1	3x	0.1	**0.327**
[0.1,0.6]	20	3x	1	0.324
[0.1,0.6]	10	3x	0.5	0.324
[0.1,0.6]	1	3x	0.1	**0.326**
[0.2,0.4]	20	3x	1	0.324
[0.2,0.4]	10	3x	0.5	0.324
[0.2,0.4]	1	3x	0.1	0.325

Table A.2: Table of pump beam arrival times as a function of instrument settings. Bold denotes settings which result in a non-negligible change in the pump arrival time. Delay line speed controls the speed at which the delay line moves over a given time interval, effectively lengthening or shorting the collection time of a time domain signal. The time interval is the interval of time measured using the delay line. The time constant is related to the frequency of collections over a given time step. The time step is the smallest time interval over which the collection is recorded.

of timestep seems to lessen when a smaller time interval is scanned. Furthermore, the pump-probe coincidence time doesn't change significantly with the time interval

except at the largest range measurable by the instrument. While these tests show that for this particular time (0.324ps) such effects are not important, it is emphasized that for datasets to remain internally consistent throughout an experimental run, *the same measurement settings must be used at all points*. It has been seen during experiments that changes in apparent travel time may be stronger at longer time-scales than the pump-probe coincidence time. As a consequence, in this thesis if settings are changed during the experiment, travel times are measured thereafter using both old and new settings.

A.2.3 Deformation Tests

There are a variety of sample synthesis methods which do not produce samples with uniform thickness or low surface roughness. In such cases, it can be challenging to measure the acoustic travel time of the sample. While machining or polishing a sample down to a few microns is a challenging task for metals, it is relatively simple to deform the sample between two diamonds to generate the necessary flat, smooth surface. However, this act can result in a change in the elasticity of the sample due to the development of residual stresses, texture and crystalline defects. In the absence of an external method for the measurement of sample thickness, large changes in elasticity can potentially bias the results of high pressure PA measurements due to the inaccurate determination of initial sample thickness. In the case of Fe5Si, this alloy was synthesized by melt-spinning which produces non-uniform surfaces, and so for sample preparation the sample was deformed slightly to create two parallel faces for picosecond acoustics experiments. Experiments on Fe-5wt%Si at high pressure showed that initially at low pressures, there was relatively high scatter in the measured travel times over different locations on the sample (shown in Figure A.1), on the order of 2% of Vp, but that the scatter decreased significantly upon transformation to the high pressure hcp phase. This indicates that a significant part of the observed scatter was due to residual stresses in the sample, as this is released upon phase transformation, while textural effects are typically preserved [Klotz and Braden, 2000], [Dewaele et al., 2015].

Additionally, it was seen that upon recovery of the sample after the experiment, the acoustic travel time was virtually identical across the sample surface, indicating a uniform texture and stress. As a result, tests were performed to see if it was possible to anneal the samples at high temperatures in order to reduce residual stresses before experiments, but at sufficiently low temperatures that oxidation of the iron silicon alloy would not occur. The results of these tests are shown below in table A.3.

It is seen that by annealing the sample at 400 K for multiple days after strong deformation (much larger than that before a typical experiment) it results in a systematic decrease of travel time, of between 1-5%. Using this information, it was observed in further experiments that starting travel times and travel times of recovered samples were generally consistent when the initial sample was annealed beforehand.

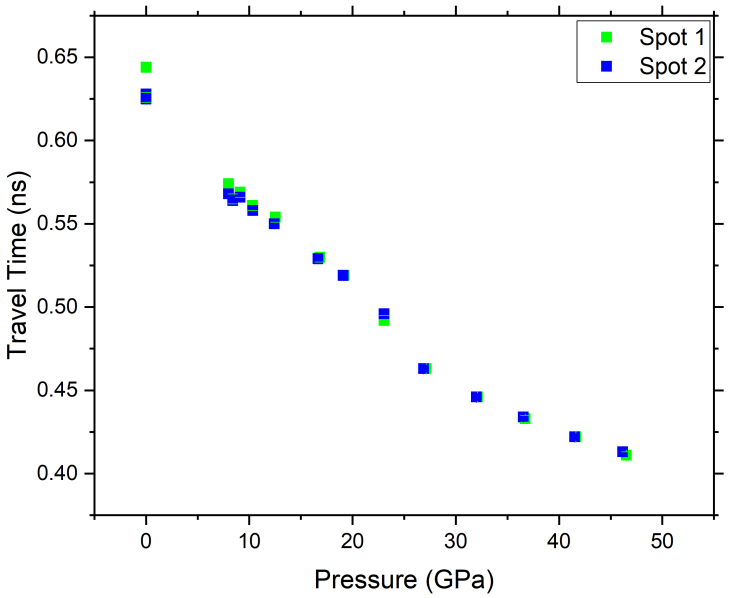

Figure A.1: Travel times of Fe5Si at high pressures.

A.3 Error Analysis

From an experimental perspective, the sound velocity of a material is given by:

$$V_p = \frac{Thickness}{Travel\,Time} \tag{A.1}$$

For the error in the measured Vp at ambient conditions, the two components of error are simple:

$$\delta V_{p,e} = \frac{\delta e_0}{t_0} \tag{A.2}$$

$$\delta V_{p,t} = -\frac{e_0}{t_0} * \frac{\delta t_0}{t_0} = -V_p * \frac{\delta t_0}{t_0} \tag{A.3}$$

Where e (e_0) and t (t_0) are thickness and acoustic travel time at high pressure (ambient pressure) respectively. In general, errors in thickness tend to be the dominant source of error in the experimental determination of Vp, due to the greater technical challenges of measuring e_0 to a high degree of accuracy on thin samples. This can be circumvented, however, by the use of high-accuracy methods for thickness determination such as Profilometry. Profilometry has been used to measure e_0 of such samples down to 10-20 nm resolution (discussed in detail in Section 2.4), however for a thickness of $1.5\mu m$, (around the typical thickness of available Fe-Si samples synthesized by physical vapor deposition) such an error is still around 1% of sample thickness. The measured acoustic travel time of such a sample can be measured to ~1-3 ps error, corresponding to an error in Vp of <1% for Fe-alloy samples (e.g. $Vp \approx 6km/s$) of thickness greater than $1.5\mu m$. For errors in V_{p0} on

Location	Note	Before Annealing	After Annealing	% Difference
Spot 1 (Avg.)		**0.546**	**0.538**	**3(1)**
Spot 1	0,0	0.546	0.539	
Spot 1	-2μm Y	-	0.538	
Spot 1	+2μm Y	-	0.54	
Spot 1	+2μm Z	-	0.535	
Spot 1	-2μm Z	-	0.54	
Spot 2 (Avg.)		**0.527**	**0.524**	**1(1)**
Spot 2	0,0	0.527	0.525	
Spot 2	-2μm Y	-	0.526	
Spot 2	+2μm Y	-	0.523	
Spot 2	+2μm Z	-	0.523	
Spot 2	-2μm Z	-	0.524	
Spot 3 (Avg.)		**0.528**	**0.519**	**4(2)**
Spot 3	0,0	0.525	0.521	
Spot 3	+3μm Y	0.526	-	
Spot 3	-3μm Y	0.53	-	
Spot 3	-2μm Y	-	0.524	
Spot 3	+2μm Y	-	0.514	
Spot 3	+2μm Z	-	0.518	
Spot 3	-2μm Z	-	0.518	
Spot 4 (Avg.)		**0.505**	**0.501**	**2(1)**
Spot 4	0,0	0.505	0.502	
Spot 4	-2μm Y	-	0.498	
Spot 4	+2μm Y	-	0.504	
Spot 4	-2μm Z	-	0.497	
Spot 4	+2μm Z	-	0.504	

Table A.3: Table of travel times of Fe-5Si samples after being strongly deformed by diamonds, before and after annealing in a vacuum oven at 130 C for 72h. All travel times uncorrected for pump-probe coincidence time. The difference column shows the percent difference between the travel times measured before and after annealing, corrected for the pump-probe coincidence time.

the order of 1% or more, this error remains the dominant source of error for up to $\sim 60GPa$ under most conditions.

For the purposes of high pressure experiments, another step must be taken - a functional form of the variation of sample thickness with pressure must be assumed. For the purposes of this Thesis, it is assumed that thickness variation is isotropic, solely depending on unit cell volume:

$$e\left(P\right) = \left(\frac{V}{V_0}\right)^{1/3} * e_0 \tag{A.4}$$

Following the initial characterization of the sample, the acoustic travel time of

a given sample is used to measure th_0. Because of this, there are additional errors associated with A.4.

$$\delta e_{Vp}\left(P=0\right)=t_0\delta V_p \tag{A.5}$$

$$\delta e_{t_0}\left(P=0\right)=\delta t_0 V_p \tag{A.6}$$

For the error in thickness due to changes with pressure:

$$\delta e_{e_0}\left(P\right)=\left(\frac{V}{V_0}\right)^{1/3}\delta e_0 \tag{A.7}$$

$$\delta e_V\left(P\right)=\frac{1}{3}\frac{\delta V}{V}\left(\frac{V}{V_0}\right)^{1/3}e_0 \tag{A.8}$$

$$\delta e_{V_0}\left(P\right)=-\frac{1}{3}\frac{\delta V_0}{V_0}\left(\frac{V}{V_0}\right)^{1/3}th_0 \tag{A.9}$$

Of these three errors in thickness, in general eq. A.9 can be safely neglected: V_0 in this case refers to V_0 of the material at ambient pressure which is generally well characterized, resulting in an error in Vp of ≈ 0.1 m/s, three orders of magnitude below typical errors in PA measurements. While A.8 is typically small as well, this depends heavily on the quality of the P-V relation used, and errors on pressure. In the absence of a well-characterized equation of state, A.8 can become a non-negligible source of error at pressures exceeding 1 Mbar, or if errors in experimentally-determined pressures become large during the PA experiment.

Typically at low pressures, the dominant source of error for Vp is the error in th_0 and at high pressures it is the error in t as shown in Fig. A.2. The strong increase in dt^2 with pressure above 80 GPa is due to increased depolarization of the pump and probe beams

While e_0 as an error is rarely less than 1%

For the determination of δV, the used P(V) equation of state is inverted numerically to solve for $V(P+\delta P)$ and $V(P-\delta P)$ using a combination of the experimentally-determined error in P during the PA run, and the full variance-covariance matrix of the used equation of state. This error in V is also used for the calculation of the error in density for a given Vp data point.

For propagating errors of dependent variables, a Jacobian transformation must be performed:

$$\delta_P^2=\mathbf{g}^T\mathbf{A}\mathbf{g} \tag{A.10}$$

where g is the vector

$$\mathbf{g}=\begin{pmatrix}\frac{\partial f}{\partial P} & \frac{\partial f}{\partial K_0} & \frac{\partial f}{\partial K'} & \frac{\partial f}{\partial V_0^*}\end{pmatrix} \tag{A.11}$$

and A is the matrix

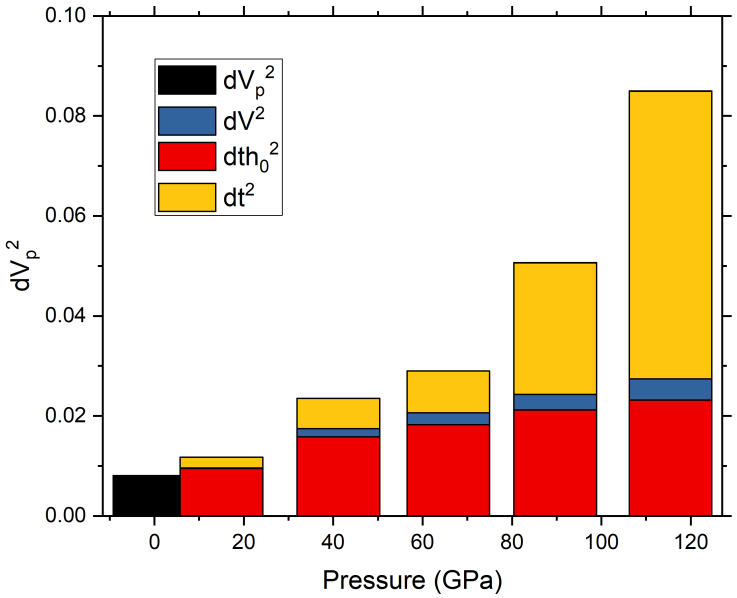

Figure A.2: The square of the error in Vp as a function of pressure for a PA experimental run. It is seen that the two dominant sources of error are the determination of the acoustic travel time and the initial thickness of the sample.

$$\mathbf{A} = \begin{pmatrix} \delta^2_{P,expt} & 0 & 0 & 0 \\ 0 & \delta^2_{K_0} & \delta_{K_0}\delta_{K'} & \delta_{K_0}\delta_{V_0^*} \\ 0 & \delta_{K_0}\delta_{K'} & \delta^2_{K'} & \delta_{K'}\delta_{V_0^*} \\ 0 & \delta_{K_0}\delta_{V_0^*} & \delta_{K'}\delta_{V_0^*} & \delta^2_{V_0^*} \end{pmatrix} \tag{A.12}$$

Where K0, K' and V0* denote the Equation of state parameters of that material *in the crystal structure being measured*. For example, studying an Fe-alloy in the high-pressure hcp phase, V0 from equation A.4 denotes V0 at ambient conditions, while V0* denotes the fitted ambient pressure volume of the hcp phase of the Fe-alloy.

Inputting the P(V) equation of state desired as f in equation A.11, naturally $\dfrac{\partial P(V)}{\partial P} = 1$ and for the other partial derivatives:

For the 3rd-order Birch Murnaghan EoS:

$$\frac{\partial P(V)}{\partial K_0} = \frac{3}{2}\left[\left(\frac{V_0^*}{V}\right)^{7/3} - \left(\frac{V_0^*}{V}\right)^{5/3}\right]\left\{1 + \frac{3}{4}\left(K' - 4\right)\left[\left(\frac{V_0^*}{V}\right)^{2/3} - 1\right]\right\} \tag{A.13}$$

$$\frac{\partial P(V)}{\partial K'} = \frac{9}{8}K_0\left(\frac{V_0^*}{V}\right)^{5/3}\left[\left(\frac{V_0^*}{V}\right)^{2/3} - 1\right]^2 \tag{A.14}$$

$$\frac{\partial P(V)}{\partial V_0^*} = \frac{1}{2}\frac{K_0}{V_0^*}\left[7\left(\frac{V_0^*}{V}\right)^{7/3} - 5\left(\frac{V_0^*}{V}\right)^{5/3}\right]\left\{1 + \frac{3}{4}\left(K' - 4\right)\left[\left(\frac{V_0^*}{V}\right)^{2/3} - 1\right]\right\} + \frac{3}{4}\frac{K_0}{V_0}\left(K' - 4\right)\left[\left(\frac{V_0^*}{V}\right)^{9/3} - \left(\frac{V_0^*}{V}\right)^{7/3}\right] \tag{A.15}$$

While Vinet EoS were not used for data analysis in this Thesis, the following are presented for completeness:

$$\frac{\partial P(V)}{\partial K_0} = 3\left(\frac{1-\eta}{\eta^2}\right) exp\left[\frac{3}{2}\left(K' - 1\right)\left(1 - \eta\right)\right] \tag{A.16}$$

$$\frac{\partial P(V)}{\partial K'} = \frac{9}{2}K_0\left(\frac{1-\eta}{\eta}\right)^2 exp\left[\frac{3}{2}\left(K' - 1\right)\left(1 - \eta\right)\right] \tag{A.17}$$

$$\frac{\partial P(V)}{\partial V_0^*} = \frac{K_0}{V_0^*}\left[\eta + 2\left(\frac{1-\eta}{\eta^2}\right) + \frac{3}{2}\left(\frac{1-\eta}{\eta}\right)\left(K' - 1\right)\right] exp\left[\frac{3}{2}\left(K' - 1\right)\left(1 - \eta\right)\right] \tag{A.18}$$

Where $\eta = \left(\frac{V}{V_0^*}\right)^{1/3}$ and A.18 was solved by chain rule from the relation $\frac{\partial P}{\partial V_0^*} = \frac{\partial P}{\partial \eta}\frac{\partial \eta}{\partial V_0^*} = -\frac{\eta}{3V_0^*}\frac{\partial P}{\partial \eta}$

Using an EoS which is measured accurately over a wide pressure range (e.g. section Fe5Si), such a method as outlined above results in errors in pressure of 2-5% and translates to errors in volume of 1-2% up to 1 Mbar. While errors in V have a negligible effect on the error of Vp, they are critical for the accurate calculation of errors in density when constructing birch plots from PA datasets.

Appendix B

Benchmarking Velocity Measurements at High Pressures via Picosecond Acoustics

B.1 Effects of non-hydrostatic stress on PA measurements

Due to the considerable technical and time limitations for experiments at synchrotron light sources, it is difficult to perform systematic studies assessing the variation of elastic behaviour under different experimental configurations with the same material. On the other hand with PA, thanks to faster collection times, better accessibility and the fact that it is a direct measurement of acoustic echoes, it provides a good benchmark from which to assess other techniques, and experimental considerations such as the effect of texture on elasticity measurements.

B.1.1 Effect of PTM on PA measurements

For Fe10Si, some studies were performed using KCl as the PTM. Shown in Figure B.1, there is clear deviation from the Vp-ρ relation measured in Ne by $\sim$7 GPa. Above 15 GPa, while Vp measured in KCl is systematically higher, this difference remains approximately constant up to the highest measured pressure. This effect results in differences in Vp at constant density of up to $\sim$2.8%.

B.1.2 Non-hydrostatic effects due to sample-gasket contact

During experiments in Fe5Si, for one run where the sample was compressed in Ne, the sample came into contact with the gasket due to instability of the gasket. Figure B.2 shows the effect which results due to non-hydrostaticity induced by the gasket collapsing onto the sample at high pressures. While in both Run 2 and Run 3 the starting travel time and the travel time of the recovered sample were within error of each other (indicating negligible plastic deformation of the sample), there was up to 6% variation in the apparent Vp of the sample, reaching a maximum at 65 GPa.

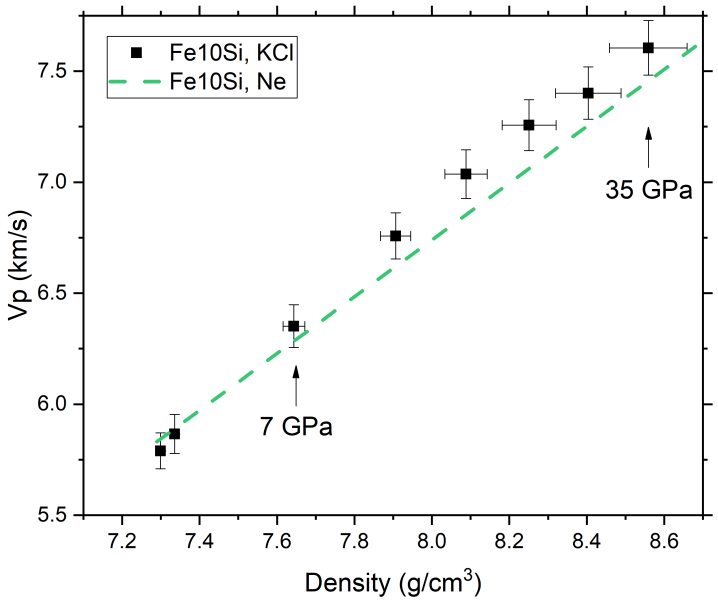

Figure B.1: Velocity-Density relations for bcc Fe10Si in KCl and Ne. It is observed that Vp measured in KCl deviates from that of Ne above 7 GPa, potentially due to sample deformation and texturing.

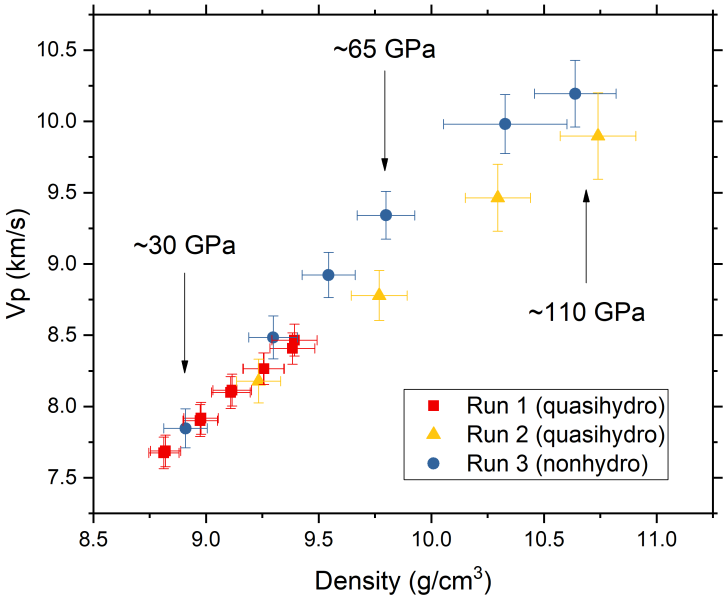

Figure B.2: Velocity-Density relations of Fe5Si in Ne under quasihydrostatic and non-hydrostatic conditions due to bridging between the sample and gasket.

Furthermore, Run 3 is in good agreement in the vicinity of the bcc-hcp transition with the quasihydrostatic data.

At moderate compressions, the influence of the gasket contact is likely strongest due to the inability of Ne to support high differential stresses, such that the bridging of the sample between two opposing sections of the gasket results in significant internal stress in the sample. At sufficiently high pressures however, due to the stiffening of the Ne PTM, the texture and stress experienced by the sample is dominated by that of compression itself, and so the difference between Run 2 and Run 3 decreases at the highest measured pressures.

It has been shown in the previous two sections that the evolution of texture and stress can cause non-linearity in the determined Vp-Rho relations. This can be important for experiments on phases which are not stable at ambient conditions (e.g. hcp Fe-alloys), because phase transitions under non-hydrostatic conditions result in an initial relaxation of stress and a difference in texture (depending strongly on the nature of the transition). The unique problem for high pressure phases is that at the transition pressure, typically the PTM is already fairly stiff, such that after the transition there will be a strong re-application of deviatoric stress on the sample. As pressure is increased, stress and texture will evolve in parallel. For measurements over limited ranges of pressure this can have significant consequences for extrapolations to inner core densities, as most sound velocity measurements reported in literature on Fe-alloys is limited to a pressure range between 40 and 90 GPa [Lin et al., 2003a], [Kantor et al., 2007], [Mao et al., 2012], [Shibazaki et al., 2012], [Kamada et al., 2014], [Sakairi et al., 2018], [Wakamatsu et al., 2018] where such effects appear to be the most pronounced.

B.2 On IXS and NRIXS as high pressure sound velocity measurement techniques

Both IXS and NRIXS have been used to study the effects of Si alloying on the elasticity of hcp Fe at high pressures [Antonangeli et al., 2010], [Lin et al., 2003b], [Badro et al., 2007], [Mao et al., 2012], [Liu et al., 2016], [Antonangeli et al., 2018], [Sakairi et al., 2018]. In spite of this, there has been little consensus on the Vp-ρ relations of Fe-Si alloys. This can be partially reconciled by the specifics of each instrument and the experimental conditions of the experiments.

IXS

For what concerns high-pressure Vp measurements on polycrystalline samples, IXS is a technique which measures the variation of longitudinal phonon energy with pressure. Vp is then derived from the measured aggregate phonon dispersion curve under the assumption of atomic interactions limited to 1st neighbours and a random distribution of crystallites. From study to study there can be small variations of the magnitude of Vp at constant density, due to differences in energy and wavevector calibration and acquisition strategy, as well as other experimental details (see [Antonangeli and Ohtani, 2015]). Furthermore, IXS requires relatively thick samples on the order of 20 μm , and the FWHM of the X-ray beam used for measurement ($\sim$ 20μm x20μm Vertical x Horizontal) is generally much larger than that which

can be attained by NRIXS ($\sim 10\mu m$ x$10\mu m$ V x H) or XRD($\sim 3\mu m$ x$3\mu m$ V x H). Consequently, it is technically challenging to measure samples compressed using any type of PTM simply due to the volume of sample required for good signal quality at the highest achievable pressures.

In spite of this, IXS is a very good technique for measuring the slope of the Vp-Density plot, in particular when *in situ* XRD is also employed such that one obtains density directly for each Vp point. As well, analysis of IXS is relatively model-free compared to NRIXS, and is a technique which does not require knowledge of the thickness of the sample as a function of pressure and hence the equation of state as a prerequisite (as with PA). In this way, IXS remains a preferred tool for constraining the elasticity of core-candidate materials.

With regards to the effects of non-hydrostatic compression on IXS experiments, it has been observed for hcp-Fe that this does not significantly affect velocity-density relations relative to PA [Antonangeli and Ohtani, 2015], and it has been discussed in Section 4.2 that in fact this may not be the case for Fe-Si alloys. In IXS measurements under nonhydrostatic conditions, both Vp and ρ are measured perpendicular to the compression axis. In this direction, under non-hydrostatic compression, IXS measures systematically lower Vp but XRD measures systematically higher volumes due to non-hydrostatic stress [Hemley et al., 1997]. Consequently, in this measurement configuration, density is reduced due to stress and Vp is reduced due to texture. If these quantities are reduced by a similar magnitude, these two effects cancel and the resulting velocity-density relation is similar to that measured under quasihydrostatic conditions. However, this cannot be the case in general, because the introduction of alloying elements acts to affect the elasticity, density and rheology of the material in different ways, such that the relationship between stress, texture at high pressures and the measured Vp-Density relations may not be the same under quasihydrostatic and nonhydrostatic conditions.

With the advent of more brilliant synchrotrons and more tightly focused beams, it remains to be seen how the current state of the art compares to future studies performed under quasihydrostatic conditions.

NRIXS

NRIXS is a technique where the measurement of nuclear resonance absorption is used to probe the lattice dynamics of a material. In such studies, the absorption of photons by a resonant isotope (in this case Fe^{57}) results in an excitation of the nuclei to higher energy levels, and the relaxation of the resonant nuclei are studied in order to extract the vibrational behaviour of that atomic and isotopic species in the material [Hu et al., 2003]. This information can be used to determine the partial phonon density of states (PDOS) for the material studied. In order to extract the sound velocity of a polycrystal, the PDOS is extrapolated to the low energy limit to determine the Debye sound velocity (V_D) - assuming a random distribution of crystallites, quasiharmonic behaviour over the fitted energy range, that the PDOS of the resonant nuclei is representative of the PDOS of the bulk sample, and that the resonant isotope is evenly distributed throughout the measured sample volume ([Hu et al., 2003], [Sturhahn and Jackson, 2007]). V_D is related to Vp and Vs by the relation:

$$\frac{3}{V_D^3} = \frac{1}{V_P^3} + \frac{2}{V_S^3} \tag{B.1}$$

It follows that in order to determine Vp from V_D, one requires knowledge of the bulk modulus, and hence the equation of state.

It has been noted previously that for hcp-Fe there is significant discrepancy between different NRIXS studies for hcp-Fe [Antonangeli and Ohtani, 2015]. For what concerns Fe-Si alloys, it appears that while dVp/dρ is comparable to other instruments, there is often an issue regarding the absolute magnitude of Vp. Both [Lin et al., 2003a] and [Liu et al., 2016] present ambient conditions Vp measurements, and in both instances the derived Vp are at least 0.2 km/s below velocities derived from single-crystal ultrasonics [Machová and Kadečková, 1977]. It is not clear if this is an effect due to the isotopic enrichment of the sample, if this is related to the underlying assumptions in this analysis, or if this is related to other experimental complications. In [Liu et al., 2016], IXS, NRIXS and a P-V EoS were measured on the same sample (isotopically enriched Fe8Ni3Si). Shown in Figure B.3, deriving Vp from NRIXS and the P-V EoS results in Vp up to 8% lower than IXS measurements on the same sample. It is important to note, however, that both the IXS and NRIXS + EoS Vp-ρ relations have dVp/dρ which are generally in good agreement with PA measurements of Fe5Si. As a result it is likely that while NRIXS is not reliable for determining the magnitude of Vp at constant density, it may remain a good technique for constraining the compositional dependence of dVp/dρ.

While it remains to be seen if NRIXS can be developed into a more quantitatively reliable technique, as discussed earlier, the beam size used for NRIXS measurements is smaller than that of IXS. This has important benefits, as this allows for the use of smaller samples, and the beam employed by NRIXS measurements would probe smaller pressure gradients than IXS under similar experimental conditions. Due to the reduced technical limitations on sample size, it is possible to more reliably extend NRIXS measurements to higher pressures than IXS when employing noble gas media.

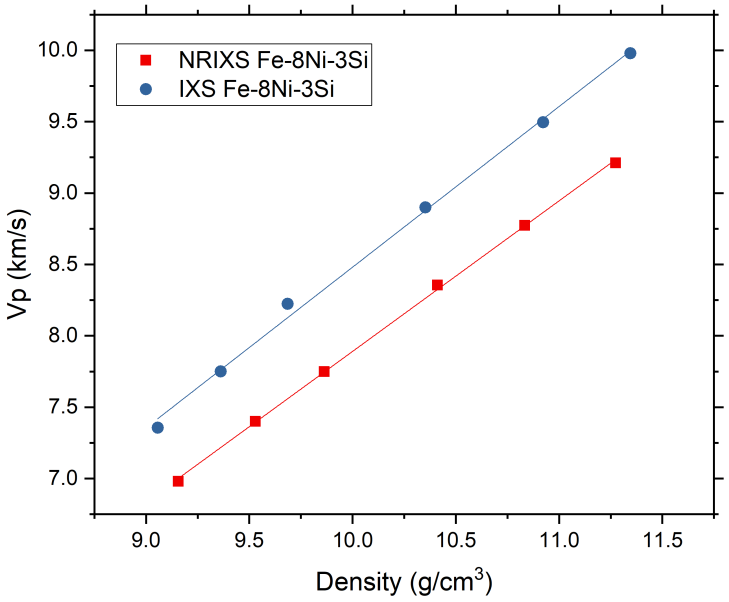

Figure B.3: Velocity-Density relations measured by IXS and determined by a combination of NRIXS and the P-V EoS from [Liu et al., 2016]. It can be seen that the results differ by nearly 8% at constant density.

Appendix C

Tabulated Datasets

C.1 Foreword

In all tabulated data, volumes of samples and X-ray calibrants are presented in units of $Å^3$. Pressures are reported in units of GPa, acoustic travel times are reported in units of nanoseconds, and thicknesses in units of μm . Densities reported in g/cm^3, Vp and Vs in km/s. All errors are provided where available. In some cases, errors in measured calibrant volumes were not analyzed, either due to their small magnitude or (in the case of hcp-Fe10Si) the pressure range measured was not large enough to produce a robust EoS. **The curious reader is warmly invited to contact the author for an electronic copy of the following datasets.**

C.2 Fe5Si

Run #	Comment	Vol C	dVol C	P	dP	Vol Sample	dVol	T	dT	Calib
	bcc			1.36	0.09	23.224	0.002			Mo
				1.41	0.08	23.221	0.001			Mo
				1.39	0.06	23.215	0.002			Mo
				1.74	0.05	23.166	0.001			Mo
				2.15	0.03	23.118	0.004			Mo
				2.56	0.03	23.049	0.001			Mo
				3.56	0.04	22.951	0.013			Mo
				4.36	0.07	22.812	0.001			Mo
				5.75	0.06	22.708	0.009			Mo
				6.75	0.10	22.551	0.001			Mo
				7.62	0.09	22.431	0.002			Mo
				9.40	0.11	22.260	0.001			Mo
				9.60	0.10	22.235	0.001			Mo
				9.80	0.11	22.195	0.001			Mo
				10.43	0.11	22.120	0.001			Mo
				11.33	0.12	22.029	0.001			Mo
				12.33	0.13	21.910	0.001			Mo
				13.79	0.15	21.794	0.001			Mo
				14.75	0.16	21.676	0.001			Mo
				16.07	0.17	21.574	0.001			Mo
		58.434	0.000	9.88	–	22.156				Pt
		58.447	0.007	9.80	–	22.155				Pt
		58.404	0.004	10.04	–	22.135				Pt
		58.307	0.000	10.59	–	22.078				Pt
		58.051	0.000	12.06	–	21.929				Pt
		57.905	0.007	12.91	–	21.860				Pt
		57.688	0.005	14.21	–	21.779				Pt
		57.559	0.006	14.98	–	21.638				Pt

Run	Comment	Vol C	dVol C	P	dP	Vol	dVol	T	dT	Calib
	hcp	29.084	0.025	20.14	0.34	20.472	0.015	300		Mo
		28.933	0.057	21.92	0.68	20.329	0.009	300		Mo
		28.882	0.011	22.53	0.26	20.242	0.008	300		Mo
		28.866	0.009	22.72	0.25	20.235	0.006	300		Mo
		28.800	0.014	23.52	0.29	20.200	0.005	300		Mo
		28.772	0.015	23.87	0.29	20.173	0.009	300		Mo
		28.737	0.029	24.30	0.42	20.141	0.008	300		Mo
		28.698	0.033	24.78	0.46	20.112	0.009	300		Mo
		28.640	0.016	25.51	0.32	20.035	0.005	300		Mo
		28.509	0.024	27.17	0.40	19.956	0.005	300		Mo
		28.410	0.045	28.45	0.63	19.863	0.008	300		Mo
		28.248	0.029	30.59	0.48	19.760	0.006	300		Mo
		28.118	0.026	32.36	0.47	19.655	0.005	300		Mo
		27.925	0.027	35.04	0.51	19.540	0.006	300		Mo
		27.801	0.032	36.83	0.57	19.433	0.006	300		Mo
		27.716	0.013	38.08	0.42	19.250	0.015	300		Mo
		27.613	0.016	39.60	0.46	19.202	0.015	300		Mo
		27.495	0.015	41.40	0.47	19.112	0.015	300		Mo
		27.355	0.022	43.42	0.43	19.001	0.017	300		Mo
		27.252	0.016	44.88	0.68	18.922	0.013	300		Mo
		27.071	0.000	47.68	0.90	18.785	0.005	300		Mo
		27.001	0.010	49.30	0.16	18.683	0.005	300		Mo
		26.895	0.012	50.76	0.66	18.606	0.007	300		Mo
		26.729	0.008	53.60	0.72	18.476	0.007	300		Mo
		26.546	0.011	56.95	0.56	18.315	0.007	300		Mo
		26.360	0.013	60.41	0.53	18.168	0.006	300		Mo
		26.189	0.015	63.63	0.60	18.037	0.006	300		Mo
		25.985	0.005	67.76	0.33	17.865	0.007	300		Mo

Run	Comment	Vol C	dVol C	P	dP	Vol	dVol	T	dT	Calib
hcp HT		33.282	0.020	35.05	0.95	20.121	0.016	1497.95	150	KCl
		33.294	0.018	34.99	0.95	20.149	0.039	1494.555	150	KCl
		33.295	0.019	34.93	0.95	20.140	0.021	1464.485	150	KCl
		33.177	0.030	35.48	0.96	20.075	0.153	1464	150	KCl
		33.151	0.017	35.56	0.95	20.045	0.034	1445.57	150	KCl
		33.044	0.017	36.01	0.96	19.975	0.013	1410.65	150	KCl
		32.940	0.018	36.59	0.97	19.984	0.020	1460.12	150	KCl
		32.785	0.015	37.28	0.98	19.908	0.030	1425.2	150	KCl
		32.668	0.015	37.95	0.99	19.876	0.018	1484.37	150	KCl
		32.168	0.015	40.49	1.03	19.707	0.038	1460.12	150	KCl
		32.102	0.015	40.82	1.03	19.680	0.048	1448.48	150	KCl
		32.010	0.015	41.30	1.04	19.644	0.000	1435.87	150	KCl
		31.911	0.014	41.95	1.05	19.617	0.051	1495.525	150	KCl
		31.781	0.014	42.62	1.06	19.573	0.036	1464.485	150	KCl
		31.635	0.015	43.39	1.07	19.506	0.026	1429.565	150	KCl
		31.486	0.015	44.31	1.08	19.455	0.000	1461.09	150	KCl
		31.325	0.015	45.28	1.10	19.408	0.000	1464	150	KCl
		31.191	0.016	46.02	1.11	19.353	0.056	1429.08	150	KCl
		31.038	0.014	47.02	1.13	19.333	0.032	1455.755	150	KCl
		30.406	0.014	51.23	1.19	19.125	0.000	1494.555	150	KCl
		30.390	0.013	51.31	1.20	19.096	0.023	1480.49	150	KCl
		30.365	0.013	51.46	1.20	19.069	0.022	1466.425	150	KCl
		30.327	0.013	51.69	1.20	19.054	0.019	1450.905	150	KCl
		30.277	0.013	52.02	1.21	19.034	0.015	1437.325	150	KCl
		30.217	0.013	52.52	1.21	19.023	0.000	1484.37	150	KCl
		30.137	0.013	53.06	1.23	18.992	0.023	1469.335	150	KCl
		30.042	0.013	53.72	1.24	18.967	0.019	1456.725	150	KCl
		29.944	0.013	54.39	1.25	18.915	0.018	1432.96	150	KCl
		29.835	0.013	55.31	1.26	18.899	0.019	1500.375	150	KCl

Run	Comment	P	dP	travel time	dt	thickness	dth	Line
Run 1	Spot 1	0.00	0	0.626*	0.003	3.7316	0.0591	1
		0.00	0	0.644+	0.003			2
bcc		7.94		0.574	0.003	3.6794	0.0583	3
		8.35		0.565	0.003	3.6769	0.0583	4
		9.05		0.569	0.003	3.6729	0.0582	5
		10.27		0.561	0.003	3.6660	0.0581	6
		12.52		0.554	0.003	3.6537	0.0579	7
transition		16.90		0.53	0.003	3.6315	0.0576	8
		19.32		0.519	0.003	3.6200	0.0575	9
		23.31		0.492	0.003	3.5624	0.0570	10
hcp		27.55	0.05	0.461	0.002	3.5406	0.0564	11
		32.78	0.4	0.445	0.002	3.5201	0.0562	12
		37.65	0.8	0.432	0.002	3.5023	0.0560	13
		42.85	0.5	0.422	0.002	3.4846	0.0557	14
		48.11	1	0.41	0.002	3.4679	0.0555	15
	Spot 2	0.00	0	0.625*	0.003	3.7316	0.0591	18
		0.00	0	0.628+	0.003			19
bcc		7.94		0.568	0.003	3.6794	0.0582	20
		8.36		0.564	0.003	3.6769	0.0582	21
		9.05		0.566	0.003	3.6729	0.0581	22
		10.31		0.558	0.003	3.6658	0.0580	23
		12.39		0.55	0.003	3.6544	0.0579	24
transition		16.72		0.529	0.003	3.6324	0.0576	25
		19.21		0.519	0.003	3.6205	0.0574	26
		23.32		0.494	0.003	3.5624	0.0569	27
hcp		27.30	0.05	0.462	0.002	3.5416	0.0564	28
		32.65	0.4	0.446	0.002	3.5206	0.0561	29
		37.43	0.8	0.433	0.002	3.5031	0.0559	30
		42.75	0.5	0.422	0.002	3.4850	0.0556	31
		47.74	1	0.413	0.002	3.4691	0.0555	32
								33
Run 2		0.00	0	0.308*	0.001	1.8360	0.0283	34
		0.00	0	0.307+	0.001			35
hcp		41.98	1.5	0.21	0.002	1.7159	0.0278	36
		63.94	2	0.192	0.002	1.6843	0.0276	37
		89.39	2	0.175	0.003	1.6552	0.0273	38
		114.02	3	0.165	0.004	1.6322	0.0274	39
								40
Run 3	NON-	0.00		0.427	0.001	2.5364	0.0389	41
hcp	HYDRO	30.55		0.306	0.002	2.4011	0.0388	42
		44.33		0.279	0.002	2.3671	0.0383	43
		54.03		0.263	0.002	2.3466	0.0378	44
		64.92		0.249	0.002	2.3261	0.0373	45
		90.39		0.229	0.002	2.2857	0.0430	46
		107.24		0.222	0.003	2.2632	0.0419	47

Run #	Comment	Rho	dRho	Vp	dVp	Vs	dVs	Line
Run 1	Spot 1	7.558	0.007	5.961	0.099			1
								2
bcc		7.884	0.012	6.410	0.107	3.285	0.160	3
		7.900	0.013	6.508	0.109	3.405	0.159	4
		7.926	0.014	6.455	0.108	3.291	0.162	5
		7.971	0.015	6.535	0.109	3.344	0.164	6
		8.051	0.018	6.595	0.111	3.317	0.168	7
transition		8.200	0.022	6.852	0.115	3.484	0.174	8
		8.278	0.025	6.975	0.118	3.554	0.178	9
		8.686	0.060	7.241	0.124	4.013	0.175	10
hcp		8.848	0.048	7.680	0.127	4.378	0.173	11
		9.004	0.054	7.910	0.131	4.526	0.179	12
		9.141	0.061	8.107	0.135	4.649	0.184	13
		9.281	0.062	8.257	0.138	4.708	0.190	14
		9.416	0.069	8.458	0.142	4.839	0.196	15
	Spot 2	7.558	0.007	5.961	0.099			18
								19
bcc		7.884	0.012	6.478	0.108	3.383	0.158	20
		7.900	0.013	6.519	0.109	3.421	0.159	21
		7.926	0.014	6.489	0.108	3.341	0.161	22
		7.972	0.015	6.569	0.110	3.393	0.163	23
		8.047	0.017	6.644	0.111	3.396	0.167	24
transition		8.194	0.022	6.867	0.116	3.514	0.173	25
		8.275	0.025	6.976	0.118	3.560	0.177	26
		8.687	0.060	7.211	0.123	3.973	0.175	27
hcp		8.840	0.047	7.666	0.126	4.366	0.172	28
		9.000	0.053	7.894	0.131	4.508	0.178	29
		9.135	0.060	8.090	0.134	4.632	0.184	30
		9.279	0.062	8.258	0.137	4.711	0.189	31
		9.407	0.069	8.400	0.140	4.771	0.195	32
								33
Run 2		7.558	0.007	5.961	0.099			34
								35
hcp		9.258	0.072	8.171	0.153	4.616	0.213	36
		9.790	0.088	8.772	0.170	4.881	0.242	37
		10.314	0.100	9.459	0.225	5.270	0.316	38
		10.756	0.118	9.892	0.292	5.403	0.415	39
								40
Run 3	NON-HYDRO	7.558	0.006	5.961	0.092	3.133	0.135	41
hcp		8.909	0.096	7.847	0.137	4.586	0.188	42
		9.298	0.109	8.484	0.150	5.015	0.206	43
		9.544	0.118	8.923	0.159	5.333	0.218	44
		9.799	0.128	9.342	0.168	5.619	0.230	45
		10.328	0.274	9.981	0.207	5.927	0.324	46
		10.638	0.181	10.195	0.234	5.902	0.332	47

C.3 Fe5Ni5Si

Vol Calib	P	Vol Sample	dVol	T	dT	Calib	c/a	dc/a
33.018	36.170	19.966	0.062	1433	150	KCl		
32.573	38.343	19.799	0.051	1430	150	KCl		
32.187	40.487	19.843	0.053	1517	150	KCl		
31.789	42.519	19.633	0.085	1430	150	KCl		
31.398	44.847	19.471	0.081	1469	150	KCl		
30.993	47.300	19.335	0.037	1455	150	KCl		
30.624	49.703	19.184	0.052	1462	150	KCl		
30.296	51.949	19.131	0.069	1473	150	KCl		
29.946	54.356	18.878	0.067	1417	150	KCl		
29.697	56.451	18.905	0.079	1562	150	KCl		
29.389	58.788	18.700	0.079	1527	150	KCl		
29.126	60.823	18.595	0.093	1470	150	KCl		
28.869	62.996	18.448	0.094	1477	150	KCl		
28.603	65.236	18.387	0.080	1424	150	KCl		
28.384	67.301	18.294	0.081	1470	150	KCl		
28.171	69.298	18.166	0.079	1474	150	KCl		
27.928	71.630	18.067	0.081	1458	150	KCl		
27.744	73.463	17.999	0.070	1452	150	KCl		
26.662	85.506	17.509	0.094	1506	150	KCl		
26.612	86.104	17.511	0.067	1501	150	KCl		
26.536	86.999	17.445	0.070	1488	150	KCl		
26.438	88.147	17.404	0.080	1453	150	KCl		
26.318	89.667	17.364	0.075	1458	150	KCl		
26.198	91.167	17.351	0.079	1440	150	KCl		
	20.801	20.345		300		Pt	1.6058	0.0050
	21.746	20.347		300		Pt	1.6173	0.0025
	23.276	20.207		300		Pt	1.6173	0.0024
	24.642	20.098		300		Pt	1.6171	0.0024
	26.102	20.007		300		Pt	1.6173	0.0024
	28.811	19.879		300		Pt	1.6160	0.0024
	30.915	19.768		300		Pt	1.6171	0.0024
	32.731	19.630		300		Pt	1.6156	0.0024
	34.769	19.442		300		Pt	1.6152	0.0024
	35.485	19.374		300		Pt	1.6151	0.0024
	37.374	19.255		300		Pt	1.6148	0.0024
	40.299	19.144		300		Pt	1.6140	0.0024
	43.658	18.995		300		Pt	1.6134	0.0023
	46.564	18.862		300		Pt	1.6130	0.0023
	49.801	18.715		300		Pt	1.6121	0.0023
	52.883	18.582		300		Pt	1.6119	0.0023
	55.660	18.405		300		Pt	1.6116	0.0023

C.4 Fe8Si

	Comment	P	dP	t	dt	th	dth	Line
		0.00		0.105	0.001	0.6153	0.0094	1
Comp	bcc	1.58		0.103	0.001	0.6133	0.0094	2
		2.76		0.1	0.001	0.6118	0.0094	3
		3.83		0.0995	0.001	0.6106	0.0093	4
		5.35		0.098	0.001	0.6088	0.0093	5
		7.66		0.0954	0.001	0.6063	0.0093	6
		10.21		0.094	0.001	0.6038	0.0092	7
	trans	12.99		0.0924	0.001	0.5996	0.0092	8
		15.23		0.0914	0.001	0.5952	0.0091	9
		18.76		0.0894	0.001	0.5910	0.0091	10
		21.69		0.0874	0.001	0.5877	0.0091	11
	hcp	25.74		0.0834	0.001	0.5845	0.0091	12
		29.18		0.0816	0.001	0.5822	0.0091	13
Decomp		27.66		0.0826	0.001	0.5832	0.0091	14
		24.60		0.0842	0.001	0.5853	0.0091	15
	trans	20.48		0.086	0.001	0.5884	0.0091	16
		17.19		0.0876	0.001	0.5911	0.0091	17
		14.15		0.0892	0.001	0.5938	0.0091	18
		10.91		0.0911	0.001	0.5979	0.0092	19
	bcc?	7.84		0.0928	0.001	0.6020	0.0092	20

	Comment	Rho	dRho	Vp	dVp	Vs	dVs	Line
		7.307	0.009	5.860	0.106	3.067	0.165	1
Comp	bcc	7.380	0.007	5.954	0.108	3.106	0.170	2
		7.432	0.008	6.118	0.112	3.267	0.173	3
		7.479	0.009	6.136	0.112	3.228	0.180	4
		7.543	0.012	6.213	0.114	3.248	0.190	5
		7.636	0.016	6.356	0.118	3.323	0.206	6
		7.734	0.022	6.423	0.120	3.281	0.229	7
	trans	7.898	0.023	6.489	0.122	3.254	0.254	8
		8.072	0.030	6.512	0.123	2.832	0.313	9
		8.245	0.040	6.611	0.126	3.442	0.288	10
		8.387	0.055	6.724	0.129	3.408	0.320	11
	hcp	8.524	0.068	7.009	0.137	3.635	0.342	12
		8.628	0.078	7.134	0.141	3.677	0.369	13
Decomp		8.583	0.074	7.060	0.139	3.631	0.359	14
		8.489	0.064	6.952	0.136	3.600	0.334	15
	trans	8.355	0.051	6.842	0.132	3.623	0.296	16
		8.241	0.040	6.748	0.129	3.640	0.266	17
		8.131	0.029	6.657	0.126	3.659	0.239	18
		7.965	0.017	6.563	0.124	3.742	0.209	19
	bcc?	7.803	0.004	6.487	0.121	3.841	0.184	20

C.5 Fe10Si

Run	Comment	Vol C	dVol C	P	dP	Vol	dVol	Calibrant
ID15b	bcc	30.4879	0.0006	6.03		22.247	0.001	Mo
		30.4668	0.0004	6.22		22.222	0.001	Mo
		30.4464	0.0004	6.42		22.201	0.002	Mo
		30.4223	0.0005	6.64		22.174	0.002	Mo
		30.3995	0.0005	6.86		22.148	0.002	Mo
		30.3461	0.0004	7.37		22.089	0.002	Mo
		30.2884	0.0004	7.92		22.021	0.002	Mo
		30.2335	0.0004	8.46		21.949	0.002	Mo
		30.1575	0.0004	9.20		21.859	0.002	Mo
		30.0328	0.0008	10.45		21.722	0.002	Mo
		29.9968	0.0008	10.81		21.683	0.002	Mo
		29.8580	0.0010	12.23		21.524	0.002	Mo
		29.7372	0.0010	13.50		21.390	0.002	Mo
		29.5830	0.0008	15.16		21.233	0.002	Mo
		29.4483	0.0006	16.64		21.062	0.001	Mo
		29.3775	0.0010	17.43		20.976	0.007	Mo
		29.2910	0.0011	18.41		20.870	0.001	Mo
		29.1950	0.0012	19.51		20.779	0.001	Mo
		29.0896	0.0011	20.74		20.686	0.001	Mo
		28.9741	0.0013	22.12		20.568	0.001	Mo
		28.8653	0.0016	23.44		20.447	0.001	Mo
		28.7353	0.0010	25.05		20.325	0.002	Mo
		28.6393	0.0009	26.26		20.210	0.002	Mo
ID27		57.1911	0.0090	17.27		21.029	0.004	Pt
		57.1678	0.0097	17.42		21.027	0.002	Pt
		56.9768	0.0040	18.64		20.899	0.010	Pt
		57.0071	0.0048	18.45		20.876	0.004	Pt
		56.8506	0.0064	19.46		20.839	0.004	Pt
		56.7438	0.0042	20.17		20.714	0.004	Pt
		56.5751	0.0035	21.29		20.673	0.010	Pt
		56.3397	0.0042	22.89		20.421	0.006	Pt
		55.8435	0.0029	26.40		20.302	0.005	Pt
		55.4432	0.0077	29.35		20.034	0.007	Pt
		54.8043	0.0078	34.32		19.703	0.013	Pt
		54.6969	0.0145	35.19		19.659	0.014	Pt
		54.6648	0.0069	35.45		19.622	0.018	Pt
		54.4000	0.0055	37.63		19.522	0.016	Pt
		54.2439	0.0132	38.95		19.436	0.011	Pt
		54.1964	0.0057	39.35		19.361	0.025	Pt

hcp	Vol C	dVol C	P	dP	Vol	dVol	Calib	c/a	dc/a
	49.0494	0.0000	96.72		17.092	0.007	Pt	1.6173	0.0031
	49.1169	0.0114	95.76		17.082	0.009	Pt		
	49.1304	0.0229	95.57		17.051	0.005	Pt	1.6137	0.0020
	48.9891	0.0122	97.58		17.004	0.011	Pt	1.6188	0.0048
	48.9377	0.0094	98.32		16.966	0.006	Pt	1.6174	0.0025
	48.7712	0.0116	100.74		16.888	0.007	Pt	1.6186	0.0030
	48.4539	0.0148	105.48		16.662	0.007	Pt	1.6190	0.0031
	48.3544	0.0088	106.99		16.637	0.006	Pt	1.6206	0.0027
	48.2601	0.0162	108.44		16.604	0.007	Pt	1.6209	0.0033
	48.1966	0.0194	109.43		16.602	0.010	Pt	1.6236	0.0047
	48.1511	0.0092	110.14		16.513	0.007	Pt	1.6190	0.0031
	48.0494	0.0088	111.73		16.499	0.009	Pt	1.6206	0.0042
	47.9486	0.0088	113.33		16.459	0.008	Pt	1.6200	0.0036
	47.8268	0.0129	115.29		16.410	0.009	Pt	1.6169	0.0040
	47.7314	0.0103	116.84		16.383	0.008	Pt	1.6181	0.0033
	47.6350	0.0115	118.41		16.343	0.009	Pt	1.6168	0.0040
	47.4549	0.0122	121.41		16.393	0.009	Pt	1.6273	0.0043
	47.3176	0.0099	123.73		16.396	0.010	Pt	1.6315	0.0045
	47.2285	0.0133	125.25		16.362	0.008	Pt	1.6315	0.0039
	47.1900	0.0103	125.91		16.265	0.009	Pt	1.6229	0.0040
	47.1350	0.0105	126.86		16.247	0.008	Pt	1.6235	0.0036
	46.9986	0.0141	129.24		16.215	0.009	Pt	1.6242	0.0044

		P	dP	t	dt	th	dth	Line
Run 2		0.00	0	0.221	0.001	1.2796	0.0165	1
	bcc	5.54	0.1	0.203	0.001	1.2645	0.0163	2
		13.09	0.6	0.19	0.001	1.2477	0.0162	3
		21.80	0.1	0.178	0.001	1.2318	0.0160	4
		30.34	0.3	0.169	0.001	1.2187	0.0159	5
		39.58	0.2	0.16	0.001	1.2064	0.0158	6
	transition	49.17	0.3	0.155	0.002	1.1953	0.0157	7
		61.10	1	0.151	0.002	1.1851	0.0154	8
	hcp	71.96	0.5	0.146	0.002	1.1752	0.0153	9
		82.59	0.8	0.138	0.002	1.1665	0.0152	10
		92.63	1	0.134	0.002	1.1590	0.0151	11
		102.73	1	0.129	0.002	1.1520	0.0150	12
		112.55	2	0.125	0.002	1.1457	0.0150	13
		125.36	2	0.123	0.002	1.1382	0.0149	14
		96.77	1	0.131	0.002	1.1560	0.0151	15
		90.39	1	0.136	0.001	1.1606	0.0151	16
		83.70	0.8	0.137	0.001	1.1656	0.0152	17
		77.82	0.8	0.14	0.001	1.1703	0.0152	18
Run 1	Sample 1	0.00	0	0.225	0.001	1.3028	0.0168	20
	bcc	4.73	0.05	0.21	0.001	1.2895	0.0166	21
		9.37	0.1735	0.1985	0.001	1.2783	0.0165	22
		12.36	0.321	0.193	0.001	1.2718	0.0164	23
		17.56	0.14	0.187	0.001	1.2616	0.0163	24
		21.06	0.0045	0.179	0.001	1.2554	0.0163	25
		25.45	0.1695	0.174	0.002	1.2481	0.0162	26
		30.48	0.224	0.171	0.002	1.2405	0.0161	27
		36.00	0.235	0.165	0.002	1.2329	0.0160	28
		41.93	0.207	0.162	0.002	1.2254	0.0160	29
	trans	49.41	0.2	0.157	0.002	1.2167	0.0159	30
		56.90	0.5	0.155	0.001	1.2108	0.0169	31
		64.63	0.5	0.154	0.001	1.2031	0.0156	32
	hcp	71.22	0.5	0.15	0.001	1.1971	0.0155	33
		77.49	0.5	0.145	0.001	1.1917	0.0154	34
		79.58	0.5	0.144	0.001	1.1900	0.0154	35
		84.39	0.5	0.142	0.001	1.1862	0.0154	36
	Sample 2	0.00	0	0.224	0.001	1.2970	0.0167	38
	bcc	4.73	0.02	0.209	0.001	1.2838	0.0166	39
		9.58	0.032	0.2	0.001	1.2722	0.0164	40
		12.77	0.1	0.194	0.001	1.2653	0.0164	41
		17.74	0.1	0.186	0.001	1.2557	0.0162	42
		21.07	0.1	0.178	0.001	1.2498	0.0162	43
		25.67	0.2	0.174	0.001	1.2422	0.0161	44
		30.82	0.2	0.1695	0.001	1.2345	0.0160	45
		36.30	0.2	0.163	0.001	1.2270	0.0160	46

		Rho	dRho	Vp	dVp	Vs	dVs	Line
Run 2		7.287	0.006	5.790	0.079	3.188	0.109	1
	bcc	7.550	0.012	6.229	0.086	3.449	0.119	2
		7.859	0.031	6.567	0.092	3.518	0.136	3
		8.168	0.033	6.920	0.098	3.609	0.154	4
		8.435	0.044	7.211	0.103	3.665	0.175	5
		8.695	0.054	7.540	0.109	3.787	0.200	6
	transition	8.939	0.065	7.712	0.142	3.691	0.271	7
		9.172	0.037	7.848	0.146			8
	hcp	9.406	0.039	8.049	0.152			9
		9.619	0.048	8.453	0.165			10
		9.807	0.055	8.649	0.171			11
		9.986	0.060	8.930	0.181			12
		10.151	0.071	9.166	0.190			13
		10.354	0.077	9.254	0.193			14
		9.882	0.057	8.825	0.177			15
		9.766	0.053	8.534	0.128			16
		9.640	0.048	8.508	0.127			17
		9.525	0.045	8.359	0.124			18
Run 1	Sample 1	7.287	0.006	5.790	0.079	3.188	0.109	20
	bcc	7.514	0.010	6.141	0.084	3.375	0.117	21
		7.713	0.017	6.440	0.089	3.531	0.126	22
		7.832	0.024	6.590	0.092	3.586	0.132	23
		8.023	0.028	6.747	0.094	3.555	0.144	24
		8.143	0.032	7.013	0.099	3.773	0.149	25
		8.286	0.038	7.173	0.124	3.812	0.189	26
		8.439	0.044	7.255	0.127	3.723	0.204	27
		8.597	0.050	7.472	0.133	3.823	0.220	28
		8.756	0.057	7.564	0.136	3.734	0.241	29
	trans	8.945	0.065	7.750	0.141	3.741	0.268	30
		9.076	0.160	7.812	0.120			31
		9.251	0.034	7.813	0.113			32
	hcp	9.391	0.039	7.981	0.116			33
		9.519	0.043	8.219	0.121			34
		9.560	0.044	8.264	0.121			35
		9.654	0.047	8.353	0.123			36
	Sample 2	7.287	0.006	5.790	0.079			38
	bcc	7.514	0.010	6.142	0.085	3.377	0.117	39
		7.721	0.016	6.361	0.088	3.411	0.127	40
		7.847	0.021	6.522	0.091	3.471	0.134	41
		8.029	0.028	6.751	0.095	3.553	0.144	42
		8.144	0.032	7.021	0.099	3.783	0.149	43
		8.293	0.038	7.139	0.101	3.755	0.161	44
		8.449	0.044	7.283	0.104	3.751	0.174	45
		8.605	0.051	7.528	0.108	3.893	0.187	46

	P	Vol		P	Vol
Run 1			Run 2		
	31.68	19.950		0.86	22.840
	37.47	19.526		0.97	22.827
	39.25	19.445		1.18	22.806
	40.84	19.346		1.44	22.762
	42.11	19.275		2.08	22.680
	44.02	19.183		3.19	22.546
	45.38	19.108		4.11	22.437
	46.66	19.036		4.54	22.358
	47.72	18.970		4.79	22.348
	48.72	18.915		5.55	22.252
	49.90	18.859		5.82	22.220
	51.35	18.786		6.41	22.147
	52.59	18.729		7.13	22.072
	54.29	18.656		8.50	21.915
	56.99	18.529		9.57	21.800
	59.63	18.418		9.99	21.753
				10.65	21.685
				11.72	21.581

C.6 Fe12Si

		P	dP	t	dt	th	dth	Line
Run 1		0.00		0.21	0.001	1.2943	0.0159	1
	Spot 1	45.04	0.2	0.148	0.001	1.2175	0.0151	2
	Spot 2	45.04	0.2	0.145	0.001	1.2175	0.0151	3
	Spot 2	51.86	0.5	0.14	0.001	1.2100	0.0150	4
	Spot 1	51.86	0.5	0.142	0.001	1.2100	0.0150	5
transition	Spot 1	62.16		0.137	0.001	1.1986	0.0148	6
	Spot 3	62.16		0.139	0.001	1.1986	0.0148	7
hcp?	Spot 1	77.04		0.1345	0.001	1.1880	0.0153	8
								9
Run 2		0.00	0	0.21	0.001	1.2943	0.0159	10
Compression	S 1	28.18	0.04	0.164	0.001	1.2391	0.0154	11
	S 2	28.18	0.04	0.162	0.001	1.2391	0.0154	12
	S 1	31.37	0.04	0.16	0.001	1.2346	0.0153	13
	S 2	31.37	0.04	0.159	0.001	1.2346	0.0153	14
Decompression	S 1	29.80	0.02	0.161	0.001	1.2368	0.0153	15
	S 2	29.80	0.02	0.16	0.001	1.2368	0.0153	16
	S 1	27.90	0.05	0.163	0.001	1.2396	0.0154	17
	S 2	27.90	0.05	0.164	0.001	1.2396	0.0154	18
	S 1	25.21	0.04	0.168	0.001	1.2436	0.0154	19
	S 2	25.21	0.04	0.167	0.001	1.2436	0.0154	20
	S 1	21.28	0.12	0.169	0.001	1.2498	0.0155	21
	S 2	21.40	0.12	0.172	0.001	1.2496	0.0155	22
	S 1	14.37	0.15	0.181	0.001	1.2619	0.0156	23
	S 2	14.52	0.15	0.184	0.001	1.2616	0.0156	24
		5.46	0.17	0.189	0.001	1.2805	0.0159	25
		3.24	0.1	0.195	0.001	1.2859	0.0159	26
Compression		8.35	0.02	0.185	0.001	1.2740	0.0158	27
		8.35	0.02	0.186	0.001	1.2740	0.0158	28
		11.64	0.15	0.179	0.001	1.2672	0.0157	29
		11.80	0.15	0.179	0.001	1.2669	0.0157	30
		17.95	0.5	0.171	0.001	1.2554	0.0156	31
		18.46	0.5	0.169	0.001	1.2546	0.0156	32
		23.29	0.45	0.163	0.001	1.2466	0.0155	33
		29.32	0.35	0.159	0.001	1.2375	0.0154	34
		29.69	0.35	0.159	0.001	1.2370	0.0153	35
		36.19	0.4	0.153	0.001	1.2282	0.0152	36
		36.61	0.4	0.154	0.001	1.2277	0.0152	37

		Rho	dRho	Vp	dVp	Vs	dVs	Line
Run 1		7.213	0.006	6.163	0.081	3.431	0.110	1
	Spot 1	8.667	0.039	8.226	0.116	4.457	0.169	2
	Spot 2	8.667	0.039	8.396	0.119	4.689	0.168	3
	Spot 2	8.829	0.041	8.643	0.124	4.830	0.175	4
	Spot 1	8.829	0.041	8.521	0.122	4.665	0.175	5
transition	Spot 1	9.083	0.022	8.749	0.125	4.558	0.189	6
	Spot 3	9.083	0.022	8.623	0.123	4.374	0.191	7
hcp?	Spot 1	9.328	0.105	8.832	0.131	4.327	0.227	8
								9
Run 2		7.213	0.006	6.163	0.081	3.431	0.110	10
Compression	S 1	8.219	0.035	7.556	0.104	4.084	0.150	11
	S 2	8.219	0.035	7.649	0.106	4.212	0.150	12
	S 1	8.310	0.036	7.716	0.107	4.194	0.154	13
	S 2	8.310	0.036	7.765	0.108	4.260	0.153	14
Decompression	S 1	8.266	0.035	7.682	0.107	4.201	0.152	15
	S 2	8.266	0.035	7.730	0.107	4.266	0.151	16
	S 1	8.211	0.035	7.605	0.105	4.162	0.149	17
	S 2	8.211	0.035	7.558	0.104	4.098	0.150	18
	S 1	8.132	0.034	7.402	0.102	3.981	0.147	19
	S 2	8.132	0.034	7.447	0.103	4.042	0.147	20
	S 1	8.011	0.033	7.395	0.102	4.120	0.141	21
	S 2	8.015	0.033	7.265	0.099	3.938	0.142	22
	S 1	7.782	0.032	6.972	0.095	3.825	0.133	23
	S 2	7.788	0.032	6.857	0.093	3.658	0.134	24
		7.448	0.031	6.614	0.091	3.750	0.123	25
		7.356	0.031	6.470	0.089	3.670	0.120	26
Compression		7.562	0.031	6.723	0.093	3.757	0.128	27
		7.562	0.031	6.687	0.093	3.708	0.128	28
		7.686	0.032	6.911	0.096	3.860	0.132	29
		7.691	0.032	6.909	0.096	3.851	0.132	30
		7.903	0.033	7.167	0.101	3.941	0.141	31
		7.920	0.033	7.247	0.102	4.029	0.141	32
		8.074	0.034	7.466	0.106	4.140	0.147	33
		8.252	0.035	7.598	0.108	4.101	0.156	34
		8.262	0.035	7.595	0.108	4.084	0.156	35
		8.441	0.037	7.836	0.113	4.196	0.164	36
		8.452	0.037	7.782	0.112	4.105	0.166	37

C.7 Fe17Si

		P	V			P	V
Run 1	Compression	5.00	21.7911	Run 1		15.11	20.7976
		5.10	21.7834			15.60	20.7440
		5.42	21.7581			16.48	20.6474
		5.98	21.6968			17.93	20.5368
		6.68	21.6314			18.61	20.5002
		7.20	21.5729			19.51	20.4246
		7.91	21.4854			20.62	20.3910
		8.56	21.4241			21.62	20.2627
		9.19	21.3572			22.95	20.1763
		10.13	21.2935			23.38	20.1330
		10.88	21.1655			23.44	20.1924
		11.31	21.1283			25.44	20.0545
		11.57	21.0976			26.64	19.9383
		11.88	21.0724			28.74	19.8110
		12.23	21.0522			29.70	19.7996
		12.82	20.9814		Decompression	27.01	19.9818
		13.11	20.9449			20.17	20.4540
		13.76	20.8902			14.87	20.8717
		14.84	20.8254			12.44	21.0672
						7.52	21.5353

		P	V			P	V
Run 2	Compression	1.73	22.1772	Run 2		38.21	19.2098
		2.14	22.1366			40.13	19.1228
		2.32	22.1094			42.62	19.0001
		3.06	22.0334			44.06	18.9282
		3.21	22.0019			46.07	18.8653
		3.61	21.9710			47.62	18.7807
		4.17	21.8968			49.13	18.6680
		4.62	21.8532			52.38	18.5111
		4.96	21.8273			53.71	18.4406
		5.29	21.7988			54.68	18.3846
		5.63	21.7135			56.60	18.3206
		8.00	21.4418			58.01	18.2603
		10.56	21.1564			58.91	18.2246
		12.40	20.9756			60.06	18.1779
		12.76	20.9402			61.40	18.1355
		14.72	20.7481			63.02	18.0835
		15.58	20.6883			63.11	18.0161
		18.89	20.4072			64.09	17.9736
		24.18	20.1006			64.59	17.9929
		25.91	19.9586		Decompression	64.80	17.9432
		29.07	19.7856			62.53	18.0285
		31.69	19.6042			57.13	18.3084
		33.18	19.5250			53.33	18.5270
		34.20	19.4414			32.79	19.5458
		35.99	19.2983				

		P	dP	t	dt	th	dth	Line
Run 1		0.00	0	0.233	0.001	1.4632	0.0175	1
		0.55	0.02	0.23	0.001	1.4617	0.0175	2
		1.53	0.2	0.229	0.001	1.4590	0.0174	3
		3.55	0.1	0.222	0.001	1.4537	0.0174	4
		6.75	0.15	0.211	0.001	1.4458	0.0173	5
		10.40	0.15	0.201	0.001	1.4376	0.0172	6
		14.21	0.35	0.194	0.001	1.4297	0.0171	7
		17.82	0.05	0.189	0.001	1.4227	0.0170	8
		22.11	0.15	0.182	0.001	1.4151	0.0169	9
								10
Run 2		0.00	0	0.2335	0.001	1.4664	0.0175	11
		1.53	0.02	0.2285	0.001	1.4621	0.0174	12
		6.41	0.05	0.2135	0.001	1.4497	0.0174	13
		10.21	0.1	0.203	0.001	1.4411	0.0175	14
		16.43	0.15	0.193	0.001	1.4284	0.0176	15
		21.22	0.18	0.1865	0.001	1.4197	0.0178	16
								17
Run 3		0.00		0.235	0.001	1.4758	0.0176	18
	Comp	2.42		0.225	0.001	1.4691	0.0174	19
		3.08		0.222	0.001	1.4674	0.0174	20
		4.14		0.218	0.001	1.4647	0.0174	21
		5.11		0.2145	0.001	1.4622	0.0173	22
		6.34		0.213	0.001	1.4592	0.0173	23
		7.82		0.2085	0.001	1.4557	0.0173	24
		9.42		0.2025	0.001	1.4521	0.0172	25
		11.29		0.201	0.001	1.4480	0.0172	26
		13.91		0.194	0.001	1.4426	0.0171	27
		17.72		0.189	0.001	1.4351	0.0170	28
	Decomp	10.03		0.201	0.001	1.4507	0.0172	29
		6.20		0.211	0.001	1.4596	0.0173	30
		4.02		0.219	0.001	1.4650	0.0174	31

		Rho	dRho	Vp	dVp	Vs	dVs	Line
Run 1		7.090	0.003	6.280	0.080	3.316	0.115	1
		7.112	0.006	6.355	0.081	3.395	0.115	2
		7.152	0.006	6.371	0.081	3.359	0.117	3
		7.230	0.007	6.548	0.084	3.493	0.119	4
		7.349	0.008	6.852	0.088	3.746	0.122	5
		7.476	0.010	7.152	0.093	3.980	0.127	6
		7.600	0.012	7.370	0.096	4.106	0.131	7
		7.712	0.014	7.528	0.098	4.169	0.136	8
		7.838	0.016	7.775	0.102	4.335	0.141	9
								10
Run 2		7.090	0.003	6.280	0.080	3.316	0.115	11
		7.151	0.020	6.399	0.081	3.399	0.117	12
		7.337	0.024	6.790	0.088	3.678	0.124	13
		7.469	0.028	7.099	0.093	3.917	0.129	14
		7.670	0.035	7.401	0.099	4.054	0.140	15
		7.813	0.040	7.612	0.104	4.148	0.148	16
								17
Run 3		7.090	0.003	6.280	0.080	3.316	0.115	18
	Comp	7.186	0.007	6.530	0.083	3.530	0.116	19
		7.212	0.007	6.610	0.084	3.605	0.117	20
		7.253	0.007	6.719	0.085	3.697	0.118	21
		7.289	0.007	6.817	0.087	3.781	0.119	22
		7.334	0.008	6.851	0.087	3.765	0.121	23
		7.387	0.009	6.982	0.089	3.871	0.122	24
		7.443	0.010	7.171	0.092	4.049	0.124	25
		7.506	0.010	7.204	0.093	4.010	0.127	26
		7.591	0.012	7.436	0.096	4.207	0.130	27
		7.709	0.014	7.593	0.099	4.261	0.134	28
	Decomp	7.463	0.010	7.218	0.093	4.084	0.125	29
		7.329	0.008	6.917	0.088	3.862	0.120	30
		7.248	0.007	6.689	0.085	3.664	0.118	31